Multi-Dimensional Quantum Tunneling in Heavy-Ion Fusion Reactions

博士論文

Multi-Dimensional Quantum Tunneling in Heavy-Ion Fusion Reactions

（重イオン核融合反応における
多次元量子トンネル現象）

萩野 浩一

平成９年

Multi-Dimensional Quantum Tunneling in Heavy-Ion Fusion Reactions

by

Kouichi Hagino

A thesis submitted in partial fulfillment
of the requirements for the degree of
Doctor of Philosophy (Physics)
at the
Tohoku University

March, 1998

Preface

Fusion is defined as a reaction where two separate nuclei combine together to form a composite system. When the incident energy is not so large and the system is not so light, the reaction process is predominantly governed by quantum tunneling over the Coulomb barrier created by the strong cancellation between the repulsive Coulomb force and the attractive nuclear interaction. Extensive experimental as well as theoretical studies have revealed that fusion reactions are strongly influenced by couplings of the relative motion of the colliding nuclei to several nuclear intrinsic motions. Heavy-ion subbarrier fusion reactions thus provide a good opportunity to address the general problem on quantum tunneling in the presence of couplings, which has been a popular subject in the past decade in many branches of physics and chemistry.

Thanks to the recent developments in experimental techniques, fusion cross sections can now become measured with high accuracy in small energy intervals. Such high precision experimental data have generated a renewed interest in heavy-ion subbarrier fusion reactions in recent years. For instance, they have enabled a detailed study of the effects of couplings on fusion reactions and have thus offered a good opportunity to test any theoretical framework for subbarrier fusion reactions.

This thesis describes recent developments in subbarrier fusion reactions from the theoretical point of view. This work was partly motivated by the high precision experimental data of fusion cross sections recently measured at the Australian National University, and has been done in collaboration with international theorists as well as experimentalists.

The work presented in this thesis has been or will be published in the following publications:

1. *Role of mass renormalization in adiabatic quantum tunneling*,
   N. Takigawa, K. Hagino, M. Abe, and A.B. Balantekin, Phys. Rev. C49 (1994)2630.

2. *Dynamical norm method for non-adiabatic macroscopic quantum tunneling*,
   N. Takigawa, K. Hagino, and M.Abe, Phys. Rev. C51 (1995)187.

3. *Effects of finite excitation energy of environment on fast quantum tunneling*,
   K. Hagino, N. Takigawa, J.R. Bennett, and D.M. Brink, Phys. Rev. C51 (1995) 3190.

4. *Path integral approach to no-Coriolis approximation in heavy-ion collisions*,
   K. Hagino, N. Takigawa, A.B. Balantekin, and J.R. Bennett, Phys. Rev. C52 (1995)286.

5. *Reply to "Comment on 'Shape and superdeformed structure in Hg isotopes in relativistic mean field model' and 'Structure of neutron-deficient Pt, Hg and Pb isotopes'"*,
   N. Takigawa, S. Yoshida, K. Hagino, S.K. Patra, and C.R. Praharaj, Phys. Rev. C53 (1996)1038.

6. *Thermal fission rate around superfluid-normal phase transition*,
K. Hagino, N. Takigawa, and M.Abe, Phys. Rev. C53 (1996)1840.

7. *Validity of the linear coupling approximation in heavy-ion fusion reactions at sub-barrier energies*,
K. Hagino, N. Takigawa, M. Dasgupta, D.J. Hinde, and J.R. Leigh, Phys. Rev. C55 (1997)276.

8. *Adiabatic quantum tunneling in heavy-ion sub-barrier fusion*,
K. Hagino, N. Takigawa, M. Dasgupta, D.J. Hinde, and J.R. Leigh, Phys. Rev. Lett. 79 (1997)2014.

9. *Role of anharmonicities of nuclear vibrations in fusion reactions at subbarrier energies*,
K. Hagino, N. Takigawa, and S. Kuyucak, Phys. Rev. Lett. 79 (1997)2943.

10. *Fusion barrier distributions in systems with finite excitation energy*,
K. Hagino, N. Takigawa, and A.B. Balantekin, Phys. Rev. C56 (1997)2104.

11. *Excitation of nuclear anharmonic vibrations in heavy-ion fusion reactions*,
K. Hagino, S. Kuyucak, and N. Takigawa, Phys. Rev. C, in press.

The work has also been reported in several international workshops, and the following papers have been, or will be, published in their proceedings:

1. *Multi-nucleon transfer reactions and fusion with unstable nuclei*,
N. Takigawa, S. Yoshida, K. Hagino, and S.K. Patra, Nucl. Phys. A588 (1995)91c.

2. *Effects of dissipation and non-adiabaticity in heavy-ion fusion reactions and fission*,
N. Takigawa, K. Hagino, and M. Abe, in proc. of the international conference on Heavy-Ion Fusion: Exploring the Variety of Nuclear Properties (World Scientific, Singapore, 1995) p. 266.

3. *Heavy-ion fusion reactions as macroscopic quantum tunneling*,
N. Takigawa and K. Hagino, Prog. Theo. Phys. Suppl. 124 (1996)101.

4. *Effects of dissipation on fast quantum tunneling*,
K. Hagino, N. Takigawa, J.R. Bennett, and D.M. Brink, Prog. Theo. Phys. Suppl. 124 (1996)123.

5. *Probing anharmonic properties of nuclear surface vibration by heavy-ion fusion reactions*,
N. Takigawa, K. Hagino, and S. Kuyucak, J. of Phys. G23 (1997)1367.

6. *Importance of non-linear couplings in fusion barrier distributions and mean angular momenta*,
K. Hagino, N. Takigawa, M. Dasgupta, D.J. Hinde, and J.R. Leigh, J. of Phys. G23 (1997)1413.

7. *Evidence of double phonon excitations in* $^{16}O + ^{208}Pb$ *reaction*,
M. Dasgupta, K. Hagino, C.R. Morton, D.J. Hinde, J.R. Leigh, N. Takigawa, H. Timmers, and J.O. Newton, J. of Phys. G23 (1997)1491.

8. *Barrier distributions as a tool to investigate fusion and fission*,
M. Dasgupta, D.J. Hinde, J.R. Leigh and K. Hagino, Nucl. Phys. A, in press.

9. *Anharmonic phonon excitations in subbarrier fusion reactions*,
K. Hagino, N. Takigawa, and S. Kuyucak, AIP, in press.

No part of this thesis has been submitted for a degree at any other university.

Kouichi Hagino

Sendai
March, 1998

Acknowledgements

I would like to thank my supervisor Prof. Noboru Takigawa for his unrelenting support throughout my time in the graduate school. His guidance and instruction has been second to none. He suggested this project and collaborated with me at all stages of the work.

I thank all the people who worked with me on the research for this thesis. Thanks to Prof. Baha Balantekin, Dr. Serdar Kuyucak, Prof. David Brink, and Jonathan Bennett for useful and stimulating discussions, their suggestions and help with several calculations. Thanks also to Masanori Abe for useful discussions at the first stage of the work. I am grateful to the people from the experimental group at the Australian National University, Canberra, Drs. Jack Leigh, Nanda Dasgupta, David Hinde, Clyde Morton, and Heiko Timmers for fruitful discussions and providing me with their high precision experimental data of fusion cross sections. Special thanks to Nanda Dasgupta also for her frequent helpful advice and carefully reading Chap. 1 and Sec. 3.1 of this thesis.

This work was supported by the Japan Society for the Promotion of Science for Young Scientists.

Abstract

Heavy-ion fusion reaction at energies near and below the Coulomb barrier is a typical example of quantum tunneling in the presence of couplings. It has been well recognised by now that fusion cross sections are strongly influenced by couplings between the relative motion of the colliding nuclei and nuclear intrinsic motions. Recently, precisely measured fusion cross sections have become available for several systems, and renewed interests have been generated in the study of heavy-ion fusion reaction. This thesis covers the recent theoretical developments in subbarrier fusion reactions and discusses them from a point of view of multi-dimensional quantum tunneling.

Theoretical frameworks to describe multi-dimensional quantum tunneling are first reviewed. Coupled-channels formalism is introduced and the two limiting cases, i.e. the sudden and the adiabatic limits are discussed. Path integral representation of multi-dimensional quantum tunneling is then introduced as an alternative approach and the deviations from the two extremes are discussed.

The coupled-channels formalism is applied to heavy-ion fusion reactions at subbarrier energies. We use the path integral approach in order to reduce the dimension of the coupled-channels equations based on the no-Coriolis approximation. Light is shed on the what is called fusion barrier distribution, in connection with the recent high precision data of fusion cross section. Several important features of the fusion barrier distribution are discussed.

Most of the coupled-channels calculations performed so far use the linear coupling approximation, where the coupling potential is expanded in powers of the coupling strength, keeping only the linear term. We investigate the role of higher order couplings in heavy-ion fusion reactions. The coupled-channels equations are solved to all orders, and also in the linear and the quadratic coupling approximations. Taking ^{64}Ni + ^{92,96}Zr and ^{16}O + ^{112}Cd, ^{144}Sm reactions as examples, it is shown that the higher order couplings play an important role.

Coupled-channels calculations of all order are then applied to discuss the role of projectile excitations in subbarrier fusion reactions. The measured fusion barrier distributions for ^{40}Ca + ^{194}Pt, ^{192}Os show significant features due to projectile excitation, while none are seen for ^{16}O + ^{144}Sm. This conflict is reconciled using realistic coupled-channels calculations, which show that the higher excitation energy of the 3^- state in ^{16}O producing an adiabatic potential renormalisation, without affecting the structure in the barrier distibution.

We also carry out detailed analyses of high precision data for the ^{16}O + ^{144,148}Sm reactions and discuss the anharmonic properties of collective phonon excitations in ^{144,148}Sm nuclei. We perform a systematic study of the effects of nuclear vibrations on cross sections of subbarrier fusion reaction and on fusion barrier distributions, by using the vibrational limit of the interacting boson model. It is shown that subbarrier fusion reactions are strongly affected by the anharmonic properties and thus offer an alternative method to extract the static quadrupole moments of phonon states in a spherical nucleus.

Finally, we briefly discuss a process after fusion reactions take place, i.e. heavy-ion induced fission. We particularly discuss the temperature dependence of nuclear fission width in the presence of dissipative environment. It is shown that the decay width rapidly decreases at the critical temperature, where the phase transition from super to normal fluids takes place. A possible relation to the recently observed threshold for the dissipative fission is also discussed.

Contents

Chapter 1

INTRODUCTION

Quantum mechanics is indispensable in understanding the behaviour of microscopic systems like atoms, molecules, atomic nuclei, and aggregates of these. One of its fundamental aspect is quantum tunneling, where a particle penetrates classically forbidden region. This is a wave phenomenon and is frequently encountered in diverse processes in physics and chemistry.

The importance of quantum tunneling has been recognised from the birth of quantum mechanics. It was first applied to the description of physical phenomena by Hund in 1927, who discussed intramolecular rearrangements in ammonia molecules, i.e. the $NH_3 \leftrightarrow H_3N$ process, in terms of quantum tunneling in a double well potential[1]. In the following year, Gamow, and independently Gurney and Condon, applied quantum tunneling to α decays of atomic nuclei and had successfully explained the experimental data of the half-life of radioactive nuclei as a function of the energy of the emitted α particle [2, 3]. Oppenheimer employed quantum tunneling to describe the ionization of atoms in intense electric fields[4]. It was also used by Fowler and Nordheim to discuss the emission of electrons from cold metals under the action of intense electric fields [5]. These pioneering works later led to the developments in the physics as well as the technology of superconductors [6].

These seminal works assumed that quantum tunneling takes place in one dimensional space. In general, however, a particle which penetrates a potential is never isolated but interacts with its surroundings or environments, resulting in modification in its behaviour. Quantum tunneling therefore inevitably takes place in multi-dimensional space. Such problem was first addressed by Kapur and Peierls in 1937 [7]. Their theory has subsequently been developped by Banks, Bender, and Wu [8], Gervais and Sakita [9], Brink, Nemes, and Vautherin [10], Schmid [11], and more recently by Takada and Nakamura [12]. If a system is somewhat larger like the trapped flux in a SQUID (superconducting quantum interference devices) ring [13], the tunneling variable couples to a large number of degrees of freedom. In such systems, since the coupling is relatively strong, the environmental degrees of freedom more or less reveal a dissipative character. Quantum tunneling under the influence of dissipative environments, often referred to as macroscopic quantum tunneling (MQT) or dissipative tunneling, plays an important role and is a fundamental problem in many fields of physics and chemistry. Nucleation in ^{3}He-^{4}He systems

[14], diffusion of heavy particle in metals[15], the Coulomb blockade phenomena in tunnel junctions[16], the quantum depinning of a domain wall in magnetic systems[17], the inflation in the early universe[18], and chemical reactions[19] are examples. This problem has been studied in detail by Caldeira and Leggett [20]. This seminal work has stimulated lots of experiments, and has made macroscopic quantum tunneling, or in more general, quantum tunneling in systems with many degrees of freedom a topic of immense interest during the past decade [21].

Despite the continual efforts, however, the dynamics of quantum tunneling in systems with many degrees of freedom has not been fully understood. For example, there is not even an established way to determine the tunneling path in multi-dimensional space when the energy is near the potential barrier. In this respect, nuclear physics could play a unique role in the general understanding of the effects of couplings to the environmental degrees of freedom[22]. One of the typical example of tunneling phenomenon in nuclear physics is a heavy-ion fusion reaction at energy near and below the Coulomb barrier. In order for fusion reaction to take place, the relative motion between the colliding nuclei has to overcome the Coulomb barrier created by the strong cancellation between the long-ranged repulsive Coulomb and the short-ranged attractive nuclear forces. The environmental degrees of freedom to which the relative motion couples are the whole spectra of excited states of the target and projectile nuclei, as well as several sorts of nucleon transfer reactions between the projectile and the target. The properties of the environmental degree of freedom, i.e. intrinsic excitations may strongly depend on individual nucleus. For example, the nucleus ^{148}Sm is spherical and has a low-lying vibrational spectrum, whereas ^{154}Sm is strongly deformed and a rotational mode of excitation characterises its low-lying spectrum. Furthermore, the Q-value of transfer reactions also depends very much on the projectile-target combination. On the other hand, the Coulomb barrier itself does not change very much even if the target is varied from ^{148}Sm to ^{154}Sm. One can therefore control several quantities which govern the dynamics of quantum tunneling, e.g. the coupling strength, the adiabaticity, and the type of environment by carefully choosing the colliding nuclei, while keeping the bare potential unchanged. Heavy-ion fusion reactions can thus provide a flexible tool to obtain a broader understanding of quantum tunneling in the presence of couplings.

The role of channel-coupling, i.e. coupling of the relative motion to intrinsic excitations in heavy-ion fusion reactions has been theoretically studied for a long time [23–27]. Their conclusions had been, however, rather inconclusive before the seminal experiments of Stokstad et al. [28] were carried out in 1978. They used an ^{16}O projectile on different samarium isotopes and showed that the cross section of the fusion reaction with the ^{154}Sm target is substantially larger than that with the ^{148}Sm target at energies below the Coulomb barrier. These experiments suggested that fusion cross sections are strongly enhanced when the target is deformed compared with cases where a spherical target is used. It was later experimentally shown that the enhancement of the fusion cross sections is a general phenomena and not necessarily associated with the static deformation of the target nucleus [29–31]. Their experimental data systematically showed large enhancements of fusion cross sections relative to predictions of a one-dimensional potential model where the effects of channel-couplings are not explicitly taken into account. This observation

was a great surprise at that time, since the potential model can successfully reproduce the experimental cross sections for fusion of light ions[32]. The inadequency of this model was then conclusively demonstrated in a systematic and transparent way by Balantekin, Koonin, and Negele [33], who applied the WKB method to invert the experimental data and constructed an effective one-dimensional potential directly from them. This inversion procedure led to a thin unphysical inter-nuclear potential, which strongly indicated the necessity of other effects which are not taken into account in the potential model. Owing to extensive experimental as well as theoretical studies that followed, it has by now been well established that the enhancement of fusion cross sections can be attributed to couplings between the relative motion of the colliding nuclei and several nuclear collective motions as well as transfer reactions [34–37].

The coupling of the relative motion to intrinsic degrees of freedom affects not only fusion cross sections, but also the angular momentum dependence of fusion probabilities and thus mean angular momenta of the compound nucleus formed in fusion reactions. These quantities are interesting to study, since one can have different angular momentum distributions which integrate to the same fusion cross section. A model which can account for experimental fusion cross sections may thus fail to explain observed angular momentum distributions of the compound nuclei[38]. The first measurement of the angular momentum distribution and mean angular momenta of the compound nucleus was performed by Vandenbosch et al. in 1983 for the $^{16}O + {}^{154}Sm$ reaction [39]. They observed a broader angular momentum distribution and larger mean angular momenta of the compound nucleus compared with those expected in the one-dimensional potential model, which again suggested the inadequency of the potential model. Subsequently, especially in the early 90s, mean angular momenta of the compound nucleus have been simultaneously measured with fusion cross sections for several systems [40]. These experimental data systematically show that the average angular momentum of the compound nucleus is larger than the value predicted by the one-dimensional potential model. Furthermore, a structure, not predicted by the potential model, was also observed in the energy dependence of the mean angular momenta for some systems [41]. These experimental observations have generated recent increasing attention of mean angular momenta of the compound nucleus in the study of heavy-ion sub-barrier fusion reactions [42–50].

Further enormous developments in heavy-ion fusion reactions was recently achieved when a beautiful series of experiments was carried out by the Canberra group (Leigh et al.) with great accuracy [51]. These experiments revived the earlier idea of potential inversion by Balantekin et al. [33] in a different way. When the excitation energy of an internal degree of freedom is much smaller than the curvature of the bare potential barrier, the effects of couplings to the environmental degree of freedom can be understood in terms of a distribution of potential barriers [52–54]. In this sudden limit, the moment of inertia of the intrinsic motion is so large that one can consider that the configuration of the environment does not change during the tunneling. A typical example in the problem of heavy-ion fusion reaction is the rotational motion of heavy deformed nuclei. The energy of the first 2^+ state of heavy nuclei which have a static quadrupole deformation is typically a few tens of keV, while the typical value of the barrier curvature of the Coulomb potential for heavy-ion fusion reactions is between 3.5 and 4 MeV. Hence, at

least to the first approximation, the orientation of the deformed target does not alter during the collision. In this approximation, the fusion potential distributes according to different orientations of the target nucleus. The fusion cross section is then given by an average over contributions from each orientations [23, 25, 26, 53, 55]. Based on such an idea, a method was proposed by Rowley, Satchler, and Stelson in 1991 to extract barrier distributions directly from fusion excitation functions by taking the second derivative of the product of the fusion cross section and the center of mass energy $E\sigma$ with respect to E, i.e. $d^2(E\sigma)/dE^2$ [56]. This quantity is referred to as the *fusion barrier distribution*, and the experiments by the Canberra group have led to the finding that it provides a unique view of heavy-ion fusion reactions[51].

Historically, the first attempt to extract barrier distributions from the experimental fusion excitation functions had been made by Keller et al. using a different method from that proposed by Rowley et al. [57, 58]. Although the distributions were reasonably well defined at low energies, only qualitative comparisons between the experimental data and theoretical calculations were possible because of the large uncertainties of the experimental data at energies around the barrier height. Also, it had been pointed out that the original data of Stokstad et al. [28] were not accurate enough to obtain well-defined barrier distributions which allow quantitative comparisons between the data and theory[56, 59]. The Canberra group, therefore, constructed a new compact velocity filter in order to measure the excitation function of fusion cross sections with a much smaller experimental uncertainty [60].

The first experiment with this compact velocity filter was performed by Wei et al. in 1991 for the ^{16}O + ^{154}Sm reaction [59]. The fusion barrier distribution directly extracted from such highly precise data was found to be well-defined and clearly showed the role of quadrupole deformation of the target nucleus in the fusion reaction. More importantly, it was also found that the positive hexadecapole deformation in ^{154}Sm is required in order to properly explain the experimental fusion barrier distribution [61]. It was very remarkable that the fusion barrier distribution is so sensitive to the small hexadecapole deformation. In order to verify this, the Canberra group measured the fusion excitation function for the ^{16}O + ^{186}W reaction [62]. This system was chosen because ^{186}W has a similar value and the same sign of quadrupole defromation parameter as the ^{154}Sm nucleus, but the sign of the hexadecapole deformation parameter is opposite from each other. The experimental data showed that the shape of the experimental fusion barrier distribution for this system is very different from that for the ^{16}O + ^{154}Sm, reflecting the fact that ^{186}W has a negative hexadecapole deformation [62]. These observations exceeded all expectations, and suggestted that subbarrier fusion reactions can be used as a powerful tool to extract the sign of deformation parameters of deformed nuclei.

In a rigorous theoretical interpretation, the fusion barrier distribution, i.e. $d^2(E\sigma)/dE^2$ has a clear physical meaning only if the excitation energy of the intrinsic motion is zero. When the excitation energy is finite, the concept of barrier distribution holds only approximately[63]. In order to test whether the concept of the fusion barrier distribution generally holds for non-zero value of excitation energies, the fusion excitation function for the ^{16}O + ^{144}Sm reaction was measured with high precision, again at the Australian National University [64]. In spite of the fact that the excitation energy of the first excited

state in ^{144}Sm is large (1.66 MeV), the observed fusion barrier distribution has a clear double-peaked structure, indicating that fusion barrier distribution offers a novel method to understand the effects of channel-couplings on fusion even when the excitation energy of the internal motion is non-zero. At the same time, the fusion cross sections for the ^{17}O + ^{144}Sm system were also measured with high precision[64]. Comparison of the experimental barrier distribution between these two systems clearly demonstrated the effects of couplings to transfer channles on fusion reactions.

In recent years, highly precise data of fusion cross section have become available at other facilities as well. The Legnaro group has measured the ^{58}Ni + ^{60}Ni system, providing a striking result concerning the effects of complex surface vibrations on heavy-ion fusion reactions[65]. The detailed comparison between the experimental data and the theoretical calculations revealed that fusion barrier distributions are quite sensitive to the number of phonons excited during fusion reactions. They have recently measured also the ^{32,36}S + ^{110}Pd and the ^{40}Ca + ^{90,96}Zr systems in order to study the effects of couplings to inelastic as well as transfer channels on fusion reactions [66, 67]. The fusion reactions ^{40}Ca + ^{192}Os, ^{194}Pt were measured by the Seattle group aiming to study the effects of shape transition from prolate (positive quadrupole deformation) to oblate (negative quadrupole deformation) on fusion [68]. The fusion barrier distributions for these systems are observed to be very different from each other. These data also demonstrated the effects of the excitation of the projectile nucleus as well as couplings to the transfer channels.

The fusion barrier distributions, extracted from the above mentioned high presicion data, were sensitive to the effects of channel-couplings and provided a much more apparent way of understanding their effects on the fusion process, than the fusion excitation function itself. These data have thus enabled a detailed study of the effects of nuclear intrinsic excitations on fusion reactions, and have generated a renewed interest in heavy-ion subbarrier fusion reactions. It is worthwhile to mention that the method of the barrier distribution has recently been successfully applied by the Canberra group also to heavy-ion elastic and quasi-elastic scatterings [69, 70] as well as to the problem of the anomalous fission fragment anisotropy in heavy-ion induced fission [71–74].

Theoretically the standard way to address the effects of the coupling between the relative motion and nuclear intrinsic degrees of freedom on fusion is to numerically solve the coupled-channels equations, including all the relevant channels. However, the full coupled-channels calculations quickly become very intricate if many physical channels are included. To solve the equations requires long computing times and also it may not be so easy to physically understand the origin of the effects of channel coupling. For these reasons, several simplifications have often been made by introducing approximations. Although such an approach was satisfactory in reproducing the old data of fusion excitation functions, a critical examination of the simplifications is necessary before making quantitative comparisons with the high precision data that have recently become available. The aim of this thesis is to carry out such inspection, and to make detailed analyses of the high presicion data using realistic coupled-channels calculations. Comparison of such calculations with the experimental data enable us to make rich discussions on subbarrier fusion reactions from a point of view of multi-dimensional quantum tunneling.

The thesis is organised as follows. In Chapter 2, theoretical frameworks to describe

multi-dimensional quantum tunneling are reviewed. Coupled-channels formalism is introduced and the two limiting cases, i.e. the sudden and the adiabatic limits are discussed. Path integral representation of multi-dimensional quantum tunneling is then introduced as an alternative approach [75]. The deviations of the two limits can be addressed relatively easily if one adopts this approach [54, 76, 77]. It will be shown that the deviation from the sudden tunneling limit can be expressed as a dissipation factor which reduces the tunneling probability estimated in the limit of sudden tunneling [54], while that from the adiabatic tunneling limit is represented in terms of mass renormalisation [76]. The eigen-channel approximation in the coupled-channels formalism is also considered.

In Chapter 3, heavy-ion fusion reactions at energy near and below the Coulomb barrier are discussed. Experimental method to measure fusion cross sections is first summarised. One dimensional potential model is then introduced and its failure in reproducing experimental cross sections of subbarrier fusion reactions is demonstrated. Importance of the effects of channels couplings is emphasised and the coupled-channels formalism for heavy-ion fusion reactions is detailed. Use is made of the path integral approach to reduce the dimension of the coupled-channels equations based on the no-Coriolis approximation [78].

In Chapter 4, light is shed on the fusion barrier distribution representation of fusion cross section, i.e. $d^2(E\sigma)/dE^2$, in connection with the recently measured high precision data of fusion excitation function. Several important features of the fusion barrier distribution are discussed. The fusion barrier distribution is intimetely related to the eigen-channel approach. This approach is exact only when the excitation energy of the intrinsic motion is zero. In order to take into account effects of finite excitation energy, an energy dependence is explicitly introduced to weight factors in the eigen-channel approximation. Using the two channel problem [79], it will be shown that the weight factors are slowly changing functions of incident energy [63].

Most of the coupled-channels calculations performed so far use the linear coupling approximation, where the coupling potential is expanded in powers of the deformation parameter, keeping only the linear term. In Chapter 5, we investigate the role of higher order coupling of surface vibrations to the relative motion in heavy-ion fusion reactions at near-barrier energies[80]. The coupled-channels equations are solved to all orders, and also in the linear and the quadratic coupling approximations. Taking ^{64}Ni + ^{92,96}Zr reactions as examples, it will be shown that all order couplings lead to considerably improved agreement with the experimentally measured fusion cross sections and average angular momenta of the compound nucleus for such heavy nearly symmetric systems. The importance of higher order coupling is also examined for asymmetric systems like ^{16}O + ^{112}Cd, ^{144}Sm, for which previous calculations of the fusion cross section seemed to indicate that the linear coupling approximation was adequate. It will be shown that the shape of the barrier distributions and the energy dependence of the average angular momentum can significantly change when the higher order couplings are included, even for systems where measured fusion cross sections may seem to be well reproduced by the linear coupling approximation.

Coupled-channels calculations of full order are then applied in Chapter 6 to discuss the role of projectile excitations in subbarrier fusion reactions [81]. High precision measurements of the fusion excitation functions for the reactions ^{40}Ca + ^{194}Pt, ^{192}Os clearly

demonstrate that projectile excitation significantly modifies the potential barrier distribution. In sharp contrast, fusion of ^{16}O + ^{144}Sm does not show any influence of the projectile excitation on the shape of the barrier distribution. These apparently conflicting conclusions are reconciled using coupled-channels calculations of all order. The effects of projectile excitation will be shown to depend on the intrinsic excitation energies of the projectiles, the high energy of the 3^- state in ^{16}O producing an adiabatic potential renormalisation, without affecting the structure in the barrier distibution. This result indicates that adiabatic effects restrict, in a natural way, the states which influence the *shape* of a fusion barrier distribution. The analysis of barrier distributions thus offers a criterion for the relevance of the 'counter term' prescription in the Caldeira-Leggett approach [20].

Recently measured high precision data of fusion excitation function have enabled a detailed study on the effects of nuclear collective excitations on fusion reactions. In this connection, in Chapter 7, we discuss the effects of multi-phonon excitations on subbarrier fusion reactions, focusing especially on the role of anharmonicities of nuclear vibrations[82, 83]. We carry out a systematic study of those effects on the cross sections of subbarrier fusion reactions and on the fusion barrier distributions, by using the vibrational limit of the interacting boson model. We analyse the recently measured high precision data of the ^{16}O + $^{144,148}Sm$ fusion reactions with this model and discuss the anharmonic properties of the quadrupole as well as the octupole vibrations in $^{144,148}Sm$. We compare the results with those in the harmonic limit to show that anharmonicities play an essential role in reproducing the experimental fusion barrier distribution. From the analysis of the high quality fusion data available for these systems, we deduce the sign as well as the magnitude of the static quadrupole moments for both the first 2^+ and 3^- states in $^{144,148}Sm$. It will be shown that the fusion barrier distribution extracted from the fusion excitation function strongly depends on the sign of the quadrupole moments, suggesting that subbarrier fusion reactions offer an alternative method to extract the static quadrupole moments of phonon states in spherical nuclei.

In Chapter 8, we briefly discuss a process after fusion reactions take place, i.e. heavy-ion induced fission. Using Langer's ImF method, we discuss the temperature dependence of nuclear fission width in the presence of dissipative environments [84]. We introduce a low frequency cut-off to the spectral density of the environmental oscillators in order to mimic the pairing gap. It will be shown that the decay width rapidly decreases at the critical temperature, where the phase transition from super to normal fluids takes place. A possible relation to the recently observed threshold for the dissipative fission is discussed.

Finally the summary of the thesis is given in Chapter 9.

Chapter 2

QUANTUM TUNNELING IN MULTI-DIMENSIONAL SYSTEMS

In this chapter, theoretical frameworks to describe quantum tunneling, which are necessary for a description of the fusion process, are detailed. After discussing the one dimensional barrier penetration problem, quantum tunneling in systems with many degrees of freedom is considered. Two different approaches, i.e. the coupled-channels formalism and the path integral method are presented.

2.1 Analytic solutions of penetrability through one dimensional potentials

2.1.1 Square potential

For most of potential barriers, the penetration probability cannot be analytically evaluated. In this section, a few examples of one dimensional potential which have an analytic solution of the penetrability are presented. The first example we consider is a square potential defined by (see Fig. 2.1)

$$\begin{aligned} V(x) &= 0 \qquad & |x| > a \\ &= V_0 \qquad & |x| < a. \end{aligned} \tag{2.1}$$

The Schrödinger equation for a particle under the influence of this potential reads

$$\begin{aligned} \left(-\frac{\hbar^2}{2\mu}\frac{d^2}{dx^2} - E\right)\psi(x) = 0 \qquad & |x| > a \\ \left(-\frac{\hbar^2}{2\mu}\frac{d^2}{dx^2} + V_0 - E\right)\psi(x) = 0 \qquad & |x| < a, \end{aligned} \tag{2.2}$$

where μ is the mass of the particle and E is the incident energy. The solution of these equations can be explicitly written down. The incident wave function to the left of the

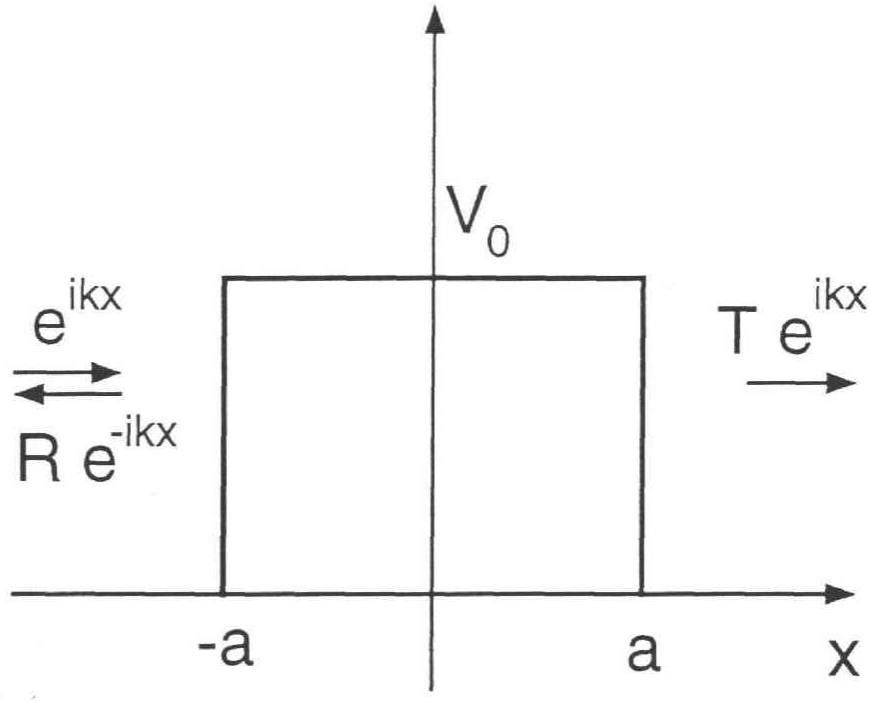

Figure 2.1: Quantum tunneling through a square potential given by Eq. (2.1).

barrier and the transmitted wave to the right are

$$\begin{aligned} \psi(x) &= e^{ikx} + \mathcal{R}e^{-ikx} \qquad x < -a \\ &= \mathcal{T}e^{ikx} \qquad\qquad x > a, \end{aligned} \tag{2.3}$$

respectively. Here k is the wave number of the particle defined by $\sqrt{2\mu E/\hbar^2}$, and $\mathcal{T}$ and $\mathcal{R}$ are the transmission and the reflection coeffecients, respectively. When the energy is below the barrier height, i.e. $E < V_0$, the wave function underneath the barrier is a superposition of exponentially decreasing and increasing components and is given by

$$\psi(x) = Ae^{\kappa x} + Be^{-\kappa x} \qquad -a < x < a, \tag{2.4}$$

where κ is defined as $\sqrt{2\mu(V_0 - E)/\hbar^2}$. The coefficients $A, B, \mathcal{T}$ and $\mathcal{R}$ are determined by the condition that the wave function $\psi(x)$ and its derivative $d\psi/dx$ are continuous at the boundaries $x = \pm a$. This condition leads to the following four equations

$$\begin{aligned} e^{-ika} + \mathcal{R}e^{ika} &= Ae^{-\kappa a} + Be^{\kappa a} \\ ik(e^{-ika} - \mathcal{R}e^{ika}) &= \kappa(Ae^{-\kappa a} - Be^{\kappa a}) \\ Ae^{\kappa a} + Be^{-\kappa a} &= \mathcal{T}e^{ika} \\ \kappa(Ae^{\kappa a} + Be^{-\kappa a}) &= ik\mathcal{T}e^{ika}, \end{aligned} \tag{2.5}$$

from which the transmission coefficient $\mathcal{T}$ follows

$$\mathcal{T} = e^{-2ika} \frac{2k\kappa}{2k\kappa \cosh 2\kappa a - i(k^2 - \kappa^2) \sinh 2\kappa a}. \tag{2.6}$$

Since the penetrability is defined as the ratio of the transmitted flux to the incident flux, it is evaluated as

$$P(E) = \frac{k\hbar|\mathcal{T}|^2/\mu}{k\hbar/\mu} = \frac{(2k\kappa)^2}{(k^2 + \kappa^2)^2 \sinh^2 2\kappa a + (2k\kappa)^2} \qquad (E < V_0). \tag{2.7}$$

In the same way, the penetrability for energies above the barrier is found to be

$$P(E) = \frac{(2kk')^2}{(k^2 - k'^2)^2 \sin^2 2k'a + (2kk')^2} \qquad (E > V_0), \tag{2.8}$$

with $k' = \sqrt{2\mu(E - V_0)/\hbar^2}$.

2.1.2 Eckart potential

The next example is an Eckart potential defined by

$$V(x) = \frac{V_0}{\cosh\left(\frac{x}{a}\right)}. \tag{2.9}$$

For $8\mu V_0 a^2/\hbar^2 < 1$, the penetrability of this potential is given by

$$P(E) = \frac{\sinh^2\left(a\pi\sqrt{\frac{2\mu E}{\hbar^2}}\right)}{\sinh^2\left(a\pi\sqrt{\frac{2\mu E}{\hbar^2}}\right) + \cos^2\left(\frac{\pi}{2}\sqrt{1 - \frac{8\mu V_0 a^2}{\hbar^2}}\right)}, \tag{2.10}$$

while it is

$$P(E) = \frac{\sinh^2\left(a\pi\sqrt{\frac{2\mu E}{\hbar^2}}\right)}{\sinh^2\left(a\pi\sqrt{\frac{2\mu E}{\hbar^2}}\right) + \cosh^2\left(\frac{\pi}{2}\sqrt{\frac{8\mu V_0 a^2}{\hbar^2} - 1}\right)}, \tag{2.11}$$

for $8\mu V_0 a^2/\hbar^2 > 1$ [85].

2.1.3 Parabolic potential

The last example is an inverted parabolic potential given by

$$V(x) = V_0 - \frac{1}{2}\mu\Omega^2 x^2, \tag{2.12}$$

where $\hbar\Omega$ is the curvature of the potential. The penetrability of this potential is given by [85–88]

$$P(E) = \frac{1}{1 + \exp\left[\frac{2\pi}{\hbar\Omega}(V_0 - E)\right]}. \tag{2.13}$$

For any potential barrier which has the same structure as the parabolic potential, its shape can be approximated in a similar form as Eq. (2.12)

$$V(x) \sim V_0 - \frac{1}{2}\mu\Omega^2(x - x_B)^2, \tag{2.14}$$

with

$$\Omega = \sqrt{-\frac{1}{\mu}\frac{d^2V}{dx^2}\bigg|_{x=x_B}}, \tag{2.15}$$

in the vicinity of the barrier position x_B. The penetrability of such potential is then approximated by Eq. (2.13). This approximation is referred to as the parabolic approximation, and has often been used in analyses of fusion excitation function in the potential model [27]. Such an approach to heavy-ion fusion reactions will be discussed in the next chapter.

2.2 Path integral representation of one dimensional penetrability and WKB approximation

Feynman's path integral method [89] provides an alternative approach to quantum mechanics. This formalism, and in particular the semi-classical approximation derived from it, has been widely used in many branches of physics. In this section, the path integral formalism is applied to the problem of quantum tunneling of one dimensional potential.

2.2.1 Definition of the path integral

The path integral is defined in the following way. Consider a transition of a particle from an initial position x_i to a final position x_f after a time interval T. The transition amplitude is expressed as

$$K(x_f, x_i, T) = < x_f|\hat{u}(x,T)|x_i >, \tag{2.16}$$

where $\hat{u}(x,t)$ is the time evolution operator of the system which obeys an equation

$$i\hbar\frac{\partial}{\partial t}\hat{u}(x,t) = H(t)\hat{u}(x,t) \tag{2.17}$$

with the initial condition $\hat{u}(x, t = 0) = 1$. Here, $H(t)$ is the Hamiltonial of the system and is assumed to be

$$H(t) = -\frac{\hbar^2}{2\mu}\frac{d^2}{dx^2} + V(x,t). \tag{2.18}$$

We are considering here a general case where the potential V explicitly depends on time. A time-independent potential can be regarded as a special case of this potential.

In order to obtain the path integral representation of the transition amplitude, we devide the time interval $(0,T)$ into N equal subintervals $0, \cdots, t_n = n\Delta t, \cdots, t_N = T$,

where $\Delta t = T/N$ is the interval of each step. During the small time interval Δt, the potential would remain a constant. The solution of Eq. (2.17) is then given by

$$\hat{u}(x, \Delta t) = 1 - \frac{i}{\hbar}\Delta t H(\Delta t) \tag{2.19}$$

up to the first order of Δt. Using this expression, the time evolution operator from the initial time $t = 0$ to the final time $t = T$ reads

$$\hat{u}(x, T) = \lim_{N\to\infty} \left(1 - \frac{i}{\hbar}\Delta t H(t_N)\right)\left(1 - \frac{i}{\hbar}\Delta t H(t_{N-1})\right)\cdots\left(1 - \frac{i}{\hbar}\Delta t H(t_1)\right). \tag{2.20}$$

Inserting the complete set of the coordinate x at each time steps, the time evolution operator is expressed as

$$\hat{u}(x, T) = \lim_{N\to\infty} \int dx_0 \cdots dx_N |x_N > \prod_{i=1}^{N} \left\{ \left\langle x_i \left| 1 - \frac{i}{\hbar}\Delta t H_i \right| x_{i-1} \right\rangle \right\} < x_0|, \tag{2.21}$$

where H_i is defined as $H(t_i)$.

Any operator $\hat{A}$ can be expressed in a different form by using the complete sets of the coordinate x and the momentum p as

$$\hat{A} = \int dp_1 dp_2 dx_1 dx_2 |x_1 >< x_1|p_1 >< p_1|\hat{A}|p_2 >< p_2|x_2 >< x_2| \tag{2.22}$$

$$= \int \frac{dp_1 dp_2 dx_1 dx_2}{2\pi\hbar} |x_1 >< p_1|\hat{A}|p_2 >< x_2| e^{i(p_1 x_1 - p_2 x_2)/\hbar}. \tag{2.23}$$

Changing the set of variables from (p_1, p_2, x_1, x_2) to (p', u, x', v), which are defined by

$$\begin{aligned} p_1 &= p' + \frac{1}{2}u, & x_1 &= x' + \frac{1}{2}v, \\ p_2 &= p' - \frac{1}{2}u, & x_2 &= x' - \frac{1}{2}v, \end{aligned} \tag{2.24}$$

Eq. (2.23) is transformed to

$$\hat{A} = \int \frac{dp' dv dx'}{2\pi\hbar} e^{ip'v/\hbar} \left| x' + \frac{1}{2}v \right\rangle \left\langle x' - \frac{1}{2}v \right| \int du \left\langle p' + \frac{1}{2}u \right| \hat{A} \left| p' - \frac{1}{2}u \right\rangle e^{ix'u/\hbar} \tag{2.25}$$

$$= \int \frac{dp' dv dx'}{2\pi\hbar} e^{ip'v/\hbar} \left| x' + \frac{1}{2}v \right\rangle \left\langle x' - \frac{1}{2}v \right| A_W(p', x'). \tag{2.26}$$

Here the momentum representation of the Wigner transform $A_W(p', x')$ of the operator $\hat{A}$ is defined by

$$A_W(p', x') \equiv \int du \left\langle p' + \frac{1}{2}u \right| \hat{A} \left| p' - \frac{1}{2}u \right\rangle e^{ix'u/\hbar}. \tag{2.27}$$

Combining Eqs. (2.21) and (2.26), we find, after a few algebra, that the time evolution operator $\hat{u}(x, T)$ is given by

$$\hat{u}(x, T) = \lim_{N\to\infty} \int dx_0 \cdots dx_N |x_N >$$

$$\times \prod_{i=1}^{N} \left\{ \int \frac{dp_i}{2\pi\hbar} e^{ip_i(x_i - x_{i-1})/\hbar} \left[1 - \frac{i}{\hbar} \Delta t H_W \left(p_i, \frac{x_i + x_{i-1}}{2}, t_i \right) \right] \right\} < x_0| \quad (2.28)$$

$$= \lim_{N\to\infty} \int dx_0 \cdots dx_N |x_N > \times \prod_{i=1}^{N} \left\{ \int \frac{dp_i}{2\pi\hbar} \exp \left[\frac{i}{\hbar} \left(p_i(x_i - x_{i-1}) - \Delta t H_W(p_i, \frac{x_i + x_{i-1}}{2}, t_i) \right) \right] \right\} < x_0|, \quad (2.29)$$

where the Wigner transform of the Hamiltonian Eq. (2.18) is given by

$$H_W(p', x', t) = \frac{p'^2}{2\mu} + V(x', t). \quad (2.30)$$

After performing the gaussian integrations with respect to the momentum, we finally obtain a desired form of the transition amplitude as

$$K(x_f, x_i, T) = \lim_{N\to\infty} \sqrt{\frac{\mu}{2\pi\hbar i \Delta t}}^{N-1} \prod_{i=1}^{} \int \left(\sqrt{\frac{\mu}{2\pi\hbar i \Delta t}} dx_i \right) \times \exp \left[\frac{i}{\hbar} \left\{ \frac{\mu}{2} \left(\frac{x_i - x_{i-1}}{\Delta t} \right)^2 - V \left(\frac{x_i + x_{i-1}}{2}, t \right) \right\} \Delta t \right] \Bigg|_{\substack{x_N = x_f \\ x_0 = x_i}} . \quad (2.31)$$

This is the definition of the path integral, and we express it as

$$K(x_f, x_i, T) = \int \mathcal{D}[x(t)] e^{\frac{i}{\hbar} S(x,T)}. \quad (2.32)$$

Here $S(x,T)$ is the classical action defined by

$$S(x,T) = \int_0^T L(x, \dot{x}) dt = \int_0^T \left(\frac{1}{2} \mu \dot{x}^2 - V(x,t) \right) dt, \quad (2.33)$$

and the integral in Eq. (2.32) is performed over all the paths which satisfy the boundary conditions $x(0) = x_i$ and $x(T) = x_f$.

2.2.2 Path integral for quantum tunneling

Quantum tunneling can be regarded as a transition in the coordinate space from an initial position x_i at the one side of a potential to a final position x_f at the other side. In scattering problems, the total energy of a system is fixed. Therefore, time is an irrelevant variable and the transition amplitude in the energy representation has to be considered. This is defined as the Fourier transform of $K(x_f, x_i, T)$ and is given by

$$G^{(+)}(x_f, x_i, E) = \frac{1}{i\hbar} \int_0^\infty dT K(x_f, x_i, T) e^{iE^{(+)}T/\hbar}. \quad (2.34)$$

Here $E^{(+)}$ is defined as $E + i\eta$, η being an infinitesimal quantity. This quantity is introduced to impose the outgoing wave boundary condition. As is shown in Appendix A, the Green function $G^{(+)}(x_f, x_i, E)$ is related to the transmission coefficient $\mathcal{T}$ by

$$\mathcal{T} = \frac{\hbar}{i} \lim_{\substack{x_i \to \infty \\ x_f \to -\infty}} \frac{k\hbar}{\mu} e^{ik(x_f - x_i)} G^{(+)}(x_f, x_i, E). \quad (2.35)$$

The penetrability is thus expressed in the path integral representation as[90]

$$P(E) = \lim_{\substack{x_i \to \infty \\ x_f \to -\infty}} \left(\frac{k\hbar}{\mu}\right)^2 \left| \int_0^\infty dT e^{iE^{(+)}T/\hbar} \int \mathcal{D}[x(t)] e^{iS(x,T)/\hbar} \right|^2 . \tag{2.36}$$

This representation of penetrability is suitable if one intends to introduce the semi-classical approximation, as will be discussed in the next subsection.

2.2.3 WKB approximation

The WKB approximation is derived by evaluating the path integral in Eq. (2.36) in the stationary phase approximation. The resultant formula for the penetrability reads [91]

$$P(E) = \frac{1}{1 + \exp\left[2\int_{x_a}^{x_b} dx \sqrt{\frac{2\mu}{\hbar^2}(V(x) - E)}\right]}. \tag{2.37}$$

Here x_a and x_b are the inner and the outer turning points defined by $V(x) = E$, respectively. Eq. (2.37) uses the uniform approximation and takes into account multiple reflections under the barrier[91]. This formula is, therefore, valid both above and below the barrier. When the energy is well below the barrier, the second term dominates in the denominator in Eq. (2.37), and the formula in the primitive WKB approximation is obtained. For energies above the barrier, the turning points are found, in general, in the complex x plane [92–95]. The integral in Eq. (2.37) is then carried out between the complex turning points.

If a potential is a quadratic function, the WKB approximation gives the rigorously exact solution. For potential given by Eq. (2.12), the integral in Eq. (2.37) can easily be evaluated to $\pi(E - V_0)/\hbar\Omega$, leading to the identical formula to the exact solution Eq. (2.13).

Using the expression of penetrability in the WKB approximation (2.37), the shape of the potential barrier can be constructed if penetrabilities at energies below the barrier height V_0 are known. The thickness of the barrier, i.e. the difference between the outer and the inner turning points $x_b - x_a$ at each energy E reads [33, 96]

$$x_b(E) - x_a(E) = -\frac{2}{\pi}\sqrt{\frac{\hbar^2}{2\mu}} \int_E^{V_0} \frac{\left(\frac{dS}{dE'}\right)}{\sqrt{E' - E}} dE', \tag{2.38}$$

where $S(E)$ is related to the penetrability as

$$S(E) = \int_{x_a}^{x_b} dx \sqrt{\frac{2\mu}{\hbar^2}(V(x) - E)} = \frac{1}{2}\log\left(\frac{1}{P(E)} - 1\right). \tag{2.39}$$

The barrier height V_0 is estimated from the condition $P(E = V_0) = 1/2$. This inversion method was used by Balantekin *et al.* to obtain an effective inter nuclear potential for heavy-ion fusion reactions (see Sec. 3.2.4) [33].

2.3 Coupled-channels method for multi-dimensional tunneling

2.3.1 Coupled-channels equations

Let us now consider the effects of coupling to intrinsic degrees of freedom on the quantum tunneling of a collective coordinate (macroscopic degree of freedom). When the number of the intrinsic degrees of freedom is not so large, one can adress this problem by explicitly solving the total Schrödinger equation.

For simplicitly, consider here the case where one dimensional macroscopic degree of freedom r couples to a single environmental degree of freedom ξ. We assume that the total Hamiltonian for this system is given by

$$H(r,\xi) = -\frac{\hbar^2}{2\mu}\frac{\partial^2}{\partial r^2} + V_0(r) + H_0(\xi) + V_{coup}(r,\xi). \tag{2.40}$$

Here, μ is the mass for the macroscopic motion, $V_0(r)$ the bare potential in the absence of the coupling, $H_0(\xi)$ the Hamiltonian for the intrinsic motion, and V_{coup} the coupling between them. The Schrödinger equation for the total wave function then reads

$$\left(-\frac{\hbar^2}{2\mu}\frac{\partial^2}{\partial r^2} + V_0(r) + H_0(\xi) + V_{coup}(r,\xi)\right)\Psi(r,\xi) = E\Psi(r,\xi). \tag{2.41}$$

We expand the total wave function $\Psi(r,\xi)$ with the eigen states of the intrinsic Hamiltonian $H_0(\xi)$ as

$$\Psi(r,\xi) = \sum_n u_n(r)\varphi_n(\xi), \tag{2.42}$$

where $\varphi_n(\xi)$ satisfies

$$H_0(\xi)\varphi_n(\xi) = \epsilon_n\varphi_n(\xi). \tag{2.43}$$

The total Schrödinger equation (2.41) can then be transformed to a set of coupled equations

$$\left[-\frac{\hbar^2}{2\mu}\frac{d^2}{dr^2} + V_0(r) - E\right]u_n(r) + \sum_m V_{n,m}(r)u_m(r) = 0, \tag{2.44}$$

where

$$V_{n,m}(r) = \epsilon_n\delta_{n,m} + \int d\xi\varphi_n^*(\xi)V_{coup}(r,\xi)\varphi_m(\xi) \tag{2.45}$$

is the coupling matrix. These equations are called the *coupled-channels equations* and are solved by impsoing the boundary conditions

$$u_n(r) \rightarrow e^{-ik_n r}\delta_{n,0} + \mathcal{R}_n e^{ik_n r} \qquad r \rightarrow \infty, \tag{2.46}$$

$$\rightarrow \mathcal{T}_n e^{-ik_n r} \qquad r \rightarrow -\infty, \tag{2.47}$$

where $k_n = \sqrt{2\mu(E-\epsilon_n)/\hbar^2}$ is the wave number of the n-th channel and we have assumed that the intrinsic motion is in the ground state (n=0) before the collision. For many examples, we are interested only in the inclusive process, where the intrinsic degree of

freedom emerges in any final state. Taking a summation over all possible intrinsic states, the inclusive penetrability is given by

$$P(E) = \sum_n \frac{k_n}{k_0} |\mathcal{T}_n|^2 . \tag{2.48}$$

The coupled-channels method presented here is the standard way to adress the effects of couplings on heavy-ion fusion reactions. Such applications will be discussed in the next chapter. The numerical method to solve the coupled-channels equations (2.44) is given in Appendix B.

2.3.2 Sudden tunneling limit and barrier distribution

In general, the solutions of the coupled-channels equations (2.44) can be obtained only by numerically solving them. What make them complicated are the couplings among the channels through the off-diagonal components of the coupling matrix (2.45). If the coupling matrix can be diagonalised, each channels are decoupled, and the problem reduces to a much simpler one dimensional problem. However, the unitary matrix Λ which diagonalises the coupling matrix depends in general on the coordinate r. Hence, if one attempts to diagonalise the coupled-channels equations (2.44) with such unitary transformation, the resaltant equations become

$$\left[-\frac{\hbar^2}{2\mu}\frac{d^2}{dr^2} + V_0(r) + \lambda_n(r) - E\right] v_n(r) + \sum_{l,m}\left[\Lambda_{nl}\left(-\frac{\hbar^2}{2\mu}\frac{d^2\Lambda^{-1}_{lm}}{dr^2}\right)\right] v_m(r)$$
$$+ \sum_{l,m} 2\Lambda_{nl}\left(-\frac{\hbar^2}{2\mu}\frac{d\Lambda^{-1}_{lm}}{dr}\right)\left(\frac{dv_m(r)}{dr}\right) = 0, \tag{2.49}$$

where $\lambda_n(r)$ are the eigenvalues of the coupling matrix at each r and $v_n(r)$, which are referred to as the eigen-channel wave functions, are defined by $v_n(r) = \sum_m \Lambda_{nm}(r)u_m(r)$. Because of the non-comutatibility between the unitary matrix Λ and the kinetic energy operator, their still remain the couplings among the eigen-channels.

There are some special cases where the coupled-channels equations can be decoupled. One of them is the sudden tunneling limit where the excitation energy of the intrinsic motion is zero. Since time is the Hermite conjugate variable of energy, the sudden tunneling limit corresponds to the case where the tunneling occurs instantaneously. To obtain the formula of penetrability in the sudden tunneling limit, we further assume here, besides the zero excitation energy, that the coupling Hamiltonian $V_{coup}(r,\xi)$ is separable, i.e. $V_{coup}(r,\xi) = F(r)\Gamma(\xi)$. Although it will be shown in Sec. 2.4.2 by using the path integral approach that the separability of the coupling Hamiltonian is not necessary to derive the final formula, we introduce this assumption in order to make the following discussion more transparent. The coupled-channels equations (2.44) then become

$$\left[-\frac{\hbar^2}{2\mu}\frac{d^2}{dr^2} + V_0(r) - E\right] u_n(r) + F(r)\sum_m \Gamma_{n,m}u_m(r) = 0, \tag{2.50}$$

where Γ_{nm} is defined as

$$\Gamma_{nm} = \int d\xi \varphi_n^*(\xi)\Gamma(\xi)\varphi_m(\xi). \tag{2.51}$$

These equations can now be diagonalised with the unitary transformation which diagonalises Γ

$$\sum_{j,k} \Lambda_{ij}\Gamma_{jk}\Lambda_{kl}^{-1} = \lambda_i \delta_{i,j}. \tag{2.52}$$

This gives a set of uncoupled equations

$$\left[-\frac{\hbar^2}{2\mu}\frac{d^2}{dr^2} + V_0(r) + \lambda_n F(r) - E\right] v_n(r) = 0. \tag{2.53}$$

By satisfying the appropriate boundary conditions, one finds that the inclusive penetrability is given by [53]

$$P(E) = \sum_n w_n P_0(E, V_0(r) + \lambda_n F(r)), \tag{2.54}$$

where $P_0(E, V(r))$ is the penetrability of a one dimensional potential $V(r)$ with the energy E, and $w_n \equiv |\Lambda_{n0}|^2$ is the probability of finding the entrance channel in the n-th eigenchannel. Note that the unitarity of the matrix Λ leads to the fact that the sum over all weight factors $\sum_n w_n$ is one [53].

The resultant formula (2.54) in the sudden tunneling limit can be interepreted in the following way. In the absence of the coupling, the incident particle encounters only the single potential barrier $V_0(r)$. When the coupling is turned on, the bare potential splits into many barriers. Some of them may be lower than the bare potential and some of them higher. In this picture, the potential barriers are distributed with appropriate weight factors w_n. Noticing that the classical penetrability of a one dimensional potential $V(r)$ is given by $P_0(E, V(r)) = \theta(E - B)$, B being the height of the potential, one finds that the first derivative of Eq. (2.54) is expressed in the classical limit as

$$\frac{dP(E)}{dE} = \sum_n w_n \delta(E - B_n), \tag{2.55}$$

where B_n is the height of the eigen-barrier $V_0(r) + \lambda_n F(r)$. One thus sees that the underlying structure of the barrier distribution is contained in the first derivative of the penetrability. Although the quantum tunneling effects smear the structure of the first derivative of the penetrability, it will still be manifest if the total width of the barrier distribution is significantly greater than the width which is originated from the quantum tunneling effects. This is the main idea of the fusion barrier distribution proposed by Rowley et al. [56]. We will discuss this application in Chapter 4.

2.3.3 Adiabatic tunneling limit and potential renormalisation

The coupled-channels equations decouple also when the excitation energy of the intrinsic motion is positive and is much larger than the curvature of the bare potential barrier. This is the opposite limit to the sudden tunneling limit discussed in the previous subsection,

and is called the adiabatic tunneling limit. In this limit, the quantum tunneling takes place so slowly that the intrinsic motion adiabatically follows the tunneling motion. The intrinsic degree of freedom, therefore, remains in the ground state at every instant. The tunneling probability is then given by

$$P(E) = P_0(E; V_0(r) + \lambda_0(r)), \tag{2.56}$$

where $\lambda_0(r)$ is the lowest eigen-value of the coupling matrix (2.45) at each position of r. In this limit, the bare potential $V_0(r)$ is replaced by the renormalised potential given by

$$V_{ad}(r) = V_0(r) + \lambda_0(r). \tag{2.57}$$

More rigorous derivation of this formula, without resorting to the intuitive discussion as above, will be given in the next section by using the path integral approach.

2.3.4 Constant coupling approximation and eigen-channel approach

Another example of solvable model is obtained by assuming that the coupling Hamiltonian $V_{coup}(r, \xi)$ is constant througout the interaction range, i.e. independent of position r. This approximation is called the constant coupling approximation[79] and is often used when the excitation energy of the intrinsic motion is intermediate between the sudden and the adiabatic limits. In this approximation, the unitary matrix Λ again becomes independent of r, and the penetrability is given by a formula similar to Eq. (2.54) but with diffent eigen-values and weiht factors. Evaluating the coupling Hamiltonian at a chosen position r_w, the unitary transformation (2.49) reads

$$\sum_{j,k} \Lambda_{ij}(r_w) V_{jk}(r_w) \Lambda^{-1}_{kl}(r_w) = \lambda_i(r_w)\delta_{i,j}. \tag{2.58}$$

The penetrability is then given by

$$P(E) = \sum_n w_n(r_w) P_0(E; V_0(r) + \lambda_n(r_w)), \tag{2.59}$$

where the weight factors are defined by $w_n(r_w) = |\Lambda_{n0}(r_w)|^2$. The sum over all the weight factors $\sum_n w_n(r_w)$ again becomes one, as is the case of zero excitation energy. In order to take into account the radial dependence of the coupling Hamiltonian, an approximation was proposed, where the coupling matrix is diagonalised to obtain the eigen-barriers at each position of the macroscopic coordinate r while the weight factors are evaluated at the chosen position r_w [97]. The penetrability in this eigen-channel approximation is given by

$$P(E) = \sum_n w_n(r_w) P_0(E; V_0(r) + \lambda_n(r)). \tag{2.60}$$

In the next section, we will reformulate this approximation based on the path integral approach, where it will be shown that the weight factors depend in general on the total energy of the system.

2.3.5 Two level model

We now concretely illustrate the effects of channel couplings on quantum tunneling discussed above by using the two level model[79]. The coupled-channels equations in this model read

$$\left[-\frac{\hbar^2}{2\mu}\frac{d^2}{dr^2} + V_0(r) + \begin{pmatrix} 0 & F(r) \\ F(r) & \epsilon \end{pmatrix}\right] \begin{pmatrix} u_0(r) \\ u_1(r) \end{pmatrix} = E \begin{pmatrix} u_0(r) \\ u_1(r) \end{pmatrix}, \tag{2.61}$$

where $F(r)$ is the coupling form factor and ϵ is the excitation energy of the intrinsic motion, respectively. The eigen values of the coupling matrix is given by

$$\lambda_\pm(r) = \left(\epsilon \pm \sqrt{\epsilon^2 + 4F(r)^2}\right)/2, \tag{2.62}$$

and if we ignore the non-commutatibility between the unitary matrix which diagonalizes the coupling matrix and the kinetic energy operator, the weight factors are given by

$$w_\pm(r) = F(r)^2/\left(F(r)^2 + \lambda_\pm(r)^2\right). \tag{2.63}$$

The approximate formula in the eigen-chanel approximation (2.60) then becomes

$$P(E) = \sum_\pm w_\pm(r_w) P_0(E; V_0(r) \pm \lambda_\pm(r)). \tag{2.64}$$

When the excitation energy ϵ is zero, i.e. in the sudden tunneling limit, the weight factors $w_\pm$ (2.63) become independent of r_w, and the barrier penetrability is *exactly* given by

$$P(E) = \frac{1}{2}\left[P_0(E; V_0(r) + F(r)) + P_0(E; V_0(r) - F(r))\right]. \tag{2.65}$$

Due to the coupling, the bare potential $V_0(r)$ splits in two eigen-barriers $V_0(r)+|F(r)|$ and $V_0(r) - |F(r)|$, which are higher and lower than the bare potential, respectively (see Fig. 2.2). A half of the incident flux encounters the lower barrier and a half the higher barrier. Fig. 2.3 illustrates the penetrability in this model as a function of energy. The solid line is the penetrability in the presence of the coupling, while that in the absence of the coupling is denoted by the dotted line. Contributions from the lower and the higher barriers are also shown separately by the dashed and the dot-dashed lines, respectively. One can immediately sees that the channel coupling leads to enhancement of the penetrability at energy below the barrier and reduction at above the barrier. The former effects can be associated with the large enhancements of fusion cross sections at subbarrier energies relative to predictions of the potential model, which will be discussed in detail in the next chapter.

When the excitation energy ϵ is huge and positive, the weight factor associated with the higher barrier is much smaller than one. Accompanied with the fact that the height of the higher barrier is substantially larger than the bare potential, the contribution to the penetrability from the higher barrier can, therefore, be neglected. The penetrability

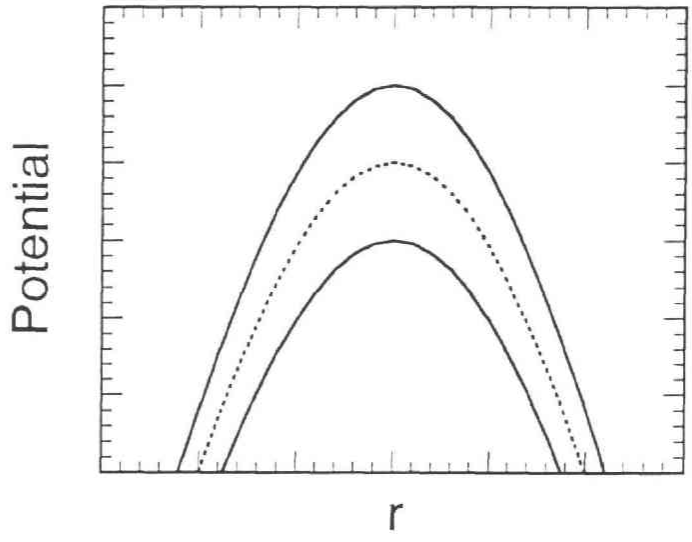

Figure 2.2: Effective potentials in the two channel problem. The excitation energy is set to zero. The solid lines are the effective potentials $V_0(r) \pm F(r)$, while the dotted line is the potential is the absense of the coupling, $V_0(r)$.

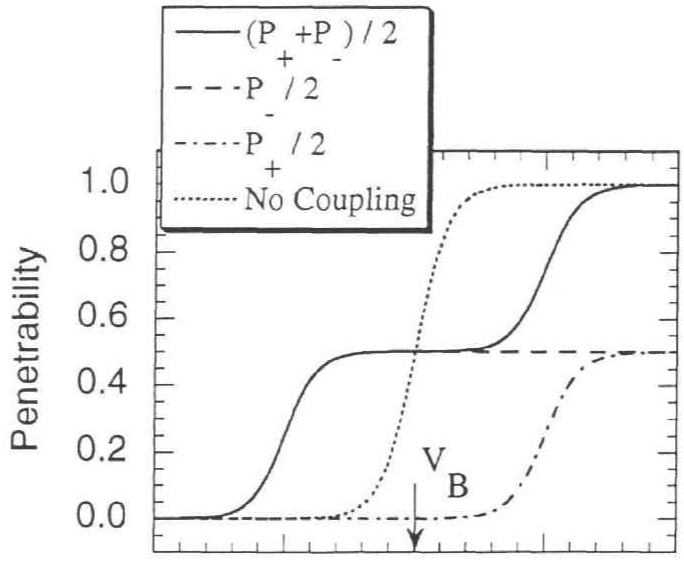

Figure 2.3: Effects of coupling to a degenerate level on penetrability. The solid line is the penetrability in the presence of the channel coupling. The contributions from the lower and the higher barriers to the penetrability are denoted by the dashed and the dot-dashed lines, respectively. The dotted line is the penetrability in the absence of the coupling. The height of the bare potential barrier V_B is represented by the arrow.

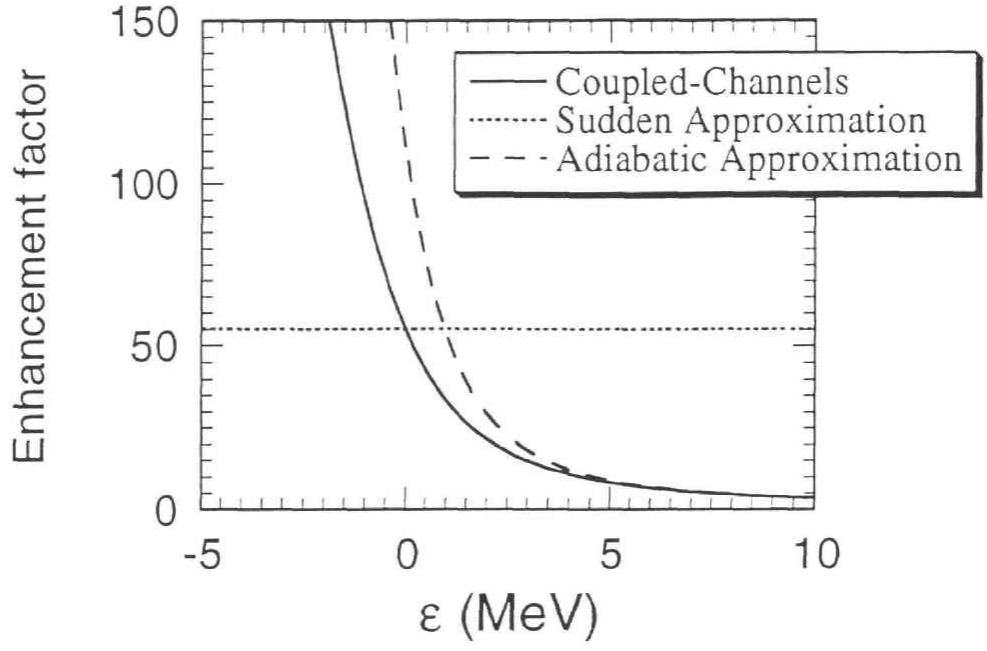

Figure 2.4: Dependence of penetrability on the excitation energy in the two level problem. The penetrability is denoted in a form of enhancement factor against the penetrability in the absense of the coupling. The solid line is obtained by numerically solving the coupled-channels equations, while the dotted and the dashed lines are the results in the sudden and the adiabatic tunneling approximations, respectively. See text for the bare potential and the coupling form factor.

in the eigen-channel approximation (2.64) thus becomes that in the adiabatic limit given by (2.56), i.e.

$$P(E) = P_0(E; V_0(R) + \lambda_-(r)). \tag{2.66}$$

The situation is, however, drastically different when the excitation energy ϵ is huge but negative, as is often encountered in heavy-ion transfer reactions. In this case, the weight factor for the lower barrier is much smaller than that for the higher barrier. One might, therefore, think that the main contribution comes from the higer barrier. However, the barrier height of the lower barrier is much lower than that of the bare potential, and the penetrability may thus be enhanced by an order of magnitude at energies below the barrier because of the exponential dependence of the penetrability on the barrier height.

Figure 2.4 shows the dependence of the enhancement factor, i.e. the ratio of the penetrability to that in the absence of the coupling on the excitation energy of the intrinsic motion. The gaussian shape for both the bare potential and the coupling form factor,

$$V_0(r) = V_0 e^{-r^2/2s^2}, \quad F(r) = F_0 e^{-r^2/2s_f^2}, \tag{2.67}$$

is assumed. The parameters are chosen following Ref. [79] to be V_0 = 100 MeV, F_0 = 3 MeV, and $s = s_f$ = 3 fm, respectively, which mimic the fusion reaction between

two ^{58}Ni nuclei. The mass μ is thus taken to be 29 m_N, m_N being the nucleon mass. The solid line is the result of the exact numerical calculations of the coupled-channels equations, while the dotted and the dashed lines are obtained by using the formulae in the sudden and the adiabatic limits, respectively. Those results are evaluated at $E = 95$ MeV, i.e. 5 MeV below the bare potential barrier. One can see that, for positive ϵ, the finite excitation energy reduces the penetrability compared with that estimated for zero excitation energy (the dotted line), though the penetrability is still larger than that in the absence of the coupling. For negative ϵ (i.e. positive Q-value), the situation is completely opposite: the penetrability is enhanced drastically compared with that in the sudden limit. The adiabtic approximation, on the other hand, always overestimates the penetrability irrespective to the sign of the excitation energy. In the next chapter, we will use the path integral approach to understand these behaviours of the penetrability, i.e. deviations from the adiabatic and the sudden approximations.

2.4 Deviation from the sudden and the adiabatic limits

2.4.1 Path integral approach to multi-dimensional quantum tunneling

Let us now discuss deviation of tunneling probability from the sudden and the adiabatic limits. Path integral approach to quantum tunneling provides a convenient framework to address this question. Balantekin and Takigawa have extended the path integral formulation for one-dimensional quantum tunneling presented in Sec. 2.2 to multi-dimensional systems[75]. For the total Hamiltonian given by Eq. (2.40), the transmission coefficient $\mathcal{T}_n$ is expressed in the path integral representation as

$$\mathcal{T}_n = \lim_{\substack{r_i \to \infty \\ r_f \to -\infty}} \frac{k_0 \hbar}{\mu} e^{i(k_n r_f - k_0 r_i)} \int_0^\infty dT\, e^{iET/\hbar} \int \mathcal{D}[r(t)] e^{iS_t(r,T)/\hbar} < \varphi_n | \hat{u}(r(t), T) | \varphi_0 > . \tag{2.68}$$

Here, $\hat{u}$ is the time evolution operator of the intrinsic motion along a given path $r(t)$ and obeys the differential equation

$$i\hbar \frac{\partial}{\partial t} \hat{u}(r(t), t) = [H_0(\xi) + V_{coup}(r, \xi)]\, \hat{u}(r(t), t), \tag{2.69}$$

with the initial condition $\hat{u}(r(t), t = 0) = 1$. $S_t(r, T)$ is the classical action of the macroscopic motion and is given by

$$S_t(r, T) = \int_0^T \left(\frac{1}{2} \mu \dot{r}^2 - V_0(r) \right) dt. \tag{2.70}$$

Eq. (2.68) is a natural extension of Eq. (2.35) to multi-dimensional system. The inclusive penetrability is then expressed by

$$P(E) \;=\; \sum_n \frac{k_n}{k_0} |\mathcal{T}_n|^2 , \tag{2.71}$$

$$= \lim_{\substack{r_i\to\infty \\ r_f\to-\infty}} \frac{k_0 k_f \hbar^2}{\mu^2} \int_0^\infty dT\ e^{iET/\hbar} \int_0^\infty d\tilde{T}\ e^{-iE\tilde{T}/\hbar}$$
$$\times \int \mathcal{D}[r(t)] \int \mathcal{D}[\tilde{r}(\tilde{t})] e^{i[S_t(r,T)-S_t(\tilde{r},\tilde{T})]/\hbar} \rho_M(\tilde{r}(\tilde{t}),\tilde{T};r(t),T), \qquad (2.72)$$

where the two-time influence functional ρ_M is defined by

$$\rho_M(\tilde{r}(\tilde{t}),\tilde{T};r(t),T) = \sum_n < \varphi_0|\hat{u}(\tilde{r}(\tilde{t}),\tilde{T})|\varphi_n >< \varphi_n|\hat{u}(r(t),T)|\varphi_0 >, \qquad (2.73)$$
$$= < \varphi_0|\hat{u}(\tilde{r}(\tilde{t}),\tilde{T})\hat{u}(r(t),T)|\varphi_0 > . \qquad (2.74)$$

In writing Eq. (2.72), it has been assumed that the energy dissipation to the intrinsic motion is small as compared to the total energy and the channel wave number k_n has been replaced by the final wave number k_f which is independent of the channels.

Eq. (2.72) is still exact and is equivalent to the coupled-channels formalism discussed in Sec. 2.3. An attempt to solve Eq. (2.72) in the semi-classical approximation has been made in Ref. [77] by introducing the so called dynamical norm method.

2.4.2 Dissipation in fast quantum tunneling

We first consider the case where the quantum tunneling takes place relatively fast, i.e. the deviation from the sudden tunneling limit[54]. In the sudden tunneling limit, the excitation energy of the intrinsic degree of freedom is zero. We hence discard the intrinsic Hamiltonian $H_0(\xi)$ in Eq. (2.69). The time evolution operator $\hat{u}$ can then be solved as

$$\hat{u}(r,t) = \exp\left(-\frac{i}{\hbar}\int_0^t dt' V_{coup}(r(t'),\xi)\right). \qquad (2.75)$$

If the coupling Hamiltonian $V_{coup}(r,\xi)$ does not contain the conjugate momentum operator of ξ, the time evolution operator $\hat{u}$ is diagonal in the coordinate space of the environmental degrees of freedom. Denoting the eigenvalue of ξ by x, the two time influence functional (2.74) therefore takes the form

$$\rho_M(\tilde{r}(\tilde{t}),\tilde{T};r(t),T) = \int_{-\infty}^{\infty} dx| < x|\varphi_0 > |^2$$
$$\times \exp\left[-\frac{i}{\hbar}\left(\int_0^T dt\ V(r(t),x) - \int_0^{\tilde{T}} d\tilde{t}\ V_{coup}(\tilde{r}(\tilde{t}),x)\right)\right] \qquad (2.76)$$

Inserting this expression into Eq.(2.72), the inclusive barrier penetrability in the sudden limit is found to be

$$P(E) = \int_{-\infty}^{\infty} dx|\varphi_0(x)|^2 \left\{ \lim_{\substack{r_i\to\infty \\ r_f\to-\infty}} \left(\frac{k_0 k_f \hbar^2}{\mu^2}\right) \left| \int_0^\infty dT\ e^{iET/\hbar} \right.\right.$$
$$\left.\left. \times \int \mathcal{D}[r(t)] \exp\left[\frac{i}{\hbar}\int_0^T dt \left(\frac{1}{2}\mu\dot{r}^2 - V_0(r) - V_{coup}(r,x)\right)\right]\right|^2 \right\} \qquad (2.77)$$
$$= \int_{-\infty}^{\infty} dx|\varphi_0(x)|^2 P_0(E; V_0(r) + V_{coup}(r,x)). \qquad (2.78)$$

This is a general expression of the penetrability in the sudden tunneling limit. This approach does not use the assumption of the separability of the coupling Hamiltonian, and it also clearly shows that the weight factors are given by the square of the ground state wave function of the environmental degrees of freedom.

In order to discuss the deviation from the sudden tunneling limit, we treat the intrinsic Hamiltonian $H_0(\xi)$ in Eq. (2.69) by a perturbation theory. To the first order of $H_0(\xi)$, we find that the penetrability is given by [54]

$$P(E) = \int_{-\infty}^{\infty} dx |\varphi_0(x)|^2 P_0(E; V_{eff}(r,x)), \tag{2.79}$$

where the effective potential V_{eff} is defined by

$$\begin{aligned} V_{eff}(r,x) &= V_0(r) + V_{coup}(r,x) + \frac{i\hbar}{2D}\int_0^t dt' \frac{\partial^2 V_{coup}(r(t'),x)}{\partial x^2} \\ &+ \frac{1}{2D}\left(\int_0^t dt' \frac{\partial V_{coup}(r(t'),x)}{\partial x}\right)^2 + \frac{i\hbar}{D}\int_0^t dt' \frac{\partial V_{coup}(r(t'),x)}{\partial x}\frac{d\varphi_0(x)}{dx}\frac{1}{\varphi_0(x)}, \end{aligned} \tag{2.80}$$

D being the moment of inertia of the intrinsic motion. If we consider as an example a linear oscillator coupling, i.e.

$$H_0(\xi) = -\frac{\hbar^2}{2D}\frac{d^2}{d\xi^2} + \frac{1}{2}D\omega^2\xi^2, \tag{2.81}$$

$$V_{coup}(r,\xi) = f(r)\xi, \tag{2.82}$$

Eq. (2.79) is transformed to [54]

$$P(E) = P_{sud}(E)\exp\left[-\frac{4\pi}{3}\left(\frac{F\alpha_0\pi}{\Omega}\right)^2\frac{\omega}{\Omega}\right]. \tag{2.83}$$

Here, $\alpha_0 = \sqrt{\hbar/2D\omega}$ is the amplitude of the zero point motion of the oscillator, and

$$P_{sud}(E) = \frac{1}{\sqrt{2\pi\alpha_0^2}}\int_{-\infty}^{\infty} dx e^{-\frac{x^2}{2\alpha_0^2}} P_0\left(E; V_0(r) + xf(r)\right) \tag{2.84}$$

is the penetrability in the sudden tunneling limit. In deriving Eq. (2.83), we have assumed a constant coupling form factor, i.e. $f(r) = F$ and that the bare potential $V_0(r)$ is expressed by a parabola (see Sec. 2.1.3). Equation (2.83) clearly shows that the finite excitation energy of the environmental degree of freedom leads to a reduction factor which reduces the barrier penetrability estimated in the sudden tunneling approximation. The reduction factor also shows that the validity of the sudden tunneling approximation depends both on the ratio of the excitation energy to the barrier curvature ω/Ω and on the coupling strength between the macroscopic and the environmental degrees of freedom F.

2.4.3 Mass renormalization in slow quantum tunneling

We next discuss the effects of the coupling to fast environmental degree of freedom, i.e. the deviation from the adiabatic tunneling limit [76]. To this end, we introduce the eigen-channel (or the adiabatic) basis as

$$(H_0(\xi) + V_{coup}(r,\xi))\chi_n(r,\xi) = \lambda_n(r)\chi_n(r,\xi), \tag{2.85}$$

and expand the intrinsic wave function at time t in this basis

$$\hat{u}(r,t)|\varphi_0> = \sum_n a_n(t) \exp\left[-\frac{i}{\hbar}\int_0^t dt' \lambda_n(r(t'))\right] |\chi_n(r(t))> . \tag{2.86}$$

Inserting Eq. (2.86) into Eq. (2.69), we obtain the following coupled equations:

$$\dot{a}_n(t) + \sum_m a_m(t) \exp\left[\frac{i}{\hbar}\int_0^t (\lambda_n(t') - \lambda_m(t'))\right] \left\langle \chi_n(r(t'),\xi) \left| \frac{\partial}{\partial r} \right| \chi_m(r(t),\xi) \right\rangle \dot{r}(t) = 0. \tag{2.87}$$

Up to the second order of $\dot{r}$, we find

$$a_0(t) \sim \exp\left[\frac{i}{\hbar}\int_0^t dt' \frac{1}{2}\delta\mu(r(t'))\dot{r}^2\right], \tag{2.88}$$

where

$$\delta\mu(r(t)) = 2\hbar^2 \sum_{m\neq 0} \frac{1}{\lambda_m(r(t)) - \lambda_0(r(t))} \left| \left\langle \chi_m(r(t),\xi) \left| \frac{\partial}{\partial r(t)} \right| \chi_0(r(t),\xi) \right\rangle \right|^2, \tag{2.89}$$

which is nothing but the cranking mass. If we assume that the intrinsic degree of freedom emerges in the ground state, i.e. the excitations to the excited states occur only virtually, the penetrability is expressed by

$$\begin{aligned} P(E) &= \lim_{\substack{r_i\to\infty \\ r_f\to-\infty}} \frac{k_0 k_f \hbar^2}{\mu^2} \int_0^\infty dT\ e^{iET/\hbar} \int_0^\infty d\bar{T}\ e^{-iE\bar{T}/\hbar} \int \mathcal{D}[r(t)] \int \mathcal{D}[\bar{r}(\bar{t})] a_0(T) a_0(\bar{T})^* \\ &\quad \times e^{i[S_t(r,T) - S_t(\bar{r},\bar{T})]/\hbar} \exp\left[-\frac{i}{\hbar}\int_0^T dt \lambda_0(r(t))\right] \exp\left[\frac{i}{\hbar}\int_0^{\bar{T}} d\bar{t} \lambda_0(\bar{r}(\bar{t}))\right], \qquad (2.90) \\ &= \left\{ \lim_{\substack{R_i\to\infty \\ R_f\to-\infty}} \left(\frac{k_0 k_f \hbar^2}{\mu^2}\right) \left| \int_0^\infty dT\ e^{iET/\hbar} \right.\right. \\ &\quad \left.\left. \times \int \mathcal{D}[r(t)] \exp\left[\frac{i}{\hbar}\int_0^T dt \left(\frac{1}{2}(\mu + \delta\mu(r))\dot{r}^2 - V_0(r) - \lambda_0(r)\right)\right] \right|^2 \right\}. \qquad (2.91) \end{aligned}$$

This result can symbolically be expressed as

$$P(E) = P_0\left(E; \mu + \delta\mu(r); V_0(r) + \lambda_0(r)\right), \tag{2.92}$$

where $P_0(E;m;V(r))$ is the probability for a particle of mass m with a kinetic energy E to traverse a potential barrier $V(r)$. One can thus see that the correction to the adiabatic approximation can be expressed in terms of *mass renormalization*[76]. Since the mass renormalization is positive, it always work to reduce the tunneling rate estimated in the adiabatic tunneling approximation. For the linear coupled oscillator Eqs. (2.81) and (2.82) discussed in the previous subsection, the modified adiabatic formula Eq. (2.92) reads[76]

$$P(E) = P_0\left(E - \frac{1}{2}\hbar\omega; \mu + 2\frac{\alpha_0^2}{\hbar\omega^3}\left(\frac{df}{dr}\right)^2; V_0(r) - \frac{\alpha_0^2}{\hbar\omega}f(r)^2\right). \tag{2.93}$$

2.4.4 Eigen-channel approximation in path integral approach

Finally we reformulate the eigen-channel approximation Eq. (2.64) based on the path integral approach[63]. Combining Eqs. (2.72) and (2.86) gives

$$\begin{aligned} P(E) &= \lim_{\substack{r_i\to\infty \\ r_f\to-\infty}} \frac{k_0 k_f \hbar^2}{\mu^2}\int_0^\infty dT\; e^{iET/\hbar}\int_0^\infty d\tilde{T}\; e^{-iE\tilde{T}/\hbar} \\ &\times \int \mathcal{D}[r(t)]\int \mathcal{D}[\tilde{r}(\tilde{t})]\sum_{n,m} a_n(T)a_m(\tilde{T})^* < \chi_m(\tilde{r}(\tilde{T})|\chi_n(r(T)) > \\ &\times e^{\frac{i}{\hbar}\int_0^T dt\left(\frac{1}{2}\mu\dot{r}^2 - V_0(r) - \lambda_n(r)\right)} e^{-\frac{i}{\hbar}\int_0^{\tilde{T}} d\tilde{t}\left(\frac{1}{2}\mu\dot{\tilde{r}}^2 - V_0(\tilde{r}) - \lambda_m(\tilde{r})\right)}. \end{aligned} \tag{2.94}$$

We use here the semi-classical approximation, and for energies well below the barrier, where the single paht dominates, evaluate the path integral along the classical path

$$r(t) = \tilde{r}(\tilde{t}) = r_{cl}(t), \quad T = \tilde{T}^* = T_{cl}. \tag{2.95}$$

In this case, the orthogonalitiy of the adiabatic basis leads to

$$P(E) = \sum_n \tilde{w}_n(E) P_0(E; V_0(r) + \lambda_n(r)), \tag{2.96}$$

where the weight factors are given by

$$\tilde{w}_n(E) = |a_n(T_{cl})|^2. \tag{2.97}$$

The weight factors depend implicitly on the energy E through the time evolution of the intrinsic system along the classical path. We will study the energy dependence in Sec. 4.4.

Chapter 3

HEAVY-ION FUSION BELOW THE COULOMB BARRIER

In this chapter, heavy-ion fusion reactions at energies near and below the Coulomb barrier are discussed as typical examples of quatum tunneling in multi-dimensional system. Systems which are dealt with in this thesis are those where the sum of the charge of the projectile and the target $Z_p + Z_T$ is larger than 12 and the charge product Z_pZ_T is less than 1800. For lighter systems, e.g. ^{7}Be + p or ^{12}C + α reactions, which play an important role in elemental nucleosynthesis in a steller environment [98], the reaction rate is often determined by specific resonances. Fusion reactions in such systems are, therefore, governed not only by quantum tunneling but also by electromagnetic radiations. Fusion may thus take place even outside the Coulomb barrier. For heavier systems, the level density of the compound nucleus is higher, and there exist bound states of the compound nucleus which are readily accessible via strong nuclear interaction. Therefore, once the Coulomb barrier is overcome, there are many ways in which the energy of the relative motion between the colliding nuclei are dissipated and details of the entrance channel are quickly lost. For such systems, fusion reactions are predominantly governed by quantum tunneling and no details after passing the Coluomb barrier have to be taken into account in evaluating fusion cross sections. When the charge product Z_PZ_T becomes larger than about 1800, however, other mechanisms come into play [58]. The large charge product causes the Coulomb barrier to appear in a relatively inside region where there is a significant overlap between the projectile and the target nuclei. Hence, the relative motion may be lost before passage inside the Coulomb barrier, and one has to take into account friction effects outside the Coulomb barrier. These effects are known as 'extra-push '[99] and play an important role in discussing the production of super heavy elements [100].

In this work, we shall treat fusion reactions in intermediate systems between the two extremes discussed above. We thus assume that fusion is certain to take place once the flux traverses the Coulomb barrier and that the fusion cross section is uniquely determined by quantum tunneling. This has appeared to be a reasonable approximation for the systems we consider in this thesis. We first review the experimental methods to measure fusion cross sections. The simplest potential model is introdunced and its failures in reproducing the observed fusion cross sections for meadium weight mass systems are demonstrated.

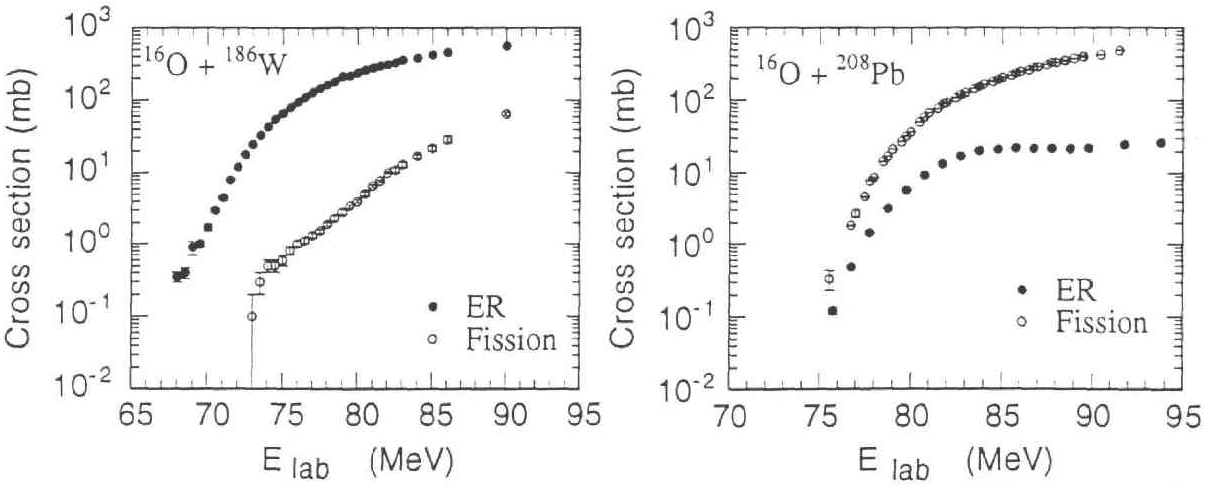

Figure 3.1: The experimental evaporation residue and fission cross sections for the ^{16}O + ^{186}W (the left panel) [62] and ^{16}O + ^{208}Pb (the right panel) [71] reactions. The evaporation residue cross sections are denoted by the filled circles, while the fission cross sections are open circles. The total fusion cross sections are defined by the sum of the evaporation and the fission cross sections.

Coupled-channels formalism formulated in the previous chapter are then applied to heavy-ion fusion reactions.

3.1 Experimental methods

In general, the compound nucleus formed in heavy-ion fusion reaction is highly excited and decays either by emitting neutrons, protons, α particles, γ- and X rays, or by fission. If the charge of the compound nucleus is smaller than about 70, the probability of fission is negligible, and the compound nucleus essentially decays only by the former processes, i.e. evaporation. The decay product is called a *evaporation residue* and has mass and charge close to the compound nucleus. For a heavier compound nucleus, decay by fission competes successfully with evaporation [101–103]. The total fusion cross section is then defined by the sum of the fission and the evaporation residue cross sections. Figure 3.1 shows measured evaporation residue and fission cross sections for the ^{16}O + ^{186}W [62] and ^{16}O + ^{208}Pb [71] reactions. The closed and the open circles are the evaporation residue and the fission cross sections, respectively. One can immediately see that evaporations dominate in the decay modes of the compound nucleus formed in the ^{16}O + ^{186}W reaction, while fission plays a major role in the more fissile ^{16}O + ^{208}Pb system.

When the charge of the compound nucleus is larger than about 90, fission dominates in the decay processes and the contribution from evaporation becomes negligible even at energies below the Coulomb barrier. For such fissile systems, quasi-fission may sometimes take place, especially when the target nucleus is deformed [72–74]. Quasi-fission is

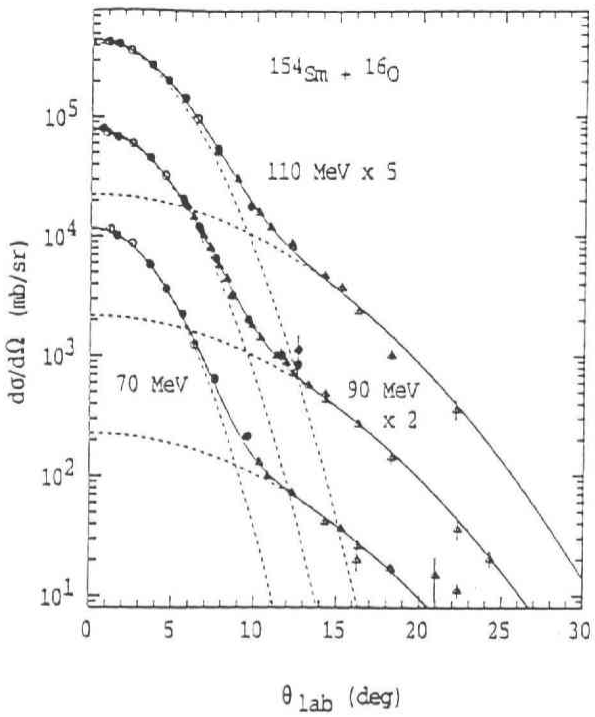

Figure 3.2: Experimental angular distributions of evaporation residues for the ^{16}O + ^{154}Sm reaction. Taken from Ref. [51].

interpreted as a process where the dinucleus, which is formed by overcoming the Coulomb barrier, separates into two nuclei before traversing the fission potential to form the compound nucleus. Strictly speaking, cross sections of quasi-fission should not be included in the total fusion cross section, since the compound nuclei is not formed in such processes. However, if a theoretical model does not take into account the dynamics after the Coulomb barrier is overcome, as that used in this thesis, measured quasi-fission cross sections have to be added to the total fusion cross section in order to make a comparison between the experimental data and such theory [72]. In such case, fusion cross sections are regarded as *barrier traverse cross sections*, rather than cross sections of the compound nucleus formation.

3.1.1 Evaporation residue detection

Direct detection

The direct detection is (if possible) the most unambiguous method of determining evaporation residue cross sections. Evaporation residues have a similar momentum to the incident beam, and their angular distribution lies within a few degrees peaked about the beam direction. Figure 3.2 shows typical angular distributions of the evaporation residues for the ^{16}O + ^{154}Sm reaction [51]. One can find that the evaporation residues are emitted in the forward direction and are peaked around 0 degree. The angular distributions of the evaporation residues have two peaks. For angles close to the beam direction, the main contribution is from neutron and proton evaporations, while the shape of the angular distributions at the larger angle results from α-particle evaporations because of the larger

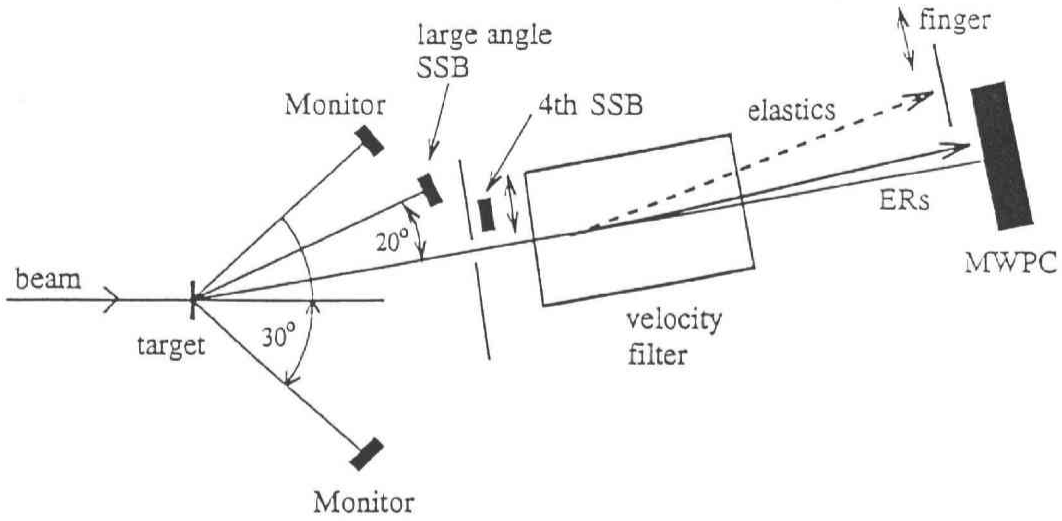

Figure 3.3: Schematic view of the experimental set-up which was used by the Canberra group to detect evaration residues. Taken from Ref. [106].

momentum transfer associated with the α-particles. The angular distribution of elastically scattered beam particles is also peaked at 0 degree, and such beam-like particles are, at forward angles, up to 10^{10} times more intense than the evaporation residues. Therefore, in order to accurately measure evaporation residue cross sections in the presense of the intense beam-like particles, one has to spatially separate the evaporation residues from the beam-like particles. Recoil separators [104], electrostatic deflectors [105], and compact velocity filters [60] are used for this purpose.

We present here as an example the compact velocity filter used by the Canberra group to measure the evaporation residue cross sections for the $^{16}O + {}^{144,148,154}Sm$, ^{186}W as well as $^{17}O + {}^{144}Sm$ reactions [51]. Figure 3.3 shows a sketch of the experimental set-up (see Refs. [51, 60, 106] for more details). Particle entering the velocity filter are subjected to orthogonal electric and magnetic fields. Assuming that the velocity of the particle is in the z-direction, the electric and the magnetic fields are imposed in the x- and the y-directions, respectively. The force acting on the particles is then directed towards the x-direction and its strength is given by

$$F = q(\mathcal{E} - v\mathcal{B}), \tag{3.1}$$

where q is the charge of the particle, v its velocity, and $\mathcal{E}$ and $\mathcal{B}$ are the strength of the electric and the magnetic fields, respectively. One can, therefore, select a particular ratio of the electric and the magnetic fields so that the force acting on a particle which has a certain velocity is zero. Only particles which have such velocity are not deflected and are then transmitted through the detector. In practice, the ratio is determined so that the

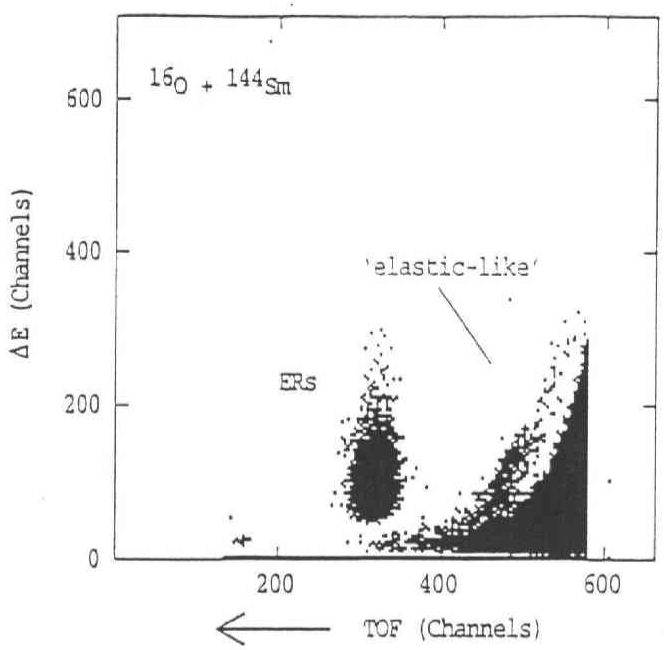

Figure 3.4: Energy loss plotted against time of flight for the ^{16}O + ^{144}Sm reaction at 68 MeV in the laboratory frame. Taken from Ref. [51].

deflection of the evaporation residues is minimised. The beam-like particles suffer from more deflection and the most of them are stopped before entering the detector.

Although the intense beam-like particles are drastically supressed by the velocity filter, not all of them are prevented from entering the detector. The identification of the evaporation residues is accomplished by measuring their energy loss in the detector and the time-of-flight (TOF). Particles which pass through the gas detector ionise the gas molecules and lose their energy according to the Bethe-Bloch formula for stopping powers, which depends on the charge, the velocity, and the mass of the particle [107]. In the gas detector, an electric field is applied in order to collect electrons generated by the ionization processes, before they recombine together with ions to form molecules. Within a certain range of the electric field, the energy loss of the particle is approximately propotional to the number of electrons which are ionised, and thus the energy loss can experimentally be determined by counting the number of electrons. Figure 3.4 shows the energy loss plotted against the time-of-flight for the ^{16}O + ^{144}Sm reaction at 68 MeV in the laboratory frame [51] as an example. The energy loss and the time-of-flight cannot simultaneously specify the charge, velocity, and mass of particles which enter the detector. Nevertheless, it is remarkable that the evaporation residues are well separated from the beam-like particles.

The number of events Y is then converted to the differential cross section $d\sigma/d\Omega$ according to

$$\frac{d\sigma(\theta,E)}{d\Omega} = \frac{Y(\theta,E)}{IN}\frac{1}{\Delta\Omega}, \tag{3.2}$$

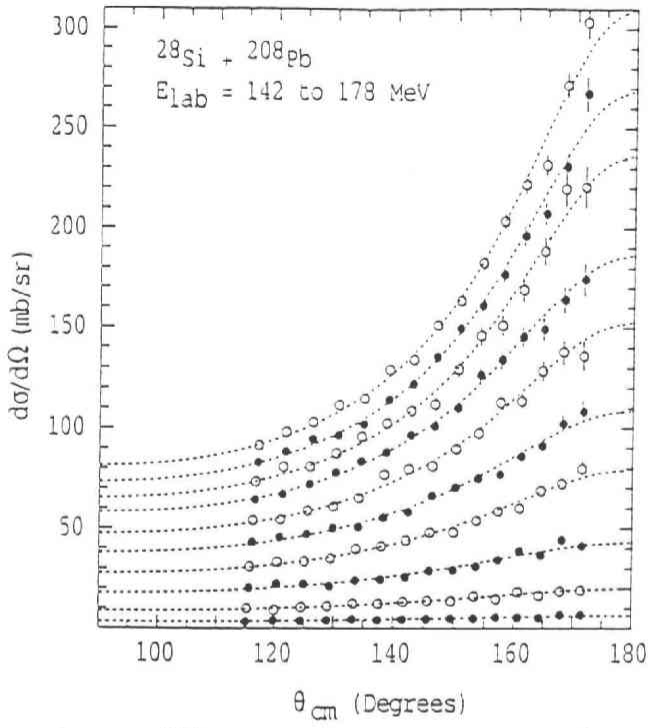

Figure 3.5: Experimental angular distribution of fission fragments for the ^{28}Si + ^{208}Pb reaction, in energy steps of 4 MeV in the laboratory frame. Taken from Ref. [72].

where I and N are the number of beam particles per unit time and the number of target nuclei per unit area, respectively. $\Delta\Omega$ is the solid angle of the velocity filter. The product IN is determined by monitoring the elastic scattering at a certain angle θ_M. Assuming that the cross section of the scattering can be well described by the Rutherford scattering at θ_M, the product IN reads

$$IN = \frac{Y_M(\theta_M, E)}{\Delta\Omega_M} \left(\frac{d\sigma_R(E, \theta_M)}{d\Omega} \right)^{-1}, \tag{3.3}$$

where Y_M is the number of elastic scattering events, and $\Delta\Omega_M$ is the solid angle of the monitor detector. $d\sigma_R/d\Omega$ is the Rutherford differential cross section given by

$$\frac{d\sigma_R(E, \theta_M)}{d\Omega} = \frac{1}{4} \left(\frac{Z_P Z_T e^2}{2E} \right)^2 \frac{1}{\sin^4(\theta_M/2)}. \tag{3.4}$$

Combining Eqs. (3.2) and (3.3) gives

$$\frac{d\sigma(\theta, E)}{d\Omega} = \frac{Y(\theta, E)}{Y_M(\theta_M, E)} \frac{\Delta\Omega_M}{\Delta\Omega} \frac{d\sigma_R(E, \theta_M)}{d\Omega}. \tag{3.5}$$

The total fusion cross section is then obtained by integrating Eq. (3.5) over all angles θ.

Indirect detection

Alternative methods to detect evaporation residues are to measure their characteristic X-rays [28] or α decays [71]. The idea of the X-ray detection is based on the fact that

electron captures and internal conversion processes become the major decay modes for heavy nuclei. For lighter systems where this method is not so efficient, γ-rays are measured instead of X-rays, if the γ decay spectrum for all the residues are known in detail. The method of the α-particle detection was recently applied by the Canberra group to detect the evaporation residues for the $^{16}O + ^{208}Pb$ reaction [71]. Since each evaporation channel for this reaction is characterised by a decay chain whose α energies and half-lives are well known, measured multiplicities of α particles, accompanied with their energy, can be converted to evaporation residue cross sections.

3.1.2 Fission detection

Fission cross sections are obtained by measuring the angular distribution of the fission fragments. Fission fragments are separated from the beam-like particles either by measuring the energy loss and the time-of-flight [71], as in the case of evaporation residue detections, or by simultaneously detecting both fission fragments from the compound nucleus or its daughters [73]. Figure 3.5 shows the experimental angular distributions of the fission fragment for the $^{28}Si + ^{208}Pb$ [72] as typical examples. In systems where the target is fissile, a transfer reaction with positive Q-value followed by fission may take place before the projectile traverses the Coulomb barrier. This yield is called the transfer fission, and has to be excluded from the total experimental fusion cross sections. Such experimental techniques have been developed by the Canberra group and applied to the $^{16}O + ^{238}U$ system to obtain the high precision fusion cross sections [73].

3.2 One dimensional potential model

3.2.1 Ion-ion potential

Theoretically, the simplest approach to heavy-ion fusion reactions is to use the one dimensional potential model where both the projectile and the target are assumed to be structureless. The potential between the projectile and the target is given as a function of the relative distance r between them. It consists of two parts:

$$V_0(r) = V_N(r) + V_C(r). \tag{3.6}$$

$V_N(r)$ is the nuclear potential, and $V_C(r)$ is the Coulomb potential given by

$$V_C(r) = \frac{Z_P Z_T e^2}{r}, \tag{3.7}$$

in the outside region where the projectile and the target do not overlap with each other. Figure 3.6 shows a typical potential $V_0(r)$ for the s- wave scattering of the $^{16}O + ^{144}Sm$ reaction. The dotted and the dashed lines are the nuclear and the Coulomb potentials, respectively, while the total potential $V_0(r)$ is denoted by the solid line. One can find that a potential barrier appears due to a strong cancellation between the short-ranged attractive nuclear interaction and the long-ranged repulsive Coulomb force. This potential

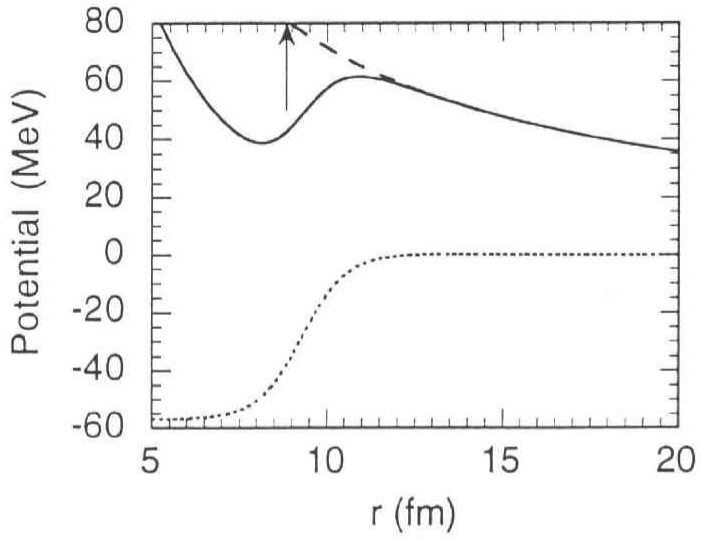

Figure 3.6: A typical potential barrier for the s-wave scattering of the the ^{16}O + ^{144}Sm reaction as a function of the relative distance between ^{16}O and ^{144}Sm. The dotted and the dashed lines are the nuclear and the Coulomb interactions, respectively. The total potential is denoted by the solid line. Also shown by arrow is the touching radius where the projectile and the target nuclei begin to overlap.

barrier is referred to as the *Coulomb barrier* and has to be overcome in order for fusion reactions to take place. The arrow in Fig. 3.6 is the touching radius where the projectile and the target nucleus begin to overlap. It is seen that the position of the Coulomb barrier is larger than the touching radius. This is a characteristic feature for systems where the charge product $Z_P Z_T$ is not so large.

There are several ways to estimate the nuclear potential $V_N(r)$. One way is to fold a nucleon-nucleon interaction in the projectile and the target densities [108]. The nuclear potential in this double folding procedure is given by

$$V_N(r) = \int d\mathbf{r}_1 d\mathbf{r}_2 v_{NN}(\mathbf{r}_2 - \mathbf{r}_1 - \mathbf{r})\rho_P(\mathbf{r}_1)\rho_T(\mathbf{r}_2), \tag{3.8}$$

where v_{NN} is an effective nucleon-nucleon interaction, ρ_P and ρ_T are the densities of the projectile and the target, respectively. Akyüz and Winther numerically performed this procedure and parametrised the nuclear interaction in the Woods-Saxon form as [109]

$$V_N(r) = -\frac{V_0}{1 + \exp[(r - R_0)/a]}, \tag{3.9}$$

with

$$V_0 = 16\pi\gamma\bar{R}a, \tag{3.10}$$

$$R_0 = R_P + R_T + 0.29, \tag{3.11}$$

$$R_i = 1.233A^{1/3} - 0.98A^{-1/3} \qquad (i = P, T), \tag{3.12}$$

$$\bar{R} = R_P R_T/(R_P + R_T), \tag{3.13}$$

$$\gamma = \gamma_0 \left[1 - 1.8 \left(\frac{N_P - Z_P}{A_P}\right)\left(\frac{N_R - Z_T}{A_T}\right)\right], \tag{3.14}$$

where $a = 0.63$ fm, and $\gamma_0 = 0.95$ MeV fm^{-2}.

Another way to determine the nuclear potential is to assume a certain form of it and determine the parameters so that they reproduce experimental data. Chistensen and Winther used the experimental data of elastic scatterings to derive the nuclear potential in a form of [110]

$$V_N(r) = 50\bar{R}\exp[-(r - R_P - R_T)/a], \tag{3.15}$$

where $R_P, R_T, \bar{R}$ and a are the same as those in the Akyüz-Winther potential described avobe. A method to use the experimental data of heavy-ion fusion reactions at energies above the Coulomb barrier is discussed in Ref. [32]. Recent high precision experimental data of fusion cross sections suggest that such procedure leads to a Woods-Saxon potential which has a much larger surface diffuseness paramter a than that extracted from the experimental data of elastic scatterings, i.e. $a = 0.63$ fm [51]. The suggested values of the surface diffuseness parameter range from 0.84 to 1.1 fm for the fusion reactions between ^{16}O and several isotopes of Sm as well as ^{186}W [51]. It has later been shown that the effects of internal excitations play an important role in determining the empirical nuclear potential for the ^{16}O + ^{144}Sm reaction [111]. However, those effects are negligible for the deformed systems ^{16}O + ^{154}Sm, ^{186}W at energies above the Coulomb barrier where the experimental data are fitted, and thus the origin of the large surface diffuseness parameter has still remained as an open problem.

The relation between the surface diffsuness parameter of nuclear potential and the parameters of the Coulomb barrier, i.e. the curvature, the barrier height, and the barrier position is given in Appendix C for exponential and Woods-Saxon potentials.

3.2.2 Formal theory of scattering

In this subsection, we derive a basic formula to calculate fusion cross sections. The Schrödinger equation in three dimensions with a potential given by Eq. (3.6) reads

$$\left[-\frac{\hbar^2}{2\mu}\nabla^2 + V_0(r) - E\right]\psi(\mathbf{r}) = 0, \tag{3.16}$$

where μ is the reduced mass of the system. In the absence of the potential $V_0(r)$, this equation can be explicitly solved in a form $\psi(\mathbf{r}) = \exp(i\mathbf{k}\cdot\mathbf{r})$, $\mathbf{k}$ being the wave number vector whose magnitude is given by $k = \sqrt{2\mu E/\hbar^2}$. This solution has an asymptotic form of

$$\psi(\mathbf{r}) = e^{i\mathbf{k}\cdot\mathbf{r}} \rightarrow \frac{i}{2k}\sum_{l=0}^{\infty}(2l+1)i^l\left(\frac{e^{-i(kr-l\pi/2)}}{r} - \frac{e^{i(kr-l\pi/2)}}{r}\right)P_l(\cos\theta) \qquad r \rightarrow \infty, \tag{3.17}$$

where θ is the angle between $\mathbf{r}$ and $\mathbf{k}$, and P_l are the Legendre polynomials. In the presence of the potential, the behaviour of the wave function is modified. Since the potential goes to zero at infinity, the asymptotic form of the wave function can be written down in a similar way to Eq. (3.17). Replacing the plane waves with the corrsponding Coulomb waves, we write it as

$$\psi(\mathbf{r}) \rightarrow \frac{i}{2k}\sum_{l=0}^{\infty}(2l+1)i^l\left(\frac{H_l^{(-)}(kr)}{r} - S_l\frac{H_l^{(+)}(kr)}{r}\right)P_l(\cos\theta) \qquad r\rightarrow\infty, \tag{3.18}$$

where $H_l^{(+)}(kr)$ and $H_l^{(-)}(kr)$ are the outgoing and the incoming Coulomb waves, respectively. S_l is called the S-matrix and is in general a complex quantity.

Fusion reactions can be regarded as absorption of the incident flux. When the potential is complex, the absolute value of the S-matrix is less than one, i.e. $|S_l| < 1$, and the difference of the total radial flux between the incoming and the outgoing waves is evaluated from Eq. (3.18) as

$$j_{in} - j_{out} = \frac{k\hbar}{\mu}\frac{\pi}{k^2}\sum_l(2l+1)\left(1-|S_l|^2\right). \tag{3.19}$$

In evaluating Eq. (3.19), the radial flux has been integrated for all possible values of θ. Divided by the incident flux, the fusion cross section is then given by

$$\sigma(E) = \frac{\pi}{k^2}\sum_l(2l+1)\left(1-|S_l|^2\right). \tag{3.20}$$

Practically, the S-matix is evaluated as follows. Expanding the wave function $\psi(\mathbf{r})$ by the spherical harmonics as

$$\psi(\mathbf{r}) = \sum_{l=0}^{\infty}\sum_{m=-l}^{l}A_{lm}\frac{u_l(r)}{r}Y_{lm}(\hat{\mathbf{r}}), \tag{3.21}$$

A_{lm} being expansion coefficients, the Schrödinger equation which $u_l(r)$ obeys reads

$$\left(-\frac{\hbar^2}{2\mu}\frac{d^2}{dr^2} + V_0(r) + \frac{l(l+1)\hbar^2}{2\mu r^2} - E\right)u_l(r) = 0. \tag{3.22}$$

This equation is solved under the boundary conditions of

$$u_l(r) \sim r^{l+1} \qquad r\rightarrow 0, \tag{3.23}$$

$$= H_l^{(-)}(kr) - S_l H_l^{(+)}(kr) \qquad r\rightarrow\infty. \tag{3.24}$$

In heavy-ion fusion reactions, instead of imposing the regular boundary condition at the origin (3.23), the so called incoming wave boundary condition (IWBC) is often applied with keeping the potential real [79, 112]. Under the incoming wave boundary condition, the wave function has a form

$$u_l(r) = \mathcal{T}_l\exp\left(-i\int_{r_{abs}}^{r}k_l(r')dr'\right) \qquad r\le r_{abs}, \tag{3.25}$$

at the distance smaller than the absorption radius r_{abs}, which is taken to be inside the Coulomb barrier. $k_l(r)$ is the local wave number for the l-th partial wave, which is defined by

$$k_l(r) = \sqrt{\frac{2\mu}{\hbar^2}\left(E - V_0(r) - \frac{l(l+1)\hbar^2}{2\mu r^2}\right)}. \tag{3.26}$$

The incoming wave boundary condition corresponds to the case where there is a strong absorption in the inner region such that the incoming flux does not return back. For heavy-ion fusion reactions, the final result does not depend so much on the choice of the absorption radius r_{abs}, and it is often taken to be at the minimum position of the potential (see Fig. 3.6). In the incoming wave boundary condition, $\mathcal{T}_l$ in Eq. (3.25) is interpreted as the transmission coefficient, and thus the S-matrix S_l in Eq. (3.24) is nothing but the reflection coefficient. Therefore, Eq. (3.20) is transformed to

$$\sigma(E) = \frac{\pi}{k^2}\sum_l (2l+1)P_l(E), \tag{3.27}$$

where $P_l(E)$ is the penetrability for the l-wave scattering defined as

$$P_l(E) = 1 - |S_l|^2 = \frac{k_l(r_{abs})}{k}|\mathcal{T}_l|^2, \tag{3.28}$$

for the boundary conditions (3.24) and (3.25). The averaged angular momentum of the compound nucleus is evaluated in a similar way as

$$< l > (E) = \left(\frac{\pi}{k^2}\sum_l l(2l+1)P_l(E)\right) \Big/ \left(\frac{\pi}{k^2}\sum_l (2l+1)P_l(E)\right). \tag{3.29}$$

3.2.3 Parabolic approximation and Wong formula

As was discussed in Sec. 2.1.3, if the Coulomb barrier is approximated by a parabola, penetrabilities in Eq. (3.27) can be analytically evaluated. In Fig. 3.7, the Coulomb barrier for the s-wave scattering of ^{16}O + ^{144}Sm reaction is compared with the parabolic potential. Akyüz-Winter potential Eqs. (3.9–14) is used for the nuclear potential. The curvature, barrier height, and barrier position of this potential are 4.52 MeV, 61.3 MeV, and 10.90 fm, respectively. Because of the long ranged Coulomb interaction, the Coulomb barrier is asymmetric, and thus the parabolic potential has less width compared with the realistic situation. However, the parabolic approximation works more than what would be expected from Fig. 3.7. Figure 3.8 compares the penetrability of the s-wave scattering obtained by numerically solving the Schrödinger equation with that obtained in the parabolic approximation. Although the parabolic approximation overestimates the penetrability at energies well below the Coulomb barrier due to the smaller thickness, the agreement between the exact solutions and the parabolic approximation is remarkable, especially at energies above the Coulomb barrier.

Using the parabolic approximation, Wong has derived an analytic expression of fusion cross sections [25]. He assumed that (i) the curvature of the Coulomb barrier is

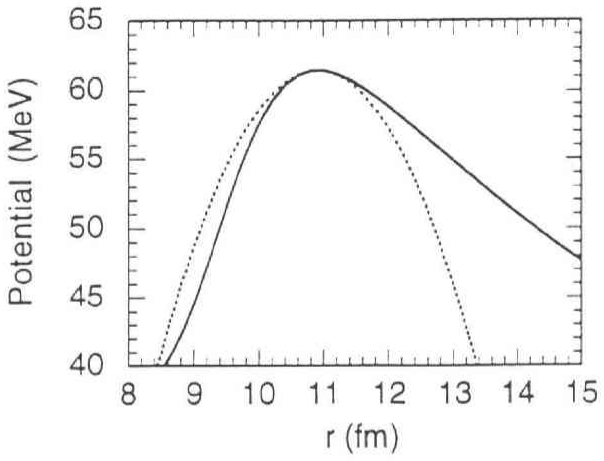

Figure 3.7: Comparison between the Coulomb barrier for the $^{16}O + ^{144}Sm$ reaction (the solid line) and a parabolic potential (the dotted line). The Akyüz-Winther potential is assumed for the nuclear interaction.

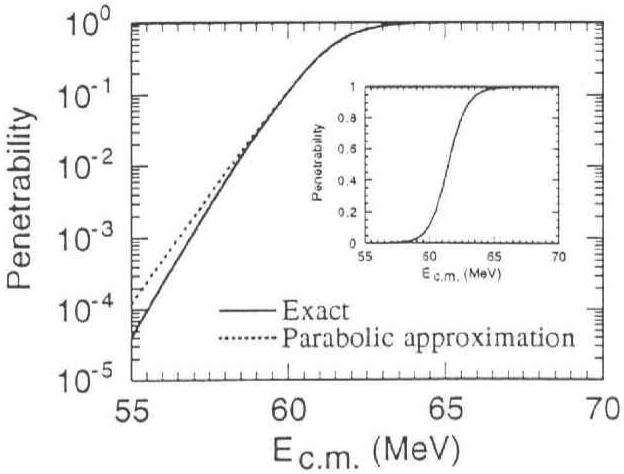

Figure 3.8: The validity of the parabolic approximation for the s-wave penetrability of the $^{16}O + ^{144}Sm$ reaction. The solid line is obtained by numerically solving the Schrödinger equation, while the dotted line is the penetrability in the parabolic approximation. Also shown in the inset is the same figure, but in the linear scale.

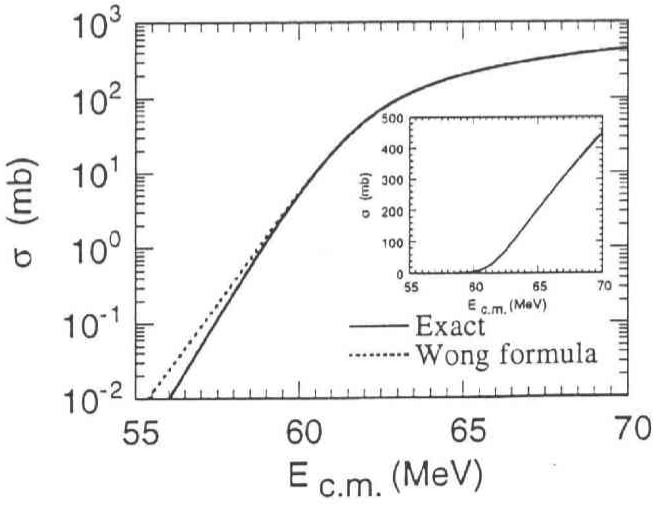

Figure 3.9: The comparison of fusion excitation functions of the $^{16}O + ^{144}Sm$ reaction. The solid line is obtained by numerically solving the Schrödinger equation, while the dotted line is the result of the Wong formula given by Eq. (3.32).

independent of the angular momentum l, and (ii) the dependence of the penetrability on the angular momentum can be well approximated by the shift of the incident energy as

$$P_l(E) = P_0\left(E - \frac{l(l+1)\hbar^2}{2\mu r_B^2}\right), \tag{3.30}$$

where r_B is the position of Coulomb barrier for the s-wave scattering. If many partial waves contribute to fusion cross section, the sum in Eq. (3.27) can be replaced by an integral:

$$\sigma(E) = \frac{\pi}{k^2}\int_0^\infty dl\ (2l+1)P_l(E). \tag{3.31}$$

Changing the variable from l to $l(l+1)$, the integration can be explicitly carried out, leading to the so called Wong formula

$$\sigma(E) = \frac{\hbar\Omega}{2E}r_B^2 \log\left[1 + \exp\left(\frac{2\pi}{\hbar\Omega}(E - V_B)\right)\right], \tag{3.32}$$

where Ω and V_B are the curvature and the height of the Coulomb barrier for the s-wave, respectively. At energies well above the Coulomb barrier, this formula gives the classical expression of fusion cross section

$$\sigma(E) = \pi r_B^2\left(1 - \frac{V_B}{E}\right) \qquad (E \gg V_B). \tag{3.33}$$

Figure 3.9 shows the comparison of fusion cross section for the ^{16}O + ^{144}Sm reaction obtained by the Wong formula with exact numerical solutions. One can observe that the Wong formula works very well except well below the Coulomb barrier, where the parabolic approximation breaks down.

Corrections to the Wong formula

Although the Wong formula works quite well in evaluating fusion cross sections, it has been pointed out that it may not be very satisfacory in applying to the inversion procedure to determin parameters of nuclear potential from experimental data [113]. In this connection, it should be mentioned that Balantekin *et al.* have improved the Wong formula by taking into account the angular momentum dependence of the barrier radius [114]. Up to the first order of $\hbar^2/\mu^2\Omega^2 r_B^4$, they found that the barrier radius for the l-th partial wave r_{Bl} is given by

$$r_{Bl} = r_B - \frac{l(l+1)\hbar^2}{\mu^2\Omega^2 r_B^3}. \tag{3.34}$$

This equation suggests that the barrier position decreases as the angular momentum l increases. Since the height of the Coulomb barrier for the l-th partial wave V_{Bl} is then given, to the same order, by

$$V_{Bl} = V_B + \frac{l(l+1)\hbar^2}{2\mu r_B^2} + \frac{l^2(l+1)^2\hbar^4}{2\mu^3\Omega^2 r_B^6}, \tag{3.35}$$

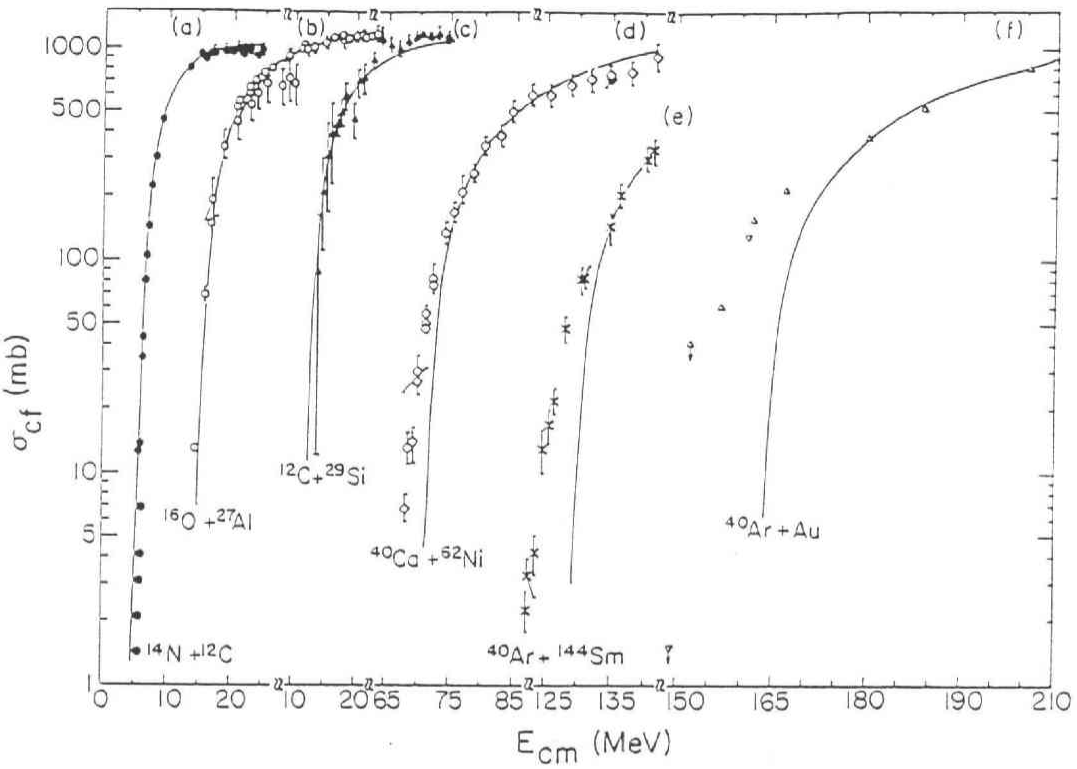

Figure 3.10: Comparison of experimental excitation functions of fusion cross section for several systems with predictions of the potential model (the solid lines). The fusion cross sections in the potential model were evaluated by using the parabolic approximation. Taken from Ref. [32].

the integral in Eq. (3.31) is modified to

$$\sigma(E) = \frac{\pi}{k^2}\int_0^\infty dl\ (2l+1)P_0\left(E - \frac{l(l+1)\hbar^2}{2\mu r_B^2} - \frac{l^2(l+1)^2\hbar^4}{2\mu^3\Omega^2 r_B^6}\right). \tag{3.36}$$

At energies well above the barrier, this equation leads to [114]

$$\sigma(E) = \pi r_B^2\left(1 - \frac{V_B}{E}\right) - \frac{2\pi}{\mu\Omega^2 E}(E - V_B)^2 \qquad (E \gg V_B). \tag{3.37}$$

Comparison between Eqs. (3.33) and (3.37) shows that the Wong formula overestimates fusion cross section at energies well above the Coulomb barrier.

3.2.4 Comparison with experimental data: failure of the potential model

We now compare the one dimensional potential model for heavy-ion fusion reaction with experimental data. Figure 3.10 show the experimental excitation functions of fusion cross section for several systems. The solid lines are predictions of the potential model obtained by using the parabolic approximation [32]. One can find that the potential model reproduces the experimental data very well for relatively light systems, i.e. the $^{14}N + ^{12}C$, $^{16}O + ^{27}Al$, and $^{12}C + ^{29}Si$ reactions. Slight deviations at low energies can be attributed

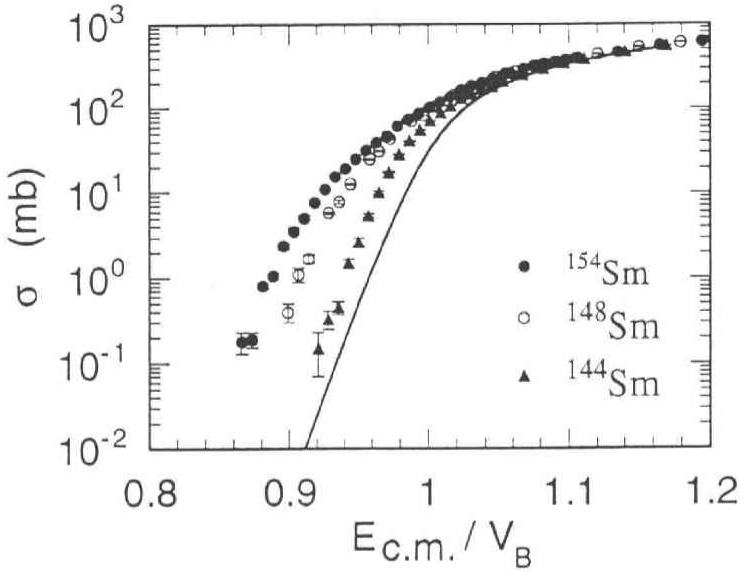

Figure 3.11: The experimental fusion excitation functions for the ^{16}O + $^{144,148,154}Sm$ reactions [51]. They are given as functions of the center of mass energy devided by the barrier height for each reactions. The solid line is a prediction of the potential model. The Akyüz-Winther potential is assumed for the nuclear interaction.

to the inadequacy of the parabolic approximation discussed in the previous subsection. The situation is, however, very different for the heavier systems. The potential model systematically underestimates fusion cross sections, suggesting that it is too simplistic to describe the realistic situation. Figure 3.11 shows the experimental fusion excitation functions for the ^{16}O + $^{144,148,154}Sm$ reactions [51] and comparisons with the potential model (the solid line). These are plotted as functions of center of mass energy divided by the barrier height for each reaction. The barrier height and the result of the potential model are obtained by using the Akyüz-Winther potential. We again observe that the experimental fusion cross sections drastically enhance compared with the prediction of the potential model. Moreover, we observe that the degree of enhancement of fusion cross section depends strongly on the target nucleus. The enhancement for the ^{16}O + ^{154}Sm system is order of magnitude, while that for the ^{16}O + ^{144}Sm system is about factor four at energies below the Coulomb barrier.

Inversion of experimental data

The inadequacy of the potential model was demonstrated in a more transparent way by Balantekin *et al.*[33]. Eq. (3.32) suggests that the barrier penetrability of s-wave scattering is propotional to the first derivative of $E\sigma$. Using the s-wave penetrabilities thus obtained from experimental data of fusion cross section, Balantekin *et al.* applied the inversion formula given by Eq. (2.38) to construct an effective one dimensional potential

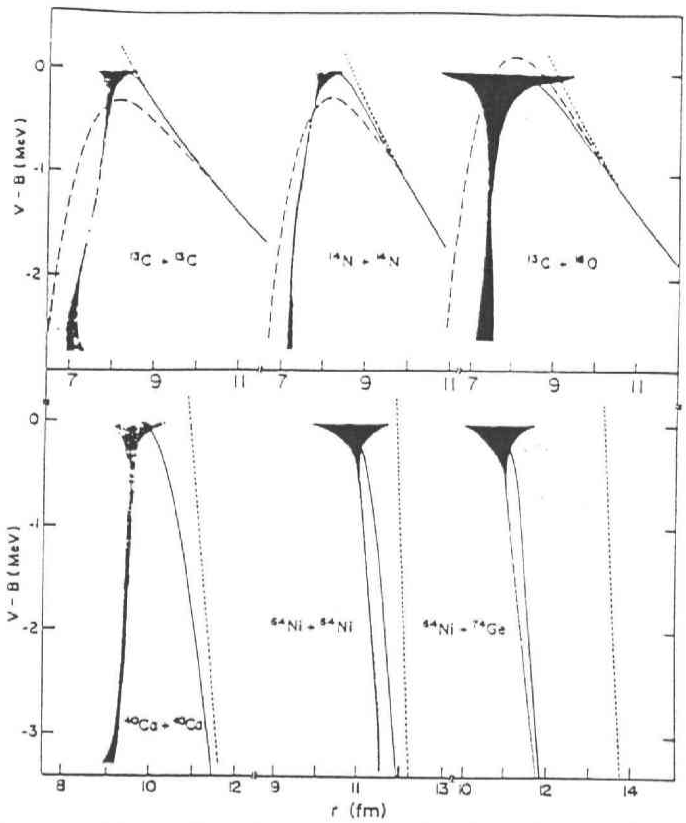

Figure 3.12: Effective one dimensional potentials obtained by the inversion procedure for several reactions (the solid line). The dotted and the dashed lines are the point Coulomb and the KNS potentials, respectively. Taken from Ref. [33].

between heavy-ions. Figure 3.12 shows effective potential barriers constructed based on the inversion procedure [33]. The phoenomenorogical potential of Krappe, Nix, and Sierk (KNS potential) [115] is also shown by the dashed lines as comparisons. For the light systems shown in the upper panel of Fig. 3.12, the obtained potentials are close to the KNS potentials. However, for heavier systems shown in the lower panel, the thickness of the effective potentials are unphysically thin, suggesting that the assumption of a local one-dimensional potential which is independent of incident energy is inconsistent for heavy-ion fusion reactions. This result was confirmed also by the systematic study of Ref. [116].

3.3 Coupled-channels formalism for heavy-ion fusion

3.3.1 Coupled-channels equations with full angular momentum coupling

Extensive experimental as well as theoretical studies have revealed that the inadequacy of the potential model, i.e. large enhancements of fusion cross section against predictions of the potential model can be attributed to the effects of couplings of the relative motion between the colliding nuclei to several nuclear intrinsic motions [33–36]. Among possible intrinsic excitations of a nucleus, single particle states couple so weakly to the

ground state that they do not affect heavy-ion fusion reactions. Also, their excitation energy is in general much larger than the curvature of the Coulomb barrier between the colliding nuclei. Couplings to giant resonances are relatively strong. However, since their excitation energy is again much larger than the barrier curvature and is also a smooth function of a mass number [117], their effects can be effectively incorporated in a choice of inter nuclear potential through the adiabatic potential renormalisation discussed in Sec. 2.3.3. Therefore, the most relevant nuclear intrinsic motions to heavy-ion fusion reactions are low-lying collective motions, e.g. low-lying vibrational excitations with several multipolarities, or rotational motions of deformed nuclei. In this section, we reformulate the coupled-channels framework discussed in Sec. 2.3 by taking into account the finite multipolarity of nuclear intrinsic motion and discuss the effects of the couplings on heavy-ion fusion reactions.

Consider a collision between two nuclei in the presence of the coupling of the relative motion between the centers of mass of the colliding nuclei, $\mathbf{r} = (r, \hat{\mathbf{r}})$, to a nuclear intrinsic motion ξ. We assume the following Hamiltonian for this system

$$H(\mathbf{r}, \xi) = -\frac{\hbar^2}{2\mu}\nabla^2 + V_0(r) + H_0(\xi) + V_{coup}(\mathbf{r}, \xi), \tag{3.38}$$

where $H_0(\xi)$ and $V_{coup}(\mathbf{r}, \xi)$ are the internal and the coupling Hamiltonians, respectively. In general the internal degree of freedom ξ has a finite spin. We therefore expand the coupling Hamiltonian in multipoles

$$V_{coup}(\mathbf{r}, \xi) = \sum_{\lambda>0} f_\lambda(r) Y_\lambda(\hat{\mathbf{r}}) \cdot T_\lambda(\xi). \tag{3.39}$$

Here $Y_\lambda(\hat{\mathbf{r}})$ are the spherical harmonics and $T_\lambda(\xi)$ are spherical tensors constructed from the internal coordinate. The dot indicates a scalar product. The sum is taken over all values of λ except for $\lambda = 0$, which is already included in $V_0(r)$.

For a fixed total angular momentum J and its z component M, the expansion basis of the coupled-channels equations are defined as

$$< \hat{\mathbf{r}}\xi|(nlI)JM >= \sum_{m_l, m_I} < lm_l Im_I|JM > Y_{lm_l}(\hat{\mathbf{r}})\varphi_{nIm_I}(\xi), \tag{3.40}$$

where l and I are the orbital and the internal angular momenta, respectively. $\varphi_{nIm_I}(\xi)$ are the wave functions of the internal motion which obey

$$H_0(\xi)\varphi_{nIm_I}(\xi) = \epsilon_{nI}\varphi_{nIm_I}(\xi). \tag{3.41}$$

Expanding the total wave function with this basis as

$$\Psi_J(\mathbf{r}, \xi) = \sum_{n,l,I} \frac{u^J_{nlI}(r)}{r} < \hat{\mathbf{r}}\xi|(nlI)JM >, \tag{3.42}$$

the coupled-channels equations for $u^J_{nlI}(r)$ read

$$\left[-\frac{\hbar^2}{2\mu}\frac{d^2}{dr^2} + \frac{l(l+1)\hbar^2}{2\mu r^2} + V_0(r) - E + \epsilon_{nI}\right] u^J_{nlI}(r) + \sum_{n',l',I'} V^J_{nlI;n'l'I'}(r) u^J_{n'l'I'} = 0, \tag{3.43}$$

where the coupling matrix elements $V^J_{nlI;n'l'I'}(r)$ are given as

$$V^J_{nlI;n'l'I'}(r) = < JM(nlI)|V_{coup}(\mathbf{r},\xi)|(n'l'I')JM >, \tag{3.44}$$

$$= \sum_\lambda (-)^{I-I'+l'+J} f_\lambda(r) < l||Y_\lambda||l' >< nI||T_\lambda||n'I' > \times\sqrt{(2l+1)(2I+1)} \begin{Bmatrix} I' & l' & J \\ l & I & \lambda \end{Bmatrix}. \tag{3.45}$$

The reduced matrix elements in Eq. (3.45) are defined by

$$< lm_l|Y_{\lambda\mu}|l'm_{l'} >=< l'm_{l'}\lambda\mu|lm_l >< l||Y_\lambda||l' > . \tag{3.46}$$

We have suppressed the index M in $V^J_{nlI;n'l'I'}(r)$, since they are independent of that quantum number as is seen in Eq. (3.45). These coupled-channels equations are solved with the incoming boundary conditions

$$u^J_{nlI}(r) \sim \mathcal{T}^J_{nlI} \exp\left(-i\int_{r_{abs}}^{r} k_{nlI}(r')dr'\right) \qquad r \le r_{abs}, \tag{3.47}$$

$$= H^{(-)}_l(k_{nI}r)\delta_{n,n_i}\delta_{l,l_i}\delta_{I,I_i} + \mathcal{R}^J_{nlI}H^{(+)}_l(k_{nI}r) \qquad r \to \infty, \tag{3.48}$$

where $k_{nI} = \sqrt{2\mu(E-\epsilon_{nI})/\hbar^2}$, and the local wave number $k_{nlI}(r)$ is defined by

$$k_{nlI}(r) = \sqrt{\frac{2\mu}{\hbar^2}\left(E - \epsilon_{nI} - \frac{l(l+1)\hbar^2}{2\mu r^2} - V_0(r) - V^J_{nlI;nlI}(r)\right)}. \tag{3.49}$$

Once the transmission coefficients $\mathcal{T}^J_{nlI}$ are obtained, the penetration probability through the Coulomb potential barrier is given by

$$P^J_{l_iI_i}(E) = \sum_{n,l,I} \frac{k_{nlI}(r_{abs})}{k}|\mathcal{T}^J_{nlI}|^2, \tag{3.50}$$

where $k = k_{n_iI_i}$ is the wave number for the entrance channel. The fusion cross section for an unpolarized target is then given by

$$\sigma(E) = \frac{\pi}{k^2}\sum_{JMl_i}\frac{P^J_{l_iI_i}(E)}{2I_i+1} = \frac{\pi}{k^2}\sum_{Jl_i}\frac{2J+1}{2I_i+1}P^J_{l_iI_i}(E). \tag{3.51}$$

If the initial intrinsic spin I_i is zero, the initial orbital angular momentum l_i is J. Supressing the indices l_i and I_i in the penetrability, Eq. (3.51) thus becomes

$$\sigma(E) = \frac{\pi}{k^2}\sum_J (2J+1)P^J(E), \tag{3.52}$$

which is similar to Eq. (3.27) except that the penetrabilities $P^J(E)$ are influenced by the channel couplings.

3.3.2 No-Coriolis approximation

The full coupled-channels calculations (3.43) quickly become very intricate if many physical channels are included. The dimension of the resulting coupled-channels problem is in general too large for practical purposes. For this reason, an approximation named the no-Coriolis approximation, which is sometimes referred to as the rotating frame approximation, has often been introduced [53,118–122]. This is a sudden tunneling approximation (see Sec. 2.3.2) concerning the centrifugal energy and it greatly reduces the number of coupled-channels to be solved. The no-Coriolis approximation was first introduced in the field of chemistry under the name centrifugal sudden approximation [123–125]. Recently, it has also been applied to the problem of electron-molecule scattering[126].

Let us assume, for simplicity, that the initial intrinsic spin is zero. Extention to the case where the intrinsic state has a finite initial spin will be given in the next sub-subsection. In the no-Coriolis approximation, one transforms the whole system to the rotating frame where the z axis is along the direction of the relative motion $\mathbf{r}$ at every instant [78]. This is achieved by replacing the angular momentum of the relative motion in each channel by the total angular momentum J, i.e.

$$\frac{l(l+1)\hbar^2}{2\mu r^2} \approx \frac{J(J+1)\hbar^2}{2\mu r^2}. \tag{3.53}$$

This corresponds to the assumption that the change of the orbital angular momentum between the colliding nuclei due to the excitation of the intrinsic degree of freedom is negligible. As the operator for a rotational coordinate transformation in the whole space then commutes with the centrifugal operator for the relative motion, one can make the transformation to the rotating frame without introducing any complications [78]. Using $Y_{\lambda\mu}(\hat{\mathbf{r}} = 0) = \sqrt{(2\lambda+1)/4\pi}\delta_{\mu,0}$, the coupling Hamiltonian (3.39) in the rotating frame becomes

$$V_{coup}(r,\xi) = \sum_{\lambda>0} \sqrt{\frac{2\lambda+1}{4\pi}} f_\lambda(r) T_{\lambda 0}(\xi). \tag{3.54}$$

Since the coupling Hamiltonian does not depend any more on the angular component of the relative coordinate between the colliding nuclei, the complicated angular momentum couplings disappear in the no-Coriolis approximation, and thus the coupled-channels equations are reduced to those in a spin-less system discussed in Sec. 2.3. A remarkable fact is that the dimension of the coupled-channels equations drastically reduces in the no-Coriolis approximation. For example, for quadrupole mode of excitation (λ=2), the original coupled-channels equations have 13 dimensions for $J > 4$, when the excitations are truncated at the second excited states, while the dimension reduces to 3 in the no-Coriolis approximation.

In order to derive the coupled-channels equations in the no-Coriolis approximation, we expand the total wave function in the rotating frame as

$$\Psi_J(\mathbf{r},\xi) = \sum_{n,I} \frac{v^J_{nI}(r)}{r} Y_{J0}(\hat{\mathbf{r}}) \varphi_{nI0}(\xi). \tag{3.55}$$

The radial wave function for the (nI)-th channel v^J_{nI} is related to the original radial wave function as [127]

$$v^J_{nI}(r) = \sum_l < I0J0|l0 > u^J_{nlI}(r). \tag{3.56}$$

The coupled-channels equations for $v^J_{nI}(r)$ then read

$$\left[-\frac{\hbar^2}{2\mu}\frac{d^2}{dr^2} + \frac{J(J+1)\hbar^2}{2\mu r^2} + V_0(r) - E + \epsilon_{nI}\right] v^J_{nI}(r)$$
$$+ \sum_{n'I'}\sum_{\lambda>0}\sqrt{\frac{2\lambda+1}{4\pi}} f_\lambda(r) < \varphi_{nI}|T_{\lambda 0}|\varphi_{n'I'} > v^J_{n'I'}(r) = 0. \tag{3.57}$$

These coupled-channels equations are solved by imposing the incoming boundary conditions

$$v^J_{nI}(r) \sim \mathcal{T}^J_{nI} \exp\left(-i\int_{r_{abs}}^{r} k_{nJI}(r')dr'\right) \qquad r \le r_{abs}, \tag{3.58}$$
$$= H^{(-)}_J(k_{nI}r)\delta_{n,n_i}\delta_{I,I_i} + \mathcal{R}^J_{nI} H^{(+)}_J(k_{nI}r) \qquad r \to \infty, \tag{3.59}$$

where k_{nI} and $k_{nJI}(r)$ are defined in the same way as in the previous subsection. The fusion cross section is then given by Eq. (3.52) with the penetrabilities of

$$P^J(E) = \sum_{n,I} \frac{k_{nJI}(r_{abs})}{k} |\mathcal{T}^J_{nI}|^2. \tag{3.60}$$

The validity of the no-Coriolis approximation for heavy-ion fusion reactions has been investigated in Refs. [119, 128]. It was shown in these references that the no-Coriolis approximation leads to negligible errors in calculating fusion cross sections. Here we reinvestigate its validity in connection with fusion barrier distribution, which will be detailed in the next chapter. We also investigate the range of accuracy by varying the excitation energy of the intrinsic motion. We choose the ^{16}O + ^{154}Sm reaction as a typical example of the rotational coupling. For simplicity, we assume that the relative motion couples linearly to the ground rotational band of ^{154}Sm, which we truncate at the first 2^+ state (see next subsection for more detail). The literature value of the deformation parameter is used and the excitation energy of the first 2^+ state is initially set to be zero. Figure 3.13 compares the results in the no-Coriolis approximation (the dotted line) with those obtained by solving the coupled-channels equations with full angular momentum couplings (the solid line). The upper panel shows the fusion cross section, while the lower panel is the so called fusion barrier distribution which is difined by the second derivative of $E\sigma$. One can find that the no-Coriolis approximation works very well both for fusion cross section and for fusion barrier distribution. This conclusion does not alter even when we set the excitation energy of the first 2^+ state to be 2 MeV (Fig. 3.14). We thus conclude that the change of the centrifugal potential due to the finite multipolarity of intrinsic degrees of freedom can safely be neglected for heavy-ion fusion reactions. We shall, therefore, always take the no-Coriolis approximation in the rest part of the thesis unless explicitly mentioned.

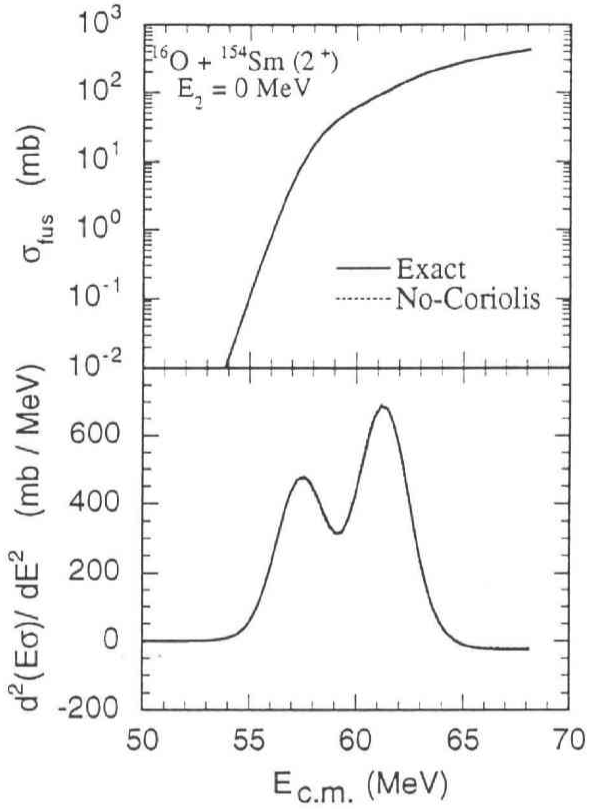

Figure 3.13: Fusion cross section (the upper panel) and fusion barrier distribution (the lower panel) for the $^{16}O + ^{154}Sm$ reaction. The ground rotational band of the ^{154}Sm nucleus is truncated at the first 2^+ state, whose excitation energy is set to be zero MeV. The dotted line is the result in the no-Coriolis approximation, whilist the solid line takes into account the full angular momentum couplings.

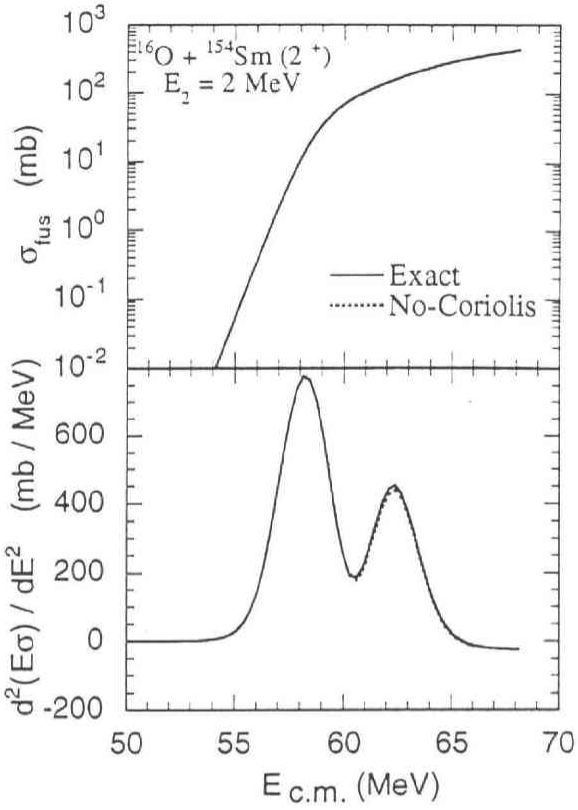

Figure 3.14: Same as Fig. 3.13, but for the case where the excitation energy of the first 2^+ state is set to be 2 MeV.

Path integral approach to no-Coriolis approximation

The no-Coriolis approximation has been derived by several different methods. The authors in Refs. [53,118–120] used properties of Racah coefficients, and Ref. [121] used the Green's function method. Symmetry considerations using tidal spin have been used in Ref. [122]. Here we present a derivation of the no-Coriolis approximation using the path integral method (see Sec. 2.4.1) [54]. This approach had already been used in Ref.[129], but the angular momentum coupling was not treated explicitly. A salient point of this derivation is that it enables us to easily extend to the cases where the initial spin of the colliding particles is not zero, and where there is a spin-orbit force in the scattering process. It can also be easily applied to the cases where the internal degrees of freedom are not collective coordinates, but the coordinates of the constituent particles of the colliding system. It also clarifies the underlying assumption of the approximation.

Since fusion reactions are processes where two nuclei approach close to each other, we treat the radial component of the relative motion as the macroscopic degree of freedom and its angular part and the internal degrees of freedom as environmental degrees of freedom. For the Hamiltonian given by Eq. (3.38), the barrier transmission probability is then expressed by (see Eq. (2.72))

$$\begin{aligned} P^J_{l_i I_i}(E) &= \lim_{\substack{r_i \to \infty \\ r_f \to -\infty}} \left(\frac{p_i p_f}{\mu^2}\right) \int_0^\infty dT\ e^{(i/\hbar)ET} \int_0^\infty d\tilde{T}\ e^{-(i/\hbar)E\tilde{T}} \\ &\times \int \mathcal{D}[r(t)] \int \mathcal{D}[\tilde{r}(\tilde{t})] e^{(i/\hbar)[S_t(r,T) - S_t(\tilde{r},\tilde{T})]} \rho_M(\tilde{r}(\tilde{t}), \tilde{T}; r(t), T), \end{aligned} \tag{3.61}$$

where p_i and p_f are the classical momenta at the initial and the final positions r_i and r_f, respectively. $S_t(r,T)$ is the action for the translational motion along a path $r(t)$, and is given by

$$S_t(r,T) = \int_0^T dt \left(\frac{1}{2}\mu \dot{r}(t)^2 - V_0(r(t))\right) \tag{3.62}$$

The effects of the couplings to the environmental degrees of freedom are included in the two time influence functional ρ_M, which is defined by Eq. (2.74)

$$\rho_M(\tilde{r}(\tilde{t}), \tilde{T}; r(t), T) = < (n_i L_i I_i) JM | \hat{u}^\dagger(\tilde{r}(\tilde{t}), \tilde{T}) \hat{u}(r(t), T) | (n_i L_i I_i) JM >, \tag{3.63}$$

with

$$i\hbar \frac{\partial}{\partial t} \hat{u}(r,t) = \left[\frac{\mathrm{l}^2 \hbar^2}{2\mu r^2} + H_0(\xi) + V_{coup}(r, \hat{\mathrm{r}}, \xi)\right] \hat{u}(r,t). \tag{3.64}$$

$\hat{u}(r,t)$ is the time evolution operator of the environmental degrees of freedom along a given path $r(t)$. The formal solution of Eq. (3.64) can be written as

$$\hat{u}(r,t) = \hat{T} \exp\left[\int_0^t dt' \left(\frac{\mathrm{l}^2 \hbar^2}{2\mu r(t')^2} + H_0(\xi) + V_{coup}(r(t'), \hat{\mathrm{r}}, \xi)\right)\right], \tag{3.65}$$

where $\hat{T}$ is the time ordering operator. Hereafter the time ordering is supposed to be properly treated in all solutions of $\hat{u}$, and we shall not write it explicitly.

We now assume that the angular part of the translational motion is much slower than the radial motion, and replace the operator $\mathbf{l}^2$ in Eq.(3.65) by some c-number $\Lambda(\Lambda+1)$[54]. This is a kind of sudden approximation and is exact if there is no angular momentum transfer from the relative motion between colliding nuclei to nuclear intrinsic motion. Λ can be any c-number, though one often takes Λ to be the total angular momentum J. If we denote the coordinate representation of $\hat{\mathbf{r}}$ by $\hat{\mathbf{r}}'$ [54], we obtain

$$< \hat{\mathbf{r}}'|\hat{u}(r,T)|(n_i l_i I_i)JM > = \exp\left[\int_0^T dt' \left(\frac{\Lambda(\Lambda+1)\hbar^2}{2\mu r(t')^2} + H_0(\xi) + V_{coup}(r(t'),\hat{\mathbf{r}}',\xi)\right)\right] \times \sum_{m_l,m_I} < l_i m_l I_i m_I|JM > Y_{l_i m_l}(\hat{\mathbf{r}}')|\varphi_{n_i I_i m_I} > . \quad (3.66)$$

We next make a rotational coordinate transformation in the whole space to the coordinate system where the z axis is along the direction of the radial vector $\mathbf{r}' = (r', \hat{\mathbf{r}}') = (r', \theta', \phi')$ [121]. We call the new coordinate system the rotating frame (RF) in order to distinguish it from the space fixed frame(SF). The operator for this coordinate transformation is given by

$$\mathcal{R}(\phi', \theta', 0) = e^{i\mathbf{J}\cdot\boldsymbol{\chi}(\hat{\mathbf{r}}')/\hbar}. \quad (3.67)$$

In Eq.(3.67), $\boldsymbol{\chi}$ is the rotation vector which specifies the direction and the magnitude of the rotation. Note that the third Euler angle in this rotating frame is zero. Since the time evolution operator $\hat{u}(r,t)$ [see Eq.(3.65)] does not change by rotation in the no-Coriolis approximation, we obtain

$$< \hat{\mathbf{r}}'|\hat{u}(r,T)|(n_i l_i I_i)JM > = < \hat{\mathbf{r}}'|\mathcal{R}^{-1}(\phi',\theta',0)\mathcal{R}(\phi',\theta',0)\hat{u}(r,T) \times \mathcal{R}^{-1}(\phi',\theta',0)\mathcal{R}(\phi',\theta',0)|(n_i l_i I_i)JM > \quad (3.68)$$

$$= \sum_K \bar{u}(r(t),T) < \hat{\mathbf{r}}' = 0|(n_i l_i I_i)JK > D^J_{KM}(\phi',\theta',0) \quad (3.69)$$

$$= \sum_K \bar{u}(R(t),T) < l_i 0 I_i K|JK > \sqrt{\frac{2l_i+1}{4\pi}} D^J_{KM}(\phi',\theta',0)|\varphi_{n_i I_i K} > \quad (3.70)$$

where D^J_{KM} is Wigner's D function and the time evolution operator in the rotating frame $\bar{u}(r,T)$ is defined as

$$\bar{u}(r,T) = \exp\left[\int_0^T dt' \left(\frac{\Lambda(\Lambda+1)\hbar^2}{2\mu r(t')^2} + H_0(\xi) + V_{coup}(r(t'),\hat{\mathbf{r}}=0,\xi)\right)\right] \quad (3.71)$$

$$= \exp\left[\int_0^T dt' \left(\frac{\Lambda(\Lambda+1)\hbar^2}{2\mu r(t')^2} + H_0(\xi) + \sum_\lambda \sqrt{\frac{2\lambda+1}{4\pi}} f_\lambda(r(t')) T_{\lambda 0}(\xi)\right)\right] \quad (3.72)$$

In order to obtain Eq. (3.70), we used

$$\mathcal{R}(\phi',\theta',0)|\hat{\mathbf{r}}' >= |\hat{\mathbf{r}}' = 0 >, \quad (3.73)$$

and

$$< \hat{\mathbf{r}}' = 0|Y_{l_i m_l} >= \sqrt{\frac{2l_i+1}{4\pi}}\delta_{m_l,0}. \tag{3.74}$$

The two time influence functional then becomes

$$\begin{aligned}\rho_M(\tilde{r}(\tilde{t}),\tilde{T};r(t),T) &= \int \sin\theta' d\theta' d\phi' < (n_i l_i I_i)JM|\hat{u}^\dagger(\tilde{r}(\tilde{t}),\tilde{T})|\hat{\mathbf{r}}' > \\ &\quad \times < \hat{\mathbf{r}}'|\hat{u}(r(t),T)|(n_i l_i I_i)JM > \qquad (3.75)\\ &= \sum_K \frac{2l_i+1}{2J+1}| < l_i 0 I_i K|JK > |^2 \\ &\quad \times < \varphi_{n_i I_i K}|\bar{u}^\dagger(\tilde{r}(\tilde{t}),\tilde{T})\bar{u}(r(t),T)|\varphi_{n_i I_i K} > . \qquad (3.76)\end{aligned}$$

In obtaining Eq.(3.76) from Eq.(3.75), we used the orthogonality of the D function

$$\int \sin\theta d\theta d\phi D^{J*}_{K'M}(\phi,\theta,0)D^J_{KM}(\phi,\theta,0) = \frac{4\pi}{2J+1}\delta_{K,K'}. \tag{3.77}$$

The time evolution operator in the rotating frame $\bar{u}(r(t),t)$ obeys

$$i\hbar\frac{\partial}{\partial t}\bar{u}(r,t) = \left[\frac{\Lambda(\Lambda+1)\hbar^2}{2\mu r^2} + H_0(\xi) + \sum_{\lambda>0}\sqrt{\frac{2\lambda+1}{4\pi}}f_\lambda(r)T_{\lambda 0}(\xi)\right]\bar{u}(r,t). \tag{3.78}$$

Eq.(3.78) shows that the z component of the internal spin m_I is conserved in the no-Coriolis approximation. Since the wave functions with different values of m_I never couple to each other during the reaction process, the dimension of the coupled-channels equations is drastically reduced. The effective Hamiltonian in Eq.(3.78) has the same form as that in the system where the internal spin is zero. The effects of the finite intrinsic spin enters only through a scaling factor $\sqrt{(2\lambda+1)/4\pi}$ of the coupling strength.

From Eqs.(3.51), (3.61), and (3.76), the fusion cross section in the no-Coriolis approximation finally becomes

$$\begin{aligned}\sigma(E) &= \frac{\pi}{k^2}\sum_{Jl_i}\sum_K \frac{2l_i+1}{2I_i+1}| < l_i 0 I_i K|JK > |^2 \\ &\quad \times \lim_{\substack{r_i\to\infty \\ r_f\to-\infty}}\left(\frac{p_i p_f}{\mu^2}\right)\int_0^\infty dT\ e^{(i/\hbar)ET}\int_0^\infty d\tilde{T}\ e^{-(i/\hbar)E\tilde{T}}\int\mathcal{D}[r(t)]\int\mathcal{D}[\tilde{r}(\tilde{t})] \\ &\quad \times e^{(i/\hbar)[S_t(r,T)-S_t(\tilde{r},\tilde{T})]} < \varphi_{n_i I_i K}|\bar{u}^\dagger(\tilde{r}(\tilde{t}),\tilde{T})\bar{u}(r(t),T)|\varphi_{n_i I_i K} > .\end{aligned} \tag{3.79}$$

This is nothing but the solution of the reduced coupled-channels equations (3.57). If the initial value of the internal spin is zero, the initial angular momentum for the relative motion l_i equals J, and the summation in Eq.(3.79) becomes simple. The fusion cross section in that case can be calculated by treating as though the relative motion couples to a spinless mode of excitation except for the scaling factor $\sqrt{(2\lambda+1)/4\pi}$ mentioned above. If the initial spin of the internal motion is finite, the influence functional is obtained by first calculating it for a fixed K-quantum number, and then by taking sum with the weight following Clebsch-Gordan coefficients.

3.3.3 Coupling to low-lying collective states

Vibrational coupling

Let us now discuss the explicit form of the coupling Hamiltonian V_{coup} in the problem of heavy-ion fusion reactions. We first consider couplings of the relative motion to the 2^λ-pole surface vibration of a target nucleus. In the geometrical model of Bohr and Mottelson, the radius of the vibrating target is parameterized as

$$R(\theta,\phi) = R_T\left(1+\sum_\mu \alpha_{\lambda\mu}Y^*_{\lambda\mu}(\theta,\phi)\right), \tag{3.80}$$

where R_T is the equivalent sharp surface radius and $\alpha_{\lambda\mu}$ is the surface coordinate of the target nucleus. To the lowest order, the surface oscillations are approximated by a harmonic oscillator and the Hamiltonian for the intrinsic motion is given by

$$H_0 = \hbar\omega\left(\sum_\mu a^\dagger_{\lambda\mu}a_{\lambda\mu}+\frac{2\lambda+1}{2}\right). \tag{3.81}$$

Here $\hbar\omega$ is the oscillator quanta and $a^\dagger_{\lambda\mu}$ and $a_{\lambda\mu}$ are the phonon creation and annihilation operators, respectively. The surface coordinate $\alpha_{\lambda\mu}$ is related to the phonon creation and annihilation operators by

$$\alpha_{\lambda\mu} = \alpha_0\left(a^\dagger_{\lambda\mu}+(-)^\mu a_{\lambda\mu}\right), \tag{3.82}$$

where α_0 is the amplitude of the zero point motion. It is related to the deformation parameter by $\alpha_0 = \beta_\lambda/\sqrt{2\lambda+1}$ [117] and can be estimated from the experimental transition probability using (see Eq. (3.89))

$$\alpha_0 = \frac{1}{\sqrt{2\lambda+1}}\frac{4\pi}{3Z_TR_T^\lambda}\sqrt{\frac{B(E\lambda)\uparrow}{e^2}}. \tag{3.83}$$

The surface vibration modifies both the nuclear and the Coulomb interactions between the colliding nuclei. In the collective model, the nuclear interaction is assumed to be a function of the separation distance between the vibrating surfaces of the colliding nuclei. It is conventionally taken as

$$V^{(N)}(\mathbf{r},\alpha_{\lambda\mu}) = V_N\left(r-R_T\sum_\mu \alpha_{\lambda\mu}Y^*_{\lambda\mu}(\hat{\mathbf{r}})\right). \tag{3.84}$$

If the amplitude of the zero point motion of the vibration is small, one can expand this equation in terms of $\alpha_{\lambda\mu}$ and keep only the linear term:

$$V^{(N)}(\mathbf{r},\alpha_{\lambda\mu}) = V_N(r)-R_T\frac{dV_N(r)}{dr}\sum_\mu \alpha_{\lambda\mu}Y^*_{\lambda\mu}(\hat{\mathbf{r}}). \tag{3.85}$$

This approximation is called the linear coupling approximation, which has often been used in coupled-channels calculations. The validity of this approximation will be examined in

Chap. 5. The first term of the r.h.s. of Eq. (3.85) is the bare nuclear potential, i.e. the nuclear potential in the absence of the coupling, while the second term is the nuclear component of the coupling Hamiltonian.

The Coulomb component of the coupling Hamiltonian is evaluated as follows. The Coulomb potential between the spherical projectile and the vibrating target is given by

$$V_C(\mathbf{r}) = \int d\mathbf{r}' \frac{Z_P Z_T e^2}{|\mathbf{r}-\mathbf{r}'|}\rho_T(\mathbf{r}') = \frac{Z_P Z_T e^2}{r} + \sum_{\lambda'\neq 0}\sum_{\mu'} \frac{4\pi Z_P e}{2\lambda'+1} Q_{\lambda'\mu'} Y^*_{\lambda'\mu'}(\mathbf{r}) \frac{1}{r^{\lambda'+1}}, \tag{3.86}$$

where ρ_T is the charge density of the target nucleus and $Q_{\lambda'\mu'}$ the electric multipole operator defined by

$$Q_{\lambda'\mu'} = \int d\mathbf{r} Z_T e \rho_T(\mathbf{r}) r^{\lambda'} Y_{\lambda'\mu'}(\hat{\mathbf{r}}). \tag{3.87}$$

The fist term of the r.h.s. of Eq. (3.86) is the bare Coulomb interaction, and the second term is the Coulomb component of the coupling Hamiltonian. In obtaining Eq. (3.86), we used the formula

$$\frac{1}{|\mathbf{r}-\mathbf{r}'|} = \sum_{\lambda'\mu'} \frac{4\pi}{2\lambda'+1} \frac{r_<^{\lambda'}}{r_>^{\lambda'+1}} Y_{\lambda'\mu'}(\hat{\mathbf{r}}') Y^*_{\lambda'\mu'}(\hat{\mathbf{r}}), \tag{3.88}$$

and assumed that the relative coordinate r is larger than the charge radius of the target nucleus. If we assume a sharp matter distribution for the target nucleus, the electric multipole operator is given by

$$Q_{\lambda'\mu'} = \frac{3e}{4\pi} Z_T R_T^{\lambda'} \alpha_{\lambda\mu} \delta_{\lambda,\lambda'} \delta_{\mu\mu'} \tag{3.89}$$

up to the first order in the surface coordinate $\alpha_{\lambda\mu}$. Therefore, by combining Eqs. (3.85), (3.86), and (3.89), the coupling Hamiltonian is expressed by

$$V_{coup}(\mathbf{r}, \alpha_\lambda) = f_\lambda(r) \sum_\mu \alpha_{\lambda\mu} Y^*_{\lambda\mu}(\hat{\mathbf{r}}), \tag{3.90}$$

up to the fist order of $\alpha_{\lambda\mu}$. $f_\lambda(r)$ is the coupling form factor, which is given by

$$f_\lambda(r) = -R_T \frac{dV_N}{dr} + \frac{3}{2\lambda+3} Z_P Z_T e^2 \frac{R_T^\lambda}{r^{\lambda+1}}, \tag{3.91}$$

where the first and the second terms are the nuclear and the Coulomb coupling form factors, respectively. The coupling form factor f_λ has the value

$$f_\lambda(r_B) = \frac{Z_P Z_T e^2}{r_B}\left(\frac{3}{2\lambda+3}\frac{R_T^\lambda}{r_B^\lambda} - \frac{R_T}{r_B}\right). \tag{3.92}$$

at the position of the bare Coulomb barrier r_B.

Transforming to the rotating frame, the coupling Hamiltonian used in the no-Coriolis approximation is then given by

$$V_{coup}(r, \alpha_{\lambda 0}) = \sqrt{\frac{2\lambda+1}{4\pi}} f_\lambda(r) \alpha_{\lambda 0} = \frac{\beta_\lambda}{\sqrt{4\pi}} f_\lambda(r) \left(a^\dagger_{\lambda 0} + a_{\lambda 0}\right). \tag{3.93}$$

In the previous subsection, we showed that the no-Coriolis approximation drastically reduces the dimension of the coupled-channels equations. A further reduction can be achieved by introducing the n-phonon channels [118, 127]. In general, the multi-phonon state of the vibrator has several levels and they are distinguished from each other by the angular momentum and the seniority [117]. For example, for the quadrupole surface vibrations, the two phonon state has three levels $(0^+, 2^+, 4^+)$. In the harmonic limit, these two-phonon triplet is degenerate in the excitation energy. One can then replace the couplings to all the members of the two-phonon triplet by the coupling to a single state given by

$$|2>=\sum_{I=0,2,4}<2020|I0>|I0>=\frac{1}{\sqrt{2!}}(a^\dagger_{20})^2|0> . \tag{3.94}$$

In the same way, one can introduce the n-phonon channel for a general multipolarity λ as

$$|n>=\frac{1}{\sqrt{n!}}(a^\dagger_{\lambda 0})^n|0> . \tag{3.95}$$

If we truncate to the two-phonon states, the corresponding coupling matrix is given by

$$V_{coup}=\begin{pmatrix} 0 & F(r) & 0 \\ F(r) & \hbar\omega & \sqrt{2}F(r) \\ 0 & \sqrt{2}F(r) & 2\hbar\omega \end{pmatrix}, \tag{3.96}$$

where, $F(r)$ is defined as $\beta_\lambda f_\lambda(r)/\sqrt{4\pi}$. The deviations from the harmonic oscillator limit presented in this subsection will be discussed in Chap. 7.

Rotational coupling

We next consider couplings to the ground rotational band of a deformed target. In discussing them, it is convenient to transform to the body fixed frame where the z axis is along the orientation of the deformed target. The surface coordinate $\alpha_{\lambda\mu}$ is then transformed to

$$a_{\lambda\mu}=\sum_{\mu'} D^\lambda_{\mu'\mu}(\phi_d,\theta_d,\chi_d)\alpha_{\lambda\mu'}, \tag{3.97}$$

where ϕ_d, θ_d, and χ_d are the Euler angles which specify the orientation of the target. If we are particularly interested in the quadrupole deformation (λ=2), the surface coordinates in the body fixed frame are expressed as

$$a_{20} = \beta_2\cos\gamma, \tag{3.98}$$

$$a_{22} = a_{2-2}=\frac{1}{\sqrt{2}}\beta_2\sin\gamma. \tag{3.99}$$

If we further assume that the deformation is axial symmetric ($\gamma = 0$), the coupling Hamiltonian for the rotational coupling becomes (see Eq. (3.90))

$$V_{coup}(\mathbf{r},\theta_d,\phi_d)=f_2(r)\sum_\mu \beta_2\sqrt{\frac{4\pi}{5}}Y_{2\mu}(\theta_d,\phi_d)Y^*_{2\mu}(\hat{\mathbf{r}}). \tag{3.100}$$

In obtaining Eq. (3.100), we use the identity

$$D^{L}_{M0}(\phi,\theta,\chi) = \sqrt{\frac{4\pi}{2L+1}} Y^{*}_{LM}(\theta,\phi). \tag{3.101}$$

The coupling Hamiltonian in the rotating frame is thus given by

$$V_{coup}(r,\theta) = f_2(r)\beta_2 Y_{20}(\theta), \tag{3.102}$$

where θ is the angle between (θ_d,ϕ_d) and $\hat{\mathbf{r}}$, i.e. the direction of the orientation of the target measured in the rotating frame. Since the wave function for the $|I0>$ state in the ground rotational band is given by $|I0>= Y_{I0}$, the corresponding coupling matrix is given by

$$V_{coup} = \begin{pmatrix} 0 & F(r) \\ F(r) & \epsilon_2 + 2\sqrt{5}F(r)/7 \end{pmatrix}, \tag{3.103}$$

when it is truncated at the first 2^+ state. In Eq. (3.103), ϵ_2 is the excitation energy of the first 2^+ state, and $F(r)$ is defined as $\beta_2 f_2(r)/\sqrt{4\pi}$. The matrix elements in Eq. (3.103) are calculated by using

$$\begin{aligned} \int Y_{l_1m_1}(\Omega)Y_{l_2m_2}(\Omega)Y_{l_3m_3}(\Omega)d\Omega &= \sqrt{\frac{(2l_1+1)(2l_2+1)(2l_3+1)}{4\pi}} \\ &\times \begin{pmatrix} l_1 & l_2 & l_3 \\ 0 & 0 & 0 \end{pmatrix} \begin{pmatrix} l_1 & l_2 & l_3 \\ m_1 & m_2 & m_3 \end{pmatrix}. \end{aligned} \tag{3.104}$$

One of the main differences between the vibrational (3.96) and the rotational (3.103) couplings is that the latter has a diagonal component which is propotional to the deformation parameter β_2. This is referred to as the 'reorientation effect'and has been used in the Coulomb excitation technique to determin the sign of the deformation parameter [130].

The effects of the γ deformation on subbarrier fusion were studied in Ref. [131]. If there is a finite γ deformation, the coupling Hamiltonian in the rotating frame becomes

$$V_{coup}(r,\theta,\phi) = f_2(r)\left(\beta_2 \cos\gamma Y_{20}(\theta) + \frac{1}{\sqrt{2}}\beta_2 \sin\gamma (Y_{22}(\theta,\phi) + Y_{2-2}(\theta,\phi))\right). \tag{3.105}$$

Higher order deformations can be also taken into account in a similar way as described above. For example, if there is an axial symmetric hexadecapole deformation in addition to an axial symmetric quadrupole deformation, the couplig Hamiltonian reads

$$V_{coup}(r,\theta) = f_2(r)\beta_2 Y_{20}(\theta) + f_4(r)\beta_4 Y_{40}(\theta), \tag{3.106}$$

where β_4 is the hexadecapole deformation parameter.

IBM coupling

An alternative approach to the low-lying collective states in medium heavy nuclei is the interacting boson model (IBM) [132]. In this model, the low-lying collective quadrupole states are described in terms of s and d bosons, which are considered to approximate the $J^\pi = 0^+$ and 2^+ coherent pairs of valence nucleons, respectively. A model for subbarrier fusion reactions, which uses the IBM to describe the effects of channel couplings, has been developed by Balantekin et al. [129,133–136]. They assume that the coupling Hamiltonian has a similar form to that of the collective model Eq. (3.90). In the linear coupling and the no-Coriolis approximations, it is given as

$$V_{coup}(r,\xi) = \frac{v_2}{< 2_1||Q_2||0_1 >}\sqrt{\frac{5}{4\pi}} f_2(r) Q_{20}. \tag{3.107}$$

Here, Q_{20} is the quadrupole operator in the IBM, which is given by

$$Q_{20} = s^\dagger d_0 + s d_0^\dagger + \chi_2 (d^\dagger \tilde{d})_0^{(2)}, \tag{3.108}$$

where tilde is defined as $\tilde{d}_\mu = (-)^\mu d_{-\mu}$. v_2 in Eq. (3.107) is the quadrupole coupling strength. The scaling factor of the coupling strength $< 2_1||Q_2||0_1 >$ has been introduced to ensure the equivalence of the results of the IBM and those of the geometric model in the large N limit, N being the total boson number.

Ref. [134] further discusses the effects of non-linear coupling, which we will detail in Chap. 5. Systematic studies of subbarrier fusion with this model indicate that the coupling strength used in this model v_2 is very similar to that in the geometrical model β_2 [135]. We will use this model in Chap. 7 to discuss the effects of anharmonicity of nuclear vibrations on heavy-ion fusion reactions.

Chapter 4

FUSION BARRIER DISTRIBUTION

4.1 Barrier distribution representation

In Sec. 2.3.2, it has been shown that the effects of channel coupling can be expressed in terms of distribution of potential barriers when the excitation energy of the intrinsic motion is zero, and the underlying structure of the barrier distribution can be detected by taking the first derivative of penetrability. It has also been shown in Sec. 2.3.4 that this picture approximately holds even when the excitation energy is finite, provided that the eigen-channel approximation is good. In the problem of heavy-ion fusion reaction, the experimental observable is not penetrability, but fusion cross section, and thus if one intends to discuss the effects of channel-coupling on fusion in terms of the first derivative of penetrability, one has to convert fusion cross sections to penetrabilities of the s-wave scattering. The Wong formula given by Eq. (3.32) suggests one prescription for this, i.e. it suggests that the first derivative of the product of fusion cross section σ and the center of mass energy E with respect to the energy, $d(E\sigma)/dE$, is propotional to the penetrability of the s-wave scattering

$$\frac{d(E\sigma)}{dE} = \frac{\pi r_B^2}{1+\exp\left[-\frac{2\pi}{\hbar\Omega}(E-V_B)\right]} = \pi r_B^2 P_0(E). \tag{4.1}$$

This equation immediately leads to a relation between the first derivative of the penetrability and the fusion cross section [56]

$$\frac{d^2(E\sigma)}{dE^2} = \pi r_B^2 \frac{2\pi}{\hbar\Omega} \frac{e^{2\pi(E-V_B)/\hbar\Omega}}{\left(1+e^{2\pi(E-V_B)/\hbar\Omega}\right)^2} = \pi r_B^2 \frac{dP_0(E)}{dE}. \tag{4.2}$$

This quantity, which is conventinally called fusion barrier distribution, is peaked at the height of the Coulomb barrier for the s-wave scattering V_B, with the height and the full-width half maximum (FWHM) of $\pi^2 r_B^2/2\hbar\Omega$ and $\hbar\Omega \log(3+\sqrt{8})/\pi \sim 0.56\hbar\Omega$, respectively.

In order to enquire how well the first derivative of $E\sigma$ describes the the s-wave penetrability, the upper panel of Fig. 4.1 compares the first derivative $d(E\sigma)/dE$ obtained by

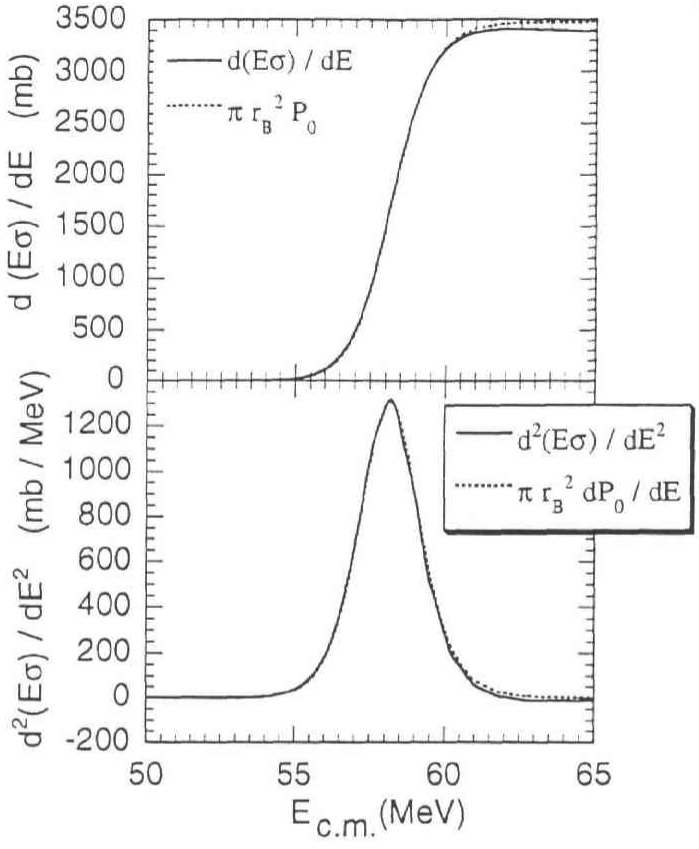

Figure 4.1: The upper panel: comparison of the first derivative of $E\sigma$ (the solid line) with the s-wave penetrability (the dotted line) for the ^{32}S + ^{64}Ni reaction. The latter quantity is scaled by πr_B^2, r_B being the radius of the Coulomb barrier. The internal excitations of both the projectile and the target nuclei are not taken into account. The lower panel: comparison between the second derivative of $E\sigma$ (the solid line) and the first derivative of the s-wave penetrability which is scaled by πr_B^2 (the dotted line).

numerically solving the Schrödinger equation without using the Wong formula, with the numerical solution of the s-wave penetrabilities scaled by πr_B^2. The system is the same as that studied in Ref. [56], i.e. ^{32}S + ^{64}Ni reaction. The same parameters as those in Ref. [56] are used for the nuclear potential. The solid line in the upper panel of Fig. 4.1 is the first derivative of $E\sigma$, while the dotted line is the product of the penetrabilities and πr_B^2. One can find a good agreement between the solid and the dotted lines, suggesting that the first derivative of $E\sigma$ is actually propotional to the s-wave penetrability. The solid line decreases at high energies, while the dotted line becomes close to one. This descrepancy can be attributed to the angular momentum dependence of the barrier radius discussed in Sec. 3.2.3. The lower panel of Fig. 4.1 shows a comparison between the second derivative of $E\sigma$ (the solid line) and the first derivative of penetrability dP_0/dE (the dotted line). We again observe that the agreement is excellent.

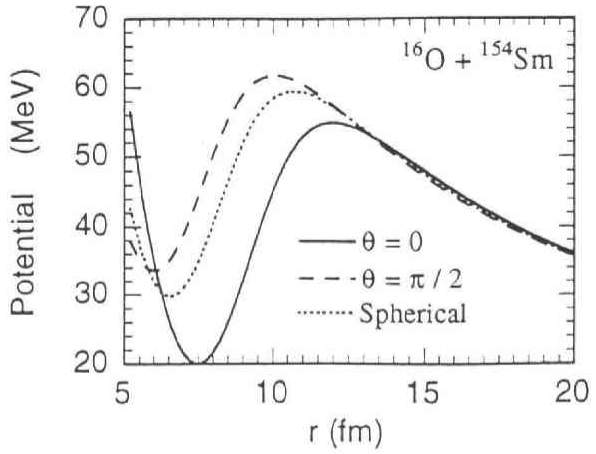

Figure 4.2: The orientation dependence of fusion potential for the $^{16}O + ^{154}Sm$ reaction. The solid and the dashed lines are the potentials when the orientation of a deformed ^{154}Sm is $\theta = 0$ and $\pi/2$, respectively. The potential when the ^{154}Sm nucleus is assumed to be spherical is denoted by the dotted line.

In the presence of the coupling, fusion cross sections may be given by an average over the contributions from each eigen-barrier with appropriate weight factors (see Eqs. (2.54) and (2.60))

$$\sigma(E) = \sum_n w_n \sigma_0(E; V_0(r) + \lambda_n(r)), \tag{4.3}$$

where $\sigma_0(E; V(r))$ is the fusion cross section of a one dimensional potential $V(r)$. The second derivative of $E\sigma$ is then expressed by

$$\frac{d^2(E\sigma)}{dE^2} = \sum_n w_n \pi r_{Bn}^2 \frac{2\pi}{\hbar\Omega_n} \frac{e^{2\pi(E-V_{Bn})/\hbar\Omega_n}}{\left(1 + e^{2\pi(E-V_{Bn})/\hbar\Omega_n}\right)^2} = \sum_n w_n \pi r_{Bn}^2 \frac{dP_0(E; V_0(r) + \lambda_n(r))}{dE}, \tag{4.4}$$

where r_{Bn}, Ω_n, and V_{Bn} are the radius, the curvature, and the height of the n-th eigen potential barrier $V_0(r) + \lambda_n(r)$, respectively. The second derivative of $E\sigma$ has many peaks at energies corresponding to the height of each eigen-potentials, and the height of each peak is propotional to the product of the corresponding weight factor and the square of barrier radius, $w_n r_{Bn}^2$. In the problem of heavy-ion fusion reactions, the barrier radius r_{Bn} strongly depends on the channels due to the fact that the coupling extends outside the Coulomb barrier. This can easily be understood by considering fusion reactions of a spherical projectile on a deformed target which has infinite rotational excited states with zero excitation energy, i.e. a classical rotor. In this case, the potential between the projectile and the target depends on the orientation of the target nucleus, which does not alter during the fusion reaction in the sudden tunneling limit. If the target has a positive β_2 deformation, the attractive nuclear interaction is applied from relatively large distance when the orientation is zero degree, i.e. when the projectile and the target aligne along the symmetry axis of the target. The Coulomb barrier is thus lowered and

appears at relatively larger distance compared with the case where the target is spherical. The opposite happens when the orientation is $\pi/2$, i.e. when the projectile incident in a direction perpendicular to the symmetry axis of the target. In this case, the Coulomb barrier increases and the barrier radius becomes smaller. Figure 4.2 shows the Coulomb barrier for the ^{16}O + ^{154}Sm reaction as a typical example of fusion of a prolate nucleus. The solid and the dashed lines correspond to the cases where the orientation of ^{154}Sm is zero and $\pi/2$, respectively. The dotted line is the potential when the ^{154}Sm is spherical. Due to the effects of deformation (β_2=0.3), the barrier height is distributed from 54.91 to 61.73 MeV, and the barrier radius from 10.07 to 11.98 fm.

Because of the strong dependence of the barrier radius on channels, one has to be careful in interpretending the shape of fusion barrier distribution, $d^2(E\sigma)/dE^2$. For example, the shape may become asymmetric after multiplying the square of barrier radius even when the original distribution is symmetric. In order to demonstrate this, let us consider the ^{16}O + ^{208}Pb fusion reaction in the presence of coupling of the relative motion to the octupole surface vibration of ^{208}Pb. If we truncate the vibrational states at the one phonon state, the coupling matrix in the linear coupling approximation Eq. (3.96) becomes identical to that in the two level problem discussed in Sec. 2.3.5. When the excitation energy of the surface vibration is zero, the fusion cross section is then expressed by

$$\sigma(E) = \frac{1}{2}\left[\sigma_0(E; V_0(r) + F(r)) + \sigma_0(E; V_0(r) - F(r))\right]. \tag{4.5}$$

The upper panel of Fig. 4.3 shows the eigen-potentials $V_0(r) \pm F(r)$ (the solid lines) and the bare Coulomb barrier $V_0(r)$ (the dotted line), while the coupling form factor $F(r)$ is shown in the lower panel. The deformation parameter β_3 was slightly modified from that estimated from the electric transition probability in order to emphasise the effects of channel coupling. Because the peak of the coupling form factor $F(r)$ appears at the different position from that of the bare potential $V_0(r)$, the barrier radii of the eigen-potentials are considerably different from each other. Figure 4.4 shows the corresponding fusion barrier distribution $d^2(E\sigma)/dE^2$ obtained by numerically solving the coupled-channels equations. Because of the peculiar radial dependence of the coupling form factor, the shape of the barrier distribution is significantly asymmetric, though the original weight factors themselves are symmetric.

This observation suggests that the constant coupling approximation Eq. (2.59) does not work well for heavy-ion fusion reactions. It is apparent from Fig. 4.3 that the variation in barrier height at the fixed barrier radius is inconsistent with the realistic situation. Figure 4.5 shows the fusion cross section (the upper panel) and the fusion barrier distribution (the lower panel) for the ^{16}O + ^{208}Pb reaction obtained by setting the excitation energy of the first 3^- to be 2.6 MeV. The double phonon coupling is also included in the harmonic limit. The exact solutions of the coupled-channels equations are denoted by the solid line, while the dotted line is the results in the constant coupling approximation. The strength of the coupling form factor used in the constant coupling approximation was estimated at the barrier position of the bare Coulomb barrier, as is often adopted [79, 97]. The constant coupling approximation overestimates the fusion

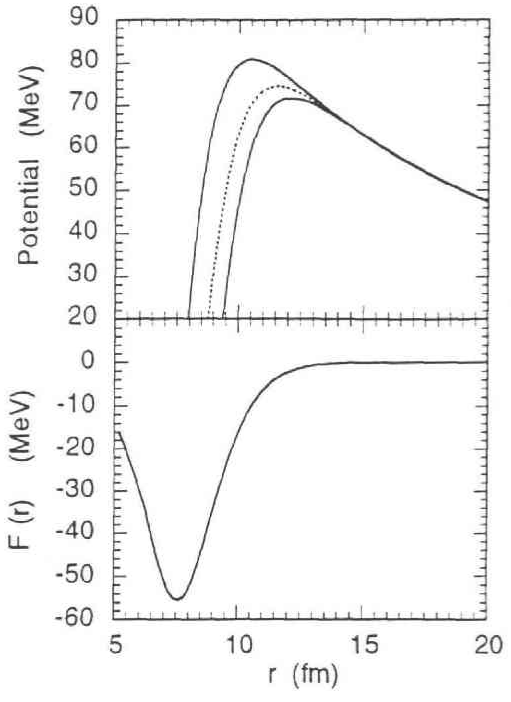

Figure 4.3: The effective potentials for the the $^{16}O + ^{208}Pb$ reaction. The coupling of the relative motion to the one phonon state of the octupole vibration in the ^{208}Pb nucleus is taken into account in the sudden tunneling approximation, i.e. zero excitation energy. The solid lines in the upper panel are the two effective potential barriers $V_0(r) \pm F(r)$, while the dotted line is the potential in the absense of the coupling, $V_0(r)$. The lower panel shows the coupling form factor $F(r)$.

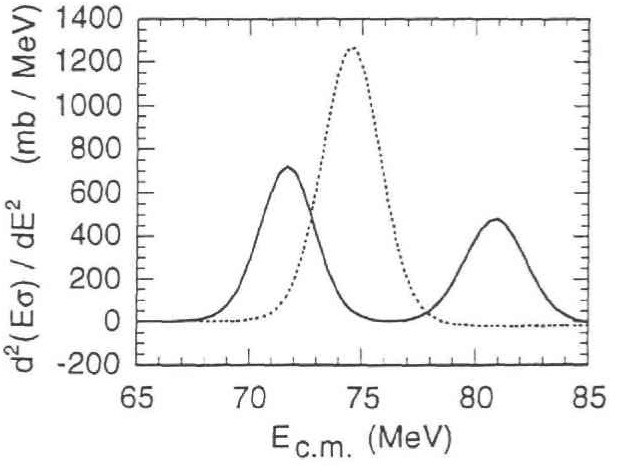

Figure 4.4: Fusion barrier distributions $d^2(E\sigma)/dE^2$ for the $^{16}O + ^{208}Pb$ reaction. The solid takes into account the couplings to the first 3^- state in the ^{208}Pb nucleus in the sudden tunneling approximation, while the dotted line is the fusion barrier distribution in the absense of the coupling.

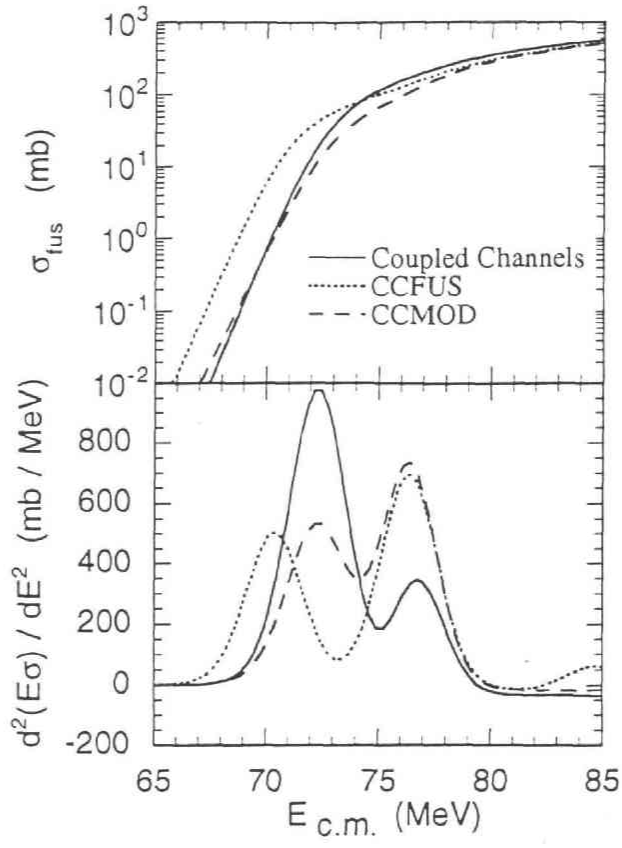

Figure 4.5: The fusion cross section (the upper panel) and the fusion barrier distribution (the lower panel) for the $^{16}O + ^{208}Pb$ reaction obtained by several methods. The double phonon excitations in the ^{208}Pb nucleus are taken into account in the harmonic limit. The solid line is the numerical result of the coupled-channels calculation. The dotted and the dashed lines are obtained by using the constant coupling (CCFUS) and the eigen-channel (CCMOD) approximations, respectively.

cross section and leads to the incosistent shape of fusion barrier distribution. Both the heigts and the position of each peaks of the fusion barrier distribution are not reproduced. One way to avoid this discrepancy is to take the eigen-channel approach. Actually, the computer code CCMOD [42] does not use the constant coupling approximation, but uses the formula in the eigen-channel approximation given by Eq. (2.60). This code adopts the barrier position of the bare Coulomb potential for the position where the weight factors are estimated. The result of CCMOD is denoted by the dashed line in Fig. 4.5. The improvement from the constant coupling approximation is significant. The CCMOD properly reproduces the peak positions of the fusion barrier distribution. Note that the relative height of each peaks of the barrier distribution is still inconsistent with that in the exact calculations. This indecates that the determining the weight factors at the barrier position of the bare barrier is not satisfactory. We will discuss this problem in Sec. 4.4.

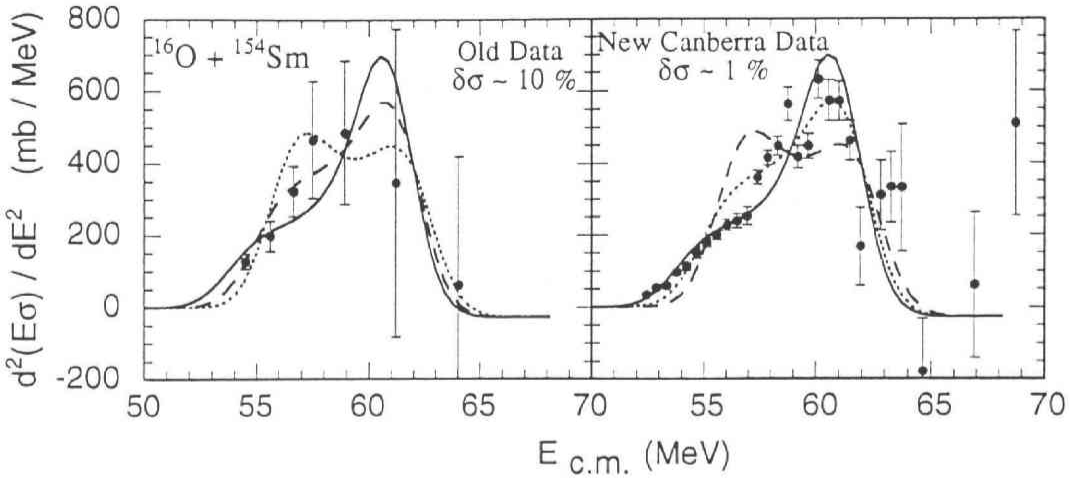

Figure 4.6: The experimental fusion barrier distribution for the ^{16}O + ^{154}Sm reaction extracted from data with uncertainties of 10% (the left panel) [28] and 1% (the right panel) [51]. The solid, the dotted, and the dashed lines are obtained by assuming a positive, negative, and zero values of the hexadecapole deformation parameter, respectively, accompanied with a positive quadrupole deformation of the ^{154}Sm nucleus.

4.2 Extraction of fusion barrier distribution from experimental data

In order to extract fusion barrier distributions directly from experimental data, the second derivative (4.4) may be approximated by point difference formulae. The simplest one is the three point formula given by

$$\left.\frac{d^2(E\sigma)}{dE^2}\right|_{E=E_i} = \frac{(E\sigma)_{i-1} - 2(E\sigma)_i + (E\sigma)_{i+1}}{(\Delta E)^2}, \tag{4.6}$$

where $(E\sigma)_i$ are evaluated at energies E_i. We have assumed the constant energy spacing ΔE. The experimental uncertainty δ_{BD} associated with the second derivative at energy E_i is then approximately given by [51]

$$\delta_{BD} \approx \frac{E}{(\Delta E)^2}\sqrt{(\delta\sigma_{i-1})^2 + 4(\delta\sigma_i)^2 + (\delta\sigma_{i+1})^2}, \tag{4.7}$$

where $\delta\sigma_i$ are the experimental uncertainties in the fusion cross sections. Equation (4.7) shows that the uncertainties of experimental fusion barrier distribution are directly propotional to the energy E, and thus excitation functions of fusion cross section have to be measured with high precision in order to deduce meaningful barrier distributions. This is clearly demonstrated in Fig. 4.6, where the fusion barrier distributions for the ^{16}O + ^{154}Sm reaction extracted from two different experimetal data set are shown. Also shown are theoretical calculations obtained by assuming a positive (the solid line), zero (the

dashed line), and negative (the dotted line) hexadecapole deformation β_4 of ^{154}Sm in accompany with the quadrupole deformation of $\beta_2 = 0.3$. The left panel is the fusion barrier distribution extracted from the experimental data measured by Stokstad et al. [28], which has an experimental uncertainty of 10%. This experimental accuracy is a typical one for the data prior to the new generation of high precision measurement. The experimental fusion barrier distribution extracted from such data is poorly defined, and it cannot distinguish the difference of the shape of the fusion barrier distribution originated from the sign of the small hexadecapole deformation parameter. The right panel of Fig. 4.6 shows the experimental fusion barrier distribution extracted from the recent high precision data of the Canberra group which has a typically 1 % of uncertainty[51]. The improvement is apparent and remarkable. The experimental fusion barrier distribution is well defined, and is consistent with the theoretical calculation with positive hexadecapole deformation [59].

Even with very high precision data, however, fine-tuning of the energy spacing ΔE is required in order to extract a well defined fusion barrier distribution [137]. Mathematically, the second derivative of $E\sigma$ is defined by Eq. (4.6) in the limit of $\Delta E \rightarrow 0$. However, in the realistic situation where the experimental uncertainty of fusion cross sections is finite, the fusion barrier distribution becomes ill defined as the energy spacing ΔE decreases, as can be detected from Eq. (4.7). One way to avoid this is to take a large value of ΔE in the point difference formula. Although the fine structure containing within an energy scale smaller than ΔE is lost, the experimental uncertainty of the fusion barrier distribution δ_{BD} reduces and the quality of the barrier distribution is better defined. When the energy spacing ΔE is too large, on the other hand, the main interesting feature originated from the couplings to the nuclear intrinsic motions is missed. Therefore, the size of ΔE is chosen as a compromise between these two cosiderations. Figure 4.7 shows fusion barrier distributions for the ^{16}O + ^{144}Sm reaction obtained by using the point difference formula with several choices of the energy spacing ΔE. Coupled-channels equations are numerically solved by including both the quadrupole and the octupole single phonon states in the harmonic limit (see the following chapters for more details). The error bars are simurated by assuming that the theoretically obtained fusion cross sections have a hypothetical uncertainty of 1%, which is a typical level of uncertainty in the present experimental status[51]. We can find that the error bars of the fusion barrier distributions obtained by setting $\Delta E = 0.5$ as well as 1 MeV are too huge to see a meaningful structure in the barrier distributions. On the contrary, if we take a larger value of the energy spacing, i.e. $\Delta E = 2$ MeV, the fusion barrier distribution is relatively well defined and a clear double peaked structure can be seen. This structure is somewhat smeared if ΔE is set to be 3 MeV. The main qualitative feature does not alter even if we use a more complicated five point formula, as is shown in Fig. 4.7. (e) and (f).

The most of high precision measurement of fusion cross sections by the Canberra group have been analysed by using the point difference formula of three point (4.6) with ΔE = 2 MeV in the laboratory frame [51]. This procedure will be adopted for most of the experimental fusion barrier distributions presented in this thesis. In order to be consistent, the theoretical fusion barrier distribution will be evaluated in an identical manner when it is compared with the experimental data.

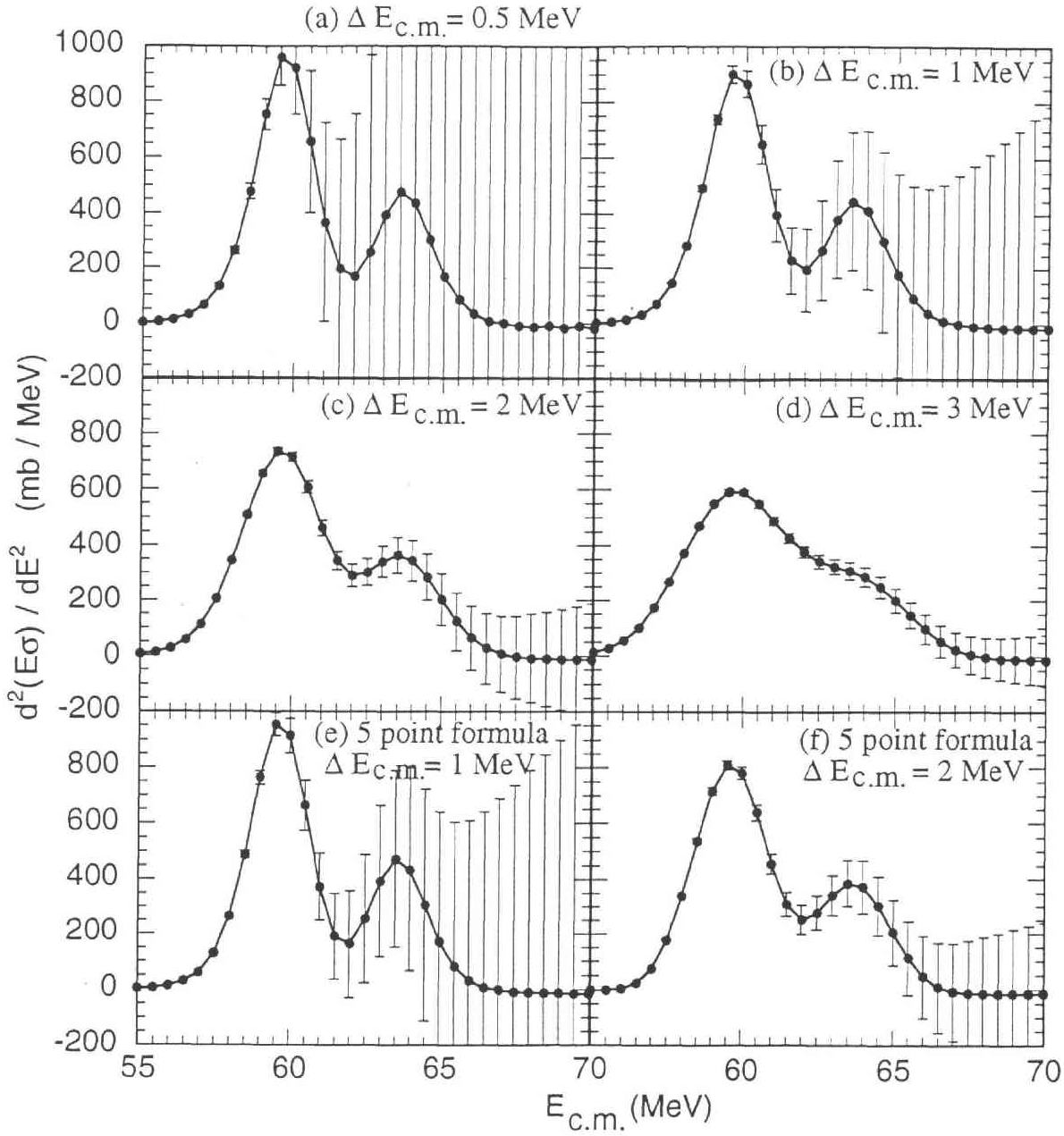

Figure 4.7: Fusion barrier distributions for the ^{16}O + ^{144}Sm reaction obtained by point difference formulae with several values of the energy spacing ΔE. The single octupole and quadrupole phonon states in the ^{144}Sm nucleus are included in the calculations. The error bars are generated by assuming that the theoretical fusion cross sections have a hypothetical uncertainty of 1%. Fig. 4.7 (a), (b), (c), and (d) are obtained by using the point difference formula of three point with ΔE of 0.5, 1, 2, and 3 MeV in the center of mass frame, respectively. Fig. 4.7 (e) and (f) are results of the five point difference formula with the energy spacing ΔE of 1 and 2 MeV in the center of mass frame, respectively.

4.3 Advantages of barrier distribution analyses

Apparently, excitation functions of fusion cross section contain the same amount of informations as the fusion barrier distributions extracted from them. What would then be advantages of analysing the experimental data of fusion cross section in terms of fusion barrier distributions? When the large enhancement of fusion cross sections at subbarrier energies was first observed, there was an argument that it may be hard to identify the underlying physical mechanism of the enhancement of fusion cross sections, since any sort of couplings of the relative motion can lead to the enhancement of the fusion cross sections. The experimental fusion cross section may thus be able to be fitted equally well by two completely different theoretical models. The recent high precision data have challenged to this claiming. The observed fusion barrier distributions were found to be quite sensitive to the details of the channel couplings, while the fusion cross sections themselves are rather featureless [51]. These analyses suggested that the representation of fusion process in terms of the second derivative of $E\sigma$ is a very powerful method to study the details of the effects of nuclear structure, and thus provides a good opportunity to test theoretical frameworks for subbarrier fusion. Here we present two examples of such analyses.

The first example is the ^{16}O + ^{186}W reaction where the effects of hexadecapole deformation on subbarrier fusion reactions were clearly demonstrated [51, 62]. Figure 4.8 shows the experimental data of fusion cross sections (upper panel) and fusion barrier distributions (lower panel) for this system, which are compared with theoretical calculations. The solid, the dotted, and the dashed lines are obtained by setting the sign of the hexadecapole deformation paramter to be negative, positive, and zero, respectively. One can find that the enhancement of the fusion cross section due to the hexacecapole deformation is very similar among these three cases. Especially, these three lines are indistinguishable at high energies. On the other hand, the fusion barrier distribution drastically changes if the sign of the hexadecapole deformation parameter is inverted, as is seen in the lower panel.

This example demonstrates that the fusion barrier distribution is very sensitive to the sign of deformation parameters. This observation was possible only when the cross sections have high precision. In this connection, a work to investigate the role of higher order deformation, i.e. the β_6 deformation in subbarrier fusion is now being in progress [138].

The next example is the ^{16}O + ^{144}Sm collision, where the effects of the couplings to the phonon states in ^{144}Sm on fusion reactions have been confirmed for the first time through the barrier distribution[51, 64]. Figure 3.11 indecated that the enhancement of fusion cross section for this system against the prediction of the one dimensional potential model is not so large. One might, therefore, think that the observed experimental fusion cross section can be fitted in the potential model by varying their parameters. Actually, Di Gregorio et al. analysed this system using the Wong formula (3.32) with the barrier radius r_B, the barrier height V_B, and the barrier curvature $\hbar\Omega$ of 10.24 fm, 59.76 MeV, and 3.9 MeV, respectively [139]. The result of such calculation for the fusion cross sections is shown by the solid line in Fig. 4.9. Although the quality of the fit at high energies is not so good, the theoretical calculation, at a glance, seems to fit the experimental data

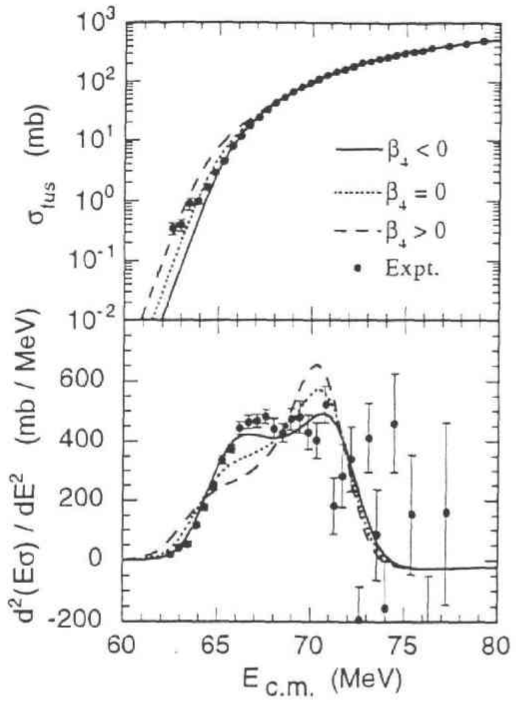

Figure 4.8: Fusion cross section (the upper panel) and fusion barrier distribution (the lower panel) for the $^{16}O + ^{186}W$ reaction. The solid, the dotted, and the dashed lines are obtained by assuming a negative, zero, and positive hexadecapole deformation of the ^{186}W nucleus, together with a positive quadrupole deformation. The experimental data are taken from Ref. [51].

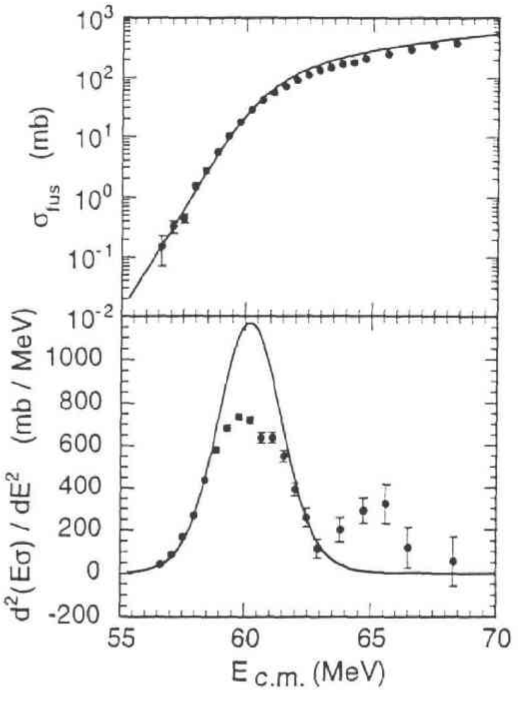

Figure 4.9: Fusion cross section (the upper panel) and fusion barrier distribution (the lower panel) for the $^{16}O + ^{144}Sm$ reaction. The solid line is a prediction of the one dimensional potential model, where the potential parameters are determined so as to reproduce the experimental fusion cross section at low energies [139]. The experimental data are taken from Ref. [51].

reasonably well over the wide energy range. The inadequacy of such approach, however, has already revealed in the fact that any Woods-Saxon potential does not lead to the Coulomb potential which has the same parameters as those used by Di Gregorio et al. (see Appendix C.2). The inconsistency of the model becomes more transparent if it is compared with the experimental fusion barrier distribution $d^2(E\sigma)/dE^2$. Such comparison is presented in the lower panel of Fig. 4.9. It is clearly seen that the one dimensional potential model cannot reproduce the experimental fusion barrier distribution. The experimental fusion barrier distribution has a clear double peaked structure, while the one dimensional potential model which Di Gregorio et al. used gives only a single peak of the fusion barrier distribution. This example clearly demonstrates the possible dangers of analysing experimental data only in a form of fusion cross section, and the advantages of being able to "see"the fusion barrier distribution [51].

4.4 Fusion barrier distribution in systems with finite excitation energy

As was shown in Chap. 2, the barrier distribution representation, i.e. the second derivative of $E\sigma$, has a clear physical meaning only if the excitation energy of the intrinsic motion is zero, and the concept holds only approximately when the excitation energy is finite. Nonetheless, this analysis has been successfully applied to systems with relatively large excitation energies[51, 64, 65]. For example, as we have already discussed in the previous section, the second derivative of $E\sigma$ for ^{16}O + ^{144}Sm fusion reaction clearly shows the effects of coupling to the octupole phonon state in ^{144}Sm, whose excitation energy is 1.8 MeV, much more clearly than the fusion cross section itself [51, 64]. Also the analysis of the fusion reaction between ^{58}Ni and ^{60}Ni, where the excitation energies of quadrupole phonon states are 1.45 and 1.33 MeV, respectively, shows that the barrier distribution representation depends strongly on the number of phonon states included in coupled-channels calculations[65]. These analyses suggest that the representation of fusion process in terms of the second derivative of $E\sigma$ is a very powerful method to study the details of the effects of nuclear structure, irrespective of the excitation energy of the intrinsic motion.

Despite these successes, however, there remains the question whether the second derivative of $E\sigma$ represents a "distribution"of fusion potential barriers when the excitation energy of the intrinsic motion is not zero. To address this problem, we treat here the weight factors as energy dependent variables, as was suggested from Eq. (2.96). The possibility of the energy dependence of weight factors when the excitation energy is finite has been suggested in Ref. [140]. Here, we explicitly study the energy dependence by performing exact coupled-channels calculations [63]. It will be shown that the energy dependence is quite weak for a wide range of excitation energy, suggesting that the eigen-channel approximation works well even when the excitation energy of the intrinsic motion is not small.

Let us consider, for example, the case where the intrinsic degree of freedom has only two levels (see Sec. 2.3.5). One may attempt to use the CCMOD approximation (2.60) discussed also in Sec. 4.1, to address the question whether the picture of barrier distribution holds in systems with finite excitation energies. Even when we introduce this approximation, however, the weight factors are still functions of the chosen position r_w at where the weight factors are evaluated, and the results might strongly depend on that choice. Usually r_w is chosen to be the position of maximum of the bare potential barrier[42, 97]. However, there is no theoretical justification that this is the optimum choice, as is indecated from Fig. 4.5, and furthermore, it is not obvious whether one can determine the weight factors independent of the incident energy.

In order to avoid these drawbacks and examine the energy dependence of the weight factors, we parametrize the penetrability as

$$P(E) = \tilde{w}_+(E)P_+(E) + \tilde{w}_-(E)P_-(E), \tag{4.8}$$

and evaluate the weight factors $\tilde{w}_\pm$ at each incident energy E. Here $P_\pm(E)$ are the penetrabilities of the eigen-potentials $V_0(r) + \lambda_\pm(r)$, respectively, $\lambda_\pm(r)$ being the eigen-

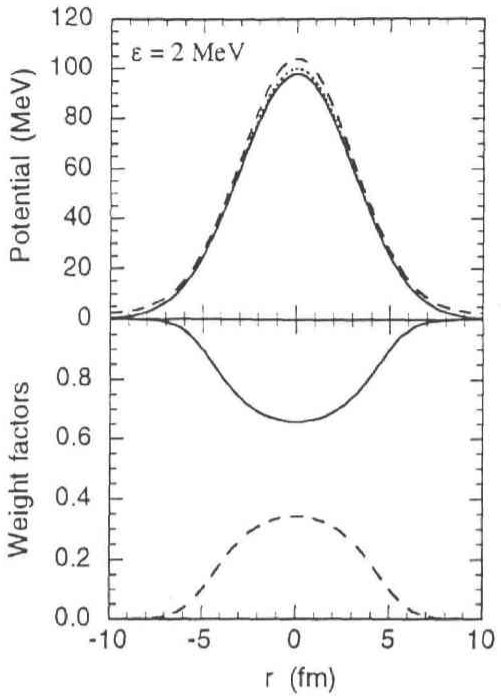

Figure 4.10: The eigen-potentials (the upper panel) and the associated weight factors (the lower panel) as a function of the relative distance r. The solid and the dashed lines in the lower panel are the weight factors for the lower and the higher eigen-potentials, respectively. The dotted line in the upper panel represents the bare potential barrier.

values of the coupling matrix at each position of r, which are given by Eq. (2.62). If the weight factors slowly vary as functions of the incident energy, the effects of channel coupling can be interpreted in terms of the barrier *distribution*, even when the excitation energy is non-zero. Since the weight factors have to satisfy the unitarity condition[53], they can be uniquely determined in the present two level problem, and are given by

$$\tilde{w}_+(E) = (P(E) - P_-(E))/(P_+(E) - P_-(E)), \tag{4.9}$$

$$\tilde{w}_-(E) = (P_+(E) - P(E))/(P_+(E) - P_-(E)). \tag{4.10}$$

We performed coupled-channels calculations to examine the energy dependence of the weight factors. To this end, the coupled-channels equations have to be solved with good accuracy, since the penetrabilities $P(E)$ and $P_\pm(E)$ in Eqs. (4.9) and (4.10) are exponentially small quantities at energies below the barrier. The incoming wave boundary condition, which is often used in coupled-channels calculations for heavy-ion collisions (see Eq. (3.47)), can bring some numerical errors, though they would be small enough for the purpose of calculating fusion cross sections. In order to avoid this, we use here a schematic model of heavy-ion fusion reactions by Dasso *et al.*[79], discussed in Sec. 2.3.5, where the radial motion between colliding nuclei is treated as a one dimensional barrier penetration

problem. We use the same bare potential and the copling form factor as thosed used in Sec. 2.3.5. The excitation energy ϵ is initially set to be 2 MeV.

The upper panel of Fig. 4.10 shows potential barriers for the present problem. The dotted line is the bare potential $V_0(r)$ and the solid and the dashed lines are the eigen-potentials $V_0(r) + \lambda_-(r)$ and $V_0(r) + \lambda_+(r)$, respectively. If we adopt the eigen-channel picture, Fig. 4.10 means that the potential barriers are "distributed"and the original bare potential (the dotted line) splits into the two potentials (the solid and the dashed lines). Because of the non-commutatibity of the unitary matrix which diagonalizes the coupling matrix, and the kinetic energy operator, the standard eigen-channel picture does not apply. If we ignore this non-commutatibity (i.e., if we adopt with the CCMOD prescription) the weight factors are given by Eq. (2.63). They are shown in the lower panel of Fig. 4.10 as a function of the distance r. Although they do not vary so much near the barrier position, their changes are appreciable throughout the barrier region. Therefore, the prescription to fix the weight factors to the values at the barrier position may not be satisfactory.

The results of exact coupled-channels calculations are shown in Fig. 4.11. The first and the second panels are the penetrabilities and their first derivative with respect to the energy, respectively. The latter corresponds to the second derivative of $E\sigma$ [56], as we discussed in Sec. 4.1. We use the point difference formula with $\Delta E = 2$ MeV to obtain the first derivative of the penetrability, as is often done in the analyses of heavy-ion fusion reactions[51] (see Sec. 4.2). The first derivative of the penetrability has a clear double-peaked structure, which could be associated with the two eigen-potential barriers and could thus be interpreted in terms of a 'barrier distribution'. In order to see whether this is the case, we plot in the last panel of Fig. 4.11 the optimum weight factors defined by Eqs. (4.9) and (4.10). The solid and the dashed lines in the figure correspond to the weight factors for the lower and the higher potentials, respectively. We observe that the optimum weight factors change only slightly as functions of the incident energy; their change is barely 2.6 % from 10 MeV below the barrier to 10 MeV above the barrier. Another important result of this calculation is that the weight factors are considerably different from those estimated in the usual way, i.e. at the barrier position. When the constant coupling approximation was first introduced, it was expected that the choice of the position where the weight factors are estimated is not critical to calculate tunneling probabilities because the weight factors vary slowly across the barrier region[79, 97]. The position was then chosen to be the barrier position of the uncoupled barrier. Contrary to this expectation, our calculations show that determining the weight factors at the barrier position does not give proper weight factors even though the weight factors do not have a strong radial dependence. The situation would be much more serious in realistic calculations, since the weights are still changing at the barrier position due to the fact that the coupling extends outside the Coulomb barrier[140] (see Fig. 4.5).

The same calculations were repeated for different values of the excitation energy ϵ and the results are shown in Fig. 4.12. The quantities shown in each panel are the same as those in Fig. 4.11 except for the third panel, where only the optimum weight factors for the lower barrier are plotted. We again observe that the weight factor changes only marginally as a function of the incident energy, even when the excitation energy is

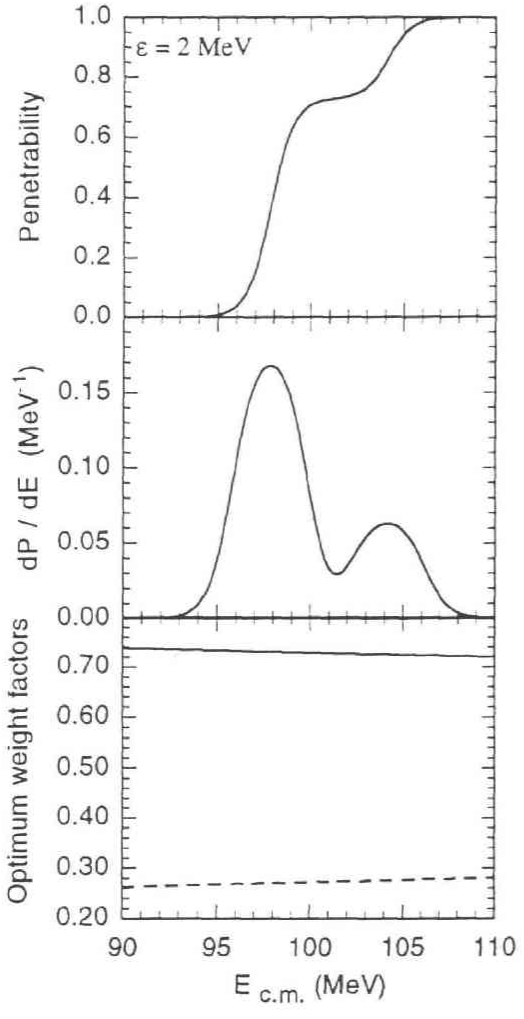

Figure 4.11: The penetrability (the first panel) and its first derivative (the second panel) for the two level problem as a function of the incident energy. The third panel shows the optimum weight factors obtained according to Eqs. (4.9) and (4.10). The solid and the dashed lines correspond to the weight factors for the lower and the higher potentials, respectively.

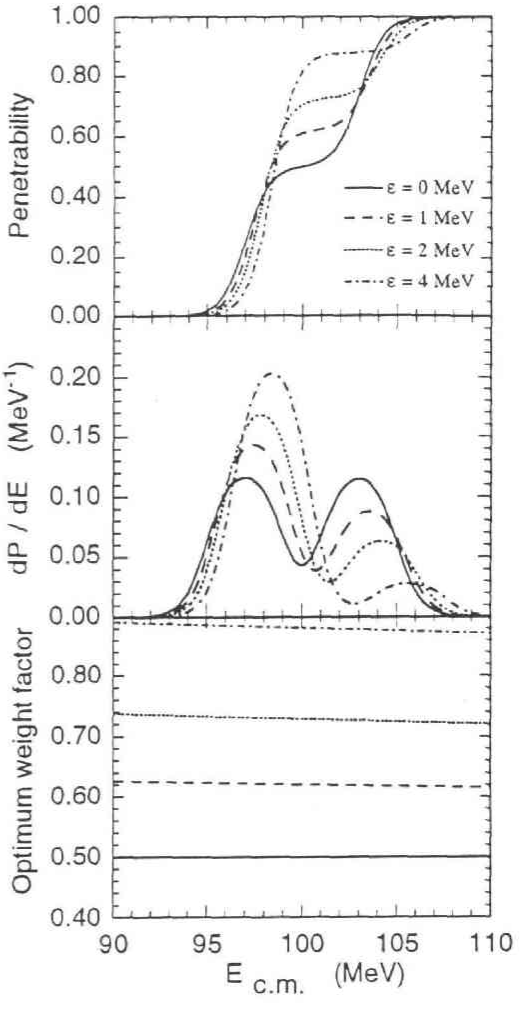

Figure 4.12: Same as Fig. 4.11, but for different values of the excitation energy of the intrinsic motion which are denoted in the inset. The third panel shows only the weight factors for the lower potential.

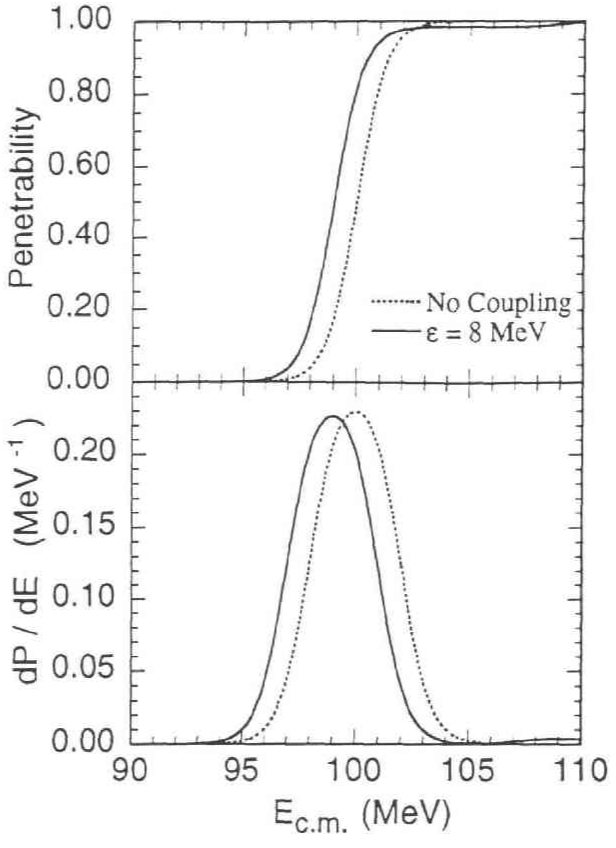

Figure 4.13: Effects of the coupling to a high excitation energy state. The dotted line is the result without channel coupling, while the solid line is obtained by taking into account the coupling to an excited state whose excitation energy is 8 MeV.

finite. We thus conclude that the eigen-channel approach is still applicable even when the excitation energy of the intrinsic motion is finite.

When the excitation energy ϵ is zero, the barrier distribution, i.e. the first derivative of the penetrability has two symmetric peaks and the weight factor has no incident energy dependence (the solid line). As the excitation energy increases, some strength is transfered from the higher peak to the lower peak, and the barrier distribution becomes asymmetric. As the excitation energy significantly exceeds the curvature of the bare barrier, which is about 4 MeV in our example, one expects to reach the adiabatic limit, as was discussed in Sec. 2.3.3. To illustrate this, Fig. 4.13 shows the influence of the coupling to an excited state whose energy is 8 MeV. The figure also contains the result for the the no coupling case (the dotted line) for comparison. In this case, the weight for the higher peak is considerably smaller than that for the lower peak, and the barrier distribution has essentially only a single peak. The peak position, however, is shifted towards a lower energy. This is consistent with the adiabatic picture, i.e. the main effect of the coupling to a state whose excitation energy is much larger the barrier curvature is to introduce an

energy independent shift of the potential accompanied with the mass renormalization (see Eq. (2.93)). Correspondingly, the barrier distribution is only shifted without significantly changing its shape unless the coupling form factor has a strong radial dependence. It is thus clear that the second derivative of $E\sigma$ can represent a wide range of situations between the two extreme limits, i.e. from the adiabatic limit where the coupling leads to an adiabatic potential renormalization, to the sudden limit where the coupling gives rise to a barrier distribution. We will apply this fact in Chap. 6 to discuss the effects of projectile excitations on subbarrier fusion reactions.

Chapter 5

VALIDITY OF THE LINEAR COUPLING APPROXIMATION IN HEAVY-ION FUSION REACTIONS

As we discussed in the previous section, fusion barrier distributions offer a useful test of theoretical models for heavy-ion fusion reactions[51]. In this Chapter, we investigate the validity of the linear coupling approximation in the coupled-channels approach. Coupled-channels equations are numerically solved both for heavy nearly symmetric and for asymmetric systems.

5.1 Present status of coupled-channels calculations

Theoretically the standard way to address the effects of the coupling between the relative motion and the intrinsic degrees of freedom is to solve the coupled-channels equations, including all the relevant channels. We have already discussed this approach in Sec. 3.3. Most of the coupled-channels calculations performed so far use the linear coupling approximation, where the coupling potential is expanded in powers of the deformation parameter, keeping only the linear term (see Eq. (3.85)). Whilst this approach reproduces the experimental data of fusion cross sections for very asymmetric systems, it does not explain the data for heavier and nearly symmetric systems [40, 42, 43, 48, 49]. Thus, it is of interest to examine the validity of one of the main approximations in these calculations, namely the linear coupling approximation, and see whether the effects of non-linear coupling improve the agreement between data and the theoretical calculations for such systems. Even in asymmetric systems, the non-linear couplings might be important to reproduce precisely measured data.

The effects of non-linear coupling can be easily studied if the excitation energy of the intrinsic motion is very small so as to allow one to use the sudden tunneling approximation (see Secs. 2.3.2 and 2.4.2). For example, when the target nucleus is axial symmetrically

deformed, the fusion cross sections in the sudden tunneling limit are expressed by

$$\sigma(E) = \int_0^{2\pi} d\phi \int_0^{\pi} d\theta \, |Y_{00}(\theta,\phi)|^2 \, \sigma_0(E; V(r,\cos\theta)), \tag{5.1}$$

$$= \int_0^1 d(\cos\theta)\sigma_0(E; V(r,\cos\theta)), \tag{5.2}$$

where the orientation dependent potential $V(r,\cos\theta)$ is given by

$$V(r,\cos\theta) = -\frac{V_0}{1+\exp[(r-R_0-R_T\sum_\lambda \beta_\lambda Y_{\lambda 0}(\cos\theta))/a]} + \frac{Z_P Z_T e^2}{r} + \sum_\lambda \beta_\lambda \frac{3}{2\lambda+1} Z_P Z_T e^2 \frac{R_T^\lambda}{r^{\lambda+1}} Y_{\lambda 0}(\cos\theta). \tag{5.3}$$

Here, a Woods-Saxon shape is assumed for the nuclear interaction, and, for simplicity, only the non-linear terms in the nuclear couplings are taken into account (see the discussion in Sec. 5.2). The experimental data of the excitation function of the fusion cross section as well as the barrier distribution for the ^{16}O + ^{154}Sm, ^{186}W reactions were analyzed in this manner[51, 61]. The effects of higher order couplings on barrier distributions in the limit of zero excitation energy has been explicitly discussed by Balantekin, Bennett, and Kuyucak in the framework of the interacting boson model(IBM) [134, 135]. However, for nuclear surface vibrations the excitation energies cannot be neglected in most cases, and one has to solve full coupled-channels equations. Due to the complexity of such calculations, very few studies have addressed the effects of the higher order couplings for the vibrational motion. Esbensen and Landowne expanded the coupling potential up to the second order with respect to the deformation parameter, and have shown that second order coupling leads to a better agreement between the theoretical calculations and the experimental fusion cross sections for reactions between different nickel isotopes[141]. The quadratic coupling approximation was applied also to the ^{58,64}Ni + ^{92,100}Mo reactions[45]. There it was shown that the experimental data of both the fusion cross sections and the angular momentum distributions are well reproduced by the coupled-channels calculations in the quadratic coupling approximation. Coupled-channels calculations including full order coupling and the finite excitation energy of nuclear surface vibrations have recently been performed for the ^{58}Ni + ^{60}Ni reaction[65, 142]. It is seen that higher order couplings are essential in reproducing the experimental data for this system, and the shape of the barrier distribution changes drastically when the effects of the higher order couplings are taken into account. Refs.[65, 142] do not, however, discuss the quality of the quadratic coupling approximation and the convergence of the expansion of the coupling potential.

Although all the above studies and the multi-dimensional tunneling model in Ref.[143] show the effects of higher order couplings in specific systems, there has not been any systematic effort to identify their degree of importance for different systems. Furthermore, it is not obvious whether calculations to all orders are necessary or the expansion up to the second order is sufficient. In view of the high precision data that have recently become available, a critical examination of the effects of these approximations on the cross-sections and barrier distribution is necessary before making quantitative comparisons with experimental data.

In this chapter we solve the coupled-channels equations including the finite excitation energies of the vibrational states, and without introducing the expansion with respect to deformation parameters [80]. The results of these calculations for fusion cross sections, average angular momenta and barrier distributions are compared with those using the linear and the quadratic coupling approximations. In Sec. 5.2, the coupled-channels calculations which include higher order couplings are formulated. Explicit expressions for the matrix elements of higher order terms in both the nuclear and the Coulomb couplings are presented. It is seen that inclusion of up to the first order term in the Coulomb coupling is sufficient, but higher order terms are necessary for nuclear coupling. In Sec. 5.3, the coupled-channels equations are solved for the ^{64}Ni + ^{92,96}Zr systems, where the experimental data of both the fusion cross sections and the average angular momenta of the compound nucleus are available. The asymmetric systems ^{16}O + ^{112}Cd, ^{144}Sm are also studied in this section and the calculations are compared with measured fusion cross sections, barrier distributions, and the average angular momenta of the compound nucleus.

5.2 Coupled-channels equations with non-linear couplings

Consider the problem where the relative motion between colliding nuclei couples to a vibrational mode of excitation of the target nucleus. For simplicity excitations of the projectile are not considered in this section. It is straightforward to extend the formulae to the case where many different vibrational modes are present and where projectile excitations also occur. Introducing the multi-phonon channel defined by Eq. (3.95), the coupled-channels equations in the no-Coriolis approximation read (see Eq. (3.57))

$$\left[-\frac{\hbar^2}{2\mu}\frac{d^2}{dr^2} + \frac{J(J+1)\hbar^2}{2\mu r^2} + V_N(r) + \frac{Z_P Z_T e^2}{r} + n\hbar\omega - E\right] v_n(r) + \sum_m V_{nm}(r) v_m(r) = 0, \tag{5.4}$$

where $\hbar\omega$ is the excitation energy of the vibrational phonon. We have dropped the index J from the wave functions for simplicity. V_{nm} are the coupling matrix elements, which in the collective model consist of Coulomb and nuclear components (see Eq. (3.91)). These two components are discussed in the following sub-sections.

5.2.1 Coulomb coupling

We first consider the effects of higher order terms of the Coulomb component. In Refs. [134, 141] it has been reported that the higher order Coulomb couplings are not important in heavy-ion fusion reactions. However, Ref.[141] studied only the excitation function of the fusion cross section, and did not discuss the barrier distribution. On the other hand, Ref.[134] ignored the finite excitation energy of nuclear intrinsic motions, though it discusses the effects on barrier distribution. Here we investigate the effects of higher order Coulomb couplings on both the excitation function of the fusion cross section and

the barrier distribution and do not ignore the energy of nuclear intrinsic excitations. Initially, we consider the case where the target has only a single phonon excitation.

The Coulomb potential between the spherical projectile and the vibrational target is given by Eq. (3.86). In the no-Coriolis approximation, it becomes

$$V_C(r) = \frac{Z_P Z_T e^2}{r} + \sum_{\lambda' \neq 0} \frac{4\pi Z_P e}{2\lambda'+1}\sqrt{\frac{2\lambda'+1}{4\pi}} Q_{\lambda' 0} \frac{1}{r^{\lambda'+1}}. \tag{5.5}$$

Eq.(5.5) uses the fact that the angular momentum for the relative motion does not change in the no-Coriolis approximation, and that the associated spherical harmonics are evaluated at the forward angle $\hat{\mathbf{r}} = 0$, leading to the factor $\sqrt{(2\lambda'+1)/4\pi}$. Provided that a phonon excitation of multipolarity λ, then the electric multipole operator is given by[144]

$$Q_{\lambda' 0} = \frac{3e}{4\pi} Z_T R_T^{\lambda'} \left\{ \alpha_{\lambda 0}\delta_{\lambda,\lambda'} + (-)^{\lambda'} \frac{(\lambda'+2)(2\lambda+1)}{2\sqrt{4\pi}} \begin{pmatrix} \lambda & \lambda & \lambda' \\ 0 & 0 & 0 \end{pmatrix} (\alpha_\lambda \alpha_\lambda)_{\lambda' 0} \right\}, \tag{5.6}$$

up to second order in the surface coordinate $\alpha_{\lambda\mu}$.

The Coulomb components of the coupling form factors V_{nm} in Eq.(5.4) are obtained by taking the matrix elements of V_C between n- and m- phonon states. Since we assume that there exists only the one phonon state in the vibrational excitation of the target, the Coulomb coupling form factors up to second order of the amplitude of the zero point motion α_0 (see Eqs. (3.82) and (3.83)) are given by

$$V_{01}^{(C)}(r) = V_{10}^{(C)}(r) = \frac{3}{2\lambda+1} Z_P Z_T e^2 \frac{R_T^\lambda}{r^{\lambda+1}} \sqrt{\frac{2\lambda+1}{4\pi}} \alpha_0 \tag{5.7}$$

$$V_{11}^{(C)}(r) = 2\sum_{\lambda' \neq 0} (-)^{\lambda'} \frac{3(2\lambda+1)(\lambda'+2)}{8\pi(2\lambda'+1)} < \lambda 0 \lambda 0 | \lambda' 0 >^2 \alpha_0^2 Z_P Z_T e^2 \frac{R_T^{\lambda'}}{r^{\lambda'+1}}. \tag{5.8}$$

If there exist two-phonon multiplets, then the formalism becomes much more complicated in the case of non-linear coupling. We have shown in Sec. 3.3.3 that, in the case of the linear coupling, the no-Coriolis approximation enables us to replace the couplings to all the members of the two-phonon multiplets by the coupling to a single state by making an appropriate unitary transformation. This leads to a significant reduction of the dimensions of the coupled-channels problem. This property is lost if one keeps higher order terms of the Coulomb coupling since the radial dependence of the coupling form factor for the Coulomb part explicitly depends on the multipolarity of the nuclear excitation.

We now apply Eqs. (5.7) and (5.8) to fusion reactions between two ^{58}Ni nuclei, where the importance of second order couplings in the nuclear interaction has been reported[141]. We take into account the quadrupole vibrational state at 1.45 MeV, and truncate the whole space at the one phonon state. The parameters for the nuclear potential and the deformation parameter from Ref.[141] have been used. Since at this stage we want to investigate the effects of higher order Coulomb coupling, a linear coupling for the nuclear interaction has been used, for ease of calculation. The coupled-channels equations are solved by imposing the incoming wave boundary condition in the inner region of the

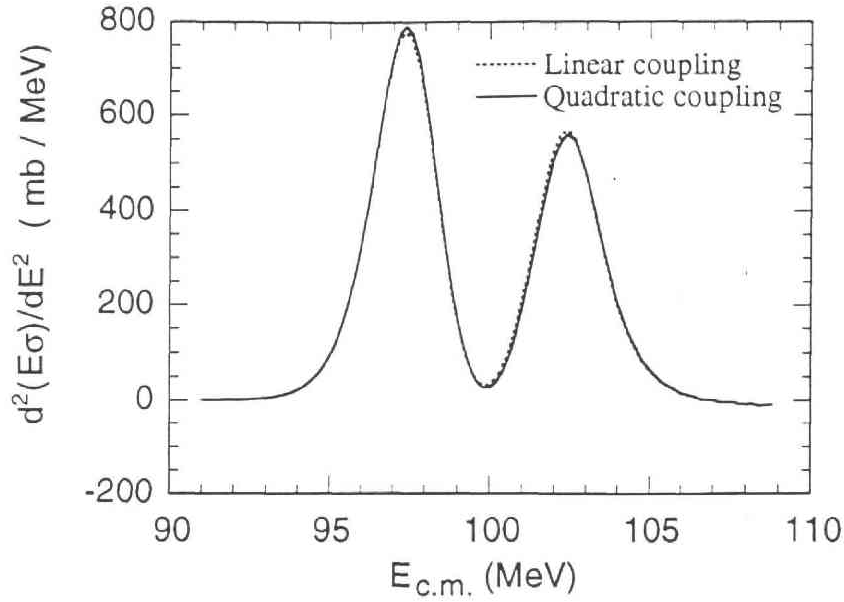

Figure 5.1: The barrier distribution for fusion between two ^{58}Ni nuclei. The one phonon state of the quadrupole surface vibration is taken into account. The nuclear interaction is treated in the linear coupling approximation. The dotted line corresponds to the case where the Coulomb coupling potential is also treated in the linear coupling approximation, while the solid line takes into account non-linear terms up to the second order.

fusion potential. We found that the second order coupling in the Coulomb interaction causes no visible effects to the fusion cross section. It changes the fusion cross section by only about 0.2 % in the energy region we considered, i.e., from about 10 MeV below the Coulomb barrier to about 10 MeV above the Coulomb barrier. Fig. 5.1 shows the fusion barrier distribution ($d^2(E\sigma)/dE^2$) as a function of the bombarding energy. As seen from the figure, second order Coulomb couplings modify only very marginally the barrier distribution. Further calculations showed that the situation does not change when the value of the deformation parameter is varied within physically plausible limits. Therefore we hereafter use the linear coupling approximation for the Coulomb coupling and investigate the effects of the higher order terms only for nuclear coupling. The matrix elements of the Coulomb coupling form factor in Eq. (5.4) are now given by

$$V_{nm}^{(C)}(r) = \frac{3}{2\lambda+1} Z_P Z_T e^2 \frac{R_T^\lambda}{r^{\lambda+1}} \sqrt{\frac{2\lambda+1}{4\pi}} \alpha_0 (\sqrt{n}\delta_{n,m+1} + \sqrt{n+1}\delta_{n,m-1}) \quad (5.9)$$

$$= \frac{3}{2\lambda+1} Z_P Z_T e^2 \frac{R_T^\lambda}{r^{\lambda+1}} \frac{\beta_\lambda}{\sqrt{4\pi}} (\sqrt{n}\delta_{n,m+1} + \sqrt{n+1}\delta_{n,m-1}). \quad (5.10)$$

Note that we have defined the multi-phonon channels by taking the appropriate linear combinations of the multi-phonon multiplets. As remarked before, this is possible only for the linear coupling approximation in the Coulomb interaction.

5.2.2 Nuclear coupling

In the collective model, the nuclear interaction is assumed to be a function of the separation distance between the vibrating surfaces of the colliding nuclei. It is conventionally taken as (see Eq. (3.84))

$$V^{(N)}(r,\alpha_{\lambda 0}) = -\frac{V_0}{1+\exp[(r-R_0-\sqrt{\frac{2\lambda+1}{4\pi}}R_T\alpha_{\lambda 0})/a]}. \tag{5.11}$$

Volume conservation introduces a small term which is non-linear with respect to the deformation parameter $\alpha_{\lambda 0}$ in the denominator of the above Eq.(5.11). This is ignored for simplicity in the present study. As in the case of Eq.(5.5) for the Coulomb coupling, here we consider the coupling form factor for the forward angle, which is needed to obtain the coupled-channels equations in the no-Coriolis approximation. We assume a Woods-Saxon form for the nuclear potential. The structure of the resultant formulae in this subsection, however, remain unchanged for other forms of the nuclear potential. Denoting the eigenvalue of $\alpha_{\lambda 0}$ by x, the matrix elements of the nuclear coupling form factor read

$$V^{(N)}_{nm}(r) = \int_{-\infty}^{\infty} dx \varphi^*_n(x)\varphi_m(x)\frac{-V_0}{1+\exp[(r-R_0-\sqrt{\frac{2\lambda+1}{4\pi}}R_T x)/a]}. \tag{5.12}$$

Here $\varphi_n(x)$ is the eigen function of the n-th excited state of the harmonic oscillator and is given by

$$\varphi_n(x) = \frac{1}{2^n n!}\frac{1}{\sqrt[4]{2\pi\alpha_0^2}} H_n\left(\frac{x}{\sqrt{2}\alpha_0}\right) e^{-x^2/4\alpha_0^2}, \tag{5.13}$$

where $H_n(x)$ is the Hermite polinomial.

The expectation value of the nuclear potential in the ground state is often replaced by the phenomenological potential

$$V_N(r) = -\frac{V_0}{1+\exp[(r-R_0)/a]}, \tag{5.14}$$

which is assumed to be known empirically[141]. If we take this prescription, the nuclear coupling matrix elements in Eq.(5.4) are calculated as

$$\begin{aligned} V^{(N)}_{nm}(r) &= \int_{-\infty}^{\infty} dx \varphi^*_n(x)\varphi_m(x)\frac{-V_0}{1+\exp[(r-R_0-\sqrt{\frac{2\lambda+1}{4\pi}}R_T x)/a]} \\ &\quad -\delta_{n,m}\int_{-\infty}^{\infty} dx|\varphi^*_0(x)|^2\frac{-V_0}{1+\exp[(r-R_0-\sqrt{\frac{2\lambda+1}{4\pi}}R_T x)/a]}. \end{aligned} \tag{5.15}$$

The last term in this equation is included to make the coupling interaction vanish in the entrance channel. Eq. (5.15) represents the coupling matrix elements which contains couplings to all orders. We use these form factors in the next section in order to discuss

the effects of higher order coupling to vibrational modes of excitation of the colliding nuclei on heavy-ion fusion reactions.

Instead of introducing a phenomenological potential given by Eq.(5.14) as the bare potential in the entrance channel, one could use $V_{00}^{(N)}$ in Eq.(5.12) as the nuclear potential in the entrance channel. The use of Eq.(5.14) makes it easier to examine the convergence of the effects of higher order terms by comparing the results of the calculations in the linear and the quadratic approximations and the full order calculations. Notice that $V_{00}^{(N)}$ is identical with the potential given by Eq.(5.14) in the linear coupling approximation.

5.3 Importance of all order couplings

5.3.1 Nearly symmetric systems

We now present the results of our calculations of fusion cross sections, average angular momenta of the compound nucleus, and fusion barrier distributions. We first discuss heavy nearly symmetric systems. The experimental data of the average angular momentum of the compound nucleus for several systems are summarized in Fig.5 of Ref.[49]. It suggests that the conventional coupled-channels calculations do not work for heavy nearly symmetric systems. We analyse in particular ^{64}Ni + ^{92,96}Zr reactions which are typical examples where the conventional coupled-channels calculations with the linear coupling approximation fail to reproduce the fusion cross sections and average angular momentum data[43]. Our aim is to investigate whether the failure is due to the linear coupling approximation by performing linear, quadratic and full coupling calculations.

We take into account the couplings up to two phonon states of the quadrupole surface vibrations of ^{64}Ni and ^{92}Zr, and of the octupole vibration of ^{96}Zr. We also take their mutual excitations into account. We ignore the effects of transfer reactions, because it has been reported in Ref.[43] that they have only small effects on the fusion cross sections and the average angular momenta in these reactions. The excitation energies of the single phonon states in ^{64}Ni, ^{92}Zr, and ^{96}Zr are 1.34, 0.934, and 1.897 MeV, respectively. We assumed the radius parameter associated with the coupling interactions to be 1.2 fm in all cases. The deformation parameter of ^{64}Ni was taken to be $\beta_2 = 0.19$ [141]. Following Refs.[127, 145] we used $\beta_2 = 0.25$ for the nuclear coupling associated with the quadrupole vibration of ^{92}Zr, while the deformation parameter in the Coulomb coupling interaction was estimated from the measured B(E2)$\uparrow$ value to be 0.108. The different value for the nuclear deformation parameter from that of the Coulomb coupling parameter was required in order to fit the angular distribution of the inelastic scattering of ^{16}O from ^{92}Zr at 56 MeV[145]. The deformation parameter β_3 of ^{96}Zr was estimated from the recently measured B(E3)$\uparrow$ value[146] to be 0.268. We assumed the same value for the deformation parameter for the nuclear coupling as that for the Coulomb deformation parameter for this nucleus. The nuclear potentials used in this paper are the same as in Ref.[43].

The excitation function of the fusion cross section for these two systems obtained by numerically solving the coupled-channels equations are compared with the experimental data in Figs. 5.2 and 5.3 (upper panels). The experimental data, taken from Ref. [43],

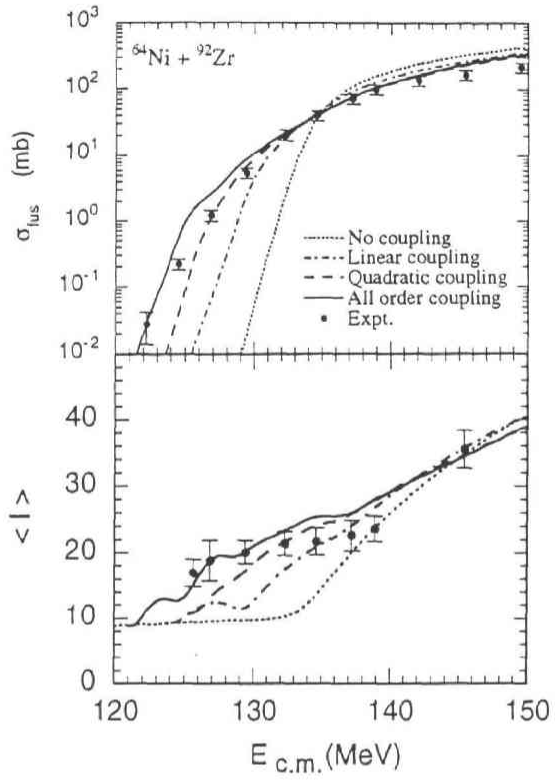

Figure 5.2: Excitation function of the fusion cross section (upper panel) and the average angular momentum of the compound nucleus (lower panel) for the ^{64}Ni + ^{92}Zr reaction. The experimental data are taken from Ref.[43]. The two phonon states of the quadrupole surface vibration of both the projectile and the target are taken into account in the coupled channels calculations. The dotted line is the result in the absence of channel coupling. The dot-dashed and the dashed lines are the results when the nuclear potential is expanded up to the first and the second order terms in the deformation parameters, respectively. The solid line is the results of the coupled channels calculations to all orders, obtained without expanding the nuclear potential.

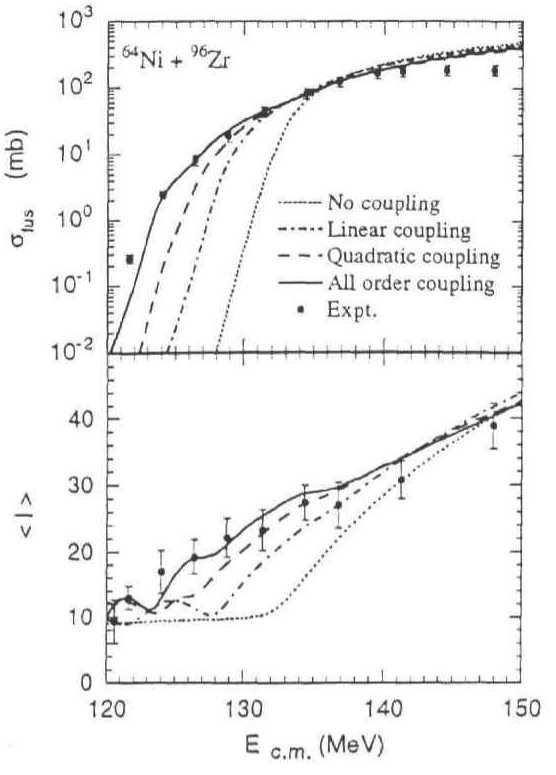

Figure 5.3: Same as Fig. 5.2, but for ^{64}Ni + ^{96}Zr fusion. The two phonon states of the quadrupole surface vibrations of the projectile and those of the octupole surface vibrations of the target are taken into account in the coupled channels calculations. The experimental data are taken from Ref.[43].

consist only of the evaporation residue cross sections, and do not include fission following fusion. The dotted lines are the results in the one dimensional potential model, i.e., without the effects of channel coupling. As is well known, the experimental fusion cross sections at subbarrier energies are several orders of magnitude larger than the predictions of this model. The dot-dashed lines are the results of the coupled-channels calculations when the linear coupling approximation is used, which are similar to the results of the simplified coupled-channels calculations reported in Ref.[43]. They considerably underestimate the fusion cross sections at sub-barrier energies for both systems. The situation is slightly improved when the quadratic coupling approximation is used, i.e., when the nuclear coupling potential up to the second order of the deformation parameter[141], is included (dashed lines). However, there still remain considerable discrepancies between the experimental data and the results of the coupled channels calculations. When we include couplings to all order, we get the solid lines, which agree very well with the experimental data. Dramatic effects of the higher order couplings on fusion cross sections are observed, especially at low energies. The slight underestimate of the fusion cross section at 121.6 MeV in the ^{64}Ni+^{96}Zr reaction will be improved by taking the effects of transfer reactions into account[147].

The lower panels in Figs. 5.2 and 5.3 compare the results of our calculations of the average angular momentum of the compound nucleus (see Eq. (3.29)) with the experimental data as a function of the bombarding energy. The meaning of each line in these figures is the same as in the upper panels. We again observe that the experimental data are much better reproduced by taking the effects of couplings to all orders into account. We thus conclude that coupling to all orders are essential to simultaneously reproduce the fusion cross sections and the average angular momentum data for heavy (nearly) symmetric systems. This is in agreement with the calculations required to fit the barrier distribution for ^{58}Ni + ^{60}Ni reaction[65].

5.3.2 Very asymmetric systems

We next consider the effects of higher order couplings for very asymmetric systems where the product of the charges $Z_P Z_T$ is relatively small. For such systems, the coupled-channels calculations in the linear coupling approximation have achieved reasonable success in reproducing fusion excitation functions. However, no study has been performed to see whether the effects of higher order couplings on the angular momentum distribution of the compound nucleus and on the barrier distributions are small. In this subsection we re-analyse the experimental data for the ^{16}O + ^{112}Cd reaction, for which both fusion cross sections and average angular momentum data are available[48], and those for the ^{16}O + ^{144}Sm reaction, where the the fusion barrier distribution has been extracted from the precisely measured fusion cross sections[51]. For simplicity in the calculations we ignore excitation of the projectile in both reactions. These effects on fusion will be discussed in the next Chapter, where it will be shown that the octupole vibration of ^{16}O leads to a static renormalization of the fusion barrier.

In calculating the fusion cross section for ^{16}O + ^{112}Cd scattering, we include the double quadrupole phonon states and the single octupole phonon state of ^{112}Cd and their mutual

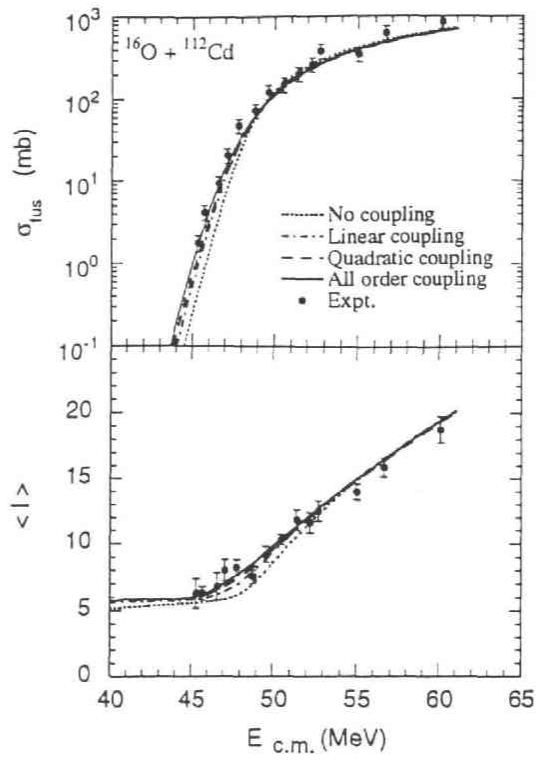

Figure 5.4: Same as Fig. 5.2, but for $^{16}O + ^{112}Cd$ fusion. In the coupled-channels calculations, the projectile is assumed to be inert. The one and two phonon quadrupole states and the one phonon octupole state of the target are taken into account. The experimental data are taken from Ref. [48].

excitations. The excitation energies are 0.617 and 2.005 MeV for the one phonon states of the quadrupole and the octupole vibrations, respectively. The deformation parameters of the quadrupole and the octupole vibrations are estimated to be $\beta_2 = 0.173$ and $\beta_3 = 0.164$, respectively[48]. The radius parameter in the coupling interaction is taken to be 1.2 fm. Following Ref.[48], we use a Woods-Saxon potential whose depth, range parameter, and surface diffuseness are V=58 MeV, r_0=1.22 fm, and a=0.63 fm, respectively.

The upper panel of Fig. 5.4 compares the results of the coupled-channels calculations of fusion cross sections with the experimental data taken from Ref.[48]. Compared with the symmetric systems studied in the previous subsection, the enhancement of the fusion cross sections is fairly small. This is partly because the product of the atomic number $Z_P Z_T$ in this asymmetric system is smaller than the symmetric systems. As is seen in Eq. (3.92), the coupling strength is proportional to the product $Z_P Z_T$. This product is 384 for $^{16}O + ^{112}Cd$ scattering, whilst it is 1120 for $^{64}Ni + ^{92,96}Zr$ reactions. The coupling strength in this asymmetric system is therefore several times smaller than in the symmetric systems even though the values of the deformation parameters are similar. Another reason that the enhancement of the fusion cross sections is small in very asymmetric systems is the

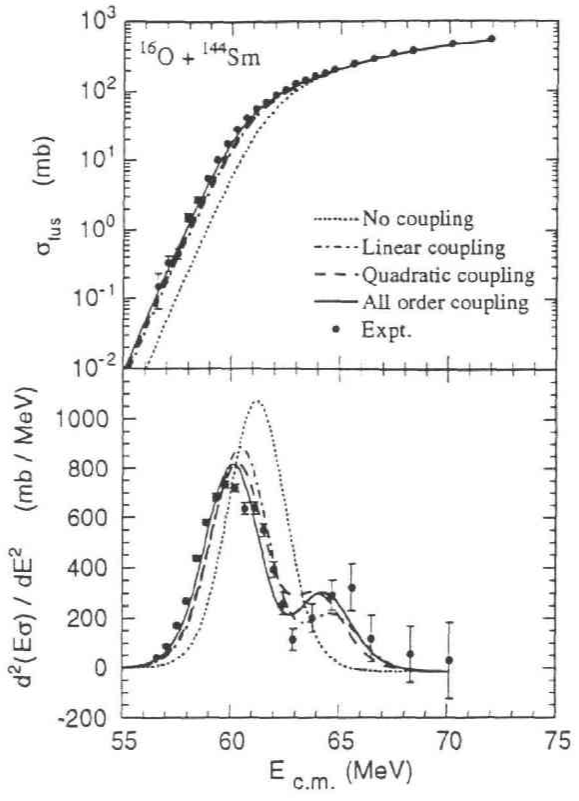

Figure 5.5: Excitation function of the fusion cross section (upper panel) and the barrier distribution (lower panel) for ^{16}O + ^{144}Sm fusion. In the coupled-channels calculations, the projectile is assumed to be inert, while the single octupole phonon state of the target is taken into account. The meaning of each line is the same as in Fig. 5.2. The experimental data are taken from Ref. [51].

small reduced mass. In the WKB formula for the barrier penetrability, the mass parameter appears in the exponent (see Eq. (2.37)). Hence the heavier the mass, the more sensitive the penetrability to a slight change of the potential. Even though the results in the linear coupling approximation (dot-dashed line) show a relatively small enhancement of the fusion cross section compared with the no-coupling limit, there is still a significant change in going to second order coupling, and then to all order coupling. The situation is similar for the average angular momentum. Thus even in such cases with low $Z_P Z_T$, if data of high precision are available, it seems that the linear coupling approximation is inadequate to allow quantitative conclusions to be drawn from a comparison of data and calculations.

The role of higher order couplings in very asymmetric systems can be more clearly seen by investigating the fusion barrier distributions. Therefore, we next consider the ^{16}O + ^{144}Sm reaction. The authors of Ref.[51] have shown that the fusion barrier distribution for this system is intimately related to the octupole vibration of ^{144}Sm, and that the

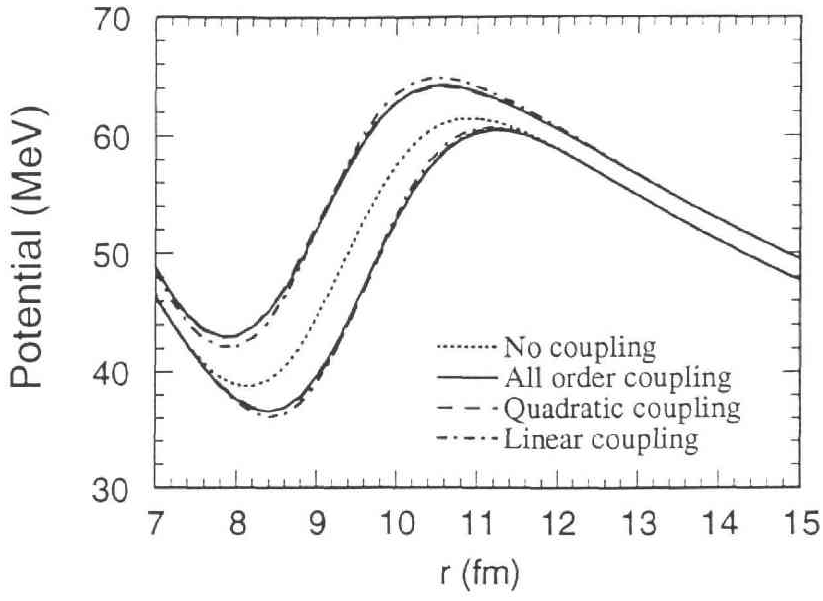

Figure 5.6: Effective potential barriers for the s-wave scattering of ^{16}O from ^{144}Sm obtained by diagonalizing the coupling matrix. The meaning of each line is the same as in Fig. 5.5.

quadrupole vibration plays only a minor role. Accordingly, we ignore the effects of the couplings to the quadrupole phonon states of ^{144}Sm and include only the single octupole phonon state at 1.81 MeV. The deformation parameter β_3= 0.205 was used as in Ref.[51]. The ion-ion potential was of a Woods-Saxon form. The depth, radius parameter and surface diffuseness were 105.1 MeV, 1.1 fm and 0.75 fm respectively, as given in Ref.[106].

The upper panel of Fig. 5.5 shows the fusion excitation function from Ref.[51], and the calculations. The meaning of each line is the same as in Fig. 5.2. As was the case for ^{16}O + ^{112}Cd, we observe that the agreement of the theory and experiment appears to be improved only slightly by the inclusion of coupling to all orders. The barrier distribution, however, reveals significant changes due to the higher order couplings(see the lower panel of Fig. 5.5). Note that there exist two barriers in the present two channel problem. Comparing the results of the linear coupling approximation(the dot-dashed line) with those of the all order coupling(the solid line), one observes that the higher order couplings transfer some strength from the lower barrier to the higher barrier, and at the same time lower the energies of both barriers.

This can be viewed in a different way by performing the diagonalization of the coupling matrix at each position of the internuclear separation to obtain the effective barriers, as is done in the computer code CCMOD [42]. Fig. 5.6 shows these effective barriers for s-wave scattering. The meaning of each line is the same as in Fig. 5.5. We observe that higher order couplings decrease the energies of both the lower and the higher barriers, consistent with the barrier distributions shown in Fig. 5.5. The higher order couplings

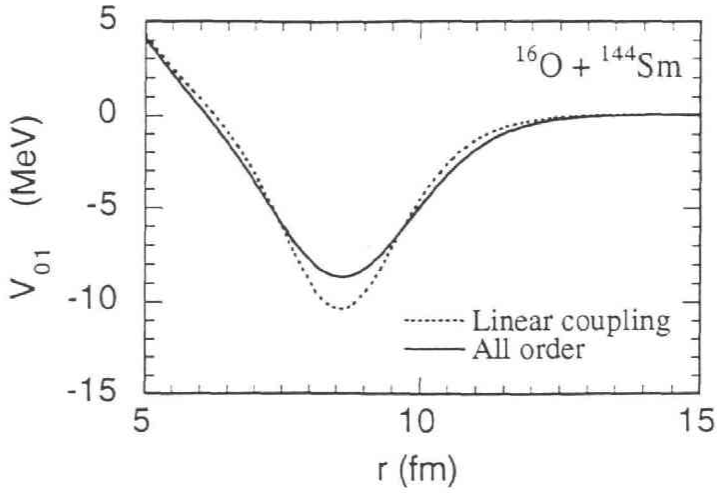

Figure 5.7: The coupling matrix element between the ground state and the one phonon state for the $^{16}O + ^{144}Sm$ reaction as a function of the separation distance between the projectile and target.

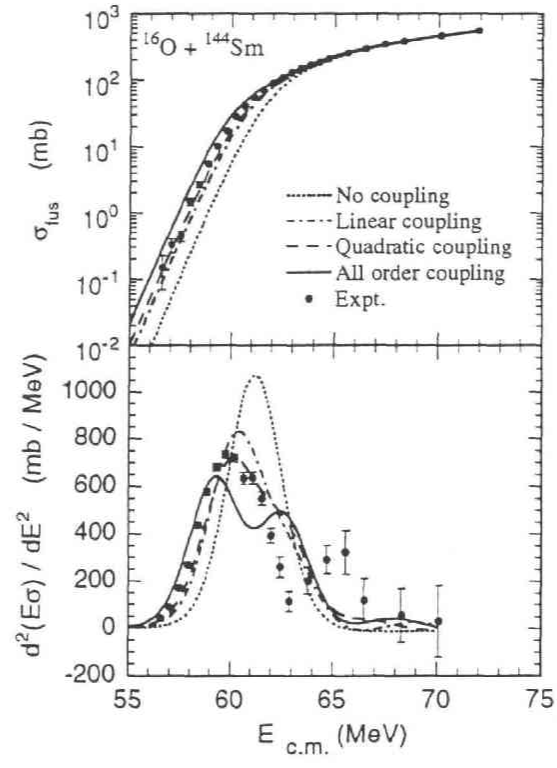

Figure 5.8: Same as Fig. 5.5, but for the case where the double octupole phonon excitations of ^{144}Sm are included in the harmonic limit.

also increase the width of both potential barriers (Fig. 5.6), leading to narrower peaks in the barrier distribution. This then results in the apparent better separation between the two barriers seen in Fig. 5.5.

Figure 5.7 shows the coupling matrix element between the ground state and the one phonon state $V_{01}(r)$ as a function of the inter nuclear separation distance r. The dotted line is the coupling matrix element in the linear coupling approximation, while the solid line includes the coupling to all orders. One can see that the linear coupling approximation underestimates the coupling strength at the barrier position of the uncoupled barrier around $r=$ 10.8 fm. On the other hand, it overestimates the coupling strength in the inner region around r=8.5 fm. As we will see in the next Chapter, the latter fact is important in discussing the effects of the projectile excitation.

The effects of higher order couplings on fusion barrier distribution become more significant when there exist more than two channels. In order to demonstrate this, we show in Fig. 5.8 the barrier distributions for the $^{16}O + ^{144}Sm$ reaction, where the double octupole phonon excitations are allowed in the harmonic limit. One now observes dramatic effects of higher order couplings on the fusion barrier distribution. The detailed studies on the effects of double phonon couplings including anharmonic effects in this reaction will be carried out in Chap. 7.

For these asymmetric reactions, the couplings are relatively weak as a result of a combination of the small product of $Z_P Z_T$ and the relatively small deformation parameters. In such cases the first order approximation might have been expected to be valid. Despite this, the calculations which include couplings to all orders show significant differences from first order calculations. It is clear therefore that high precision measurements should be analysed using all order couplings even when coupling is weak.

Chapter 6

ADIABATIC QUANTUM TUNNELING IN HEAVY-ION FUSION

One of the interesting aspects of the problem of quantum tunneling with many degrees of freedom is in determining which of the multitude of degrees of freedom must be explicitly included in any theoretical description, and which can be omitted. In particular, it is essential to define the role of excitation energy, or the degree of adiabaticity, in limiting the effectiveness of a specific degree of freedom. In nuclear physics, heavy-ion fusion reactions at energies near and below the Coulomb barrier provide an ideal opportunity to address this question through the fusion barrier distributions. We have already shown in Chap.4 that the analyses of the fusion barrier distributions have beautifully demonstrated the effects of couplings of the relative motion to several nuclear intrinsic motions.

Despite these successes, however, there are apparent conflicts regarding the role of projectile excitation. Each barrier distribution for the reactions ^{40}Ca + ^{194}Pt, ^{192}Os shows a characteristic structure, with a higher energy peak which has been associated with the octupole excitation of ^{40}Ca[68]. Calculations of fusion cross-sections for the reactions ^{16}O + ^{154}Sm, ^{A}Ge in Refs. [148, 149] indicated that excitation of ^{16}O is important. In marked contrast, there are no specific features in the measured barrier distribution for the ^{16}O + ^{144}Sm reaction[64] which can be associated with the excitation of ^{16}O; indeed it was shown in Ref. [51] that a good theoretical representation of the barrier distribution is destroyed when the projectile excitation is included.

All the above conclusions were based on comparison of the experimental results with simplified coupled-channels calculations. The simplification has been achieved by using one or more of the following approximations :

1. the no–Coriolis approximation, where the centrifugal potential is assumed to be the same for all channels and equal to that in the elastic channel;

2. the linear coupling approximation, where the nuclear coupling potential is assumed to be linear *w.r.t.* the coordinate of the nuclear vibrational excitation;

3. the constant coupling approximation, where the coupling potential is assumed to be constant over the interaction range;

4. intrinsic excitation energies are assumed to be negligible or are treated approximately.

The first approximation, common to most coupled-channel calculations, including those presented in this thesis, has been shown to work well for heavy-ion fusion calculations (see Sec. 3.3.2). Simplified coupled-channel calculations[51, 66, 97, 149] use the second approximation in conjuction with either the third or fourth. In the previous Chapter, we have shown that the linear coupling approximation is not valid even in systems where the coupling is weak, and that higher order couplings strongly influence the calculated barrier distributions. It is therefore probable that in reactions with nuclei like ^{16}O and ^{40}Ca, where the couplings to the octupole vibrational excitations are strong, barrier distributions calculated with simplified coupled-channel codes like CCFUS[97] do not provide a good representation of the fusion process.

In this Chapter, we present the results of realistic coupled-channels calculations which demonstrate the effects of non-linear coupling and finite excitation energy of intrinsic nuclear (environmental) degrees of freedom, and resolve the apparently conflicting conclusions regarding the influence of the projectile excitation [81]. The relevance of the 'counter term' prescription of Caldeira and Leggett[20] in heavy-ion fusion reactions is also discussed and the double counting problem of coupling effects is clarified.

6.1 Role of ^{16}O excitation in subbarrier fusion

We first discuss the role of projectile excitations in the ^{16}O + ^{144}Sm reaction. The coupled-channels equations are solved by imposing the incoming wave boundary condition to simulate the strong absorption inside the fusion barrier. The real nuclear potential is assumed to have a Woods-Saxon shape and the depth was chosen to reproduce the experimental fusion cross sections at high energies using the single-barrier penetration model. The same potential and the deformation parameters as those in Sec. 5.3.2 are used in the calculations.

In order to show the inadequacies of the often used linear coupling approximation, calculations were performed using the linear coupling approximation. The results of our calculations for the fusion excitation function and the barrier distribution are shown in Fig. 6.1. In the following discussion in this chapter, we concentrate on the latter since they are a more sensitive way to compare experimental data and calculations. The dotted line shows the result when the excitation of ^{16}O is not included in the calculations. This calculation well reproduces the features of the experimental barrier distribution. Calculations including the excitation of the lowest-lying octuple state of ^{16}O are shown by the solid line. Even though the experimental barrier distribution around the lower energy peak ($\sim$ 60 MeV) is reproduced, significant strength is missing around the higher energy peak near 65 MeV. A similar discrepancy between theory and experimental data was encountered in Ref. [51], where calculations, shown by the long–dashed line, were

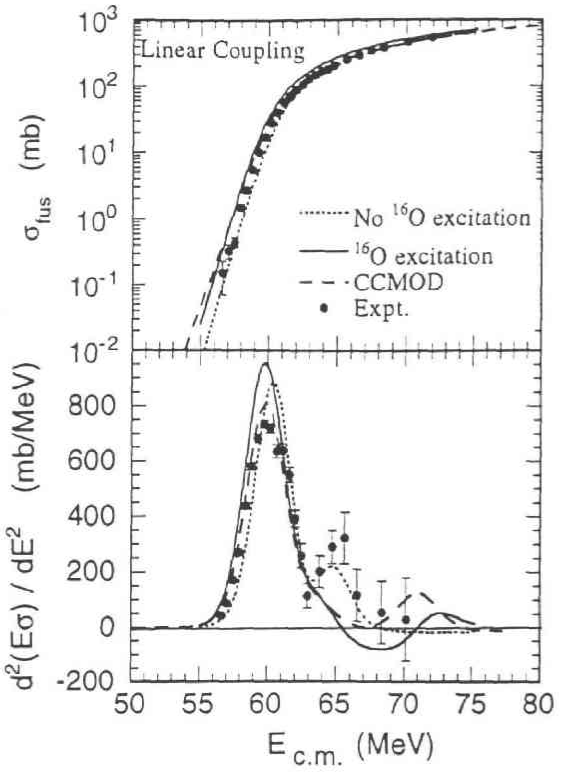

Figure 6.1: Fusion excitation functions (upper panel) and the barrier distributions (lower panel) for the $^{16}O + ^{144}Sm$ reaction. The experimental data (filled circles) are taken from Ref. [51]. The linear coupling approximation is used in the coupled-channels calculations. In all calculations, the effects of the octupole vibration of ^{144}Sm are taken into account. The dotted line is the results when ^{16}O is treated as inert. The solid line is the result of the coupled channels calculations when the coupling to the octupole vibration of ^{16}O is also taken into account; the dashed line is the result of an equivalent CCMOD calculation.

performed using a modified version of the CCFUS code, i.e. CCMOD [42]. It is clear that both calculations which include the octupole excitation of ^{16}O in the linear coupling approximation fail to reproduce the experimental barrier distribution.

Realistic coupled-channels calculations were then performed, where the couplings to the octupole vibrations of both ^{16}O and ^{144}Sm are treated to all orders as we have discussed in the previous Chapter. It is remarkable that these calculations, shown in Fig. 6.2, re-establish the double–peaked structure seen in the experimental data, which was absent in the equivalent linear coupling calculations. The shape of the barrier distribution obtained by including the octupole vibration of ^{16}O using all order coupling is now very similar to that obtained by ignoring it. This similarity becomes particularly evident when the calculated barrier distribution is shifted in energy, as shown by the dashed line in the figure. This is consistent with the general conclusion that the main effect of the coupling to inelastic channels whose excitation energies are larger than the curvature of the bare

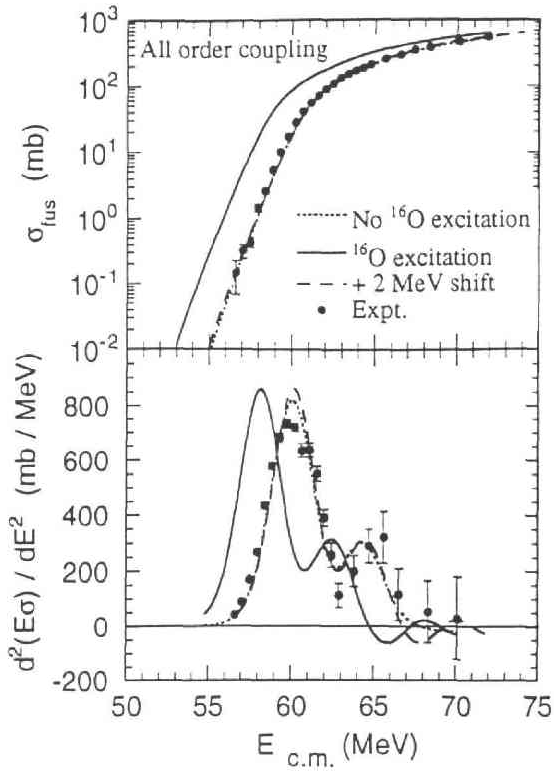

Figure 6.2: As Fig. 6.1, but for the case when the coupled-channels calculations have been performed by including all order coupling. The meaning of the solid and the dotted lines is the same as in Fig. 6.1, while the dashed line is the same calculation as the solid line with the average barrier increased by 2 MeV.

fusion barrier, i.e. an adiabatic coupling, is to introduce a static potential shift as well as a mass renormalization (see Sec. 2.4.3), and hence, the shape of the barrier distribution does not change unless the coupling form factor itself has a strong radial dependence. The same conclusion has been reached in Sec. 4.4, where we discussed the effects of finite excitation energy of the internal motion on fusion barrier distribution.

In macroscopic quantum tunneling in condensed matter physics, the so–called counter term is often introduced in order to compensate for the static potential renormalization due to the coupling to the environment[20]. In contrast, in heavy-ion reactions, one usually estimates the bare potential, for example by fitting the fusion cross section at high energies, and discusses the effects of channel coupling without introducing the counter term. Fig. 6.2 shows that this approach reproduces the experimental fusion cross sections and fusion barrier distributions without explicitly taking into account the excitation of the octupole vibrational state of ^{16}O. This indicates that the effects of its excitation is already included in the bare potential. If this is the case, the effect of the coupling to the 3^- state of ^{16}O is double counted if the coupled-channels calculations explicitly take it into account, resulting in a dramatic overestimate of the the experimental cross-sections. A recipe to

Reaction	Channel Couplings					Potential parameters		
	Nucleus	Type	λ^π	E* (MeV)	β_λ	V_0 (MeV)	r_0 (fm)	a (fm)
$^{16}O + ^{144}Sm$	^{144}Sm	vib	3^-	1.81	0.205	105.1	1.1	0.75
	^{16}O	vib	3^-	6.13	0.733			
$^{40}Ca + ^{194}Pt$	^{40}Ca	vib	3^-	3.70	0.339	330.0	1.0	0.84
	^{194}Pt	rot	2^+	0.328	$\beta_2 = -0.154$			
					$\beta_4 = -0.045$			
$^{40}Ca + ^{192}Os$	^{192}Os	rot	2^+	0.206	$\beta_2 = 0.167$	148.0	1.1	0.84
					$\beta_4 = -0.043$			

Table 6.1: Parameters used in the coupled-channels calculations for the indicated reactions.

cure this problem is to introduce the counter term as in condensed matter physics. Since the experimental data are well reproduced when the calculated distributions are shifted to higher energies by 2 MeV, this shift evidently mimics the effects of the counter term.

6.2 Adiabaticity of ^{40}Ca excitation

In contrast to the $^{16}O+^{144}Sm$ case, the analyses of $^{40}Ca + ^{192}Os$ and ^{194}Pt reactions, also performed using simplified coupled-channel calculations[68], suggest that the excitation of ^{40}Ca is important in determining the observed barrier distribution. An important difference between the ^{16}O and ^{40}Ca projectiles is that the excitation energy of the octupole vibration in the latter is smaller and nearly equal to the energy scale of the curvature of the fusion barrier, hence the coupling is intermediate between adiabatic and sudden. It is therefore interesting to investigate the degree of adiabaticity of the octupole excitation of the ^{40}Ca projectile.

The results of the coupled-channels calculations are compared with the experimental data in Fig. 6.3. All order couplings to both the target and the projectile excitations have been included. The nuclear coupling matrix elements for the rotatioal coupling between I^+ and I'^+ states in the ground rotational band, which corresponds to Eq. (5.12), is given by (see also Eqs. (5.1)–(5.3))

$$V_{II'}^{(N)}(r) = \int_0^1 d(\cos\theta) Y_{I0}^*(\cos\theta) Y_{I'0}(\cos\theta) \frac{-V_0}{1+\exp[(r - R_0 - R_T \sum_\lambda \beta_\lambda Y_{\lambda 0}(\cos\theta))/a]}. \tag{6.1}$$

Although ^{194}Pt and ^{192}Os are transitional nuclei which lie between the γ-unstable and rotational limits in the interacting boson model[150], we have assumed that they are rigid rotors with axial symmetry. The ground state rotational band of the target nucleus, with states up to the 10^+ member, has been included in the calculations. The parameters of the calculations are listed in Table 6.1.

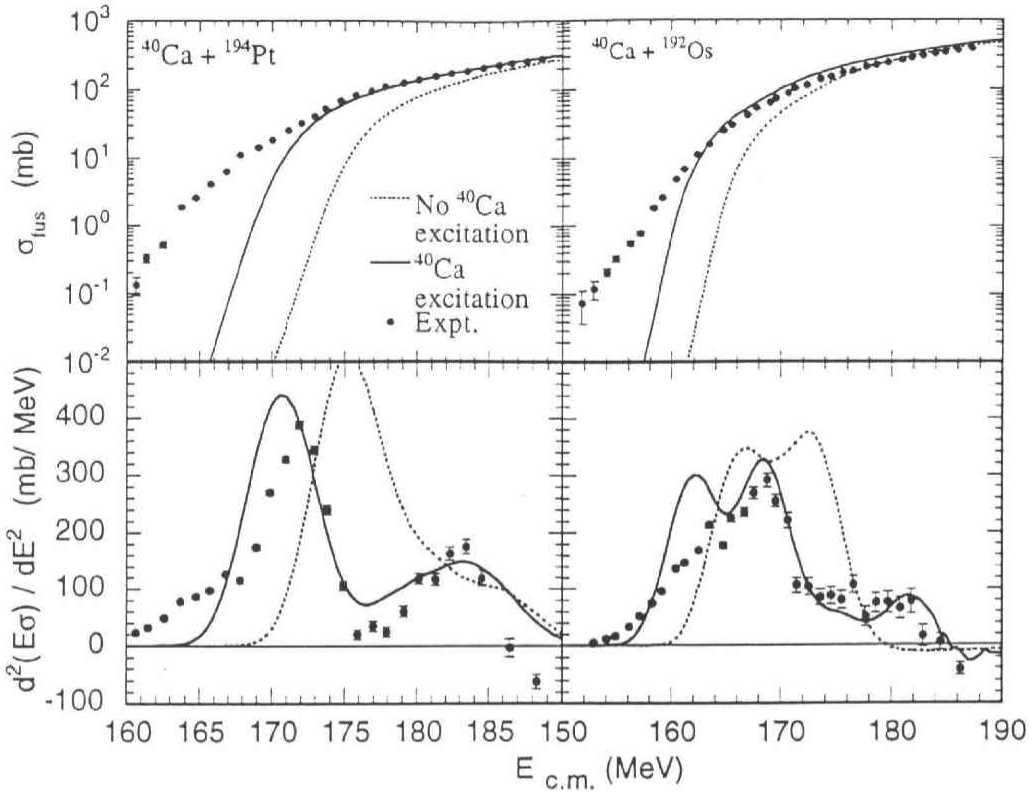

Figure 6.3: The comparison of the experimental fusion cross sections (upper panels) and fusion barrier distributions (lower panels) for the ^{40}Ca + ^{194}Pt, ^{192}Os reactions with the coupled-channels calculations. In all calculations, the effects of the excitation of the target nuclei are treated in the rotational model and couplings to all orders are included. The dotted lines are the results when ^{40}Ca is treated as inert. The solid lines include the coupling to the octupole vibrational state in ^{40}Ca. The experimental data are taken from Ref. [68].

When the ^{40}Ca excitation is ignored, barrier distributions are obtained which are similar to those expected for a classically deformed nucleus and these are inconsistent with the experimental data. When the octupole excitation of ^{40}Ca is included in the calculations, a higher energy peak is introduced which agrees well with that observed in each reaction. The mutual excitation channels up to $4^+ \otimes 3^-$, the former and the latter refering to the targets and the projectile respectively, are also included in the calculations. It is apparent that the projectile excitation significantly affects the shape of the barrier distribution in this case, as suggested in the simplified coupled-channel calculations in Ref. [68].

As has been shown in the discussions for ^{16}O + ^{144}Sm reactions, the correct treatment of the coupling, without making the linear coupling approximation, significantly reduces the effect of projectile excitation on the shape of the barrier distribution. Calculations

of the CCFUS-type, which fail in these regards, would therefore be expected to predict larger coupling effects than observed experimentally. The apparent success of the CCFUS calculations reported in Ref. [68] was probably due to the compensation for this overestimate by the use of a smaller deformation parameter than that obtained from the octupole transition strength.

The theoretical calculations for the reactions with the ^{40}Ca projectile still significantly underestimate the fusion cross section at low energies, even after the excitation of the projectile is taken into account. As suggested in Ref. [68], coupling to transfer channels, which have been ignored in the present calculations, might enhance the fusion cross section at low energies.

It was recently shown that the excitation of the ^{40}Ca projectile does not affect the shape of fusion barrier distribution of the ^{40}Ca + ^{90}Zr reaction [67]. The difference between the ^{40}Ca + ^{194}Pt, ^{192}Os reactions studied in this thesis and this reaction is originated from the fact that the validity of the adiabatic approximation depends not only on the difference of the time scale between the relative motion and the intrinsic motion, but also on the coupling strength between them (see Eq. (2.93) as well as Ref. [77]). Although the adiabatic approximation significantly breaks down in the heavier ^{40}Ca + ^{194}Pt, ^{192}Os systems, it may work quite well for the lighter ^{40}Ca + ^{90}Zr system, because of the smaller coupling strength compared with that in the heavier systems due to the smaller charge product. A work is now in progress to clarify the relation among the coupling strength, the excitation energy, and the barrier curvature, in connection with fusion barrier distribution.

Chapter 7

ANHARMONIC PHONON EXCITATIONS IN HEAVY-ION FUSION REACTIONS

As we have discussed so far, the high precision data have enabled a detailed study of the effects of nuclear collective excitations on fusion reactions, and have generated a renewed interest in heavy-ion subbarrier fusion reactions. Nuclear surface oscillations with various multipolarities are typical examples where the barrier distribution analyses for fusion reactions may be applied to study their detailed properties. For instance, the barrier distribution analysis of the recently measured accurate data on the ^{58}Ni + ^{60}Ni fusion reaction has shown evidence for couplings to double-phonon states in ^{58}Ni and ^{60}Ni [65]. The barrier distributions were shown to be quite sensitive to the number of phonons excited during fusion reactions. In marked contrast, no evidence for double phonon couplings is seen in the experimental fusion barrier distribution for the ^{16}O + ^{144}Sm reaction [51, 64, 106]. The aim of this Chapter is to discuss the role of anharmonicities of surface vibration in subbarrier fusion reactions and show that it plays a very important role in the latter reaction [82, 83]. We also carry out a systematic study on the effects of anharmonicities on subbarrier fusion, and apply the same analysis to the ^{16}O + ^{148}Sm fusion reaction to study the anharmonic properties of the vibrational excitations in ^{148}Sm and their effects on the fusion reaction. Although the importance of the anharmonic effects on proton scattering [151], as well as the reorientation effects in phonon spectra on heavy-ion elastic and inelastic scattering [145, 152] has been pointed out, no systematic studies of the effects of anharmonicities on subbarrier fusion and on fusion barrier distributions have been performed so far. In view of the high precision data on subbarrier fusion reactions, which have recently become available, such studies are necessary in discussing the effects of vibrational excitations on subbarrier fusion reactions. In the next section, we briefly summarise the anharmonic effects of nuclear surface vibrations. In Sec. 7.2, we formulate coupled-channels calculations which explicitly take into account the anharmonic properties of vibrational excitations using the vibrational limit of the interacting boson model [132]. We compare the formalism with that in the harmonic limit and point out several important features of the anharmonic vibrational excitations. In Sec. 7.3, a systematic

study of the effects of anharmonicities on fusion reactions is presented. These include the effects of unequal spacing of levels, reorientation, and finite boson number. In Sec. 7.4, the formalism is applied to the ^{16}O + $^{144,148}Sm$ fusion reactions. We extract the quadrupole moments of the first 2^+ and 3^- states in $^{144,148}Sm$ from the analysis of the high quality fusion data available for these system.

7.1 Anharmonicities in nuclear vibrations

Collective phonon excitations are common phenomena in fermionic many-body systems. In nuclei, low-lying surface oscillations with various multipolarities are typical examples. The harmonic vibrator provides a zeroth order description for these surface oscillations, dictating simple relations among the level energies and the electromagnetic transitions between them. Some of the characteristic features of harmonic oscillators are summarized as follows: (i) all the levels in a phonon multiplet are degenerate and the energy spacing between neighboring multiplets is a constant, (ii) the electric transitions between neighboring multiplets are linearly related, e.g. $B(E2; I_1^+ \rightarrow (I-2)_1^+) = (I/2)\ B(E2; 2_1^+ \rightarrow 0_1^+)$, (iii) the static quadrupole moment is zero for all the phonon states. In realistic nuclei, however, there are residual interactions between phonons, which cause deviations from the harmonic limit [153]. Because of these anharmonic effects, levels are split within a multiplet and the ratios between various electromagnetic transition strengths are modified. Furthermore, the anharmonicities generate a finite value of static quadrupole moment in excited states [154].

In even-even nuclei near closed shells, there are many examples of two-phonon triplets $(0^+, 2^+, 4^+)$ of quadrupole surface vibrations [117]. Though the center of mass of their excitation energies are approximately twice the energy of the first 2^+ state, they usually exhibit appreciable splitting within the triplet. A theoretical analysis of the anharmonicities for the quadrupole vibrations was first performed by Brink et al. [153], who related the excitation energies of three-phonon quintuplet $(0^+, 2^+, 3^+, 4^+, 6^+)$ to those of the double-phonon triplets, and also gave relations between the electric transition strengths from the three- to the two-phonon states and those from the two- to the one-phonon states (see Table 7.1). These relations, however, had not been confirmed until recently because of the sparse experimental data on three-phonon states. The experimental situation has improved rapidly in recent years [155], and data on multi-phonon states are now available for several nuclei. As a consequence, study of multi-phonon states, and especially their anharmonic properties, is attracting much interest [156–160]. It is worthwhile to mention that anharmonic effects are not restricted to low-lying vibrations but have also been observed in multi-phonon excitations of giant resonances in heavy-ion collisions [161–163].

In many even-even nuclei near closed shells, a low-lying 3^- excitation is observed at a relatively low excitation energy, which competes with the quadrupole mode of excitation [117, 164]. These excitations have been frequently interpreted as collective octupole vibrations arising from a coherent sum of one-particle one-hole excitations between single particle orbitals differing by three units of orbital angular momentum [117, 165]. This picture is supported by large E3 transition probabilities from the first 3^- state to

state	energy
2_1^+	$\hbar\omega$
0_2^+	$2\hbar\omega + \epsilon_0$
2_2^+	$2\hbar\omega + \epsilon_2$
4_1^+	$2\hbar\omega + \epsilon_4$
0_3^+	$3\hbar\omega + 3\epsilon_2$
2_3^+	$3\hbar\omega + \frac{7}{5}\epsilon_0 + \frac{4}{7}\epsilon_2 + \frac{36}{35}\epsilon_4$
3_1^+	$3\hbar\omega + \frac{15}{7}\epsilon_2 + \frac{6}{7}\epsilon_4$
4_2^+	$3\hbar\omega + \frac{11}{7}\epsilon_2 + \frac{10}{7}\epsilon_4$
6_1^+	$3\hbar\omega + 3\epsilon_4$

Table 7.1: Relation among the excitation energy of phonon states in the geometrical model [153].

the ground state, and suggests the possibility of multi-octupole-phonon excitations. In contrast to the quadrupole vibrations, however, so far there is only little experimental evidence for double-octupole-phonon states. One reason for this is that E3 transitions from two-phonon states to a single-phonon state compete against lower multipolarity E1 transitions. This makes it difficult to unambiguously identify the two-phonon quartet states $(0^+, 2^+, 4^+, 6^+)$. Thus despite the fact that the first 3^- state of ^{208}Pb has a large quadrupole moment, which is indicative of the anharmonic effects in octupole vibrations [166–169], a direct study of the anharmonic properties in multi-octupole phonon spectra has not been possible for a long time. Only in recent years, convincing evidences have been reported for double-octupole-phonon states, as well as double-phonon states built from single octupole and quadrupole phonon states, in some nuclei, e.g., ^{208}Pb [170], ^{144}Sm [171–174], ^{147}Sm [175], ^{146}Sm [176], ^{145}Nd [175], ^{144}Nd [176], and ^{148}Gd [177, 178].

7.2 Coupled-channels equations for anharmonic phonon excitations

In this section, we introduce the basic formalism for the problem of anharmonic vibrational excitation in subbarrier fusion reactions. Let us first consider the case where the relative motion between the colliding nuclei couples to the quadrupole vibrations in the target nucleus. The Hamiltonian for the fusing system is assumed to be given by Eq. (3.38), where the vibrational excitations in the target nucleus are generically denoted by ξ. In Sub-section 7.2.1, we discuss the coupling of the anharmonic vibrator within the linear coupling approximation. Although this approximation is too simplistic to describe realistic systems as we discussed in Chap. 5, it enables us to understand easily the effects of anharmonicity. Extensions of the model so as to include the couplings to all orders and

state	n_d	v	I	energy
2_1^+	1	1	2	$\epsilon + 5\alpha + 4\beta + 6\gamma$
0_2^+	2	0	0	$2\epsilon + 12\alpha$
2_2^+	2	2	2	$2\epsilon + 12\alpha + 10\beta + 6\gamma$
4_1^+	2	2	4	$2\epsilon + 12\alpha + 10\beta + 20\gamma$
0_3^+	3	3	0	$3\epsilon + 21\alpha + 18\beta$
2_3^+	3	1	2	$3\epsilon + 21\alpha + 4\beta + 6\gamma$
3_1^+	3	3	3	$3\epsilon + 21\alpha + 18\beta + 12\gamma$
4_2^+	3	3	4	$3\epsilon + 21\alpha + 18\beta + 20\gamma$
6_1^+	3	3	6	$3\epsilon + 21\alpha + 18\beta + 42\gamma$

Table 7.2: Quantum numbers in the interacting boson model for U(5) nuclei.

to the octupole vibrations in the target nucleus are given in Sub-sections 7.2.2 and 7.2.3, respectively.

7.2.1 Coupling to anharmonic vibrator

We have already discussed the harmonic oscillator coupling in Sec. 3.3.3. Higher order corrections to Eq. (3.81) lead to anharmonicities in the vibrational spectrum. The effects of anharmonicity in surface vibrations can be described in many different ways. Among them, the interacting boson model (IBM) [132] in the vibrational (U(5)) limit provides a convenient calculational framework to discuss the anharmonic effects. The vibrational limit of the IBM and the anharmonic vibrator (AHV) in the geometrical model are very similar, the only difference coming from the finite number of bosons in the former [155, 179, 180]. The eigenvalues of the intrinsic Hamiltonian H_{int} in the U(5) limit are given by [132]

$$E_{n_d v I} = \epsilon n_d + \alpha n_d(n_d + 4) + \beta v(v + 3) + \gamma I(I + 1), \tag{7.1}$$

where n_d, v, and I are the quantum numbers giving the number of d-bosons, the d-boson seniority, and the intrinsic angular momentum, respectively. ϵ, α, β, and γ are adjustable parameters. The first term gives equally spaced and degenerate phonon spectra, while the splitting of multi-phonon multiplets due to the anharmonic effects are caused by the remaining terms. The quantum numbers for each phonon states are summarised in Table 7.2.

We have discussed in Sec. 3.3.3 a model for subbarrier fusion reactions, which uses the IBM to describe the effects of channel couplings. In the linear coupling and the no-Coriolis approximations, the coupling Hamiltonian to the U(5) spectrum of the target nucleus is given as

$$V_{coup}(r, \xi) = \frac{\beta_2}{\sqrt{4\pi N}} f_2(r) Q_{20}. \tag{7.2}$$

Here, N is the boson number and we have introduced the scaling of the coupling strength with $\sqrt{N}$ to ensure the equivalence of the IBM and the geometric model results in the large N limit (see Eq. (3.107)). Q_{20} is the quadrupole operator in the IBM, which is given by Eq. (3.108). As we have mentioned, it was found that the coupling strengths used in the model are very similar to those in the geometrical model [47]. We, therefore, assume that the coupling strength in Eq. (7.2) is the same as that in the harmonic limit of the geometrical model, Eq. (3.93). This approximation is valid when the anharmonic effects are not very large, so as to allow description of vibrational mode of excitations in terms of the U(5) limit.

In anharmonic vibrators, the multi-phonon states are split within the multiplets. Thus one has to treat each state as a different channel. The introduction of the multi-phonon channel, as in the harmonic limit, is possible only when the multi-phonon states are degenerate in the excitation energies. It will be shown in the next section that one can safely neglect the effects of the splitting of the multiplets on fusion cross section as well as fusion barrier distribution. Accordingly, to keep the calculations simple, we assume in the following that the multi-phonon multiplets are degenerate in the excitation energy unless explicitly mentioned. The wave function of the n-phonon channel in the framework of the IBM then reads

$$|n>=\frac{1}{\sqrt{n!(N-n)!}}(s^\dagger)^{N-n}(d_0^\dagger)^n|0>, \tag{7.3}$$

and the corresponding coupling matrix, truncated to the two-phonon states, is given by

$$V_{coup}=\begin{pmatrix} 0 & F(r) & 0 \\ F(r) & \hbar\omega-\frac{2}{\sqrt{14N}}\chi_2 F(r) & \sqrt{2(1-1/N)}F(r) \\ 0 & \sqrt{2(1-1/N)}F(r) & 2\hbar\omega+\delta-\frac{4}{\sqrt{14N}}\chi_2 F(r) \end{pmatrix}. \tag{7.4}$$

The parameter δ is introduced to represent deviation of the energy spectrum from the harmonic limit. $F(r)$ is $\beta_2 f_2(r)/\sqrt{4\pi}$, as in Eq. (3.96). When the χ_2 parameter in the quadrupole operator is zero, quadrupole moments of all states vanish, and one obtains the harmonic limit in the large N limit. Non-zero values of χ_2 generate quadrupole moments and, together with finite boson number, they are responsible for the anharmonicities in electric transitions. The differences in the coupling scheme between a harmonic oscillator and an anharmonic one are summarized schematically in Fig. 7.1.

7.2.2 All order couplings

We have discussed in Chap. 5 that the linear coupling approximation for the nuclear coupling is not adequate in heavy-ion fusion reactions. Higher order nuclear couplings have to be included in order to describe realistic systems and compare with experimental data. Extension of the anharmonic oscillator coupling to all orders can be carried out in a similar manner as that discussed in Chap. 5. Following Refs. [134–136], we assume that the nuclear coupling Hamiltonian is given in the no-Coriolis approximation by

$$V^{(N)}(r)=\frac{-V_0}{1+\exp\left[\left(r-R_0-R_T\frac{\beta_2}{\sqrt{4\pi N}}Q_{20}\right)/a\right]}. \tag{7.5}$$

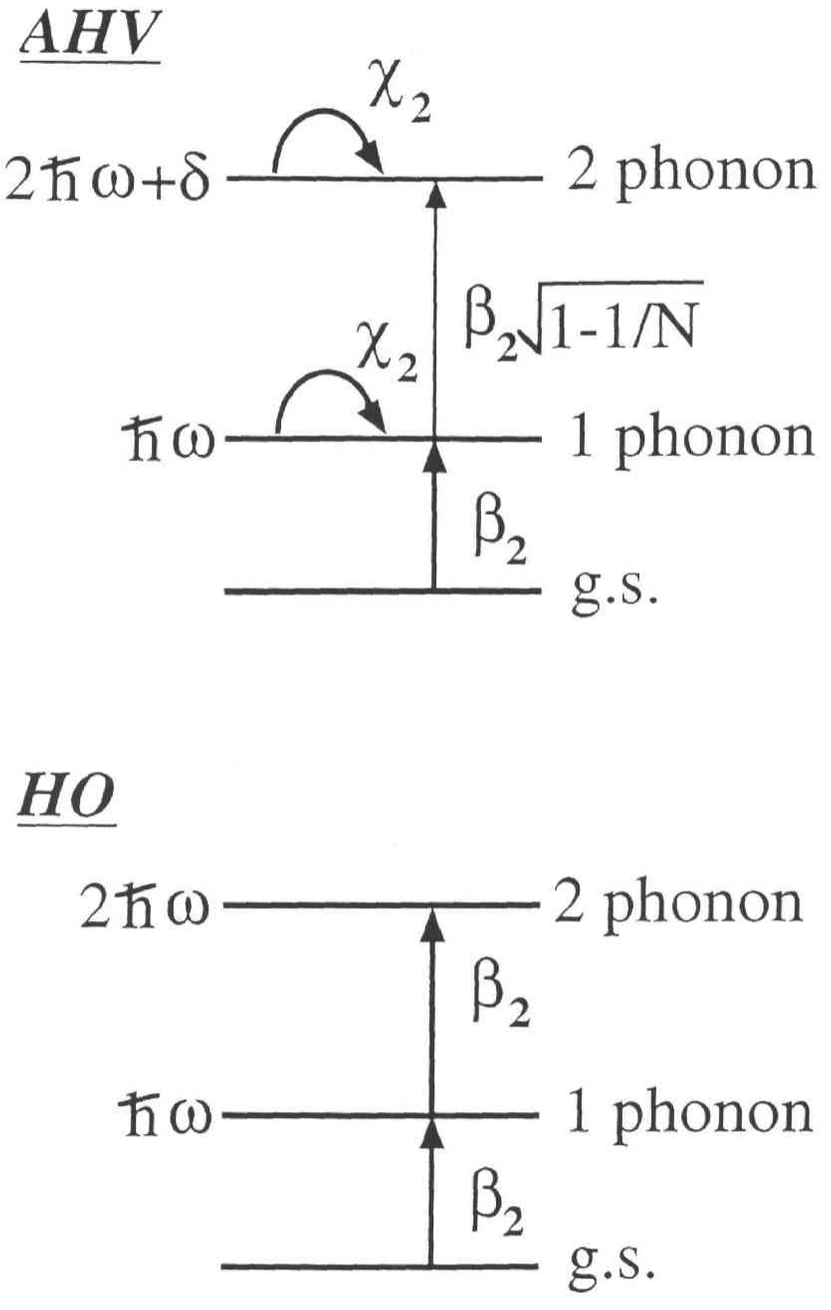

Figure 7.1: Schematic representation of the coupling scheme in vibrational models. The upper part is for the anharmonic vibrator, while the lower part for the harmonic oscillator. See text for the notation.

The matrix elements of Eq. (7.5) can be evaluated most easily by introducing the interaction representation which diagonalizes the quadrupole operator Q_{20} [136]. Note that this equation includes the bare nuclear potential V_N in the total Hamiltonian Eq. (3.38). Since phonon states $|n, I, M\rangle$ with $M \neq 0$ do not couple to the ground state in the no-Coriolis approximation, we do not need to consider the terms $d_m^\dagger d_m$ with $m \neq 0$ in the quadrupole operator, Eq. (3.108). Accordingly, we diagonalize the operator

$$Q_{20} = s^\dagger d_0 + s d_0^\dagger + c_0 d_0^\dagger d_0, \tag{7.6}$$

where $c_0 = -\sqrt{2/7}\chi_2$, in some basis as

$$Q_{20} = e_+ B_+^\dagger B_+ + e_- B_-^\dagger B_-, \tag{7.7}$$

where $B_\pm^\dagger$ ($B_\pm$) are creation (annihilation) operators of the eigenbosons and $e_\pm$ are their eigenvalues. After working out the commutators

$$\left[Q_{20}, B_\pm^\dagger\right] = e_\pm B_\pm^\dagger, \tag{7.8}$$

we find that they are given by

$$B_+^\dagger = y_0 s^\dagger + y_2 d_0^\dagger, \tag{7.9}$$

$$B_-^\dagger = -y_2 s^\dagger + y_0 d_0^\dagger, \tag{7.10}$$

$$e_\pm = \frac{c_0 \pm \sqrt{4 + c_0^2}}{2}, \tag{7.11}$$

with y_0 and y_2 are defined as

$$y_0 = \frac{1}{\sqrt{1 + e_+^2}} = \sqrt{\frac{\sqrt{4 + c_0^2} - c_0}{2\sqrt{4 + c_0^2}}}, \tag{7.12}$$

$$y_2 = \frac{e_+}{\sqrt{1 + e_+^2}} = \sqrt{\frac{\sqrt{4 + c_0^2} + c_0}{2\sqrt{4 + c_0^2}}}. \tag{7.13}$$

The eigenvectors of the quadrupole operator are then given by

$$|n_+, n_-\rangle = \frac{1}{\sqrt{n_+! n_-!}} (B_+^\dagger)^{n_+} (B_-^\dagger)^{n_-} |0\rangle, \tag{7.14}$$

and the matrix elements of the nuclear coupling Hamiltonian between n- and m- phonon channels read

$$\begin{aligned} V_{nm}^{(N)}(r) = & \sum_{k=0}^{N} \frac{-V_0}{1 + \exp\left[\left(r - R_0 - R_T \frac{\beta_2}{\sqrt{4\pi N}} (k e_+ + (N-k) e_-)\right)/a\right]} \\ & \times \sum_{i,j=0}^{k} (-)^{n+m+i+j} \begin{pmatrix} k \\ i \end{pmatrix} \begin{pmatrix} N-k \\ N-n-i \end{pmatrix} \begin{pmatrix} k \\ j \end{pmatrix} \begin{pmatrix} N-k \\ N-m-j \end{pmatrix} \\ & \times \frac{\sqrt{(N-n)!n!(N-m)!m!}}{k!(N-k)!} y_0^{2i+2j-2k+m+n} y_2^{2k+2N-m-n-2i-2j}. \end{aligned} \tag{7.15}$$

In evaluating Eq. (7.15), we have used the fact that the sum of the number of each eigen bosons, $n_+ + n_-$, must be equal to the total boson number N.

7.2.3 Coupling to octupole mode

In most of spherical nuclei, the octupole vibrational state has a large collectivity and their excitations play an important role in subbarrier fusion reactions. Therefore, in order to apply the model which we discussed above to realistic systems, it is necessary to extend them so that they include the octupole mode as well. To this end, we use the vibrational limit of the *sdf*- IBM [132, 181]. This model has been extensively used to describe negative parity states in rotational [181] as well as vibrational [182–184] nuclei. As a natural extension, we assume the following coupling Hamiltonians based on this model for the nuclear and the Coulomb couplings.

$$V^{(N)}(r,\xi) = \frac{-V_0}{1+\exp\left[\left(r - R_0 - R_T\frac{\beta_2}{\sqrt{4\pi N}}Q_{20} - R_T\frac{\beta_3}{\sqrt{4\pi N}}Q_{30}\right)/a\right]}, \tag{7.16}$$

$$V^{(C)}(r,\xi) = \frac{3}{5}Z_P Z_T e^2\frac{R_T^2}{r^3}\frac{\beta_2}{\sqrt{4\pi N}}Q_{20} + \frac{3}{7}Z_P Z_T e^2\frac{R_T^3}{r^4}\frac{\beta_3}{\sqrt{4\pi}}Q_{30}. \tag{7.17}$$

Here, β_3 is the octupole deformation parameter, and we take the quadrupole and the octupole operators in the *sdf*- IBM as

$$\hat{Q}_2 = s^\dagger\tilde{d} + sd^\dagger + \chi_2(d^\dagger\tilde{d})^{(2)} + \chi_{2f}(f^\dagger\tilde{f})^{(2)}, \tag{7.18}$$

$$\hat{Q}_3 = sf^\dagger + \chi_3(\tilde{d}f^\dagger)^{(3)} + h.c., \tag{7.19}$$

respectively, where $\tilde{f}_\mu$ is defined as $(-)^{3+\mu}f_{-\mu}$. We will apply these models in Sec. 7.4 to analyze the ^{16}O + ^{144,148}Sm fusion reactions.

7.3 Anharmonic effects on fusion barrier distributions

In order to discuss the effects of anharmonicity on subbarrier fusion reactions, we perform in this section a series of model calculations without particular regard for the physical values of the parameters. We consider a fictitious nucleus whose excitation energies are given by Eq. (7.1) with $\epsilon = 800$, $\alpha = 10$, $\beta = 0$ and $\gamma = 25$, all in keV. The excitation energy of the first 2^+ state of this nucleus is 1 MeV and the double phonon states are split by 0.5 MeV. We take the total boson number N to be 4 and thus take into account coupling of up to four phonon states. The χ_2 operator in the quadrupole operator Eq. (3.108), the quadrupole deformation parameter β_2 and the target radius are set to be -3, 0.25 and 6.35 fm, respectively. Finally, the Christensen-Winther parameterization of the Woods-Saxon potential [110] for the ^{16}O + ^{148}Sm system is used for the ion-ion potential V_N.

As we discussed in the previous section, introduction of the multi-phonon channels significantly reduces the dimension of the coupled-channels equations. To see whether this approximation is good, a calculation is first made by taking fully into account the effects of the splittings in the phonon spectrum. In order to keep the calculation simple, we make here the linear coupling approximation. In Fig. 7.2, we show the excitation

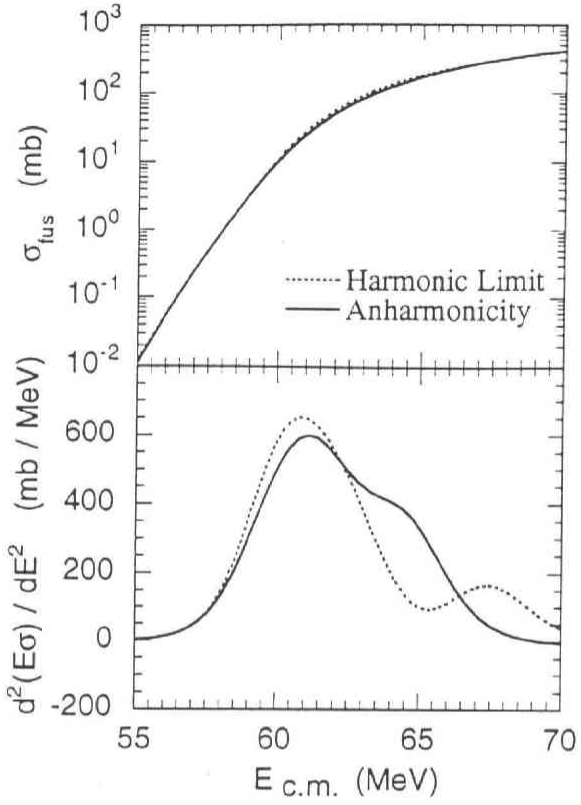

Figure 7.2: Effects of anharmonicity of the quadrupole vibration on the excitation function of the fusion cross section (the upper panel) and fusion barrier distribution (the lower panel). The dotted line is the result in the harmonic limit, while the solid line takes the anharmonic effects of the vibrational excitations into account. The linear order coupling is assumed.

function of the fusion cross section (the upper panel) and the barrier distribution (the lower panel) that follow from using the U(5) limit as described above (solid line). Barrier distributions are obtained using a point-difference formula [51] with ΔE =2 MeV in the laboratory frame. To see the effect of the splittings of the multi-phonon states, we have repeated the same calculation by assuming that the n-phonon multiplets are degenerate at the excitation energy of the first $(2n)^+$ state. We found that this prescription leads to no visible change in the fusion barrier distribution compared to the actual case with splitt energy levels. In the following, we shall therefore assume a degenerate multi-phonon spectrum and use a single multi-phonon channel representing all the states in a multiplet.

In Fig. 7.2, we also compare the results for the anharmonic vibrator with those in the harmonic limit (the dotted line). One can observe that the anharmonic effects in the vibrational excitations lead to a significant change in the barrier distribution, though the excitation function of the fusion cross section itself is modified only marginally.

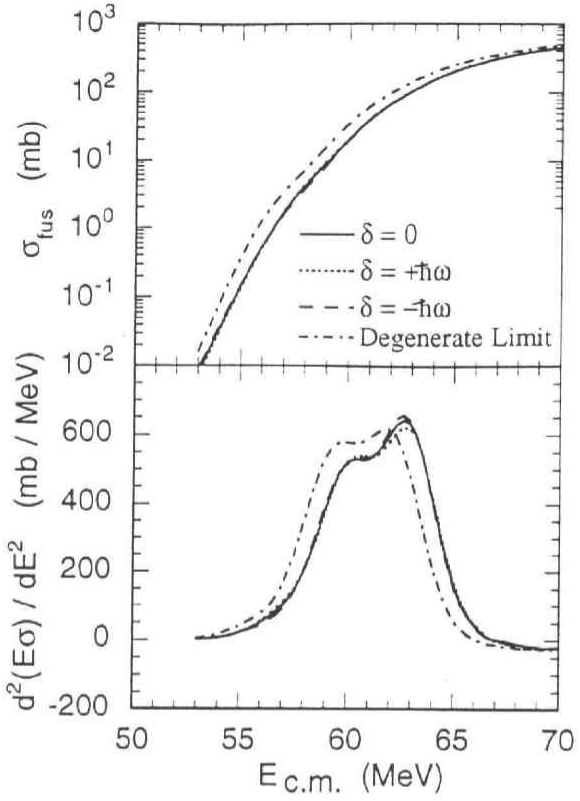

Figure 7.3: Dependence of the fusion cross section (the upper panel) and fusion barrier distribution (the lower panel) on the deviation of the energy spectrum from the harmonic limit. The solid, the dotted, and the dashed lines are obtained by setting the parameter δ in Eq. (7.4) to be zero, 0.5, and -0.5 MeV, respectively. The dot-dashed line is the result in the degenerate limit in the anharmonic vibrator coupling. The phonon spectrum is truncated at the double phonon levels. The full order couplings are included.

7.3.1 Anharmonicities in excitation energies

In all the following calculations, we take into account the couplings to all orders. We first discuss the effects of the deviation of the energy spectrum from the harmonic limit. In order to isolate these effects, we truncate the phonon spectrum at the double-phonon states in this subsection. Fig. 7.3 shows the dependence of the fusion cross section (the upper panel) and the fusion barrier distribution (the lower panel) on the parameter δ in Eq. (7.4). The cross section and the barrier distribution are calculated for three different values of δ. The solid line is the result when $\delta = 0$, while the dotted and the dashed lines are obtained by setting δ to be 0.5 and -0.5 MeV, respectively. Despite the fact that an unrealistically large value is used for δ so as to maximize its effect, the barrier distribution changes only slightly for different choices of δ. This indicates that the main effects of anharmonicity on fusion barrier distributions come from the deviation of the transition probabilities from the harmonic limit, including the reorientation effect, rather

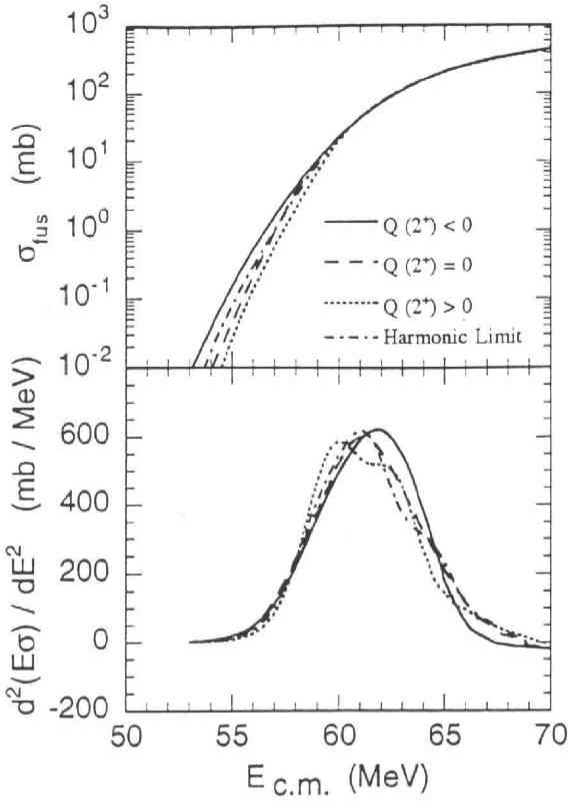

Figure 7.4: Dependence of the fusion cross section (the upper panel) and fusion barrier distribution (the lower panel) on the sign of the quadrupole moment of the first 2^+ state. The solid and the dotted lines correspond to the cases for the negative and the positive static quadrupole moments, respectively. The dashed line was obtained by setting the quadrupole moment of the excited states to be zero. The dot-dashed line is the result of the corresponding calculations in the harmonic limit.

than anharmonicities in the level energies. Note that this observation does not necessarily mean that fusion reactions are not sensitive to the excitation energy of the phonon states. To demonstrate this, we show in Fig. 7.3 also the result when both $\hbar\omega$ and δ is set to be zero (the dot-dashed line). One can see sizable effects of the finite excitation energy of the phonon states on the fusion barrier distribution as well as fusion cross section. We thus conclude that, though the fusion cross section and the barrier distribution are sensitive to the energy of the single-phonon state, they do not depend so much on the excitation energies of the multi-phonon states once the phonon quanta $\hbar\omega$ is fixed.

7.3.2 Reorientation effects

One of the pronounced features of an anharmonic vibrator is that the excited states have non-zero quadrupole moments [154, 117]. In the IBM, the E2 operator is defined as

$T(\mathrm{E2}) = e_B \hat{Q}_2$, where the quadrupole operator was introduced in Eqs. (3.108) and (7.18) for the *sd*- and *sdf*-IBM, respectively, e_B being is the effective charge. In the U(5) limit, the E2 effective charge e_B is related to the E2 transition probability by

$$B(E2; 0_1^+ \rightarrow 2_1^+) = 5e_B^2 N. \tag{7.20}$$

Using the definition of the static quadrupole moment of a state with spin I

$$Q(I) = \sqrt{\frac{16\pi}{5}} < II|T(E2)|II >, \tag{7.21}$$

we obtain for the quadrupole moment of the 2^+ state

$$Q(2^+) = \sqrt{\frac{32\pi}{35}} e_B \chi_2. \tag{7.22}$$

The corresponding formula for the first 3^- state reads

$$Q(3^-) = \sqrt{\frac{20\pi}{21}} e_B \chi_{2f}. \tag{7.23}$$

Fig. 7.4 shows the influence of the sign of the quadrupole moment of the first 2^+ state on the fusion cross section (the upper panel) and the fusion barrier distribution (the lower panel). The solid line corresponds to the negative static quadrupole moment, while the dotted line is obtained by inverting the sign of the χ_2 parameter in Eq. (3.108). As seen from Eq. (7.22), this is equivalent to taking the opposite sign for the quadrupole moment of the excited state. The dashed line is the result when $\chi_2 = 0$. Fig. 7.4 demonstrates that the fusion cross section, and especially fusion barrier distribution, strongly depend on the sign of the χ_2 parameter, hence on that of the static quadrupole moment. This fact will be used in the next section to determine the quadrupole moments of the first 2^+ and 3^- states in ^{144,148}Sm from the experimental fusion barrier distribution for the ^{16}O + ^{144,148}Sm reaction.

7.3.3 Finite N effects

The other important effect of the deviation of the electric transition rates from the harmonic limit is caused by the finiteness of the boson number. Eq. (7.4) and Fig. 7.1 indicate that the anharmonic effects weaken the coupling between the one- and two-phonon states by the factor $\sqrt{1 - 1/N}$ compared with that in the harmonic limit. For small values of the boson number N, this factor is significantly smaller than one and large anharmonic effects on fusion reactions are expected. In order to demonstrate the finite boson number effects, we show in Fig. 7.4 also the results in the harmonic limit by the dot-dashed line. One can see a significant difference between this result and that for the zero quadrupole moment (the dashed line), indicating the importance of the finite boson number effect.

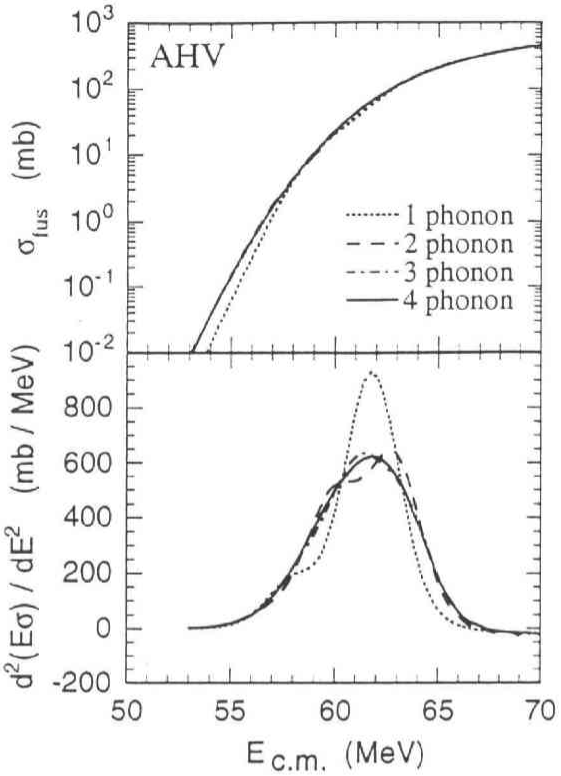

Figure 7.5: Convergence of the fusion cross section (the upper panel) and fusion barrier distribution (the lower panel) as functions of the number of phonon states included in the coupled-channels equations, which are indicated in the inset. The total boson number N is fixed to be four in all cases.

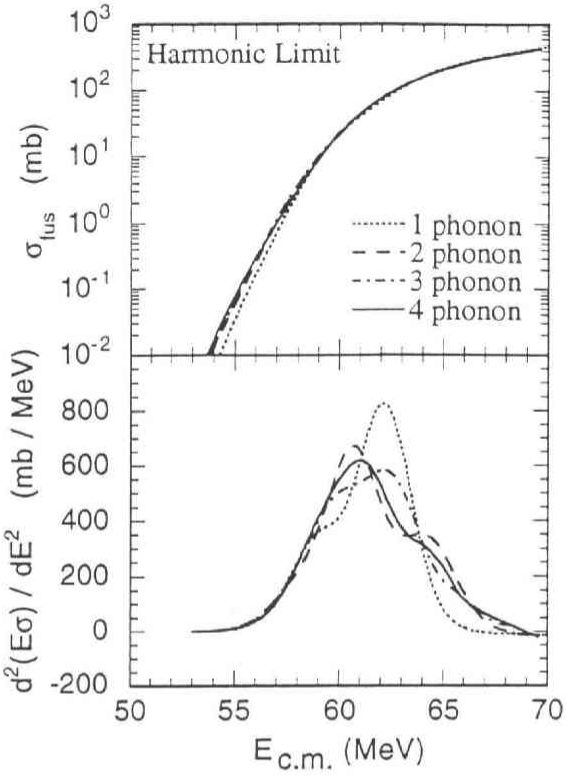

Figure 7.6: The same as Fig. 7.5, but for the harmonic oscillator coupling.

Finite boson number effects can also be studied in another, perhaps more instructive way. Since the couplings to the multi-phonon states are weaker than those in the harmonic limit if the anharmonic effects are present, one expects that fusion excitation function converges more rapidly compared with the case in the absence of the anharmonic effects. Fig. 7.5 shows how the fusion cross sections (the upper panel) and the fusion barrier distributions (the lower panel) converge with the phonon number for fixed total boson number $N = 4$. Although the fusion cross section and the fusion barrier distribution obtained by including only the single-phonon excitations are quite different from those in the double-phonon couplings, the difference between the two- and the three-phonon couplings are small. We observe that the fusion barrier distribution almost converges at the three-phonon level. The corresponding calculations in the harmonic limit are performed for comparison. These results are shown in Fig. 7.6. Contrary to the results

for the anharmonic vibrator, the barrier distribution obtained by taking into account up to the four-phonon excitations is still significantly different from that obtained by including up to the three-phonon excitations. We thus conclude that the finite boson number significantly influences the role of higher phonon states in determining the fusion barrier distribution.

7.4 Comparison with experimental data

7.4.1 $^{16}O + ^{144}Sm$ reaction

We now apply the formalism to realistic systems. We first analyze in particular the $^{16}O + ^{144}Sm$ reaction [82]. We showed in Fig. 5.8 that inclusion of the double-phonon excitations of ^{144}Sm in coupled-channels calculations in the harmonic limit destroys the good agreement between the experimental fusion barrier distribution and the theoretical predictions obtained when only the single-phonon excitations are taken into account [106]. On the other hand, there are experimental [171, 173] as well as theoretical [185] support for the existence of the double-octupole-phonon states in ^{144}Sm. Reconciliation of these apparently contradictory facts may be possible if one includes the anharmonic effects, which are inherent in most multi-phonon spectra.

The model parameters are determined as follows. The standard prescription for the boson number (i.e. counting pairs of nucleons above or below the nearest shell closure) would give $N = 6$ for ^{144}Sm. However, it is well known that due to the $Z = 64$ subshell closure, the effective boson numbers are much smaller. The suggested effective numbers in the literature for the proton bosons vary between $N_\pi = 1$ and 3 [186, 187]. We adopted $N = 2$ in our calculations, since there are experimental signatures for the two-phonon states, but no evidence for three-phonon states in ^{144}Sm. The parameters of the intrinsic Hamiltonian are simply determined from the excitation energies of the first 2^+ and 3^- states in ^{144}Sm as $\epsilon_d = 1.66$ MeV and $\epsilon_f = 1.81$ MeV. The nuclear potential parameters are taken from the exhaustive study of this reaction in Ref. [106] as $V_0 = 105.1$ MeV, $R_0 = 8.54$ fm and $a = 0.75$ fm. Finally, the target radius is taken to be $R_T = 5.56$ fm, and the deformation parameters are estimated to be β_2=0.11 and β_3=0.21 from the electric transition probabilities.

The results of the coupled-channels calculations are compared with the experimental data in Fig. 7.7. The upper and the lower panels in Fig. 7.7 show the excitation function of the fusion cross section and the fusion barrier distributions, respectively. The experimental data are taken from Ref. [51]. The dotted line is the result in the harmonic limit, where couplings to the quadrupole and octupole vibrations in ^{144}Sm are truncated at the single-phonon levels and all the χ parameters in Eqs. (7.18) and (7.19) are set to zero. The dotted line reproduces the experimental data of both the fusion cross section and the fusion barrier distribution reasonably well, though the peak position of the fusion barrier distribution around $E_{cm} = 65$ MeV is slightly shifted. As was shown in Ref. [106], the shape of the fusion barrier distribution becomes inconsistent with the experimental data when the double-phonon channels are included in the harmonic limit (the dashed line). To see whether this discrepancy is due to neglect of anharmonic effects, we have repeated

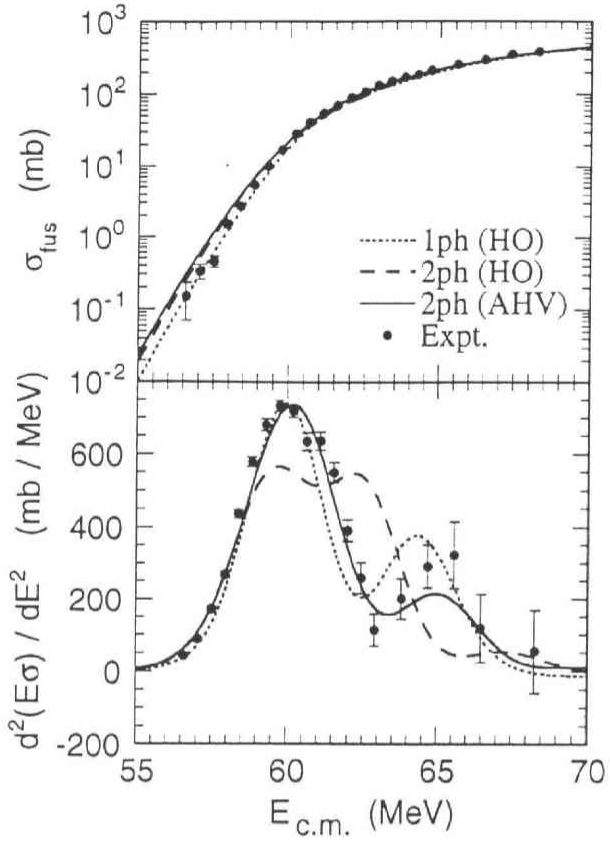

Figure 7.7: Comparison of the experimental fusion cross section (the upper panel) and fusion barrier distribution (the lower panel) with the coupled-channels calculations for ^{16}O + ^{144}Sm reaction. The experimental data are taken from Ref. [51]. The solid line shows the results of the present IBM model including the double-phonon states and anharmonic effects. The dotted and the dashed lines are the results of the single- and the double-phonon couplings in the harmonic limit, respectively.

the calculations including the χ parameters in the fits and using $N = 2$ in the IBM. Following the discussion in the previous section, harmonic spectra for the excitation energies of the phonon states are assumed. The χ^2 fit to the fusion cross sections resulted in the set of parameters, $\chi_2 = -3.30 \pm 2.30$, $\chi_{2f} = -2.48 \pm 0.07$, and $\chi_3 = 2.87 \pm 0.16$, regardless of the starting values. The best fit was obtained by using slightly larger values for the deformation parameters than those in the harmonic limit, i.e. $\beta_2 = 0.13$, $\beta_3 = 0.23$. The slight change in the values of the deformation parameters from those in the harmonic limit results from the renormalization effects due to the extra terms in the operators in Eqs. (7.18) and (7.19). Since there is no information on quadrupole moments in ^{144}Sm, the χ parameters cannot be estimated from data. Nevertheless, in the neighboring ^{148}Sm, where the quadrupole moment of the first 2^+ state has been measured, one needs $\chi_2 = -3.6$, consistent with the above value (see next subsection for more details).

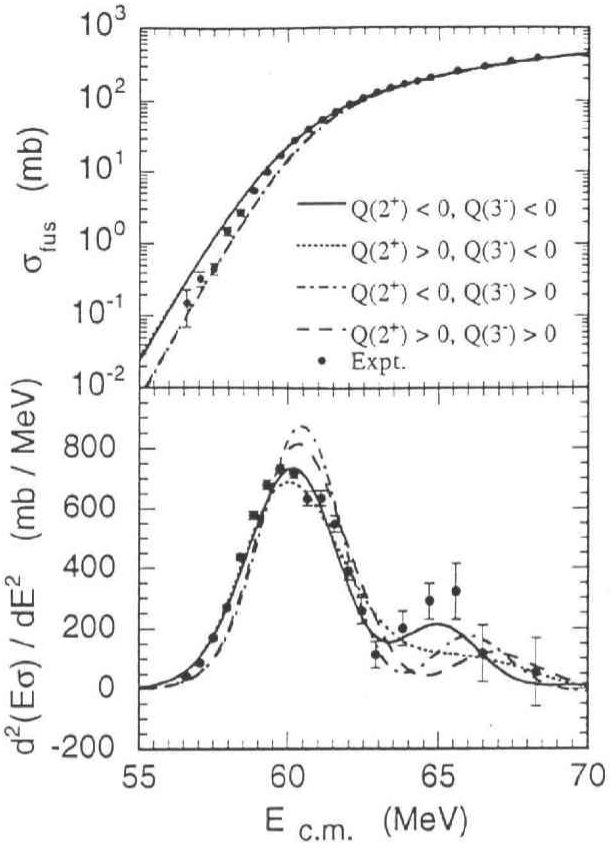

Figure 7.8: Dependence of the fusion cross section and barrier distribution on the sign of the quadrupole moment of the excited states in ^{144}Sm. The meaning of each line is indicated in the inset.

The resulting fusion cross sections and barrier distributions are shown in Fig. 7.7 by the solid line, which agree with the experimental data much better than those obtained in the harmonic limit. Thus, inclusion of the anharmonic effects in vibrational motion appear to be essential for a proper description of barrier distributions in the reaction ^{16}O + ^{144}Sm.

Using the χ parameters extracted from the analysis of fusion data in the E2 operator, and the effective charge e_B, which is determined from the experimental $B(\mathrm{E2}; 0 \rightarrow 2_1^+)$ value as $e_B = 0.16\ eb$, we estimate the static quadrupole moments of various states in ^{144}Sm. For the quadrupole moment of the first 2^+ and 3^- states, we obtain -0.89 ± 0.63 b and -0.70 ± 0.02 b, respectively. The negative sign of the quadrupole moment of the octupole-phonon state is consistent with that suggested from the neutron pick-up reactions on ^{145}Sm [178, 188].

In Fig. 7.4, we have demonstrated that the shape of fusion barrier distributions changes significantly when one inverts the sign of the quadrupole moment in a spherical target. Fig. 7.8 shows the influence of the sign of the quadrupole moment of the excited states on the fusion cross section and the fusion barrier distribution. The solid line is the

same as in Fig. 7.7 and corresponds to the optimal choice for the signs of the quadrupole moments of the first 2^+ and 3^- states. The dotted and dashed lines are obtained by changing the sign of the χ_2 and χ_{2f} parameters in Eqs. (7.18) and (7.19), respectively, while the dot-dashed line is the result where the sign of both χ_2 and χ_{2f} parameters are inverted. Fig. 7.8 demonstrates that subbarrier fusion reactions are indeed sensitive to the sign of the quadrupole moment of excited states. The experimental data are reproduced only when the correct sign of the quadrupole moment are used in the coupled-channels calculations. Notice that the fusion excitation function is completely insensitive to the sign of the quadrupole moment of the first 2^+ state, but strongly depends on that of the first 3^- state. In contrast, the fusion barrier distribution can probe the signs of the quadrupole moments of both the first 2^+ and 3^- states.

7.4.2 ^{16}O + ^{148}Sm reaction

We next analyze the ^{16}O + ^{148}Sm reaction, whose excitation function of the fusion cross section was recently measured with high accuracy [51]. We take both the quadrupole and the octupole vibrational excitations in ^{148}Sm, while the excitations of ^{16}O are not explicitly included in the coupled-channels calculations following the conclusion which we have reached in the previous chapter, i.e. the latter effects lead only to the shift of the fusion barrier distribution in energies without significantly changing its shape, and hence can be incorporated in the choice of the bare potential.

In order to qualitatively understand the effects of the channel couplings on this reaction, calculations are first performed by assuming the harmonic limit. The quadrupole and the octupole deformation parameters are estimated from the experimental electric transition probabilities between the ground and the one-phonon states [189] to be $\beta_2 = 0.182$ and $\beta_3 = 0.236$, respectively, by assuming the target radius of $R_T = 1.06A^{1/3}$ fm. The excitation energies of the phonon states in ^{148}Sm are 0.55 and 1.16 MeV, for the first 2^+ and 3^- states, respectively. The parameters for the bare ion-ion potential are obtained by fitting the experimental fusion cross sections. It has been pointed out that the effects of channel couplings play an important role in determining the bare potential for the ^{16}O + ^{144}Sm reaction [111]. Accordingly, we fit the experimental data by assuming the three phonon couplings in the harmonic limit (see the following discussion). We use the experimental data between 200 mb and 400 mb to determine the bare potential. We choose this range because, at the lower energy region, more details of the channel couplings would be important, and also at the higher energy region some other effects, e.g. the angular momentum truncation or the dissipation mechanism might play some role [32]. The best fit parameters which we obtain are $V_0 = 155.1$ MeV, $R_0 = 0.95(A_P^{1/3} + A_T^{1/3})$ fm, and $a = 1.05$ fm, for the depth, the radius parameter, and the diffuseness parameter, of the Woods-Saxon potential, respectively. Note that the experimental data at high energy region still require a large diffuseness parameter [51] even after including the effects of the channel couplings. The origin of this is not fully understood (see Sec. 3.2.1).

Our results for the fusion barrier distribution for the ^{16}O + ^{148}Sm reaction are shown in Fig. 7.9. The panels differ from each other by the number of the quadrupole phonons coupled. The experimental data are taken from Ref. [51]. The point difference formula

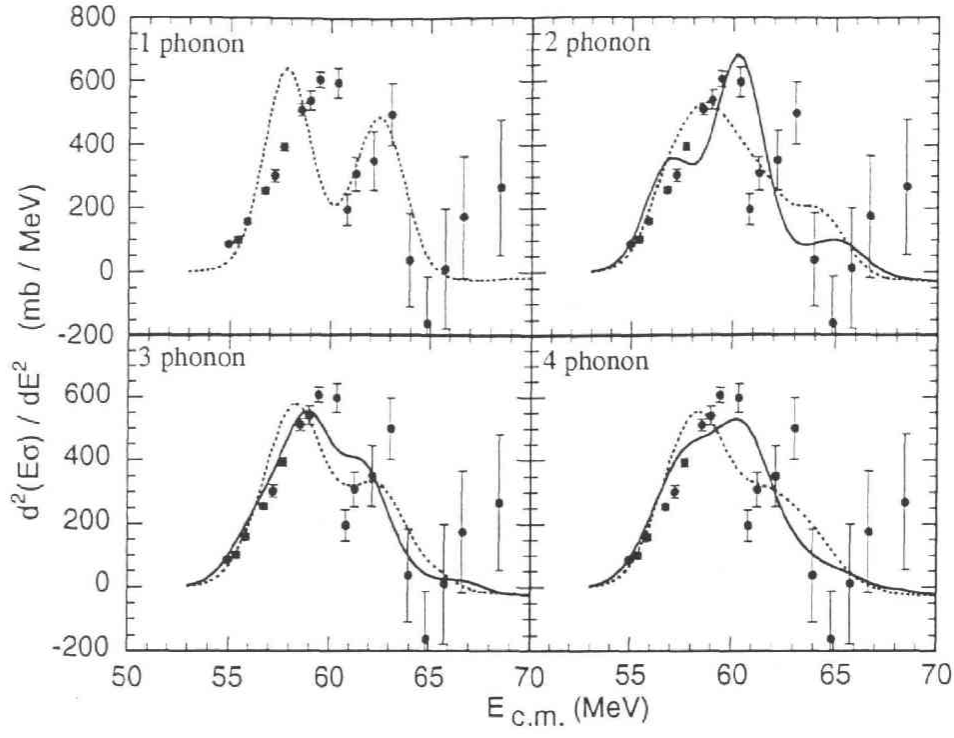

Figure 7.9: Comparison of the experimental fusion barrier distribution with the results of coupled-channels calculations in the harmonic limit for the $^{16}O + ^{148}Sm$ reaction. The dotted lines include the single octupole excitations, while the solid lines take the double octupole phonon couplings into account. The experimental data are taken from Ref. [51].

with $\Delta E = 2$ MeV in the laboratory frame is used to obtain the fusion barrier distributions. Calculations, which assume that the octupole vibration in ^{148}Sm has only a single-phonon state, are indicated by the dotted lines in Fig. 7.9. In the three phonon calculation, for example, we included the 2^+, 3^-, $2^+ \otimes 2^+$, $2^+ \otimes 3^-$, $2^+ \otimes 2^+ \otimes 2^+$, and $2^+ \otimes 2^+ \otimes 3^-$ states in ^{148}Sm in the harmonic limit. The coupling scheme in the other panels is defined in the same way. All the dotted lines which are obtained by assuming the single-octupole-phonon excitations in ^{148}Sm do not account for the experimental fusion barrier distribution. However, double-phonon excitations have been found in the neighbouring nuclei, i.e. ^{144}Sm [171–174], ^{146}Sm [176], and ^{147}Sm [175]. We therefore repeat the same calculations by assuming the double-octupole excitations in ^{148}Sm (the solid lines). One can now observe that the experimental data can be explained reasonably well by the three-phonon calculations. The fit is not as good if the four phonon quadrupole excitations are included in the coupled-channels analysis. These calculations in the harmonic limit thus suggest that there are strong couplings up to the three quadrupole phonon states in ^{148}Sm and the coupling between the three and four phonon states are not as strong as that expected from the harmonic oscillator coupling. They also suggest that there might be double- octupole phonon excitations in ^{148}Sm.

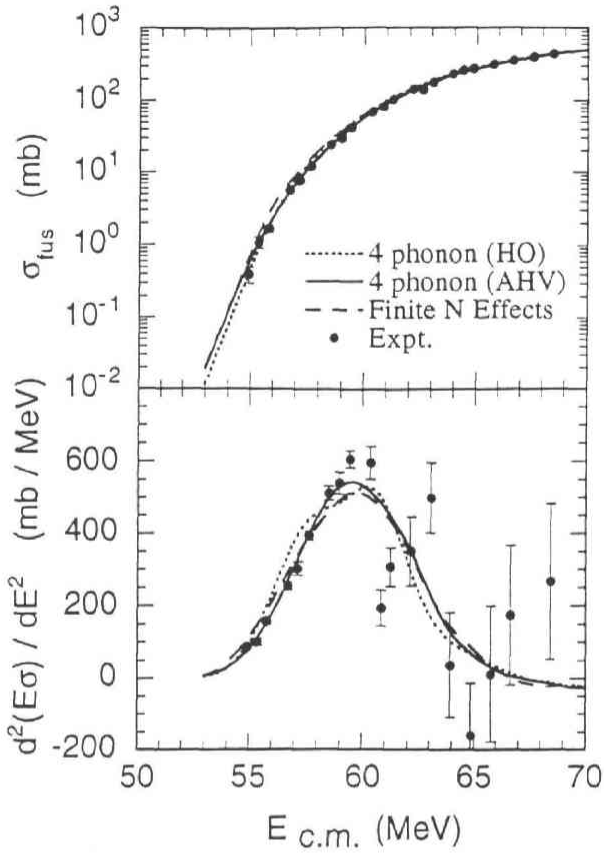

Figure 7.10: Comparison of the experimental fusion cross section (the upper panel) and fusion barrier distribution (the lower panel) with the coupled-channels calculations for the $^{16}O + ^{148}Sm$ reaction. The experimental data are taken from Ref. [51]. The anharmonic effects in the quadrupole and the octupole vibrational excitations in ^{148}Sm are taken into account in the *sdf*- IBM. The solid line is the result when the best fit parameters are used, while the dashed line is obtained by setting the quadrupole moments of all the excited states to be zero. The results including the four phonon couplings in the harmonic limit is denoted by the dotted line.

Calculations which take into account the anharmonicities of the vibrational excitations are performed next. Following the suggestions of the calculations in the harmonic limit, we include the octupole excitations up to the double phonon levels and take the total boson number $N = 4$. The latter is consistent with the observations concerning the effects of the $Z = 64$ subshell closure, which we discussed in the previous subsection. There are three other parameters, i.e. χ_2, χ_{2f}, and χ_3 parameters in the transition operators Eqs. (7.18) and (7.19), which need to be determined. Two of them, χ_2 and χ_{2f}, are directly related to the quadrupole moment of the phonon states, and the other the coupling between the quadrupole and the octupole modes. Though there exist experimental data on the quadrupole moment of the first 2^+ state of ^{148}Sm [189], the experimental uncertainty is

not small. There are no other experimental data which can be used to estimate the χ_{2f} and χ_3 parameters. Therefore, a χ^2 fit to the experimental fusion cross sections is carried to determine all the three parameters. In the fitting procedure, all the experimental data below 200 mb are used, except for the one at E_{lab}= 69.36 MeV, which seems to fall outside the systematics. The best fit values are $\chi_2 = -3.12 \pm 0.77, \chi_{2f} = 4.63 \pm 0.43$, and $\chi_3 = -1.99 \pm 0.26$. The solid line in Fig. 7.10 shows the fusion cross section (the upper panel) and the fusion barrier distribution (the lower panel) thus obtained. One observes that the shape of the fusion barrier distribution is very similar to that for the three phonon couplings in the harmonic limit (see Fig. 7.9) and that they agree quite well with the experimental data.

In the last section, we discussed two main effects of the anharmonicities in the electric transition, i.e. the reorientation effects and the finite N effects, on subbarrier fusion reactions. In order to see each effect separately, we repeat the same calculation by setting both the χ_2 and χ_{2f} parameters to be zero. As was discussed in the previous section, this prescription is equivalent to taking only the finite N effects into account. This result is shown by the dashed line in Fig. 7.10. The figure also shows the result obtained by assuming that there are four quadrupole phonon states in the harmonic oscillator limit in ^{148}Sm, as a comparison (the dotted line). The difference between the dotted and the dashed lines, and also between the dashed and the solid lines, is significant. This suggests that both the reorientation effects and the finite N effects play an important role in the fusion reaction.

From the χ_2 and χ_{2f} parameters which are obtained by the χ^2 fit to the experimental fusion cross sections, we estimate the quadrupole moments of the first 2^+ and 3^- states of ^{148}Sm. The E2 effective charge e_B is estimated to be 0.19 eb from the experimental $B(E2)$ value (see Eq. (7.20)). Using Eqs. (7.22) and (7.23), we estimate the quadrupole moments of the first 2^+ and 3^- states to be $Q(2^+) = -1.00 \pm 0.25$ b and $Q(3^-) = +1.52 \pm 0.14$ b, respectively. Note that the value of the quadrupole moment of the first 2^+ state which we obtained from the fusion analysis is very close to that measured from the Coulomb excitation technique, i.e. $-0.97 \pm 0.27b$ [189]. For the quadrupole moment of the first 3^- state, there is no experimental data to compare our result with. Nevertheless, we can test the consistency of the fit by taking its opposite sign in the coupled-channels calculation. Fig. 7.11 shows the sensitivity of the fusion cross section and the fusion barrier distribution to the sign of the quadrupole moment of the first 3^- state. The solid line corresponds to the optimal choice for the sign of the first 3^- state, while the dotted line is obtained by inverting it. We observe that the use of the incorrect sign of the quadrupole moment destroys the good fit to the experimental data. Our calculations thus strongly suggest that subbarrier fusion can provide an alternative method to determine the sign as well as the magnitude of the quadrupole moments in spherical nuclei.

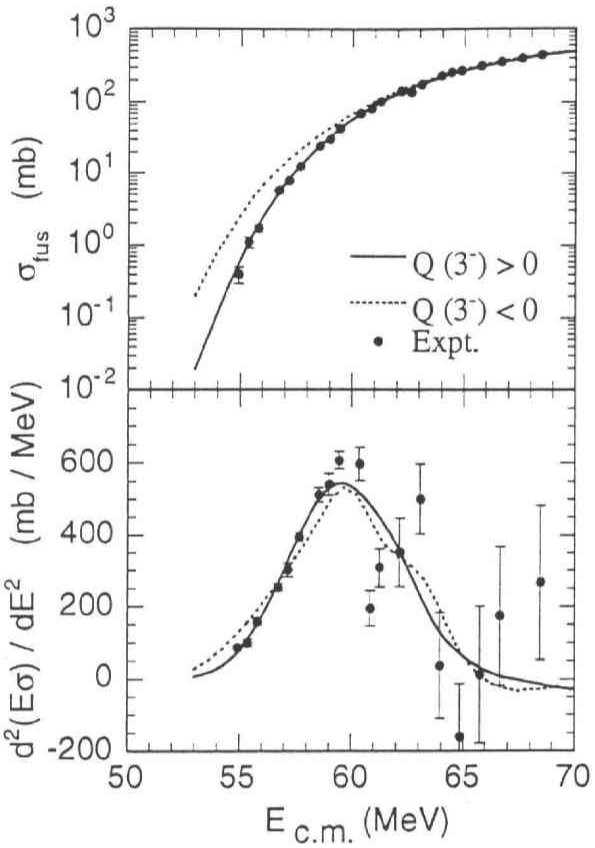

Figure 7.11: Dependence of the fusion cross section (the upper panel) and fusion barrier distribution (the lower panel) for the ^{16}O + ^{148}Sm reaction on the sign of the static quadrupole moment of the first 3^- state in ^{148}Sm. The solid and the dotted lines correspond to the cases where the quadrupole moment is positive and negative, respectively.

Chapter 8

THERMAL FISSION RATE AROUND SUPERFLUID-NORMAL PHASE TRANSITION

As we discussed in Sec. 3.1, one of the decay modes of a compound nucleus formed in heavy-ion fusion reactions is fission. Fission of such hot nucleus has attracted much interest of nuclear physicists in the past several years to study nuclear dissipation together with deep inelastic heavy-ion collisions [190–192]. It is known that statistical codes to calculate the decay of a compond nucleus significantly underestimate the experimentally observed prefission neutron, charged particle, and γ-ray multiplicities at high excitation energies if the original Bohr-Wheeler formula for the fission width [193] is used, though they work pretty well at low energies [194–199]. Two alternative interpretations of this fact have so far been proposed. The one attributes the large prefission neutron emmision to the so called transient effect[199]. In this case, one assumes that some amounts of neutrons are emitted before the asymptotic fission rate given by the Bohr-Wheeler formula is achieved. The other is to consider that fission is hinderd by nuclear dissipation. Based on the latter idea, Thoennessen and Bertsch have analysed fission data on prefission neutron, charged particle and γ ray multipicities for various systems by using statistical codes, and obtained systematics of the threshold energy, where a dissipation starts to play a significant role in fission[194]. This systematics has been confirmed by experimentally studying the excitation energy dependence of the fission probability in ^{200}Pb compound nuclei[197].

On the other hand, the nuclear dissipation does not play any significant role in spontaneous fission because of the strong pairing correlation between nucleons[200, 201]. When one discusses nuclear fission at moderate excitation energies, one has to take into account the temperature dependence of the pairing gap. The pairing gap decreases with temperature and the nucleus eventually undergoes a phase transition from a superfluid to a normal fluids [202–205]. In this Chapter, we investigate the effects of the super-normal phase transition on the fission width at finite temperatures [84]. This study was partly motivated by

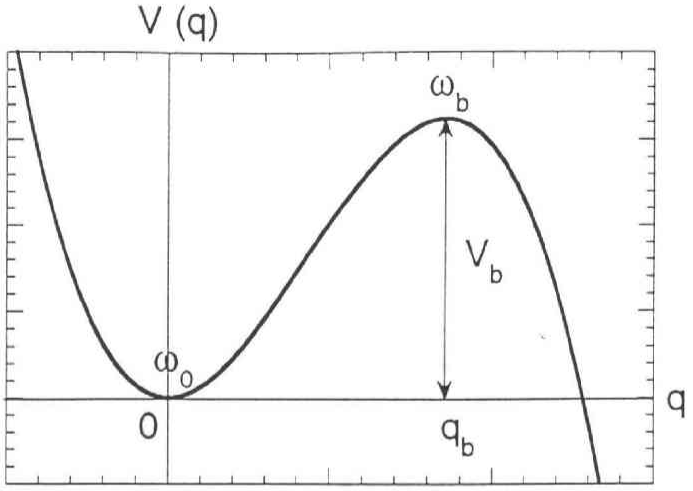

Figure 8.1: A typical potential for decay problems.

that in Ref.[200], where the effect of pairing on the fission at zero temperature has been discussed. It is worth mentioning that the pairing interaction plays an important role in determining the shape of the ground state of a nucleus at zero temperature [206, 207].

8.1 Langer's ImF method

In order to calculate thermal fission rate, we use Langer's ImF method, where the decay width of a metastable state is related to the imaginary part of the free energy [208–212]. In this method one can describe the decay process for a very wide range of temperature, i.e. from zero temperature, where the decay process is governed by the quantum tunneling, to high temperatures, where thermal decay dominates[213]. Also, the method can be applied to a system with many degrees of freedom[209].

8.1.1 One dimensional decay problem

We first discuss the decay of a metastable state in the absence of couplings to dissipative environment. The Lagrangian in this system is given by

$$L = \frac{1}{2}M\dot{q}^2 - V(q), \tag{8.1}$$

where q is the fission coordinate and M is the associated mass. $V(q)$ is a potential which has a local minimum and maximum at $q = 0$ and $q = q_b$, respectively (see Fig. 8.1).

In order to obtain the free energy, we first express the partition function in the path integral form. At the temperature $k_B T = 1/\beta$ it takes the form[214]

$$Z(\beta) = Tr(e^{-\beta H}) = \int \mathcal{D}[q(\tau)] e^{-S_B[q(\tau)]/\hbar}, \tag{8.2}$$

where the path integral is performed over all the periodic paths with the period $\beta\hbar$. The Euclidean action $S_E[q(\tau)]$ is given by

$$S_E[q(\tau)] = \int_0^{\beta\hbar} d\tau \left(\frac{1}{2} M \dot{q}^2 + V(q(\tau)) \right). \tag{8.3}$$

The free energy is then evaluated as

$$F = -\frac{1}{\beta} \log Z(\beta). \tag{8.4}$$

In a high temperature regime, where the decay of a metastable state is governed by the thermal hopping, the decay width Γ is related to the imaginary part of the free energy by [208]

$$\Gamma(T) = -\frac{2}{\hbar} \frac{T_c}{T} ImF, \tag{8.5}$$

T_c being the cross over temperature where the transition between the thermal activated decay and the quantum tunneling occurs.

We evaluate the path integral in Eq. (8.2) in the saddle point approximation. The least action paths satisfy the equation of motion

$$M \ddot{q_{cl}}(\tau) - \frac{dV(q_{cl})}{dq_{cl}(\tau)} = 0 \tag{8.6}$$

with the periodic boundary condition $q_{cl}(0) = q_{cl}(\hbar\beta)$. The solutions of this equation correspond to a real motion in the inverted potential $-V(q)$. In the high temperature regime where we consider in this chapter, the so called bounce trajectry ceases to exist, at least in the real q space, and the main contribution comes from the two trivial periodic solutions. The one of them is $q_{cl}(\tau) = 0$, which sits on the top of the inverted potential in all the times, the other, $q_{cl}(\tau) = q_b$, at the bottom of the well.

A periodic trajectory near the classical path $q_{cl}(\tau) = 0$ can be expressed by

$$q(\tau) = q_{cl}(\tau) + x(\tau) = \sum_{n=-\infty}^{\infty} X_n e^{i\nu_n \tau}, \tag{8.7}$$

where $\nu_n = 2\pi n/\beta\hbar$ are the Matsubara frequencies, and X_n are the expansion coefficients. Using the identity

$$\int_0^{\beta\hbar} d\tau e^{i(\nu_n + \nu_{n'})\tau} = \delta_{n,n'}, \tag{8.8}$$

the contribution of this path to the Euclidean action (8.3) is found to be

$$S_E[q(\tau)] = \frac{1}{M} \beta\hbar \sum_{n=-\infty}^{\infty} \lambda_n^0 X_n X_{-n}, \tag{8.9}$$

where

$$\lambda_n^0 = \nu_n^2 + \omega_0^2, \tag{8.10}$$

$\omega_0 = \sqrt{V''(0)/M}$ being the curvature of the potential at $q = 0$. The partition function (8.2) evaluated in the vicinity of the classical path $q_{cl}(\tau) = 0$ is then expressed by

$$Z_0 = \int_{-\infty}^{\infty} \prod_{n=-\infty}^{\infty} dX_n \exp\left(-\frac{1}{2}M\beta \sum_{n=-\infty}^{\infty} \lambda_n^0 X_n X_{-n}\right) = \prod_{n=-\infty}^{\infty} \sqrt{\frac{2\pi}{M\beta}\frac{1}{\lambda_n^0}}. \tag{8.11}$$

The contribution from the other periodic path near $q_{cl}(\tau) = q_b$ is evaluated as follows. Expanding the path as

$$q(\tau) = q_{cl}(\tau) + y(\tau) = q_b + \sum_{n=-\infty}^{\infty} Y_n e^{i\nu_n \tau}, \tag{8.12}$$

the Euclidean action in the limit of small flactuation $y(\tau)$ is given by

$$S_E[q(\tau)] = \hbar\beta V_b + \frac{1}{2}M\beta\hbar \sum_{n=-\infty}^{\infty} \lambda_n^b Y_n Y_{-n}, \tag{8.13}$$

where V_b is the height of the potential barrier and λ_n^b are given by

$$\lambda_n^b = \nu_n^2 - \omega_b^2, \tag{8.14}$$

$\omega_b = \sqrt{-V''(q_b)/M}$ being the curvature of the potential at $q = q_b$. In evaluating the partition function from this Euclidean action, one encounters a problem. Since the eigen value $\lambda_0^b = -\omega_b^2$ is negative, the gaussian integral over the amplitude Y_0 diverges. In order to keep the integral convergent, Langer distorted the integration contour into the upper half of the complex plane and the evaluated the integral as [208]

$$\int_{-\infty}^{\infty} dY_0 \exp\left(\frac{1}{2}M\beta\omega_b^2 Y_0^2\right) \overset{Y_0 \to iY_0}{\longrightarrow} i\int_0^{\infty} dY_0 \exp\left(-\frac{1}{2}M\beta\omega_b^2 Y_0^2\right). \tag{8.15}$$

Taking this prescription, the partition function is evaluated as

$$Z_b = \frac{i}{2} \prod_{n=-\infty}^{\infty} \sqrt{\frac{2\pi}{M\beta}\frac{1}{|\lambda_n^b|}} e^{-\beta V_b}. \tag{8.16}$$

The partition function now has an imaginary part as a consequence of the distortion of the integration path into the complex plane. Noticing that Z_b/Z_0 contains the exponentially small quantity $\exp(-\beta V_b)$, the imaginary part of the free energy F is evaluated as

$$ImF = -\frac{1}{2\beta}\sqrt{\prod_{n=-\infty}^{\infty} \frac{\lambda_n^0}{|\lambda_n^b|}} e^{-\beta V_b} = -\frac{1}{2\beta}\frac{\omega_0}{\omega_b} \prod_{n=1}^{\infty} \frac{\lambda_n^0}{\lambda_n^b} e^{-\beta V_b}. \tag{8.17}$$

In evaluating Eq. (8.17), we have used

$$ImF = Im\left[-\frac{1}{\beta}\left\{\log Z_0 + \log\left(1 + \frac{Z_b}{Z_0}\right)\right\}\right] \sim Im\left[-\frac{1}{\beta}\frac{Z_b}{Z_0}\right]. \tag{8.18}$$

The imaginary part of the free energy is related to the decay rate through Eq. (8.5). The crossover temperature T_c is identified with the highest temperature at which Eq. (8.17) diverges [209]. This is the temperature where the so called bounce path which describes a tunneling decay disappears as one increases the temperature from zero. At temperatures below T_c, the bounce solution domonates the decay and the decay rate has less temperature dependence[209]. This prescription assigns $k_B T_c$ to be $\hbar\omega_b/2\pi$, where λ_1^b becomes zero. This is consistent with the earlier observation by Affleck on the crossover temperature [208]. Combining Eqs. (8.5) and (8.17), the decay rate at themperature T is then given by

$$\Gamma = \frac{\omega_0}{2\pi} f_q e^{-\beta V_b}, \tag{8.19}$$

where f_q is the quantum correction factor due to the quantum fluctuation of the paths around the classical paths $q_{cl}(\tau) = q_b$ and $q_{cl}(\tau) = 0$, and is given by

$$f_q = \prod_{n=1}^{\infty} \frac{\lambda_n^0}{\lambda_n^b} = \prod_{n=1}^{\infty} \frac{\nu_n^2 + \omega_0^2}{\nu_n^2 - \omega_b^2}. \tag{8.20}$$

At temperature much larger than the crossover temperature, the quantume correction factor f_q is close to one, and thus the decay rate Eq. (8.19) becomes identical to that in the classical formula [193], i.e.

$$\Gamma_{cl} = \frac{\omega_0}{2\pi} e^{-\beta V_b}. \tag{8.21}$$

This equation is often referred to as the Bohr-Wheeler formula [193], and is frequently used in statistical codes to calculate the decay of a hot nucleus [215].

8.1.2 Decay rate in dissipative systems

We now discuss the decay rate in the presence of dissipative environment. We consider a system where a macroscopic degree of freedom q couples to environmental heat bath. We assume the following Lagrangian for this system[20]

$$L = \frac{1}{2} M(q)\dot{q}^2 - V(q) + \sum_i \frac{1}{2} m_i(\dot{x}_i^2 - \omega_i^2 x_i^2) - \sum_i c_i x_i f(q) + \sum_i \frac{c_i^2 f(q)^2}{2 m_i \omega_i^2} \tag{8.22}$$

where $\{x_i\}$ and $\{\omega_i\}$ are the coordinates of the environmental oscillators and the corresponding excitation energies, respectively. $M(q)$ and $f(q)$ are the mass of the macroscopic motion and the coupling form factor, respectively. We assume general functions of q for them[210, 212]. The last term is the so called counter term which cancels the static potential renormalization due to the coupling between the macroscopic and the environmental degrees of freedom [20]. Takigawa and Abe have suggested that, in contrast to heavy-ion fusion reactions at subbarrier energies where the static potential renormalization plays an important role in enhancing the fusion cross section over the predictions of the one dimensional potential model (see Sec. 2.3.3), the static potential renormalization in the fission problem can lead to two opposite effects, i.e. it could either lower or increase the effective fission barrier compared with the bare potential barrier, thus leading to either

hindrance or enhancement of the fission rate, depending on the properties of the coupling form factor $f(q)$ [210]. Both cases lead to a temperature dependent fission barrier height [195]. In this thesis, we introduce the counter term similarly to Ref.[20].

After integrating out the environmental degrees of freedom, the partition function at the temperature $k_BT = 1/\beta$ takes the form[216]

$$Z(\beta) = \int \mathcal{D}[q(\tau)] e^{-S_{eff}[q(\tau)]/\hbar}. \tag{8.23}$$

Here, the effective Euclidean action $S_{eff}[q(\tau)]$ is given by

$$S_{eff}[q(\tau)] = \int_0^{\beta\hbar} d\tau \left(\frac{1}{2}M(q(\tau))\dot{q}^2 + V(q(\tau))\right) + \frac{1}{2}\int_0^{\beta\hbar} d\tau \int_0^{\beta\hbar} d\tau' k(\tau-\tau') f(q(\tau)) f(q(\tau')) \tag{8.24}$$

with the influence kernel $k(\tau)$ [210, 216]

$$k(\tau) = \sum_i \left[\frac{c_i^2}{m_i\omega_i^2} : \delta(\tau) : -\frac{c_i^2}{2m_i\omega_i}\frac{\cosh[\omega_i(|\tau| - \frac{1}{2}\beta\hbar)]}{\sinh(\frac{1}{2}\hbar\omega_i\beta)}\right] \tag{8.25}$$

where

$$: \delta(\tau) := \sum_{n=-\infty}^{\infty} \delta(\tau - n\beta\hbar) \tag{8.26}$$

is a generalized delta function with period $\beta\hbar$.

Following to the same procedure as in the previous subsection, we find that the decay width at temperature T can be expressed as[210]

$$\Gamma = \frac{\omega_0}{2\pi}\frac{\omega_R}{\omega_b}\sqrt{\frac{M(q_0)}{M(q_b)}} f_q e^{-\beta V_b}, \tag{8.27}$$

where ω_R is defined as $2\pi k_B T_c/\hbar$. The quantum correction factor f_q is given by

$$f_q = \prod_{n=1}^{\infty} \frac{\nu_n^2 + \omega_0^2 + \left(\frac{df}{dq}\right)^2_{q=q_0} \nu_n \hat{\gamma}_0(\nu_n)}{\nu_n^2 - \omega_b^2 + \left(\frac{df}{dq}\right)^2_{q=q_b} \nu_n \hat{\gamma}_b(\nu_n)}. \tag{8.28}$$

$\hat{\gamma}$ is the Laplace transform of the retarded friction kernel [210], and is given by

$$\hat{\gamma}(z) = \frac{1}{M(q)}\sum_i \frac{c_i^2}{m_i\omega_i^2}\frac{z}{z^2+\omega_i^2} \tag{8.29}$$

The subscripts 0 and b in Eq. (8.28) denote that the quantities with those indices should be evaluated at $q = 0$ and $q = q_b$, respectively. As in the case without couplings, the crossover temperature T_c is identified with the highest temperature at which the quantum correction factor f_q diverges.

When the coupling form factor $f(q)$ and the mass $M(q)$ are given by $f(q) = q$, and $M(q) = M$, respectively, and if the environmental oscillators are distributed according to [20]

$$J(\omega) \equiv \frac{\pi}{2}\sum_i \frac{c_i^2}{m_i\omega_i}\delta(\omega - \omega_i) = \eta\omega \qquad (Ohmic\ dissipation), \tag{8.30}$$

η being the friction constant, Eq. (8.27) for the decay width leads to [209]

$$\Gamma = f_q \Gamma_K, \tag{8.31}$$

where Γ_K is the well known Kramers's formula [217] at moderate to strong friction for the decay rate given by

$$\Gamma_K = \frac{\omega_0}{2\pi}(\sqrt{1+\alpha^2} - \alpha)e^{-\beta V_b}, \tag{8.32}$$

α being $\eta/2M\omega_b$. The quantum correction factor f_q is given in terms of Γ functions by [209]

$$f_q = \frac{\Gamma(1-\lambda_b^+/\nu)\Gamma(1-\lambda_b^-/\nu)}{\Gamma(1-\lambda_0^+/\nu)\Gamma(1-\lambda_0^-/\nu)}, \tag{8.33}$$

where $\nu = 2\pi k_B T/\hbar$. $\lambda_b^\pm$ and $\lambda_0^\pm$ are given by

$$\lambda_b^\pm = -\frac{\gamma}{2} \pm \sqrt{\frac{\gamma^2}{4} + \omega_b^2}, \tag{8.34}$$

$$\lambda_0^\pm = -\frac{\gamma}{2} \pm \sqrt{\frac{\gamma^2}{4} - \omega_b^0}, \tag{8.35}$$

respectively, γ being η/M. It should be noticed that Langer's ImF method implicitly assumes that the coupling of the macroscopic degree of freedom to the environmental degrees of freedom is strong enough to assure that the system is always in a thermal equillibrium.

8.2 Fission of a hot nucleus

We now apply Eq. (8.27) to the problem of the fission of a hot nucleus. Following Ref.[200] we introduce a low cutoff frequency ω_c to the distribution of the environmental oscillators in order to mimic that there is no nuclear levels below the two quasi particle state in even-even nuclei. Accordingly, we set the cutoff frequency to $2\Delta(T)/\hbar$, $\Delta(T)$ being the pairing gap at the temperature T, and take the spectrum density of the environmental oscillators as[200]

$$J(\omega) = \eta(\omega - \omega_c)\theta(\omega - \omega_c). \tag{8.36}$$

Note that $\omega_c = \infty$ and $\omega_c = 0$ correspond to two extreme cases where there is no dissipation at all and where the spectrum density is given by the usual Ohmic dissipation given by Eq. (8.30), respectively. The former and the latter cases give the Bohr-Wheeler formula and the well known Kramers's formula at moderate to strong friction for the decay rate, respectively, with a quantum correction factor (see Eqs. (8.19) and (8.31)). For the spectrum density given by Eq.(8.36), Eq.(8.29) for the Laplace transform of the damping kernel reads

$$\hat{\gamma}(z) = \frac{\eta}{M(q)} + \frac{2}{\pi}\frac{\eta}{M(q)}\left(\frac{\omega_c}{z}\log\frac{\omega_c}{\sqrt{\omega_c^2+z^2}} - \tan^{-1}\frac{\omega_c}{z}\right). \tag{8.37}$$

Note that the second term in this equation vanishes when the cutoff frequency ω_c is set zero.

We consider here the fission of ^{248}Cf. We take the reduced mass for the symmetric fission for $M(q)$ and the potential given in Ref.[218] for $V(q)$. $\hbar\omega_0, \hbar\omega_b, q_b$ and V_b then take the values of 1.18 MeV, 1.06 MeV, 3.4 fm, and 3.67 MeV, respectively. Though there are extensive experimental as well as theoretical studies on the dissipation coefficient for fission, its value is yet quite scattered[190]. In this thesis, we assume 20×10^{21}/sec. for the reduced dissipation coefficient $\beta \equiv \eta/M$. This is a typical value which one can find in the literature[190, 191]. We checked that the results of the following part of this chapter does not qualitatively change as long as one assumes a value for β, which is consistent with data. We assume a bi-linear coupling form factor i.e., $f(q) = q$. Since we are interested in the effects of pairing in the super to normal transition region, we use a simplified expression for the temperatre dependent pairing gap,

$$\Delta(T) = k_B T_c^{pair} \sqrt{\frac{8\pi^2}{7\zeta(3)}(1-(T/T_c^{pair}))} \qquad (for\ T < T_c^{pair}) \tag{8.38}$$

$$= 0 \qquad (for\ T > T_c^{pair}) \tag{8.39}$$

which is valid near the transition temperature[205]. In Eq. (8.38) ζ is the zeta function and T_c^{pair} the critical temperature for the super-normal phase transition. We assign the pairing gap at zero temperature to be $12/\sqrt{A}$ [117], A being the mass number of a nucleus, and estimate the critical temperature T_c^{pair} using the relation $T_c^{pair} \sim 0.567\Delta_0$[204, 205].

Figure 8.2 shows the crossover temperature T_c as a function of the cutoff parameter $\hbar\omega_c$. This is given by the positive root of the equation

$$\omega_R^2 + \omega_R\frac{\eta}{M} - \omega_b^2 + \omega_R\frac{2}{\pi}\frac{\eta}{M}\left(\frac{\omega_c}{\omega_R}\log\frac{\omega_c}{\sqrt{\omega_c^2+\omega_R^2}} - \tan^{-1}\frac{\omega_c}{\omega_R}\right) = 0. \tag{8.40}$$

Notice that there is only one positive root for Eq.(8.40). It should be remarked that in calculating the decay rate based on Eq.(8.27) the crossover temperature ω_R has to be evaluated at each temperature T with corresponding cuttoff frequency ω_c i.e., one must solve Eq.(8.40) by treating ω_c as though it is independent of temperature. Otherwise, one cannot recover the decay rate formula of Kramers modified by the quantum correction factor at temperatures higher than T_c^{pair}, where the pairing gap vanishes. The solid line in Fig. 8.2 is the solution of Eq.(8.40). The dashed line is the crossover temperature in the absence of environments, i.e. $\hbar\omega_b/2\pi$. If one sets ω_c to be zero, the crossover temperature is given by $(\sqrt{1+\alpha^2}-\alpha)\hbar\omega_b/2\pi$, α being $\eta/2M\omega_b$ [209]. This value is denoted by the dotted line in the figure. The crossover temperature gradually decreases as the cut-off frequency decreases reflecting the increasing dissipation [200].

Figure 8.3 shows the quantum correction factor given by Eq.(8.28) as a function of the temperature. In the limits of $\omega_c \to 0$ and ∞, the infinite product in Eq.(8.28) can be simplified by using Γ function[209, 211] (see Eq. (8.33)). In the case of finite ω_c, one has to evaluate it directly until one gets convergence. In general cases, however, this is a fairly difficult numerical task because the ratio for each n in Eq.(8.28) never

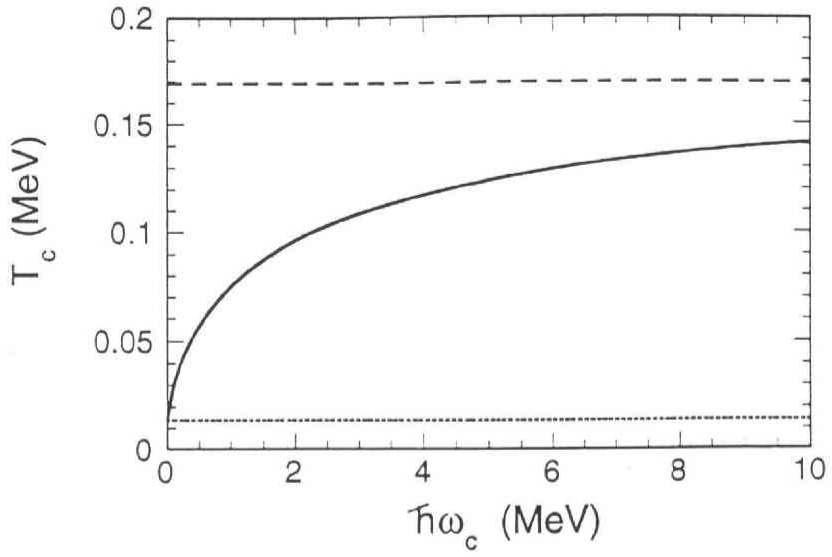

Figure 8.2: The cutoff frequency dependence of the cross over temperature T_c between the quantum and the thermal regimes. The solid line was obtained by numerically solving Eq.(8.40). The dashed and the dotted lines are the crossover temperature in the absence of environments and that in the system with Ohmic dissipation without cutoff, respectively.

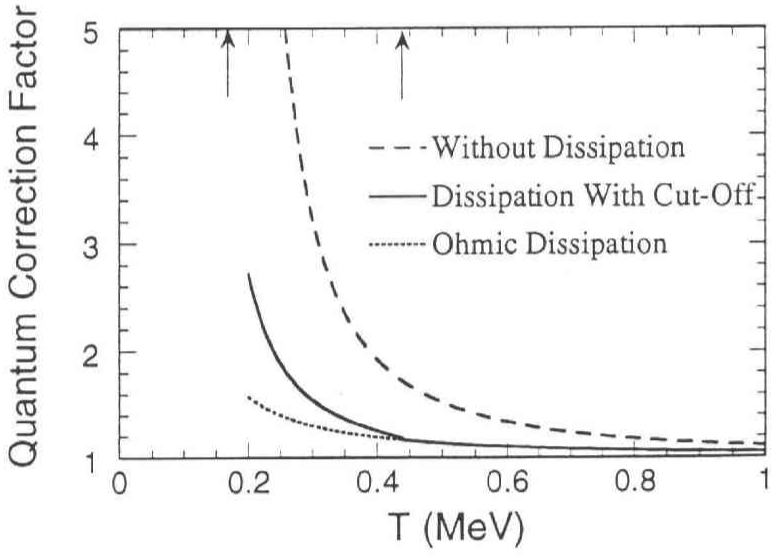

Figure 8.3: Quantum correction factor as a function of temperature. The dashed and the dotted lines are the quantum correction factor in the absence of environment and that in the system with Ohmic dissipation without cutoff, respectively. The solid line is the quantum correction factor when a lower cutoff frequency has been introduced throuth the temperature dependence of the pairing gap. The left and the right arrows are the crossover temperature from a quantal to a thermal decay, and the critical temperature for the super to normal phase transition, respectively.

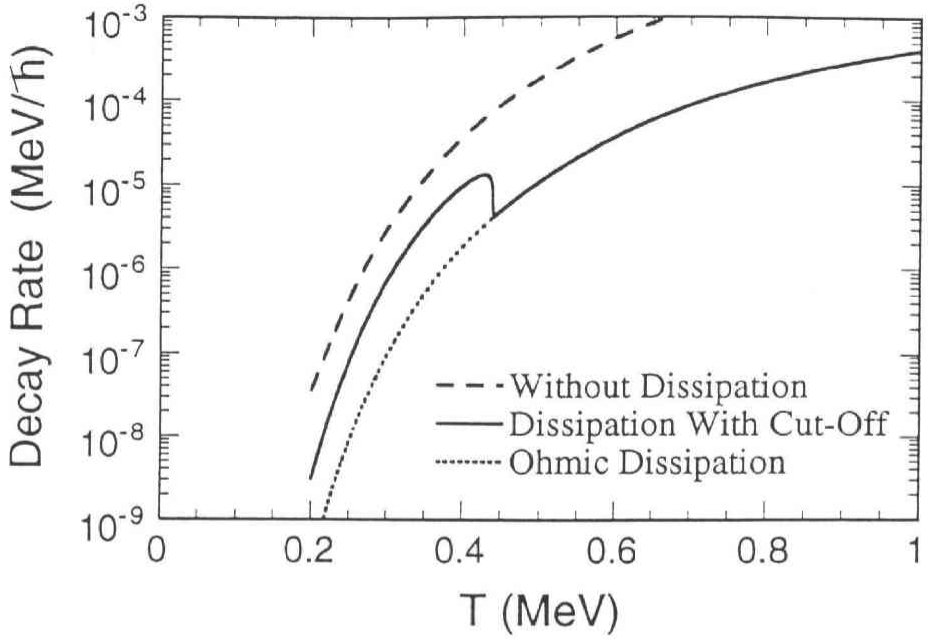

Figure 8.4: Decay rate as a function of temperature. The dashed and the dotted lines are the decay rate in the absence of environment and in the Kramers limit, where there is no cutoff, respectively. The solid line takes the effects of cutoff into account.

becomes sufficiently close to one even for very large n. Consequently, numerical errors accumulate as one performs the production many times. In our applications, where we used a constant mass and a bilinear coupling, the infinite product series converged. The dashed and the dotted lines are the quantum correction factor in the limit of $\omega_c \to 0$ and ∞, respectively. The solid line is the quantum correction factor when the lower cutoff for each temperature has been introduced. The left and the right arrows in the figure show the crossover temperature from a quantal to a thermal decay, i.e. T_c=0.169 MeV, in the absence of environment and the transition temperature from super to normal fluids, i.e. T_c^{pair}=0.432 MeV. The solid line coincides with the dotted line at temperatures higher than T_c^{pair}, as is expected. Note that the quantum correction factor approaches to one at high temperatures.

The decay rate for this system is shown in Fig. 8.4 as a function of the temperature. The meaning of each line is the same as that in Fig. 8.3. We observe a sudden decrease of the decay rate at the critical temperaure T_c^{pair}. This behavior agrees with that found in Ref.[219], where the diffusion of muons in metal was studied by taking a superconducting phase transition of the environmental electrons into account. Notice that the cusp behaiour in the transitional region will be smeared out to some extent in actual cases, for example, by the gradual disappearance of the pairing gap with temperature.

The critical temperature T_c^{pair} which we adopted in this thesis is much lower than the threshold temperature for the dissipative fission discussed in Ref.[194]. The non-

monotonic behaviour of the decay rate shown in Fig. 8.4 might therefore indicate the existence of the second critical temperature other than the threshold temperature discussed in Ref.[194]. In this connection, we wish to add comments on the possible change of our critical temperature due to the yet unsetteled value of the pairing gap in large nuclear deformation. The important thing is that we should use the pairing gap at the saddle point in our calculations, because our formula for fission is intimately related to that in the transition state theory. Studying the influence of the pairing vibration on the spontaneous fission, the authors in Ref.[220] obtained a fairly large value of the pairing gap at the saddle point of the fission, which is about two times larger than the standand value. The large effective pairing gaps were also used in the time dependent Hartree Fock (TDHF) calculations for the induced fission of ^{236}U[221]. If we replace the pairing gap which we used to obtain Fig. 8.4 by such large effective pairing gaps, the sudden decrease of the fission rate due to the disappearance of the pairing gap occurs nearly at the threshold temperature found in Ref.[194]. In order to draw a definite conclusion on the connection between our critical temperature and the threshold temperature in Ref.[194], more detailed studies of the coupling form factor as well as of the temperature and the coordinate dependences of the friction constant [190,198,222–224] will be required.

Chapter 9

SUMMARY AND CONCLUDING REMARKS

Heavy-ion fusion reactions at energies near and below the Coulomb barrier have been discussed from the point of view of quantum tunneling with many degrees of freedom. When the excitation energy of nuclear intrinsic motions which couple to the reltaive motion is zero, quantum tunneling takes place instantaneously, and the effects of the couplings can be expressed in terms of the distribution of potential barriers. The underlying structure of the barrier distribution is most dramatically seen when the first derivative of penetrabilities dP/dE is plotted as a function of energy. In the problem of heavy-ion fusion reactions, this quantity corresponds to the second derivative of $E\sigma$, which is referred to as fusion barrier distribution. Extensive experimental efforts have been successfully carried out in recent years in aiming at extracting fusion barrier distributions.

Even when the excitation energy of the intrinsic motion is not zero, the eigen-channel approximation provides the barrier distribution picture. If the probability of finding each eigen-barriers in the entrance channel, i.e. the weight factor in the eigen-channel approximation has a weak energy dependence, the barrier distribution picture holds to a good approximation, and thus it makes sense to call the second derivative of $E\sigma$ as the fusion barrier distribution. Performing exact coupled-channels calculations, we showed that the energy dependence is actually very weak, regardless of the excitation energy of the intrinsic motion. Therefore, the interpretation of $d^2(E\sigma)/dE^2$ as a distribution of fusion barriers is justified, which makes interpretation of the subbarrier fusion process much clearer. We also discussed a transition from the sudden to the adiabatic tunneling limits, and showed that the fusion barrier distribution can represent these two limits in a natural way.

The adiabatic quantum tunneling can be actually recognised in experimental fusion barrier distributions. We have performed coupled-channels calculations for the fusion reactions ^{16}O + ^{144}Sm and ^{40}Ca + ^{194}Pt, ^{192}Os. The calculations show that the dominant effect of the excitation of the ^{16}O octupole state at 6.1 MeV is to renormalise the static potential without significantly changing the shape of the barrier distribution. On the other hand, the excitation of the 3^- state at 3.7 MeV in ^{40}Ca introduces well defined peaks in the barrier distribution. These results suggest a natural limit to the energy

of states which need to be considered explicitly in coupled-channels calculations. The myriad of weak, high energy excitations which might be possible, contribute only to a potential renormalization without affecting the shape of the barrier distribution. The effects of these excitations can then be included in the bare potential in coupled-channels calculations. If these channels are explicitly included in the coupled-channels calculations without introducing the counter term, they could be double counted depending on the choice of the bare potential.

In order to reach these conclusions, higher order couplings to nuclear surface vibrations were shown to play an essencial role. Such higher order terms in the Coulomb coupling can be safely neglected. Previous work indicated that standard coupled-channels calculations are not very successful in describing fusion of heavy symmetric systems. We have shown that the data can be described well by coupled-channels calculations once couplings to all orders are included. We found that for the ^{64}Ni + ^{92,96}Zr reactions, terms beyond those in the quadratic coupling approximation result in further enhancement of the fusion cross sections at subbarrier energies. The additional enhancement is as large as that due to the inclusion of quadratic coupling. The inclusion of the coupling to all orders is crucial to reproduce the experimental fusion cross sections and the average angular momenta. We performed calculations also for the ^{16}O + ^{112}Cd, ^{144}Sm reactions as examples of very asymmetric systems where the coupling is weaker. It is found that in such cases higher order couplings result in a non-negligible enhancement of the fusion cross sections and a significant modification of barrier distributions as well as the average angular momenta.

High precision fusion cross section measurements to deduce the barrier distribution, and measurements of angular momentum distributions, are designed to study the important couplings in a reaction. The sensitivity to couplings is greatly enhanced by performing experiments involving target projectile combinations with a large value of $Z_P Z_T$. It has been shown in this thesis that higher order coupling significantly affects the barrier distribution and average angular momentum even for weak coupling cases like ^{16}O + ^{112}Cd, ^{144}Sm with values of $Z_P Z_T$ ~400. Whilst coupled-channles calculations in the linear coupling approximation have apparently been very successful in reproducing observed barrier distributions for asymmetric systems, it is clear from our results that care must be taken in their interpretation; the approximations used are unreliable even for relatively weak coupling strengths. Spurious conclusions regarding the nature of couplings could be reached if high quality experimental data, particularly for heavier systems, are compared with calculations performed only with first order coupling. Exact coupled-channels calculation with all orders is the only reliable means of quantitatively understanding the fusion barrier distributions. The stage has now been reached when the standard codes of the coupled-channels calculations should be revised to include coupling to all orders.

We have also discussed the effects of anharmonic phonon excitations on heavy-ion fusion reactions at subbarrier energies, using coupled-channels calculations with all orders. Our calculations showed that they play an important role in subbarrier fusion. We showed that the vibrational limit of the interacting boson model provides a useful framework to address these questions. There are mainly three effects of anharmonicities; the anharmonicity in excitation energy, the reorientation effects, and the finite boson number effects. We showed that the anharmonic effects associated with the excitation energy play

only a minor role and the main effects come from the deviation of transition probabilities from the harmonic limit, i.e. both the reorientation effects and the finite N effects. We found that fusion barrier distributions strongly depend on the sign of the quadrupole moment of excited states in phonon spectra. Using this property, we have analyzed the high precision experimental data of the $^{16}O + ^{144,148}Sm$ fusion reactions and discussed the anharmonic properties of the phonon excitations in $^{144,148}Sm$. It was found that the best fit to the experimental data requires a negative and a positive quadrupole moments for the first 2^+ and 3^- states of ^{148}Sm, respectively, whilist negative quadrupole moments for both the first 2^+ and the first 3^- states of ^{144}Sm are needed to explain the experimental fusion barrier distributions. Since the sign of the quadrupole moment of the first 3^- state of $^{144,148}Sm$ are found to be opposite with each other, it would be interesting to measure that of the nucleus in between, i.e. ^{146}Sm.

We have shown that calculations in the harmonic limit provide only qualitative results and the realistic situations are much more complicated due to the anharmonicities. It has been expected that subbarrier fusion reactions may offer an alternative method to identify multi-phonon states. It is, however, apparent from our results that care must be taken in the analyses. Although harmonic calculations may be able to determine the minimum phonon number, it is vital to take into account the anharmonic effects to identify the maximum phonon number in vibrational nuclei.

One of the decay modes of the compound nucleus formed in a heavy-ion fusion reaction is fission, which is also affected by the couplings to environment. In this connection, we made use of the ImF method of Langer to discuss the fission dynamics of hot nuclei in the presence of a dissipative environment. We modified the Caldeira-Leggett model by introducing a low cutoff frequency in order to mimic the effects of nuclear superfluidity due to pairing interaction. We took into account the temperature dependence of the pairing gap, and thus the phase transition from a super to a normal liquids. The cutoff makes the dissipation weak. This accords with the fact that the nuclear dissipation plays less or no significant role in nuclear fission at low temperatures[225]. The pairing gap gets smaller as the temperature increases. We suggested that the decay rate suddenly decreases at the critical temperature where the pairing gap disappears. This could be related to the threshold phenomena of dissipative fission as well as the sudden decay of superdeformed band at some critical angular momentum[226].

Cross sections of heavy-ion fusion reactions can now be measured with high precision. The effects of couplings are much more transparently seen by representating such high precision experimental data in a form of $d^2(E\sigma)/dE^2$. Together with the fact that one can easily control several quantities which govern quantum tunneling by a careful choice of the projectile and target combination, heavy-ion subbarrier fusion reactions thus provide a flexible tool to understand the dynamics of quantum tunneling in multi-dimensional space. It would be interesting to exploit the ability of such flexibility of heavy-ion fusion reactions to address more general problems, i.e. quantum tunneling in systems with many degrees of freedom.

Appendix A

RELATION BETWEEN GREEN'S FUNCTION AND TRANSMISSION COEFFICIENT

In this appendix, we derive the relation between Green's function and the transmission coefficient, given by Eq. (2.35). Green's function is defined by

$$(E - H)G(E) = 1. \tag{A.1}$$

Taking the coordinate representation, this equation is expressed as

$$\left(E + \frac{\hbar^2}{2\mu}\frac{d^2}{dx^2} - V(x)\right) G(x, x', E) = \delta(x - x'). \tag{A.2}$$

The general solution of this second order differential equation can be written down using the two independent solutions $y_1(x)$ and $y_2(x)$ of the homogeneous equation

$$\left(E + \frac{\hbar^2}{2\mu}\frac{d^2}{dx^2} - V(x)\right) y(x) = 0 \tag{A.3}$$

as

$$\begin{aligned} G(x, x', E) \;=\; & A(x')y_1(x) + B(x')y_2(x) \\ & + \theta(x - x')\frac{2\mu}{\hbar^2}\left[-\frac{y_2(x')}{W}y_1(x) + \frac{y_1(x')}{W}y_2(x)\right] \\ & + \theta(x' - x)\frac{2\mu}{\hbar^2}\left[\frac{y_2(x')}{W}y_1(x) - \frac{y_1(x')}{W}y_2(x)\right], \end{aligned} \tag{A.4}$$

where $A(x)$ and $B(x)$ are arbitary functions of x and W is the Wronskian of y_1 and y_2 defined by $W = y_2'(x)y_1(x) - y_1'(x)y_2(x)$, which is independent of x.

We choose $y_1(x)$ to have an ingoing and reflected wave to the left of the barrier and an outgoing wave to the right

$$y_1(x) \;\to\; e^{ikx} + \mathcal{R}e^{-ikx} \qquad x \to -\infty, \tag{A.5}$$

$$\;\to\; \mathcal{T}e^{ikx} \qquad x \to \infty, \tag{A.6}$$

and $y_2(x)$ to have an outgoing wave to the left of the barrier

$$y_2(x) \rightarrow e^{-ikx} + \mathcal{R}e^{ikx} \qquad x \rightarrow \infty, \tag{A.7}$$

$$\rightarrow \mathcal{T}e^{-ikx} \qquad x \rightarrow -\infty. \tag{A.8}$$

Here k is the wave number, and $\mathcal{T}$ and $\mathcal{R}$ are the transmission and the reflection coefficients, respectively. The Wronskian for this choice is evaluated as $W = -2ik\mathcal{T}$.

We impose here the outgoing wave boundary consition. Green's function which satisfies this condition has the following coordinate dependence:

$$G^{(+)}(x, x', E) \sim e^{ik(x-x')} \qquad x > x', \tag{A.9}$$

$$\sim e^{ik(x'-x)} \qquad x < x'. \tag{A.10}$$

From this condition, it follows that the solution of Eq. (A.1) is given by

$$G^{(+)}(x, x', E) = -\frac{2\mu}{\hbar^2}\frac{1}{W}\left[y_1(x)y_2(x')\theta(x-x') + y_2(x)y_1(x')\theta(x'-x)\right]. \tag{A.11}$$

Combining Eqs. (A.6), (A.8), and (A.11), we obtain Eq. (2.35).

Appendix B

NUMERICAL METHOD FOR COUPLED-CHANNELS CALCULATIONS

In this appendix, we present one of the numerical methods [227] to solve coupled-channels equations (2.44). This method directly integrates the second order differential equations, and is different from the iterative method often used in computer codes for coupled-channels calculations with full angular momentum couplings, like ECIS [228] or FRESCO [229].

Our task is to numerically solve a set of coupled equations

$$\frac{d^2}{dr^2}\vec{u}(r) = \mathcal{A}(r)\vec{u}(r) \tag{B.1}$$

from r_{min} to r_{max} with the boundary conditions that there are only incoming waves at r_{min}, and there are only outgoing waves at r_{max} for all channels except the entrance channel, which has an incoming wave with amplitude 1 as well. If the bare potential rapidly decreases to zero as $r \to r_{min}$ and r_{max}, these boundary conditions are expressed as

$$u_n(r) \to e^{-ik_n r}\delta_{n,0} + \mathcal{R}_n e^{ik_n r} \qquad r \to r_{max}, \tag{B.2}$$

$$\to \mathcal{T}_n e^{-ik_n r} \qquad r \to r_{min}, \tag{B.3}$$

where $k_n = \sqrt{2\mu(E-\epsilon_n)/\hbar^2}$ is the wave number of the n-th channel. The n-th component of the rhs of Eq. (B.1) is defined by $\sum_m \mathcal{A}_{nm}(r)u_m(r)$ where the (nm)-th component of the matrix $\mathcal{A}(r)$ is defined by

$$\mathcal{A}_{nm}(r) = \frac{2\mu}{\hbar^2}\left(V_0(r) - E + V_{nm}(r)\right), \tag{B.4}$$

V_{nm} being the (nm)-th component of the coupling matrix defined by Eq. (2.45). If the potential $V_0(r)$ does not decreases to zero at r_{min}, as in the incoming wave boundary condition for heavy-ion fusion reactions (see Eq. (3.58)), k_n should be replaced by local

wave numbers. Also, if the Coulomb field exists in the bare potential $V_0(r)$, the plane waves in Eq. (B.2) should be replaced by the corresponding Coulomb wave functions.

In order to ensure that there are only incoming waves at $r \to r_{min}$, we solve the coupled-channels equations outerwards from r_{min}, first by setting

$$u_n(r_{min}) = e^{-ik_n r_{min}}, \quad u_m(r_{min}) = 0 \quad (m \neq n). \tag{B.5}$$

Since the derivative of the wave functions at r_{min} can be explicitly written down from Eq. (B.5), the wave functions at $r = r_{min} + h$, h being the radial mesh to integrate the equations, can be determined, for example, in the Runge-Kutta method. The Runge-Kutta method may not be, however, so efficient to solve the second order differential equations. We therefore solve the coupled-channels equations, after determining the wave functions at $r = r_{min} + h$, from $r = r_{min} + h$ to $r = r_{max}$ in either the Numerov [230] or the modified Numerov methods [231]. The Numerov method relates the wave functions at $r_{i+1} \equiv r_{min} + (i+1)h$, $\vec{u}^{i+1}$, to those at r_i and r_{i-1} as

$$\vec{u}^{i+1} = \left(1 - \frac{h^2}{12}\mathcal{A}^{i+1}\right)^{-1} \left[2\left(1 + \frac{5h^2}{12}\mathcal{A}^i\right)\left(1 - \frac{h^2}{12}\mathcal{A}^i\right)\vec{u}^i - \left(1 - \frac{h^2}{12}\mathcal{A}^{i-1}\right)\vec{u}^{i-1}\right], \tag{B.6}$$

while the relation in the modified Numerov method is given by

$$\vec{u}^{i+1} = \left(1 - \frac{h^2}{12}\mathcal{A}^{i+1}\right)^{-1} \left[\left\{\left(\frac{h^2}{\sqrt{12}}\mathcal{A}^i + \sqrt{3}\right)^2 - 1\right\}\left(1 - \frac{h^2}{12}\mathcal{A}^i\right)\vec{u}^i - \left(1 - \frac{h^2}{12}\mathcal{A}^{i-1}\right)\vec{u}^{i-1}\right]. \tag{B.7}$$

Let $\chi_{nm}(r)$ be the wave function of the m-th channel thus obtained, i.e. it is $u_m(r)$ which satisfies the boundary conditions Eq. (B.5) at $r = r_{min}$. At $r = r_{max}$, χ_{nm} can be expressed by a superposition of the incoming and outgoing waves as

$$\chi_{nm}(r) = C_{nm}e^{-ik_m r} + D_{nm}e^{ikr_m r} \qquad r \to r_{max}. \tag{B.8}$$

The coefficients C_{nm} and D_{nm} are determined either by matching the logarithmic derivatives at r_{max} or by matching the ratio of the wave functions at $r_{max} - h$ to those at $r_{max} + h$. Since both the Numerov and the modified Numerov methods do not automatically generate the derivative of the wave functions, the latter procedure is more suitable here. The coefficients are then obtained as

$$C_{nm} = \frac{e^{ik_m(r_{max}+h)}\chi_{nm}(r_{max} - h) - e^{ik_m(r_{max}-h)}\chi_{nm}(r_{max} + h)}{e^{ik_m h} - e^{-ik_m h}}, \tag{B.9}$$

and

$$D_{nm} = \frac{e^{-ik_m(r_{max}+h)}\chi_{nm}(r_{max} - h) - e^{-ik_m(r_{max}-h)}\chi_{nm}(r_{max} + h)}{e^{-ik_m h} - e^{ik_m h}}, \tag{B.10}$$

respectively. This procedure is repeated for all n and m to determin the matrices C and D.

The solution of the coupled-channels equations (B.1) with the proper boundary conditions (B.2) and (B.3) is given by a linear combination of χ_{nm} as

$$u_m(r) = \sum_n \mathcal{T}_n \chi_{nm}(r). \tag{B.11}$$

This equation satisfies the boundary condition (B.3) at $r = r_{min}$. At $r = r_{max}$, it leads to

$$u_m(r_{max}) = \sum_n \mathcal{T}_n \chi_{nm}(r_{max}) = \sum_n \mathcal{T}_n \left(C_{nm} e^{-ik_m r_{max}} + D_{nm} e^{ik_m r_{max}} \right). \tag{B.12}$$

By comparing between Eqs. (B.2) and (B.12), one finds

$$\sum_n \mathcal{T}_n C_{nm} = \delta_{n,0}. \tag{B.13}$$

The transmission coefficients are then finally obtained by

$$\mathcal{T}_n = \left(C^{-1} \right)_{n0}. \tag{B.14}$$

This method is used in the computer code for coupled-chnnels calculations for heavy-ion fusion reactions which takes into account couplings to all orders[232].

Appendix C

RELATION BETWEEN SURFACE DIFFUSENESS AND BARRIER PARAMETERS

In this Appendix, we discuss the relation between the surface diffuseness parameter of nuclear potential and the parameters which characterise the Coulomb barrer, i.e. the curvature, the barrier height, and the barrier position. For a given nuclear potential $V_N(r)$, the barrier position r_B is obtained according to

$$\left.\frac{d}{dr}V_0(r)\right|_{r=r_B} = \left[\frac{dV_N(r)}{dr} - \frac{Z_P Z_T e^2}{r^2}\right]_{r=r_B} = 0. \tag{C.1}$$

The barrier height V_B and the curvature Ω are then evaluated as

$$V_B = V_N(r_B) + \frac{Z_P Z_T e^2}{r_B}, \tag{C.2}$$

$$\Omega = \sqrt{-\frac{V_N''(r_B) + 2Z_P Z_T e^2/r_B^3}{\mu}}, \tag{C.3}$$

where $V_N''(r)$ is the second derivative of the nuclear potential.

C.1 Exponential potential

We fist consider an exponential potential given by

$$V_N(r) = V_0 e^{-r/a}. \tag{C.4}$$

From Eq. (C.1), the strength of the nuclear potential V_0 is related to the charge product $Z_P Z_T$ as

$$-\frac{V_0}{a}e^{-r_B/a} - \frac{Z_P Z_T e^2}{r_B^2} = 0. \tag{C.5}$$

This equation leads to the following two relations which relates the surface diffuseness parameter a to the barrier height and the curvature.

$$V_B = \frac{Z_P Z_T e^2}{r_B}\left(1 - \frac{a}{r_B}\right), \tag{C.6}$$

$$\Omega^2 = \frac{Z_P Z_T e^2}{\mu r_B^2}\left(\frac{1}{a} - \frac{2}{r_B}\right). \tag{C.7}$$

C.2 Woods-Saxon potential

We next consider a Woods-Saxon potential given by

$$V_N(r) = -\frac{V_0}{1 + e^{(r-R_0)/a}}. \tag{C.8}$$

Combining Eqs. (C.1) - (C.3), we find that the surface diffuseness parameter a is expressed in terms of r_B, V_B and Ω as

$$a = r_B \Big/ \left(-\frac{\mu\Omega^2 r_B^3}{Z_P Z_T e^2} - 2 + \frac{2 Z_P Z_T e^2}{Z_P Z_T e^2 - r_B V_B}\right). \tag{C.9}$$

Once the surface diffuseness parameter is evaluated, the other two parameters in the nuclear potential are obtained as

$$1 + e^{-x} = \frac{1}{a}\frac{r_B^2}{Z_P Z_T e^2}\left(\frac{Z_P Z_T e^2}{r_B} - V_B\right), \tag{C.10}$$

$$V_0 = a e^{-x}(1 + e^x)^2 \frac{Z_P Z_T e^2}{r_B^2}, \tag{C.11}$$

where x is defined by $(r_B - R_0)/a$.

References

[1] F. Hund, Z. Phys. **43**, 805(1927).

[2] G. Gamow, Z.Phys. **51**, 204(1928).

[3] R.W. Gurney and E.U. Condon, Nature **122**, 439(1928); Phys. Rev. **33**, 127(1929).

[4] J.R. Oppenheimer, Phys. Rev. **31**, 80(1928).

[5] R.H. Fowler and L. Nordheim, Proc. Roy. Soc., **A119**, 173(1928).

[6] A. Barone and G. Paterno, *Physics and applications of the Josephson effect* (John Wiley & Sons, New York, 1982).

[7] P.L. Kapur and R. Peierls, Proc. Roy. Soc., **A163**, 606(1937).

[8] T. Banks, C.M. Bender and T.T. Wu, Phys. Rev. D**8**, 3346(1973); D**8**, 3366(1973).

[9] J.L. Gervais and B. Sakita, Phys. Rev. D**16**, 3507(1977).

[10] D.M. Brink, M.C. Nemes and D. Vautherin, Ann. Phys. (N.Y.) **147**, 171(1983).

[11] A. Schmid, Ann. Phys. (N.Y.) **170**, 333(1986).

[12] S. Takada and H. Nakamura, J. Chem. Phys. **100**, 98(1994).

[13] D.B. Schwartz, B. Sen, C.N. Archie, and J.E. Lukens, Phys. Rev. Lett. **55**, 1547(1985).

[14] T. Satoh, M. Morishita, S. Katoh, K. Hatakeyama, and M. Takashima, Physica **B197**, 397(1994).

[15] E. Karlsson, R. Wappling, S.W. Lidstrom, O. Hartmann, R. Kadono, R.F. Kiefl, R. Hempelmann, and D. Richter, Phys. Rev. B**52**, 6417(1995).

[16] M. Ueda and T. Ando, Phys. Rev. B**50**, 7820(1994).

[17] P.C.E. Stamp, Phys. Rev. Lett. **66**, 2802(1991).

[18] A. Vilenkin, Phys. Rev. D**37**, 888(1988).

[19] Chem. Phys., special issue on *Tunneling in Chemical Reactions*, edited by V.A. Benderskii, V.I. Goldanskii and J. Jortner, **170**, 265(1993).

[20] A.O. Caldeira and A.J. Leggett, Phys. Rev. Lett. **46**, 211(1981); Ann. of Phys. (N.Y.), **149**, 374(1983).

[21] *Proceedings of the Fourth International Symposium on Foundations of Quantum Mechanics,* edited by M. Tsukada *et al.,* Japanese Journal of Applied Physics Series Vol. 9 (Publication Office of Japanese Journal of Applied Physics, Tokyo, 1993).

[22] N. Rowley, contribution in Ref. [21], p. 218.

[23] H. Holm, W. Scheid, and W. Greiner, Phys. Lett. **29B**, 473 (1969).

[24] P.W. Riesenfeldt and T.D. Thomas, Phys. Rev. C**2**, 711(1970).

[25] C.Y. Wong, Phys. Rev. Lett., **31**, 766(1973).

[26] J.O. Rasmussen and K. Sugawara-Tanabe, Nucl. Phys. **A171**, 497 (1971).

[27] L.C. Vaz and J.M. Alexander, Phys. Rev. C**10**, 464(1974).

[28] R.G. Stokstad, Y. Eisen, S. Kaplanis, D. Plete, U. Smilansky, and I. Tserruya, Phys. Rev. Lett., **41**, 465 (1978); Phys. Rev. C**21**, 2427 (1980).

[29] M. Beckerman, M. Salomaa, A. Sperduto, H. Enge, J. Ball, A. DiRenzo, S. Gazes, Yan Chen, J.D. Molitoris, and Mao Nai-feng, Phys. Rev. Lett. **45**, 1472(1980).

[30] W. Reisdorf, F.P. Hessberger, K.D. Hildenbrand, S. Hofmann, G. Münzenberg, K. -H. Schimidt, J.H.R. Schneider, W.F.W. Schneider, K. Sümmerer, G. Wirth, J.V. Kratz, and K. Schlitt, Phys. Rev. Lett. **49**, 1811 (1982).

[31] U. Jahnke, H.H. Rossner, D. Hilscher, and Houlb, Phys. Rev. Lett. **48**, 17(1982).

[32] L.C. Vaz, J.M. Alexander, and G.R. Satchler, Phys. Rep. **69**, 373 (1981).

[33] A.B. Balantekin, S.E. Koonin, and J.W. Negele, Phys. Rev. C**28**, 1565 (1983).

[34] M. Beckerman, Rep. Prog. Phys.**51**, 1047(1988); Phys. Rep. **129**, 145(1985).

[35] S.G. Steadman and M.J. Rhoades-Brown, Ann. Rev. Nucl. Part. Sci. **36**, 649(1986).

[36] W. Reisdorf, J. of Phys. **G20**, 1297 (1994).

[37] A.B. Balantekin and N. Takigawa, Rev. Mod. Phys., in press.

[38] R. Vandenbosch, T. Murakami, C.C. Sahm, D.D. Leach, A. Ray, and M.J. Murphy, Phys. Rev. Lett. **56**, 1234(1986).

[39] R. Vandenbosch, B.B. Back, S. Gil, A. Lazzarini, and A. Ray, Phys. Rev. C**28**, 1161 (1983).

[40] R. Vandenbosch, Annu. Rev. Nucl. Sci. **42**, 447(1992), and references therein.

[41] S. Gil, D. Abriola, D.E. DiGregorio, M. di Tada, M. Elgue, A. Etchegoyen, M.C. Etchegoyen, J. Fernández Niello, A.M.J. Ferrero, A.O. Macchiavelli, A.J. Pacheco, J.E. Testoni, P. Silveira Gomes, V.R. Vanin, A. Charlop, A. García, S. Kailas, S.J. Luke, E. Renshaw, and R. Vandenbosch, Phys. Rev. Lett. **65**, 3100 (1990).

[42] M. Dasgupta, A. Navin, Y.K. Agarwal, C.V.K. Baba, H.C. Jain, M.L. Jhingan, and A. Roy, Nucl. Phys. **A539**, 351(1992).

[43] A.M. Stefanini, L. Corradi, D. Ackermann, A. Facco, F. Gramegna, H. Moreno, L. Mueller, D.R. Napoli, G.F. Prete, P. Spolaore, S. Beghini, D. Fabris, G. Montagnoli, G. Nebbia, J.A. Ruiz, G.F. Segato, C. Signorini, and G. Viesti, Nucl. Phys. **A548**, 453(1992).

[44] N. Rowley, J.R. Leigh, J.X. Wei, and R. Lindsay, Phys. Lett. **B314**, 179(1993).

[45] K.E. Rehm, H. Esbensen, J. Gehring, B. Glagola, D. Henderson, W. Kutschera, M. Paul, F. Soramel, and A.H. Wuosmaa, Phys. Lett. **B317**, 31(1993).

[46] A. Charlop, J. Bierman, Z. Drebi, A. García, D. Prindle, A.A. Sonzogni, R. Vandenbosch, D. Ye, S. Gil, F. Hasenbalg, J.E. Testoni, D. Abriola, M. di Tada, A. Etchegoyen, M.C. Berisso, J.O. Fernández-Niello, and A.J. Pacheco, Phys. Rev. C**49**, R1235(1994).

[47] A.B. Balantekin, J.R. Bennett, and S. Kuyucak, Phys. Lett. **B335**, 295(1994).

[48] D. Ackermann, L. Corradi, D.R. Napoli, C.M. Petrache, P. Spolaore, A.M. Stefanini, F. Scarlassara, S. Beghini, G. Montagnoli, G.F. Segato, and C. Signorini, Nucl. Phys. **A575**, 374(1994).

[49] A. Charlop, J. Bierman, Z. Drebi, A. García, S. Gil, D. Prindle, A. Sonzogni, R. Vandenbosch, and D. Ye, Phys. Rev. C**51**, 628(1995).

[50] D. Ackermann, P. Bednarczyk, L. Corradi, D.R. Napoli, C.M. Petrache, P. Spolaore, A.M. Stefanini, K.M. Varier, H. Zhang, F. Scarlassara, S. Beghini, G. Montagnoli, L. Müller, G.F. Segato, F. Soramel, and C. Signorini, Nucl. Phys. **A609**, 91 (1996).

[51] J.R. Leigh, M. Dasgupta, D.J. Hinde, J.C. Mein, C.R. Morton, R.C. Lemmon, J.P. Lestone, J.O. Newton, H. Timmers, J.X. Wei, and N. Rowley, Phys. Rev. C**52**, 3151(1995).

[52] H. Esbensen, Nucl. Phys. **A352**, 147 (1981).

[53] M.A. Nagarajan, A.B. Balantekin, and N. Takigawa, Phys. Rev. C**34**, 894(1986).

[54] K. Hagino, N. Takigawa, J.R. Bennett, and D.M. Brink, Phys. Rev. C**51**, 3190 (1995).

[55] R.G. Stokstad and E.E. Gross, Phys. Rev. C**23**, 281 (1981).

[56] N. Rowley, G.R. Satchler, and P.H. Stelson, Phys. Lett. **B254**, 25 (1991).

[57] J.G. Keller, K.-H. Schmidt, F.P. Hesseberger, G. Münzenberg, and R. Reisdorf, Nucl. Phys. **A452**, 173 (1986).

[58] K.-H. Schmidt and W. Morawek, Rep. Prog. Phys. **54**, 949(1991).

[59] J.X. Wei, J.R. Leigh, D.J. Hinde, J.O. Newton, R.C. Lemmon, S. Elfstrom, J.X. Chen, and N. Rowley, Phys. Rev. Lett. **67**, 3368 (1991).

[60] J.X. Wei, J.R. Leigh, D.C. Weisser, J.O. Newton, S. Elfström, J.P. Lestone, J.X. Chen, D.G. Popescu, and D.J. Hinde, Nucl. Instrum. Methods Phys. Res. A **306**, 557 (1991).

[61] J.R. Leigh, N. Rowley, R.C. Lemmon, D.J. Hinde, J.O. Newton, J.X. Wei, J.C. Mein, C.R. Morton, S. Kuyucak, and A.T. Kruppa, Phys. Rev. C**47**, R437(1993).

[62] R.C. Lemmon, J.R. Leigh, J.X. Wei, C.R. Morton, D.J. Hinde, J.O. Newton, J.C. Mein, M. Dasgupta, and N. Rowley, Phys. Lett. **B316**, 32(1993).

[63] K. Hagino, N. Takigawa, and A.B. Balantekin, Phys. Rev. C **56**, 2104 (1997).

[64] C.R. Morton, M. Dasgupta, D.J. Hinde, J.R. Leigh, R.C. Lemmon, J.P. Lestone, J.C. Mein, J.O. Newton, H. Timmers, N. Rowley, and A.T. Kruppa, Phys. Rev. Lett. **72**, 4074(1994).

[65] A.M. Stefanini, D. Ackermann, L. Corradi, D.R. Napoli, C. Petrache, P. Spolaore, P. Bednarczyk, H.Q. Zhang, S. Beghini, G. Montagnoli, L. Mueller, F. Scarlassara, G.F. Segato, F. Sorame, and N. Rowley, Phys. Rev. Lett. **74**, 864(1995).

[66] A.M. Stefanini, D. Ackermann, L. Corradi, J.H. He, G. Montagnoli, S. Beghini, F. Scalassara, and G.F. Segato, Phys. Rev. C**52**, R1727(1995).

[67] H. Timmers, L. Corradi, A.M. Stefanini, D. Ackermann, J.H. He, S. Beghini, G. Montagnoli, F. Scarlassara, G.F. Segato, and N. Rowley, Phys. Lett. **B399**, 35 (1997).

[68] J.D. Bierman, P. Chan, J.F. Liang, M.P. Kelly, A.A. Sonzogni, and R. Vandenbosch, Phys. Rev. Lett. **76**, 1587(1996); Phys. Rev. C**54**, 3068 (1996).

[69] H. Timmers, M. Dasgupta, D.J. Hinde, J.R. Leigh, R.C. Lemmon, J.C. Mein, C.R. Morton, J.O. Newton, and N. Rowley, Nucl. Phys. **A584**, 190(1994).

[70] N. Rowley, H. Timmers, J.R. Leigh, M. Dasgupta, D.J. Hinde, J.C. Mein, C.R. Morton, and J.O. Newton, Phys. Lett. **B373**, 23(1996).

[71] C.R. Morton, D.J. Hinde, J.R. Leigh, J.P. Lestone, M. Dasgupta, J.C. Mein, J.O. Newton, and H. Timmers, Phys. Rev. C**52**, 243(1995).

[72] D.J. Hinde, C.R. Morton, M. Dasgupta, J.R. Leigh, J.C. Mein, and H. Timmers, Nucl. Phys. **A592**, 271 (1995).

[73] D.J. Hinde, M. Dasgupta, J.R. Leigh, J.C. Mein, C.R. Morton, J.O. Newton, and H. Timmers, Phys. Rev. Lett. **74**, 1295 (1995); Phys. Rev. C**53**, 1290(1996).

[74] J.C. Mein, D.J. Hinde, M. Dasgupta, J.R. Leigh, J.O. Newton, and H. Timmers, Phys. Rev. C**55**, R995(1997).

[75] A.B. Balantekin and N. Takigawa, Ann. Phys. (N.Y.) **160**, 441(1985).

[76] N. Takigawa, K. Hagino, M. Abe, and A.B. Balantekin, Phys. Rev. C**49**, 2630(1994).

[77] N. Takigawa, K. Hagino, and M. Abe, Phys. Rev. C**51**, 187(1995).

[78] K. Hagino, N. Takigawa, A.B. Balantekin, and J.R. Bennett, Phys. Rev. C**52**, 286 (1995).

[79] C.H. Dasso, S. Landowne, and A. Winther, Nucl. Phys. **A405**, 381(1983); *ibid* **A407**, 221(1983).

[80] K. Hagino, N. Takigawa, M. Dasgupta, D.J. Hinde, and J.R. Leigh, Phys. Rev. C**55**, 276 (1997).

[81] K. Hagino, N. Takigawa, M. Dasgupta, D.J. Hinde, and J.R. Leigh, Phys. Rev. Lett. **79**, 2014 (1997).

[82] K. Hagino, N. Takigawa, and S. Kuyucak, Phys. Rev. Lett. **79**, 2943 (1997).

[83] K. Hagino, S. Kuyucak, and N. Takigawa, Phys. Rev. C, in press.

[84] K. Hagino, N. Takigawa, and M.Abe, Phys. Rev. C**53**, 1840(1996).

[85] L.D. Landau and E.M. Lifschitz, *Quantum Mechanics*, 3rd ed., (Pregamon, Oxford, 1975).

[86] E. Kemble, Phys. Rev. **48**, 549 (1935).

[87] D.L. Hill and J.A. Wheeler, Phys. Rev. **89**, 1102 (1953).

[88] P. Fröbrich and R. Lipperheide, *Theory of Nuclear Reactions*, (Clarendon, Oxford, 1996).

[89] R.P. Feynman and A.R. Hibbs, *Quantum Mechanics and Path Integrals*, (McGraw-Hill, New York, 1965).

[90] D.M. Brink, *Semi-Classical Methods for Nucleus-Nucleus Scattering*, (University Press, Cambridge, 1985).

[91] D.M. Brink and U. Smilansky, Nucl. Phys. **A405**, 301 (1983).

[92] D.M. Brink and N. Takigawa, Nucl. Phys. **A279**, 159 (1977).

[93] S.Y. Lee, N. Takigawa, and C. Marty, Nucl. Phys. **A308**, 161 (1978).

[94] S.Y. Lee and N. Takigawa, Nucl. Phys. **A308**, 189 (1978).

[95] E. Vigezzi and A. Winther, Ann. Phys. (N.Y.) **192**, 432 (1989).

[96] M.W. Cole and R.H. Good, Phys. Rev. A**18**, 1085 (1978).

[97] C.H. Dasso and S. Landowne, Phys. Lett. **B183**, 141(1987).

[98] K. Langanke, *Advances in Nuclear Physics* vol. 21, edited by J.W. Negele and E. Vogt (Plenum, New York, 1993), p. 85.

[99] S. Bjønholm and W.J. Swiatecki, Nuc. Phys. **A391**, 471(1982).

[100] S. Hofmann, V. Niniv, F.P. Hessberger, P. Arbruster, H. Folger, G. Muenzenberg, H.J. Schoett, A.G. Popeko, A.V. Yeremin, S. Saro, R. Janik, and M. Leino, Z. Phys. **A354**, 229(1996).

[101] J.R. Leigh, D.J. Hinde, J.O. Newton, W. Galster, and S.H. Sie, Phys. Rev. Lett. **48**, 527 (1982).

[102] D.J. Hinde, J.R. Leigh, J.O. Newton, W. Galster, and S.H. Sie, Nucl. Phys. **A385**, 109 (1982).

[103] R.J. Charity, J.R. Leigh, J.J.M. Bokhorst, A. Chatterjee, G.S. Foote, D.J. Hinde, J.O. Newton, S. Ogaza, and D. Ward, Nucl. Phys. **A457**, 441 (1986).

[104] P.H. Stelson, H.J. Kim, M. Beckerman, J. Shapiro, and R.L. Robinson, Phys. Rev. C**41**, 1584(1990).

[105] W.S. Freeman, H. Ernst, D.F. Geesaman, W. Henning, T.J. Humanic, W. Kühn, G. Rosner, J.P. Schiffer, B. Zeidman, and F.W. Prosser, Phys. Rev. Lett. **50**, 1563 (1983); Phys. Rev. C**28**, 919 (1983).

[106] C. Morton, Ph.D. thesis, the Australian National University, 1995.

[107] L.C. Northcliffe, Ann. Rev. Nucl. Sci. **13**, 67 (1963).

[108] R.A. Broglia and A. Winther, *Heavy-Ion Reactions*, (Addison-Wesley, New York, 1991).

[109] Ö. Akyüz and A. Winther, in *Nuclear Structure and Heavy-Ion Collisions,* Proceedings of the International School of Physics "Enrico Fermi, "Course LXXVII, Varenna, 1979, edited by R.A. Broglia *et al.* (North- Holland, Oxford, 1981).

[110] P.R. Christensen and A. Winther, Phys. Lett. **B65**, 19 (1976).

[111] H. Esbensen and B.B. Back, Phys. Rev. C**54**, 3109 (1996).

[112] S. Landowne and S.C. Pieper, Phys. Rev. C**29**, 1352 (1984).

[113] N. Rowley, A. Kabir, and R. Lindsay, J. of Phys. **G15**, L269(1989).

[114] A.B. Balantekin, A.J. DeWeerd, and S. Kuyucak, Phys. Rev. C**54**, 1853 (1996).

[115] H.J. Krappe, J.R. Nix, and A.J. Sierk, Phys. Rev. C**20**, 992 (1979).

[116] M. Inui and S.E. Koonin, Phys. Rev. C**30**, 175 (1984).

[117] A. Bohr and B. Mottelson, *Nuclear Structure* (Benjamin, New York, 1975), vol. 2.

[118] N. Takigawa and K. Ikeda, in *Proceedings of the Symposium on Many Facets of Heavy Ion Fusion Reactions*, edited by W. Henning *et al.*(Argonne National Laboratory Report No. ANL-PHY-87-1), 1986, p.613.

[119] O. Tanimura, Phys. Rev. C**35**, 1600(1987).

[120] H. Esbensen, S. Landowne, and C. Price, Phys. Rev. C**36**, 1216(1987); Phys. Rev. C**36**, 2359(1987).

[121] N. Takigawa, Y. Alhassid, and A.B. Balantekin, Phys. Rev. C**45**, 1850(1992).

[122] J. Gomez-Camacho and R.C. Johnson, J. Phys. **G12**, L235(1986); J. Phys. **G14**, 609(1988).

[123] K. Mclenithan and D. Secrest, J. Chem. Phys. **80**, 2480(1984).

[124] P. McGuire and D.J. Kouri, J. Chem. Phys. **60**, 2488(1974).

[125] K. Moribayashi, S. Takada, and H. Nakamura, J. Chem. Phys. **100**, 4284(1994).

[126] Y. Alhassid, V. Liu, and B. Shao, Phys. Rev. **A48**, 2832(1993); Phys. Rev. **A46**, 3865(1992).

[127] A.T. Kruppa, P. Romain, M.A. Nagarajan, and N. Rowley, Nucl. Phys. **A560**, 845 (1993).

[128] O. Tanimura, Z. Phys. **A327**, 413 (1987).

[129] A.B. Balantekin, J.R. Bennett and N. Takigawa, Phys. Rev. C**44**, 145 (1991).

[130] J. de Boer and J. Eichler, *Advances in Nuclear Physics*, (Plenum, New York, 1968), vol. 1, p. 1.

[131] C.H. Dasso, J. Fernández-Niello, and A. Vitturi, Phys. Rev. C**55**, 2112 (1997).

[132] F. Iachello and A. Arima, *The Interacting Boson Model* (Cambridge University Press, Cambridge, England, 1987).

[133] A.B. Balantekin, J.R. Bennett, A.J. DeWeerd, and S. Kuyucak, Phys. Rev. C**46**, 2019 (1994).

[134] A.B. Balantekin, J.R. Bennett, and S. Kuyucak, Phys. Rev. C **48**, 1269 (1993).

[135] A.B. Balantekin, J.R. Bennett, and S. Kuyucak, Phys. Rev. C**49**, 1079 (1994).

[136] A.B. Balantekin, J.R. Bennett, and S. Kuyucak, Phys. Rev. C**49**, 1294 (1994).

[137] T. Izumoto, T. Udagawa, and B.T. Kim, Phys. Rev. C**51**, 761 (1995).

[138] K. Hagino, T. Rumin, and N. Takigawa, to be published.

[139] D.E. Di Gregorio, J.O.F. Niello, A.J. Pacheco, D. Abriola, S. Gil, A.O. Macchiavelli, J.E. Testoni, P.R. Pascholati, V.R. Vanin, R.L. Neto, N. Carlin Filho, M.M. Coimbra, P.R.S. Gomes, and R.G. Stokstad, Phys. Lett. **B176**, 322 (1986).

[140] N. Rowley and M. Dasgupta, in *Proceedings of the International Workshop on Heavy-Ion Reactions with Neutron-rich Beams*, RIKEN, Saitama, Japan 1993, edited by M. Ishihara, N. Takigawa, and S. Yamaji (World Scientific, Singapore, 1993), p. 232.

[141] H. Esbensen and S. Landowne, Phys. Rev. C**35**, 2090(1987).

[142] N. Rowley, in *Proceedings of the International Workshop on Heavy-Ion Fusion: Exploring the Variety of Nuclear Properties*, edited by A.M. Stefanini *et al.* (World Scientific, Singapore, 1994), p.66.

[143] V. Yu. Denisov and G. Royer, Phys. At. Nucl. **58**, 397(1995); J. Phys. **G20**, L43(1994).

[144] P. Ring and P. Schuck, *The Nuclear Many Body Problem* (Springer-Verlag, New York, 1980).

[145] E.M. Takagui, G.R. Satchler, H. Takai, K. Koide, and O. Dietzsch, Nucl. Phys. **A514**, 120(1990).

[146] D.J. Horen, R.L. Auble, G.R. Satchler, J.R. Beene, I.Y. Lee, C.Y. Wu, D. Cline, M. Devlin, R. Ibbotson, and M.W. Simon, Phys. Rev. C**48**, R2131(1993).

[147] H. Esbensen and S. Landowne, Nucl. Phys. **A492**, 473(1989).

[148] P.R.S. Gomes, I.C. Charret, R. Wanis, G.M. Sigaud, V.R. Vanin, R. Liguori Neto, D. Abriola, O.A. Capurro, D.E. DiGregorio, M. di Tada, G. Duchene, M. Elgue, A. Etchegoyen, J.O. Fernández Niello, A.M.J. Ferrero, S. Gil, A.O. Macchiavelli, A.J. Pacheco, and J.E. Testoni, Phys. Rev. C**49**, 245(1994).

[149] E.F. Aguilera, J.J. Kolata, and R.J. Tighe, Phys. Rev. C**52**, 3103(1995).

[150] V.-S. Lac and S. Kuyucak, Nucl. Phys. **A539**, 418 (1992).

[151] E. Cereda, M. Pignanelli, S. Micheletti, H.V. von Geramb, M.N. Harakeh, R. De Leo, G. D'Erasmo, and A. Pantaleo, Phys. Rev. C**26**, 1941 (1982).

[152] M.J. Smithson, J.S. Lilley, M.A. Nagarajan, P.V. Drumm, R.A. Cunningham, B.R. Fulton, and I.J. Thompson, Nucl. Phys. **A517**, 193 (1990).

[153] D.M. Brink, A.F.R. de Toledo Piza, and A.K. Kerman, Phys. Lett. **B19**, 413 (1965).

[154] T. Tamura and T. Udagawa, Phys. Rev. **150**, 783 (1966).

[155] A. Aprahamian, D.S. Brenner, R.F. Casten, R.L. Gill, and A. Piotrowski, Phys. Rev. Lett. **59**, 535 (1987).

[156] R.F. Casten, N.V. Zamfir, and D.S. Brenner, Phys. Rev. Lett. **71**, 227 (1993).

[157] N.V. Zamfir and R.F. Casten, Phys. Lett. **B341**, 1 (1994).

[158] J. Kern, P.E. Garrett, J. Jolie, and H. Lehmann, Nucl. Phys. **A593**, 21 (1995).

[159] J. Kern and J. Jolie, Phys. Lett. **B364**, 207 (1995).

[160] K.-H. Kim, T. Otsuka, A. Gelberg, P. von Brentano, and P. Van Isacker, Phys. Rev. Lett. **76**, 3514 (1996).

[161] C. Volpe, F. Catara, Ph. Chomaz, M.V. Andrés, and E.G. Lanza, Nucl. Phys. **A589**, 521 (1995).

[162] E.G. Lanza, M.V. Andrés, F. Catara, Ph. Chomaz, and C. Volpe, Nucl. Phys. **A613**, 445 (1997).

[163] G.F. Bertsch and H. Feldmeier, Phys. Rev. C**56**, 839 (1997).

[164] M.P. Metlay, J.L. Johnson, J.D. Canterbury, P.D. Cottle, C.W. Nestor Jr., S. Raman, and V.G. Zelevinsky, Phys. Rev. C**52**, 1801 (1995).

[165] P.D. Cottle and D.A. Bromley, Phys. Rev. C**35**, 1891 (1987).

[166] I. Hamamoto, Nucl. Phys. **A155**, 362 (1970).

[167] B. Sorensen, Phys. Lett. **35B**, 10 (1971).

[168] M. Guidetti, D.J. Rowe, and H. Chow, Nucl. Phys. **A238**, 225 (1975).

[169] A.M.R. Joye, A.M. Baxter, M.P. Fewell, D.C. Kean, and R.H. Spear, Phys. Rev. Lett. **38**, 807 (1977).

[170] M. Yeh, P.E. Garrett, C.A. McGrath, S.W. Yates, and T. Belgya, Phys. Rev. Lett. **76**, 1208 (1996).

[171] R.A. Gatenby, J.R. Vanhoy, E.M. Baum, E.L. Johnson, S.W. Yates, T. Belgya, B. Fazekas, Á. Veres, and G. Molnár, Phys. Rev. C**41**, R414 (1990).

[172] R.A. Gatenby, E.L. Johnson, E.M. Baum, S.W. Yates, D. Wang, J.R. Vanhoy, M.T. McEllistrem, T. Belgya, B. Fazekas, and G. Molnár, Nucl. Phys. **A560**, 633 (1993).

[173] M. Wilhelm, E. Radermacher, A. Zilges, and P. von Brentano, Phys. Rev. C **54**, R449 (1996).

[174] E. Müller-Zanotti, R. Hertenberger, H. Kader, D. Hofer, G. Graw, Gh. Cata-Danil, G. Lazzari, and P.F. Bortingnon, Phys. Rev. C**47**, 2524 (1993).

[175] W. Urban, J.C. Bacelar, J. Jongman, W. Gast, G. Hebbinghaus, A. Krämer-Flecken, R.M. Lieder, M. Thoms, and O. Zell, Phys. Rev. C**53**, 2516 (1996).

[176] L. Bargioni, P.G. Bizzeti, A.M. Bizzeti-Sona, D. Bazzacco, S. Lunardi, P. Pavan, C. Rossi-Alvarez, G. de Angelis, G. Maron, and J. Rico, Phys. Rev. C**51**, R1057 (1995).

[177] M. Piiparinen, P. Kleinheinz, J. Blomqvist, A. Virtanen, A. Atac, D. Müller, J. Nyberg, T. Ramsoy, and G. Sletten, Phys. Rev. Lett. **70**, 150 (1993).

[178] P. Kleinheinz, Prog. Part. Nucl. Phys. **28**, 369 (1992).

[179] R.F. Casten and D.D. Warner, Rev. Mod. Phys. **60**, 389 (1988).

[180] J.N. Ginocchio, Nucl. Phys. **A376**, 438 (1982).

[181] A.F. Barfield, B.R. Barrett, J.L. Wood, and O. Scholten, Ann. Phys. (N.Y.) **182**, 344 (1988).

[182] A.F. Barfield, P. von Brentano, A. Dewald, K.O. Zell, N.V. Zamfir, D. Bucurescu, M. Ivascu, and O. Scholten, Z. Phys. **A332**, 29 (1989).

[183] M. Pignanelli, N. Blasi, S. Micheletti, R. de Leo, M.A. Hofstee, J.M. Schippers, S.Y. van der Werf, and M.N. Harakeh, Nucl. Phys. **A519**, 567 (1990).

[184] A. Jungclaus, H.G. Börner, J. Jolie, S. Ulbig, R.F. Casten, N.V. Zamfir, P. von Brentano, and K.P. Lieb, Phys. Rev. C**47**, 1020 (1993).

[185] M. Grinberg and Ch. Stoyanov, Nucl. Phys. **A573**, 231 (1994).

[186] A. Wolf and R.F. Casten, Phys. Rev. C**36**, 851 (1987).

[187] O. Scholten, Phys. Lett. B**127**, 144 (1983).

[188] H. Kader, G. Graw, F.J. Eckle, G. Eckle, P. Schiemenz, P. Kleinheinz, B. Rubio, G. De Angelis, T.N. Massey, L.G. Mann, and J. Blomqvist, Phys. Lett. **B227**, 325 (1989).

[189] L.K. Peker, Nucl. Data Sheets **59**, 393 (1990).

[190] D. Hilscher and H. Rossner, Ann. Phys. Fr. **17**, 471(1992).

[191] T. Wada, Y. Abe, and N. Carjan, Phys. Rev. Lett. **70**, 3538(1993).

[192] D.J. Hinde, D. Hilscher, and H. Rossner, Nucl. Phys. **A502**, 497c(1989).

[193] N. Bohr and J.A. Wheeler, Phys. Rev. **56**, 426 (1939).

[194] M. Thoennessen and G.F. Bertsch, Phys. Rev. Lett. **71**, 4303(1993).

[195] R. Vandenbosch, Phys. Rev. C**50**, 2618(1994).

[196] H. van der Plog, J.C.S. Bacelar, I. Dioszegi, G. van't Hof and A. van der Woude, Phys. Rev. Lett. **75**, 970(1995).

[197] D. Fabris, G. Viesti, E. Fioretto, M. Cinausero, N. Gelli, K. Hagel, F. Lucarelli, J.B. Natowitz, G. Nebbia, G. Prete, and R. Wada, Phys. Rev. Lett. **73**, 2676 (1994).

[198] P. Fröbrich, I.I. Gontchar, and N.D. Mavlitov, Nucl. Phys. **A556**, 281(1993).

[199] P. Grangé, S. Hassani, H.A. Weidenmüller, A. Gavron, J.R. Nix, amd A.J. Sierk, Phys. Rev. C**34**, 209(1986).

[200] N.R. Dagdeviren and H.A. Weidenmüller, Phys. Lett. **B186**, 267(1987).

[201] F. Barranco, G.F. Bertsch, R.A. Broglia, and E. Vigezzi, Nucl. Phys. **A512**, 253(1990).

[202] P. Lotti, F. Cazzola, P.F. Bortignon, R.A. Broglia, and A. Vitturi, Phys. Rev. C**40**, 1791(1989).

[203] F. Alassia, O. Civitarese, amd M. Reboiro, Phys. Rev. C**35**, 812(1987).

[204] O. Civitarese, G.G. Dussel, and R.P.J. Perazzo, Nucl. Phys. **A404**, 15(1983).

[205] A. Iwamoto and W. Greiner, Z. Phys. **A292**, 301(1979).

[206] N. Takigawa, S. Yoshida, K. Hagino, S.K. Patra, and C.R. Praharaj, Phys. Rev. C**53**, 1038 (1996).

[207] S. Yoshida and N. Takigawa, Phys. Rev. C**55**, 1255 (1997).

[208] J.S. Langer, Ann. Phys. (N.Y.) **41**, 108(1967); G. Callan and S. Coleman, Phys. Rev. D**16**, 1762(1977); I.K. Affleck, Phys. Rev. Lett. **46**, 388(1981).

[209] H. Grabert, P. Olschowski and U. Weiss, Phys. Rev. **B36**, 1931(1987).

[210] N. Takigawa and M. Abe, Phys. Rev. C**41**, 2451(1990).

[211] P. Fröbrich and G.-R. Tillack, Nucl. Phys. **A540**, 353(1992).

[212] J.-D. Bao, Y.-Z. Zhuo and X.-Z. Wu, Phys. Lett. **B327**, 1(1994); Z. Phys. **A347**, 217(1994).

[213] P. Hänggi, P. Talkner,and M. Borkovec, Rev. Mod. Phys. **62**, 251(1990).

[214] R.P. Feynman, *Statistical Mechanics*, (Benjamin, Reading, Massachussets, 1972).

[215] A. Gavron, in *Computational Nuclear Physics 2 Nuclear Reactions*, edited by K. Langanke, J.A. Maruhn, and S.E. Koonin, (Springer-Verlag, New York, 1993), p. 108.

[216] H. Grabert, P. Schramm, and G.-L. Ingold, Phys. Rep. **168**, 115(1988).

[217] H. Kramers, Physica (Utrecht) **7**, 284 (1940).

[218] P. Grangé, L. Jun-Qing, and H.A. Weidenmüller, Phys. Rev. C**27**, 2063(1983).

[219] M. Matsumoto and Y. Ohashi, J. Phys. Soc. Jpn. **62**, 2088(1993); Y. Ohashi and M. Matsumoto, J. Phys. Soc. Jpn. **62**, 3532(1993).

[220] A. Staszczak, S. Pilat, and K. Pomorski, Nucl. Phys. **A504**, 589(1989).

[221] J.W. Negele, S.E. Koonin, P. Möller, J.R. Nix, and A.J. Sierk, Phys. Rev. C**17**, 1098(1978).

[222] H. Hofmann, F.A. Ivanyuk, and S. Yamaji, Nucl. Phys. **A598**, 187(1996).

[223] P. Paul and M. Thoennessen, Ann. Rev. Part. Nucl. Sci. **44**, 65(1994).

[224] D.J. Hofman, B.B. Back, and P. Paul, Phys. Rev. C**51**, 2597(1995).

[225] J.R. Nix, Nucl. Phys. **A502**, 609c(1989).

[226] Y.R. Shimizu, E. Vigezzi, T. Døssing, amd R.A. Broglia, Nucl. Phys. **A557**, 99c(1993).

[227] P. Ring, H. Massmann, and J.O. Rasmussen, Nucl. Phys. **A296**, 50 (1978).

[228] J. Raynal, Phys. Rev. C**23**, 2571(1981).

[229] I.J. Thompson, Comput. Phys. Rep. **7**, 167 (1988).

[230] S.E. Koonin and D.C. Meredith, *Computational Physics Fortran Version*, (Addison-Wesley, 1990).

[231] M.A. Melkanoff, T. Sawada, and J. Raynal, *Methods in Computational Physics*, vol. 6, 1 (1966).

[232] K. Hagino, N. Rowley, and A.T. Kruppa, (to be published).